UNIVERSITE DE LORRAINE
Ecole Nationale Supérieure des Mines de Nancy
Laboratoire GeoRessources
Ecole Doctorale RP2E

THESE

Présentée en vue du grade de

DOCTEUR DE L'UNIVERSITE DE LORRAINE
en Génie Civil-Hydrosystèmes-Géotechnique

Par

Yinfei CAI

Simulation of underground mining subsidence and its induced damages on buildings

Simulation des affaissement miniers et de leurs conséquences sur le bâti

le 13 Mars 2015

Devant le jury composé de

Alec M. MARSHALL – University of Nottingham – UK	Rapporteur
José M. GALERA – Universidad Politécnica de Madrid – Spain	Rapporteur
Marwan AL-HEIB – INERIS – France	Examinateur
Hussein MROUEH – Université Lille 1 – France	Examinateur
Thierry VERDEL – Université de Lorraine – France	Directeur de thèse
Olivier DECK – Université de Lorraine – France	Co-directeur de thèse
Karim BEN SLIMANE – BRGM – France	Invité

Abstract

The exploitation of underground mineral resources often causes subsidence phenomena on the ground surface. In urban regions, these phenomena may induce small to severe damage to buildings.

The objective of this thesis is to improve the methods of subsidence computation and building damage evaluation, and to develop some tools based on these methods to study the mining subsidence and building damage cases in Lorraine.

By investigating the topography influence on subsidence under simplified mining conditions, and using numerical models with varying mining depths and ground surface angles, a new influence function method, which is based on a probability density function of a skew normal distribution, to simulate the element subsidence, was firstly developed and can be used to compute the mining subsidence caused by the excavation under non-flat surface. Several numerical simulations and two field subsidence cases were studied and showed that compared to the original influence function method, the improved method better simulated subsidence, especially in terms of horizontal displacements.

Then, plane framed structural models were chosen to study the mechanical behavior of 3D buildings. For each building, two plane models located in the vertical sections passing through the principle inertia axes of the building's projective polygon were considered. Their geometry and mechanical characteristics were chosen according to the construction type and used materials of the building under consideration. Then, by using the matrix displacement method with some modifications, the internal forces and displacements for the entire structure could be computed. The achieved internal forces could then be compared to damage grade criteria to determine the extent of building damage.

Finally, by using the improved methods of subsidence computation and building damage evaluation, a real case application was performed in Joeuf city (France). The subsidence was computed and applied to the defined structural models as support displacements, and then the damage extents of the buildings in Joeuf were predicted. In the worst case, if all six

possible mining zones in two layers under Joeuf city were considered collapsed, the maximum vertical subsidence and horizontal displacement were approximately equal to 2 m and 1 m, respectively, and 37% of the buildings in the city were in high danger.

Keywords: mining subsidence, topography influence, numerical simulation, asymmetrical influence function, building damage assessment, matrix displacement method, structural modeling

Résumé

L'exploitation des ressources minérales souterraines entraîne souvent des affaissements de terrain à la surface. Dans les zones urbanisées, ces affaissements peuvent entraîner des dommages importants aux bâtiments.

L'objectif de cette thèse est de proposer une amélioration des méthodes d'estimation des cuvettes d'affaissement et des méthodes d'évaluation des dommages susceptibles de se produire sous leurs effets puis de développer des outils basés sur ces méthodes pour étudier les affaissements et les dommages sur des cas pratiques.

Par l'étude de l'influence de la topographie sur la formation des cuvettes d'affaissement, sous des conditions d'exploitation simplifiée et par l'utilisation de modèles numériques sous différentes conditions de profondeur et de pente en surface, une nouvelle fonction d'influence, basée sur une densité de probabilité normale asymétrique, est proposée. Au contraire des méthodes courantes existantes, elle permet d'améliorer le calcul de la cuvette d'affaissement quand la surface du sol n'est pas plane, comme le montrent plusieurs comparaisons avec des simulations numériques et deux cas d'études.

Ensuite, nous introduisons une modélisation simplifiée des habitations en maçonnerie sous la forme de 2 modèles de structures bidimensionnels croisés, alignés avec les axes d'inertie de la structure étudiée et dans lesquels la méthode des déplacements est mise en œuvre pour calculer les efforts internes et les déformations sous l'effet de déplacements imposées des fondations. Ces modèles simplifiés dont les caractéristiques géométriques et mécaniques sont définis pour chaque type de bâtiment étudié, permettent d'estimer les efforts appliqués à chaque bâtiment d'une ville exposée à un affaissement de terrain et de fournir de nouveaux critères d'évaluation des dommages prenant en compte davantage d'informations que les méthodes habituelles.

Finalement, sur la base des nouvelles méthodes proposées tant pour le calcul de l'affaissement que pour l'estimation des dommages, nous proposons une estimation des dommages dans la ville de Joeuf qui nous amène au chiffre de 37% des habitations

susceptibles d’être gravement endommagées, dans le pire des scénarios d’affaissement considéré.

Cette thèse est structurée en quatre chapitres:

Chapitre 1

Les affaissements miniers et leurs dégâts sur les constructions sont l’objet de cette thèse, et sont brièvement présentés dans ce chapitre.

Tout d'abord, nous présentons et illustrons le concept de cuvette d’affaissement, les facteurs qui la définissent tels l'affaissement vertical, le déplacement horizontal, la pente, la courbure, et certains paramètres qui la caractérisent comme la valeur de l'affaissement maximal et l'angle de l'influence. Puis, les affaissements historiques causés par les exploitations souterraines en Lorraine (France) en utilisant la méthode des chambres et piliers sont examinés. Ainsi, depuis 1996, plusieurs affaissements ont endommagé plus de cinq cents bâtiments. Enfin, nous présentons plusieurs méthodes utilisées pour prédire l'affaissement induit par une exploitation minière souterraine telles que des méthodes empiriques, la méthode des profils, la méthode des fonctions d'influence, la méthode des modèles physiques ou encore les méthodes numériques. La méthode des fonctions d'influence est présentée plus en détail et fera l’objet d’amélioration dans les chapitres suivants afin de prendre en compte l'influence des variations topographiques.

Dans la pratique, la déformation horizontale et la courbure, qui sont respectivement induites par des déplacements horizontaux et verticaux non uniformes, sont des paramètres critiques responsables des dommages dans les constructions. Leurs influences sur un bâtiment sont présentées. Les méthodes empiriques, analytiques et numériques peuvent être utilisées dans l'évaluation des dommages aux bâtiments situés en zone d’affaissement. La méthode des éléments finis (FEM), sera utilisée dans un cadre particulier afin d'évaluer les dommages de construction à grande échelle (une ville par exemple).

Chapitre 2

La méthode des fonctions d'influence est largement utilisée dans le calcul des affaissements

miniers. La méthode originale est bien adaptée à la prédiction de l'affaissement induit par l'extraction d'une couche horizontale d'une mine souterraine située sous une surface plane, mais fournit des résultats incorrects lorsque la surface n'est pas plane. Une première partie présente quelques fonctions d'influence usuelles, le principe originel de la méthode des fonctions de d'influence et les caractéristiques de l'affaissement pour une topographie plane.

Les conditions d'exploitation réelles sont généralement trop compliquées pour séparer l'influence topographique de l'influence d'autres facteurs. Néanmoins, par le biais de modélisations numériques simplifiées, nous pouvons analyser l'influence de la topographie seulement. C'est ce que nous faisons en utilisant des modèles comportant une seule formation rocheuse au dessus d'une couche exploitée horizontale et dans lesquels la topographie est constituée d'une pente constante. Dans de telles conditions d'exploitation simplifiées, la manière dont les caractéristiques de l'affaissement sont affectées par la topographie peut être étudiée.

Ainsi, deux nouvelles fonctions d'influence asymétriques sont suggérées pour calculer le déplacement vertical et horizontal. Elles sont basées sur des fonctions de densité de probabilité normales corrigées par des fonctions d'erreur complémentaires. Leurs paramètres peuvent être reliés à l'angle d'inclinaison de la surface et la profondeur moyenne de l'exploitation minière, ce qui permet à ces nouvelles fonctions d'influence de prendre en compte les variations topographiques. Après cela, les déplacements verticaux et horizontaux à chaque point de surface peuvent être calculées par la méthode de superposition standard et la cuvette d'affaissement à grande échelle peut être calculée.

La méthode ainsi améliorée requiert la connaissance ou l'estimation de l'affaissement maximal attendu ainsi que des angles d'influence qui peuvent être obtenus à partir de données de terrain. Plusieurs simulations numériques et deux cas test, respectivement en France et en Chine, ont été étudiés et montrent l'amélioration obtenue par rapport à la méthode des fonctions d'influence originale, notamment en termes de déplacements horizontaux.

Chapitre 3

Ce chapitre vise à présenter une méthode de modélisation du comportement mécanique d'habitations civiles à une grande échelle (une ville par exemple) afin de fournir une estimation préliminaire des dommages induits par un affaissement minier. Comme la précision requise n'est pas nécessairement élevée, il est communément admis que des modèles 2D, qui ont l'avantage de la programmation facile et du calcul rapide, peuvent être utilisés pour résoudre des problèmes structuraux 3D.

Dans le présent chapitre, deux modèles structurels plans sont mis en place dans des sections verticales passant par les axes principaux d'inertie du polygone de projection horizontale d'un bâtiment. Ils sont utilisés pour simuler un bâtiment 3D du monde réel.

La méthode matricielle des déplacements est alors utilisée. Quelques modifications sont apportées à cette méthode pour tenir compte des avantages de Mathematica™. Les modèles structurels, simplication de la structure réelle, sont d'abord préparés par la discrétisation du modèle en listes de nœuds et d'éléments. Ensuite, les relations force-déplacement d'un élément sont introduites de façon traditionnelle. Après cela, en vue d'organiser les relations force-déplacement de l'ensemble du modèle structurel, nous sautons l'étape de l'organisation de la matrice de rigidité de la structure en résolvant directement un ensemble d'équations composées des conditions d'équilibre des forces dans le système de coordonnées global à chaque noeud. Enfin, les forces internes et les déplacements dans le modèle structurel peuvent être résolus. Notre méthode a été vérifiée par des comparaisons avec deux logiciels commerciaux.

Les niveaux de dégradation du bâtiment modélisé peuvent être déterminées à partir des forces internes calculées dans la structure : forces axiales, forces de cisaillement et moments de flexion, grâce à l'utilisation de critères associant des plages de valeurs de ces forces aux différents niveaux de dommages. L'étendue des dommages peut être appréciée à partir de l'une des forces internes et son critère correspondant, ou à partir de deux d'entre elles et de leurs critères correspondants, ou de toutes les trois et leurs critères. Grâce au code

développé, les dommages peuvent être intuitivement présentés sur la structure déformée par des lignes colorées utilisées pour distinguer les différents niveaux de dommage. La cinématique des dommages de la structure est également disponible.

En pratique, la portée de la méthode développée dans ce chapitre est plus grande que l'évaluation des dommages de construction induites par un affaissement minier. Elle peut également être utilisée pour étudier les dommages dus à des forces externes et des déplacements arbitraires.

Chapitre 4

Dans ce chapitre, en utilisant les méthodes de calcul d'affaissement (présenté dans le chapitre 2) et du calcul de dommages aux bâtiments (présenté dans le chapitre 3), une application est effectuée dans la ville de Joeuf, qui est située au-dessus d'une zone d'extraction minière et se trouve dans une vallée. Plus de 1 500 bâtiments composent cette ville habitée de plus de 7000 personnes. L'affaissement minier est l'aléa principal auquel est exposé cette ville.

Sous Joeuf, six zones ont été exploitées en deux couches (couche grise et couche S2-S3). Prenant les données topographiques et minières en compte, et compte tenu de la valeur de l'affaissement maximum local attendue et de l'angle d'influence dans cette région, nous pouvons calculer l'affaissement prévisionnel à Joeuf. Lors du calcul, plusieurs combinaisons d'effondrement des zones minières peuvent être envisagées.

Selon les données relatives aux bâtiments de la ville de Joeuf, cinq ensembles de modèles structurels typiques (deux modèles pour chaque) sont choisis pour les simuler. Les propriétés des éléments de structure (la rigidité en flexion EI et la rigidité axiale EA) ainsi que les charges initiales sont définies (pour les murs, le premier étage, et les autres étages) pour les différents types de bâtiments, de même que les assemblages d'éléments relativement à la géométrie des ouvrages. Un modèle longitudinal et un modèle transversal sont considérés pour chaque bâtiment.

L'affaissement calculé est ensuite utilisé dans les modèles structurels en tant que

déplacements imposés aux éléments support afin de calculer les forces internes. En comparant les forces internes avec des critères de dommages, les niveaux de dommages de tous les bâtiments de Joeuf peuvent être évalués. Selon les forces axiales et les moments fléchissant sur les structures, 19%, 23%, et 37% des bâtiments sont en danger élevé en vertu de l'affaissement causé par l'effondrement de la couche grise, la couche S2-S3, ou des deux couches, respectivement. Une comparaison avec une méthode existante montre également que la nouvelle méthode fournit des résultats crédibles.

Mots-clefs : Affaissement minier, influence de la topographie, simulation numérique, fonction d'influence asymétrique, évaluation des dommages aux bâtiments, méthode des déplacements, modélisation des structures

Remerciements

I would like to express my gratitude to all those who helped me during the writing of this thesis.

My deepest gratitude goes first and foremost to Professor Thierry Verdel and Olivier Deck, my supervisors, for their constant encouragement and guidance. They have walked me through all the stages of the writing of this thesis. Without their consistent and illuminating instruction, this thesis could not have reached its present form.

Second, I would like to express my heartfelt gratitude to my dear colleagues, especially to Abla-Mimi Edjossan-sossou, who has always been helping me out of difficulties and supporting without a word of complaint.

Last my thanks would go to my beloved family for their loving considerations and great confidence in me all through these years.

Table of contents

List of figures

List of tables

General introduction

France was one of the major mining nations until the second half of the 20th century. In Lorraine, the iron basin was intensively exploited from the late 19th century, and the last exploitation was stopped in 1997. The exploitation in Lorraine left 120 km^2 of undermined zones, including 20 km^2 under urban zones.

The room and pillar mining method is usually employed in the mining fields under or close to cities where subsidence is not desired. Now, in Lorraine, there are a lot of abandoned extraction zones supported by pillars at different depths due to old exploitations; some of them are very close to the ground surface. In terms of risk analysis, these extraction zones are a hazard. Because, after a quite long time since the excavation, the pillars may no more withstand the weight of the overburden and fall to rupture, then a subsidence may appear on the ground surface and induce damages to surface buildings and infrastructures.

Since 1996, several subsidence accidents occurred in the iron basin in Lorraine. The subsidence, which happened in Auboué (1996), Moutiers (1997) and Roncourt (1999), has damaged more than five hundred buildings. Subsidence in a city does not have the same consequences to subsidence in a wild area because it might cause unexpected economical, environmental, social, and political chain reactions.

The development of cities located in old mining zones is highly dependent on the controls of the mining risks, particularly those regarding buildings. So, it is quite necessary to improve and extend the current subsidence calculation and risk assessment technologies. Therefore, the objective of this thesis is to improve and develop methods and tools of subsidence computation as well as of building damage evaluation.

To achieve the objective, this thesis is composed of four parts.

The first part introduces briefly the mining subsidence and the evaluation of building damage. Above all, some necessary concepts of subsidence, the historical subsidence issues in Lorraine, and the available methods of subsidence computation are presented. Then, the behavior of buildings affected by subsidence and the methods of building damage evaluation are introduced.

The second part is dedicated to an improvement of the original influence function method in order to take the surface topography into account in the calculation of vertical subsidence and horizontal displacement due to underground excavation. We make use of simplified numerical simulations to study the relationships between topography and subsidence. We then suggest not only parameter adjustments but also new influence functions, so that the influence function method can better simulate non-horizontal surface conditions.

The third part makes use of simplified plane framed structural models to study the mechanical behaviors of real 3D buildings influenced by mining subsidence. By using the matrix displacement method with some modifications, and applying the subsidence to the structure as support displacements, the internal forces and displacements over the structure can be computed and compared to criteria related to damage assessment.

The fourth part deals with a real case application in Joeuf city. Taking the topography and mining polygon data into account, we calculate the expected subsidence all over the city. Then, considering different building shapes, element properties, initial loads, and the computed subsidence, the internal forces and displacements of the buildings' models are obtained for all buildings of the city. The assessment of building damage caused by subsidence can then be obtained through the comparison between the computed internal forces and predefined damage grade criteria.

The general introduction of this thesis, the main achievements (two improved methods and corresponding developed codes), the brief solving processes of subsidence computation and building damage evaluation can be found in Figure 0.

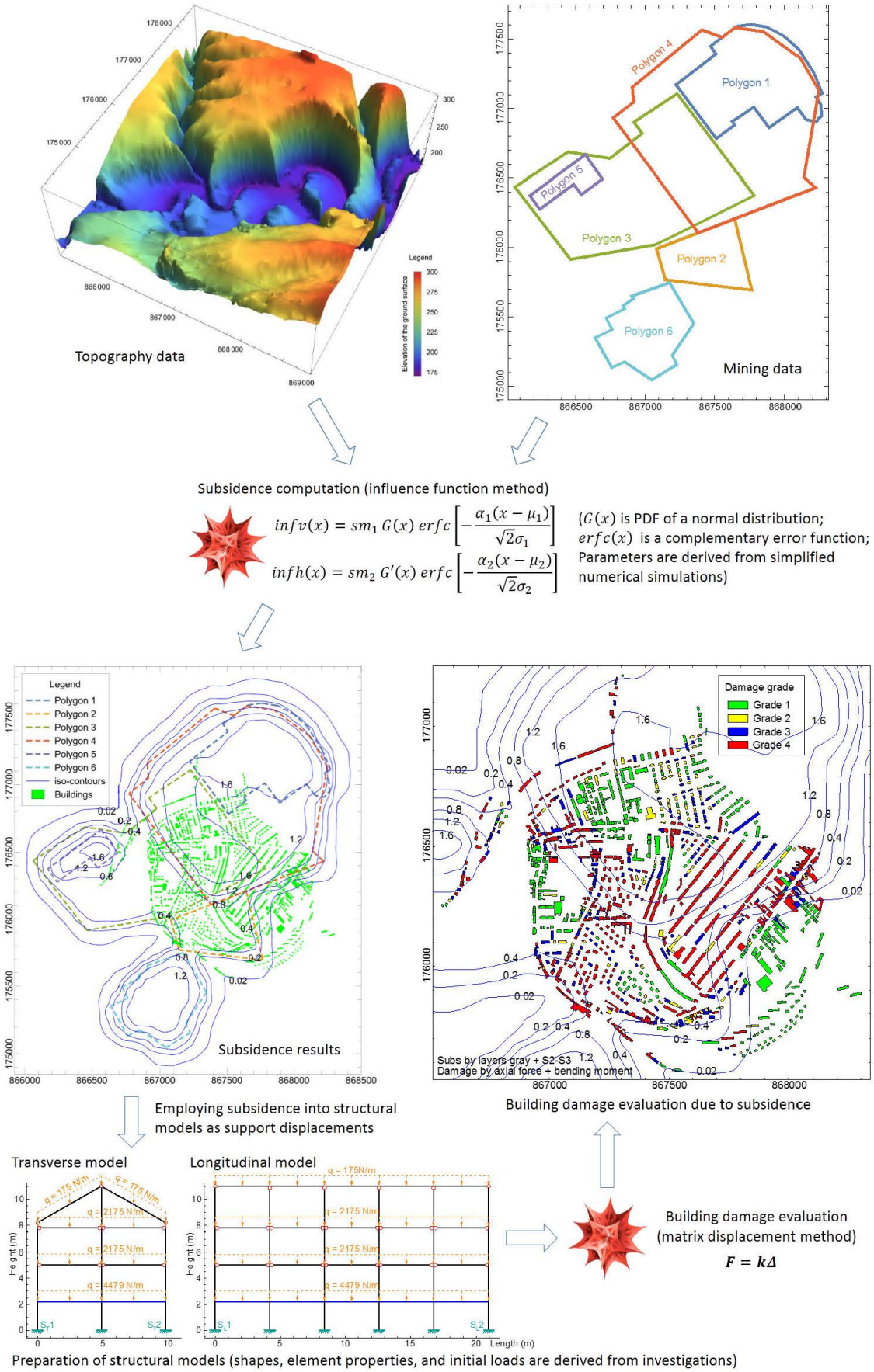

Figure 0. Scheme of the general organization of this thesis

Introduction générale

La France fut l'une des principales nations minières jusqu'à la moitié du 20e siècle. En Lorraine, le bassin ferrifère fut ainsi exploité intensivement à partir de la fin du 19^{e} siècle et la dernière exploitation a fermé en 1997. Elle a représenté 120 km^2 de zones sous-cavées parmi lesquelles 20 km^2 sont urbanisées. C'est la méthode des chambres et piliers abandonnés qui est généralement utilisée dans les gisements se trouvant sous des zones habitées afin d'éviter l'affaissement des terrains. Aujourd'hui en Lorraine, il existe un très grand nombre d'excavations minières ainsi abandonnées à des profondeurs variables. En termes d'analyse de risque, ces excavations constituent un aléa car, longtemps après l'exploitation, les piliers peuvent ne plus résister au poids des terrains sus-jacents et leur rupture peut alors entraîner un mouvement du sol qui lui-même peut entraîner des dommages aux bâtiments et infrastructures en surface.

Depuis, 1996, plusieurs affaissements miniers se sont produit en Lorraine. Ceux de Auboué (1996), Moutiers (1997) et Roncourt (1999) ont ainsi endommagé plus de 500 habitations. U délà des dommages aux habitations, de tels affaissements, quand ils se produisent en zone urbaine, peuvent également entraîner des conséquences économiques, environnementales, sociales et politiques.

Le développement des villes situées dans des zones d'exploitation minières dépend beaucoup des moyens de contrôle des aléas miniers, en particulier ceux qui peuvent affecter les bâtiments. Ainsi, il est tout à fait nécessaire d'améliorer les moyens actuels de calcul prévisionnel des affaissements et de leurs conséquences. Ainsi, l'objectif de cette thèse est d'améliorer et de développer les méthodes et outils de calcul des cuvettes d'affaissement ainsi que d'évaluation des dommages au bâti.

Pour atteindre cet objectif, le mémoire comprend 4 parties.

La première décrit brièvement les affaissements miniers et l'évaluation des dommages au bâti. Les concepts et méthodes de calcul disponibles sont présentés, tant pour la cuvette d'affaissement que pour l'étude du comportement des bâtiments en zone affaissées et des dommages occasionnés sur eux.

La deuxième partie est consacrée à une amélioration de la méthode des fonctions d'influence afin de prendre en compte la topographie de surface dans le calcul de l'affaissement vertical et du déplacement horizontal induit par une excavation souterraine. Nous faisons usage de simulations numériques simplifiées pour étudier les relations entre la topographie et l'affaissement. Nous proposons alors non seulement le réglage de certains paramètres mais aussi de nouvelles fonctions d'influence, de sorte que la méthode introduite permet de mieux simuler les déplacements de la surface quand celle-ci n'est pas horizontale.

La troisième partie fait usage de modèles structuraux simplifiés pour étudier le comportement mécanique de bâtiments réels influencés par un affaissement minier. En utilisant la méthode des déplacements avec certaines modifications, et en utilisant les

déplacements calculés pour l'affaissement comme sollicitation des fondations de ces modèles, les forces internes et les déplacements sur la structure peuvent être calculées et comparées à des critères d'évaluation des dommages.

La quatrième partie traite d'une application réelle au cas de la ville de Joeuf en Lorraine pour une hypothèse d'étendue de mine effondrée. Sur la base des données topographiques et de la géométrie du secteur minier effondré, nous calculons l'affaissement attendu partout dans la ville. Ensuite, compte tenu de différentes formes de construction, de leurs propriétés, des charges initiales, et de l'affaissement calculé en tout point, les forces internes et les déplacements des modèles des bâtiments sont obtenus pour tous les bâtiments de la ville. L'évaluation des dommages aux bâtiments peut alors être obtenue par la comparaison entre les forces internes calculées et les critères d'endommagement prédéfinis.

Chapter 1: State of the art in mining subsidence and building damage assessment

Chapitre 1: Etat de l'art dans le calcul des affaissements miniers et des dommages induits aux bâtiments

Abstract of chapter 1

Mining subsidence and its induced building damage are the topics of this thesis, and introduced briefly in this chapter.

First, the mining subsidence trough on the ground surface, subsidence factors, including vertical subsidence, horizontal displacement, slope, horizontal strain, and curvature, and some subsidence parameters, such as maximum subsidence value and influence angle, are illustrated. Then, the historical subsidence phenomena caused by underground exploitations in Lorraine (France) using the room and pillar method are reviewed. Currently in Lorraine, there are a lot of abandoned extraction zones supported by pillars due to old exploitations, including 20 km^2 under urban zones. Since 1996, several subsidence accidents that have occurred in the cities have damaged more than five hundred buildings. There are many methods that have been used to predict the subsidence induced by underground mining, including empirical methods, profile function methods, influence function methods, analytical methods, physical model methods and numerical methods. The influence function method will be studied and improved in the following chapters to take topographic influence into account.

In practice, the horizontal strain and curvature, which are induced by non-uniform horizontal displacement and vertical subsidence, respectively, are critical factors that cause building damages in subsidence area. Their influences on a building are introduced. Empirical, analytical, and numerical methods can be used in the assessment of building damage in mining subsidence areas. The numerical method, specifically the finite element method (FEM), will be used and improved in the following chapters in order to evaluate the building damages at a large scale (a city for instance).

Résumé du chapitre 1

Les affaissements miniers et leurs dégâts sur les constructions sont l'objet de cette thèse, et sont brièvement présentés dans ce chapitre.

Tout d'abord, nous présentons et illustrons le concept de cuvette d'affaissement, les facteurs qui la définissent tels l'affaissement vertical, le déplacement horizontal, la pente, la courbure, et certains paramètres qui la caractérisent comme la valeur de l'affaissement maximal et l'angle de l'influence. Puis, les affaissements historiques causés par les exploitations souterraines en Lorraine (France) en utilisant la méthode des chambres et piliers sont examinés. Ainsi, depuis 1996, plusieurs affaissements ont endommagé plus de cinq cents bâtiments. Enfin, nous présentons plusieurs méthodes utilisées pour prédire l'affaissement induit par une exploitation minière souterraine telles que des méthodes empiriques, la méthode des profils, la méthode des fonctions d'influence, la méthode des modèles physiques ou encore les méthodes numériques. La méthode des fonctions d'influence est présentée plus en détail et fera l'objet d'amélioration dans les chapitres suivants afin de prendre en compte l'influence des variations topographiques.

Dans la pratique, la déformation horizontale et la courbure, qui sont respectivement induites par des déplacements horizontaux et verticaux non uniformes, sont des paramètres critiques responsables des dommages dans les constructions. Leurs influences sur un bâtiment sont présentées. Les méthodes empiriques, analytiques et numériques peuvent être utilisées dans l'évaluation des dommages aux bâtiments situés en zone d'affaissement. La méthode des éléments finis (FEM), sera utilisée dans un cadre particulier afin d'évaluer les dommages de construction à grande échelle (une ville par exemple).

1.1 Mining subsidence caused by underground excavation

Subsidence is the motion of a surface (usually, the ground surface) as it shifts downward relative to its initial position. In this research, the large-scale continuous ground surface subsidence, which is caused by the extraction of sub-surface ore bodies, is concerned. Discontinuous subsidence (due to existing faults for instance), sudden subsidence (landslides and sinkholes for instance), sub-surface rock layers' subsidence, or subsidence caused by non-mining reasons are not under study in the present work.

Around the world, underground mineral resources, particularly carbon (coal) and iron, have been exploited in many countries, like England, France, Germany, Poland, Russia and Ukraine in Europe, and Australia, China, South Africa, United States, and Peru on other continents. The exploitation of these underground resources usually leads to mining subsidence.

1.1.1 Underground extraction zone and ground mining subsidence

Mining subsidence causes the appearance of a bowl-shape subsidence trough (also named subsidence basin) on the ground surface. The subsidence trough has a three-dimensional geometry that depends on many factors related to the mining method, the geometry of the extraction zone, the underground geology and its mechanical properties, the surface topography, and so on.

As in Figure 1, which illustrates half of a vertical section of the subsidence trough, several parameters of the mining zone are relevant in subsidence studies, including the depth, thickness, and length. With these parameters, the location and the shape of the extraction zone can be determined.

The curves of vertical subsidence (or vertical displacement), horizontal displacement, slope, horizontal strain, and curvature, which can be used to quantitatively represent the mining subsidence, are shown in Figure 1. For each surface point, the vertical subsidence and horizontal displacement can be considered as the movement distance from the original position to the position after subsidence in the vertical and horizontal directions, respectively. These quantities often can be obtained by in situ measurements. The slope is defined as the first derivative of the vertical subsidence, and the curvature is defined as the first derivative of the slope (i.e. the second derivative of the vertical subsidence). The horizontal strain is the first derivative of the horizontal displacement.

The maximum vertical subsidence (Sm), angle of influence (φ), and angle of break (β) are commonly concerned subsidence parameters as shown in Figure 1, and sometimes are known in a particular mining zone. In Lorraine, for instance, the maximum vertical subsidence value is about 20 – 40% of the mining thickness (Deck 2002). The influence angle is used to describe the edge of the subsidence trough, while the break angle is employed to depict the location of the maximum positive horizontal strain (in the tension area). Usually, the angles of influence and break are 10 – 40° and -10 – 20° (Deck 2010, Saeidi 2009, 2015), respectively.

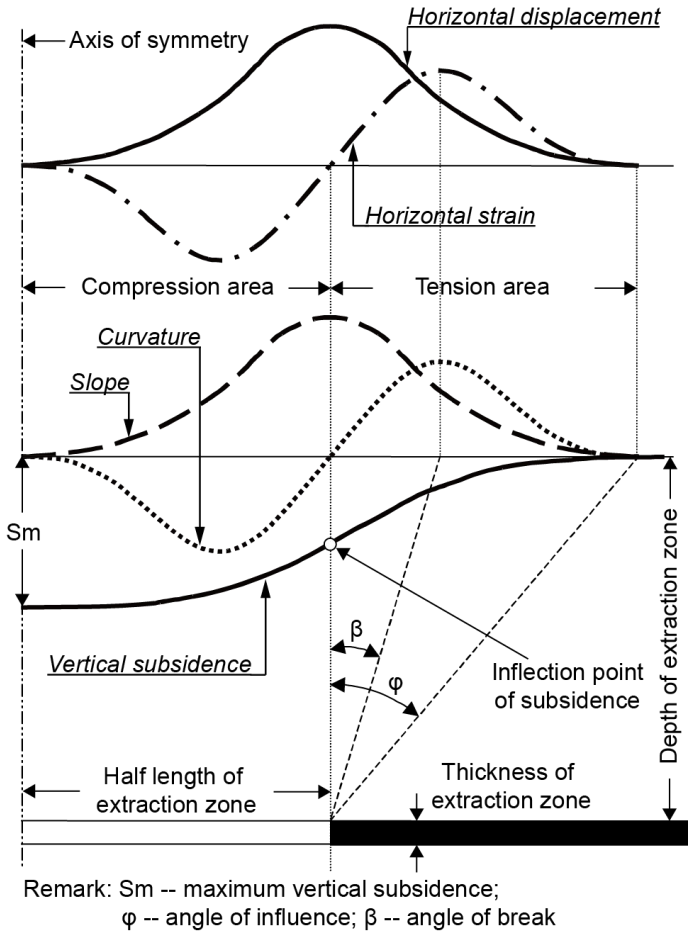

Figure 1. The presentation of extraction zone and mining subsidence (Deck 2002)

To distinguish the mining extent, three terminologies are used, including critical area, subcritical area, and supercritical area (NCB 1975). Critical area refers to an area of working, which causes the complete subsidence (i.e. the maximum subsidence under a certain mining condition) of one point on the surface; subcritical area and supercritical area are the areas of working smaller and greater than a critical area. Subsidence caused by the critical, subcritical, and supercritical mining areas can be termed as critical, subcritical, and supercritical subsidence, respectively.

1.1.2 Mining subsidence in Lorraine

France was one of the major mining nations until the second half of the 20th century, especially rich in coal and iron minerals. But the exploitations in France are totally stopped now.

In Lorraine, the iron basin was intensively exploited from the late 19th century. Until the 1960s, 63 million tons of minette, which consists of iron ore of sedimentary origin, were extracted, benefiting from an increase in industrial production. After that, the production fell due to international competition. The last exploitation was closed in 1997. In Lorraine, the excavated area was around 1300 km^2, and more than 3 billion tons of iron ore were extracted

(DDE, 2005).

Two major mining technologies, both based on the room and pillar method, were employed: in the first, after excavating the rooms, the remaining pillars were also excavated starting at the farthest point from the stope access so that the overburden collapsed, usually leading to a surface subsidence but eliminating almost any residual risk; while in the second, the rooms and pillars were left in place to serve as a long-term ground support, especially under urban zones where any ground movement is not desired. With the second method, a sufficient number of pillars (with a sufficient size) must be left in order to ensure the stability of the extracted zones. In many cases, protective pillars were kept under urban areas to prevent any risk of subsidence (Geoderis, 2000).

As a result, now in Lorraine, there are a lot of abandoned extraction zones supported by pillars at different depths due to old exploitations; some of them being relatively very close to the surface (few meters). In terms of risk analysis, these extraction zones can be considered as hazard zones. As mentioned in many researches carried out by the GISOS[1], it is exactly the excavations with the method of abandoned rooms and pillars that cause subsidence problems today. The subsidence process is shown as in Figure 2: due to the fact that pillars can no longer withstand the weight of the overburden after a quite long time and fall to rupture, the overlying layers may gradually settle due to the instability of the remaining pillars, then the subsidence appears on the surface and the buildings (or other surface features) suffer destructions.

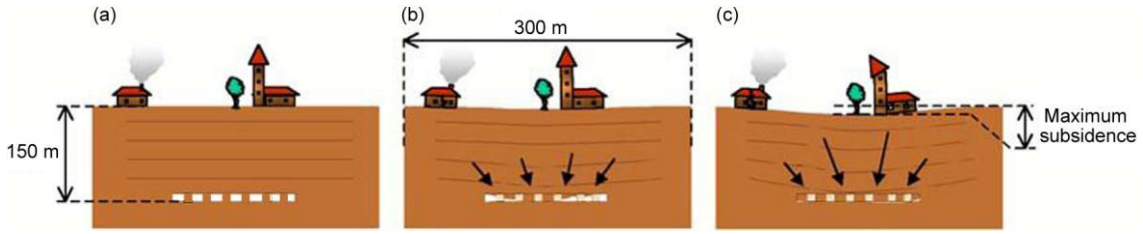

Figure 2. Subsidence due to the rupture of the pillars when using the room and pillar method: (a) excavation using the room and pillar method; (b) the rupture of the pillars, the collapse of the extraction zone, and the settlement of the overlying strata; 90% of the subsidence occurs in a few hours or days; (c) the final subsidence trough becomes stable in a few months

Some photographs of subsidence examples in Lorraine are shown in Figure 3. In these photographs, the securities and functions of farmlands, buildings, and roads are affected by subsidence.

[1] Groupement de recherche sur l'Impact et la Sécurité des Ouvrages Souterrains (the Research Group for the Impact and Safety of Underground Works), was created on 5 July 1999 by BRGM, INERIS, INPL and MINES ParisTech.

Figure 3. Subsidence phenomena in Lorraine: (a) farmland (source: INERIS); (b) building (source: GISOS); (c) road (source: INERIS)

The cases of subsidence led public authorities to carry out investigations over the entire mining field. In the year of 2000, an investigation about the mining subsidence risk was implemented in Lorraine, including 20 km^2 of urban zones and 120 km^2 of non-urban zones (Petit, 2000). Figure 4 gives a brief description of the dimensions of the iron basin in Lorraine, and the locations of undermined urban areas where well-known subsidence has already happened: the sudden subsidence happened in Sainte Marie in 1932 and the gradual subsidence in the cities of Jarny in 1949, Auboué in 1972, and Crusnes in 1975. Recently, from 1996 to 1999, in the cities of Auboué, Moutiers and Roncourt, gradual subsidence has been found again. Table 1 summarizes the main characteristics of these recorded subsidence events that happened in the iron basin in Lorraine. Actually, about 70 past subsidence events have been identified.

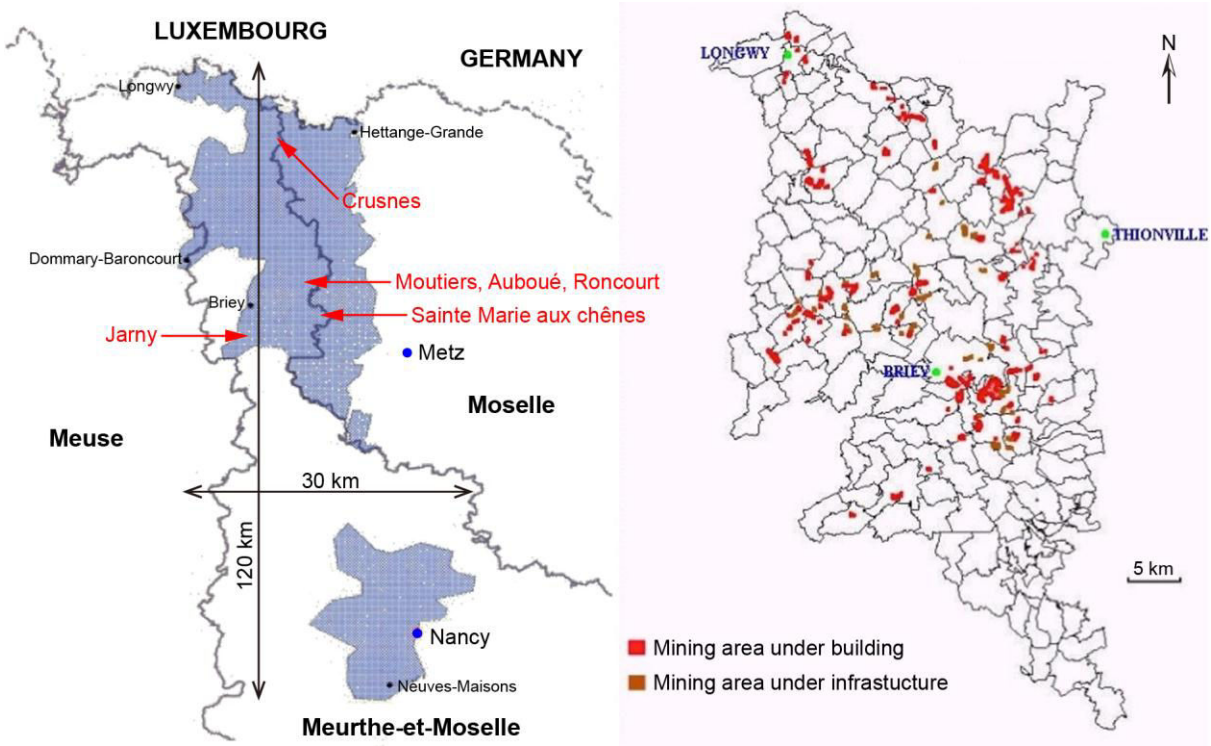

Figure 4. Presentation of the subsidence issues in Lorraine (Geoderis 2000): (a) the iron basin in Lorraine; (b) the undermined urban zones

Table 1. Some mining subsidence events recorded in the iron basin in Lorraine (Deck 2002)

City & year	Mining parameter			Subsidence parameter			Number of influenced buildings
	Depth (m)	Thickness (m)	Exploitation rate (%)	Influence angle (°)	Maximum subsidence (m)	Diameter of subsidence basin (m)	
Jarny 1949	200	5	53	Unknown	1.2	Unknown	Unknown
Auboué 1972	170	6	60	Unknown	Unknown	Unknown	Unknown
Crusnes 1975	180	3.8	50	Unknown	0.88	Unknown	Unknown
Auboué (rue de Metz) 1996	150 - 162	6	45	Unknown	2.23	400 - 600	130
Auboué (cité Coinville) 1996	170	5	53	Unknown	1.23	200 - 400	100
Moutiers (Haut) 1997	120	4	55	Unknown	1.38	400 - 500	70
Moutiers (stade) 1997	140	2.5	55 - 60	Unknown	> 0.55	150 - 300	60
Roncourt 1999	150	2.5	53	26 - 38	0.65	150 - 300	18

1.1.3 Methods of mining subsidence calculation

Mining subsidence calculation is a complicated problem because it depends on the excavation geometry, types and properties of surrounding rocks, and surface conditions.

There are many methods that have been used to predict the subsidence induced by underground mining. They can be classified as follows: empirical methods, profile function methods, influence function methods, analytical methods, physical model methods and numerical methods (NCB 1975, Kratzsch 1983, Whittaker and Reddish 1989, He *et al*. 1991, Kwiatek 1998, Deck 2002, Saeidi *et al*. 2013, Cai *et al*. 2014). The empirical methods are usually adopted for predicting subsidence in a particular mine or mine area. They are based on local field measured data, but cannot be well applied to other regions. Profile functions are also empirical but are dedicated to the subsidence prediction of a particular section such as a longitudinal or transverse profile. Profile functions make use of an equation or table, which is usually derived from field data, to define the profile and are fitted to mathematical functions. The influence function methods, which this thesis concerns, are the most common methods used in subsidence prediction. They make use of a function to describe the surface subsidence due to the excavation of one elementary mining zone, and then use the summation principle or the integration method to obtain the total subsidence of the whole excavated (or collapsed) mining area. Analytical methods use equations or sets of equations based on rock mechanics to assess rock deformation then ground movement from the excavation process. They are rarely used in practice because real conditions are typically not similar to the conditions on which these methods are based (i.e., isotropic, continuous, and elastic materials). The physical model methods use small-scale models (laboratory scale) to simulate field mining subsidence. Lastly, numerical simulations can be carried out to directly estimate subsidence from the geometric and mechanical conditions of the excavated zone and its surroundings. These two final methods are quite useful in subsidence studies as the influence function methods, but their precisions depend on the availability of data regarding the types and properties of surrounding rocks. When accurate subsidence results are expected, a detailed geological investigation, which means a heavy workload, should be carried out before simulations or model tests are run. Moreover, they may require a long experimentation or computation time, usually several days or weeks for a physical model experiment and several hours or even days for a numerical simulation test (depending on the size of the models and the complexity of the geometry to be studied).

Some researchers have tried to use new methods to compute subsidence such as fuzzy genetic programming methods (Li *et al*. 2007), BP-neural networks (Zhang *et al*. 2011) and so on. These works expand subsidence technology, but their reliability and accuracy require more in situ confirmation.

As the most extensively used subsidence prediction method, the influence function method has several advantages such as wide applicability (compared to empirical methods and physical methods), full-scale basin prediction (compared to profile function methods), implementation and computational ease (compared to numerical model methods) and speed (some seconds or minutes). However, the influence function method is limited by its

principles. The first limitation is that this method basically assumes that ground properties are linear; however, practically speaking, this limitation is overcome by adjusting the two main parameters of the method which are the influence angle and the maximum subsidence on field data, so that these parameters reflect non linearities (except faults or major discontinuities) of the ground through equivalent linear properties. Another limitation, and the focus of this thesis, is that the influence function method considers only flat surfaces and horizontal stratiform underground ore bodies. Some researchers have studied how subsidence is affected by topography, especially in mountainous regions, and tried to modify the parameters of the influence function to better fit field data (Liao 1993, Holla 1997, Cui *et al*. 2000, Dai *et al*. 2000, Donnelly *et al*. 2001, He 2003, Luo *et al*. 2009, Dai *et al*. 2010). They showed that as the surface dip angle increases, the maximum vertical subsidence value increases, and the subsidence basin shifts in the downward direction and becomes asymmetrical.

In the following sections of this thesis, the influence function method will be used to compute the mining subsidence, and its principles and new improvements will be introduced in section 2. Our improved method can take the topography into account by using an asymmetrical influence function.

1.2 Building damage caused by mining subsidence

1.2.1 Behavior of building affected by subsidence

Generally speaking, uniform vertical subsidence or horizontal displacement of the ground surface will not cause building damage, because the synchronous movement of an entire building will not produce any internal force or shape deformation. In contrast, the horizontal strain (defined as the first derivative of the horizontal displacement) and curvature (defined as the second derivative of the vertical subsidence), which are induced by non-uniform horizontal displacement and vertical subsidence, respectively, are the critical factors that cause building damages in subsidence area.

(1) Influence of horizontal strain on a building

The horizontal strain (also called horizontal deformation) can induce compression (by compressive strain) or extension (by tensile strain) of the ground surface, and then cause deformation of a surface building. It acts on the structure through two main transmission ways: the first way, which is only for buildings located in the compressive area of the subsidence trough as in Figure 1, is acting on the structure as pressure forces on its walls as shown in Figure 5(a); the other way is acting on the structure as friction forces on the interface between the ground and the structural foundation as shown in Figure 5(a) and Figure 5(b). The behavior of buildings under horizontal strain has been studied by many researchers, such as Lesage (1954), Neuhaus (1965), Soots (1969), Burland and Wroth (1974), Burland *et al*. (1977), Arcamone (1980), Kratzsch (1983), Geddes (1984), Speck and Bruhn (1995), Boon (1996), and Son and Cording (2005, 2007, and 2008). The transmission rate of the horizontal strain from the ground to the building depends on the relative stiffness

between the soil and the building. Several researchers, such as Klezhev *et al*. (1980), Boscardin and Cording (1989), Ji-Xian (1985 and 1992), Potts and Addenbrooke (1997), attempted to quantify the transmission rate for rigid buildings (reinforced concrete or masonry, with the shape of tall height and short length) and flexible buildings (metallic, with the shape of low height and long length). For example, according to the study of Boscardin and Cording (1989), this rate should be 10 to 30% and 30 to 100% for rigid and flexible buildings, respectively.

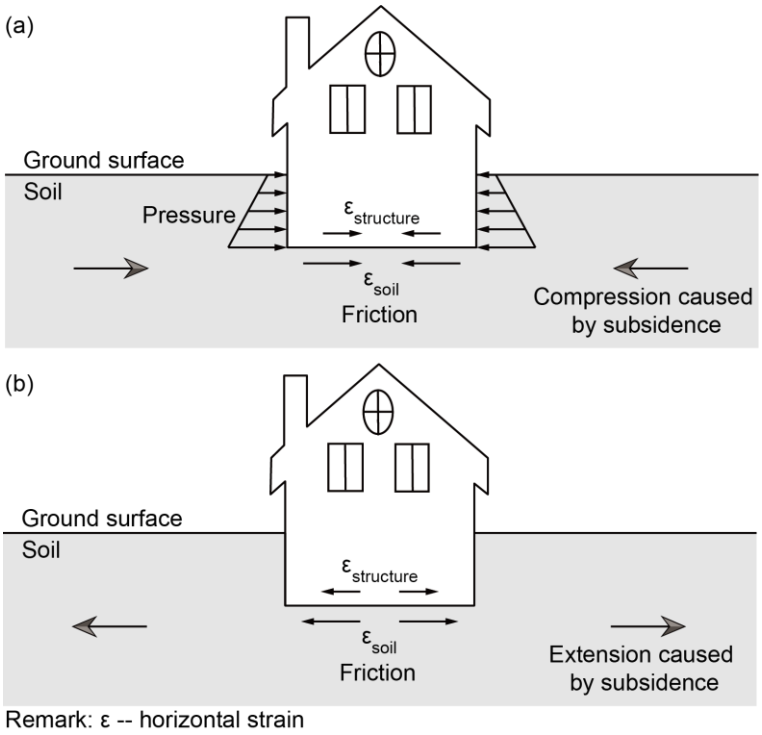

Figure 5. Behavior of a building influenced by horizontal strain: (a) by the compressive strain; (b) by the tensile strain

(2) Influence of curvature on a building

Due to the influence of curvature, the ground surface shape becomes concave or convex. The concave area is located near the center of the subsidence trough and the convex area is close to the subsidence edge. Buildings tend to bend to match the surface shape, as shown in Figure 6. Authors, who were interested in the behavior of buildings under curvature, reported many achievements, such as Neuhaus (1965), Soots (1969), Burland and Wroth (1974), Burland *et al*. (1977), Arcamone (1980), Kratzsch (1983), Attewell and Yeates (1984), Geddes and Kennedy (1984), Boscardin and Cording (1989), Potts and Addenbrooke (1997), Franzius *et al*. (2005). The transmission rate of the curvature from the ground to the building also depends on the relative stiffness between the soil and the building. Flexible buildings suffer a curvature close to that caused by subsidence, while rigid buildings oppose the transmission of the curvature. Several authors such as Boscardin and Cording (1989), Potts

and Addenbrooke (1997) calculated the transmission rate. For example, Boscardin and Cording (1989) proposed a range of 15 to 50% for rigid buildings and 50 to 75% for flexible buildings.

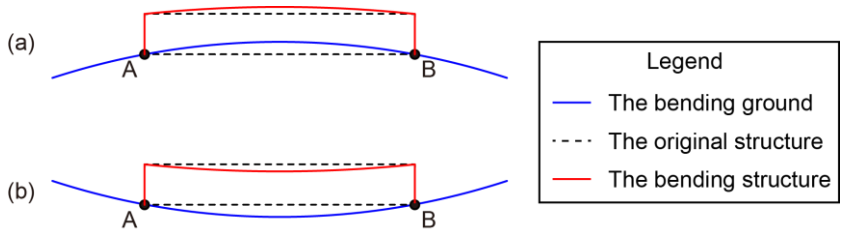

Figure 6. Behavior of a building influenced by curvature: (a) on a convex ground surface; (b) on a concave ground surface

(3) Global influence on a building

The behavior of a building caused by the integral influence of horizontal strain and curvature is shown in Figure 7, after Kratzsch (1983). The main observations from this figure, which must be considered as possibilities suggested by Kratzsch, are listed as follows.

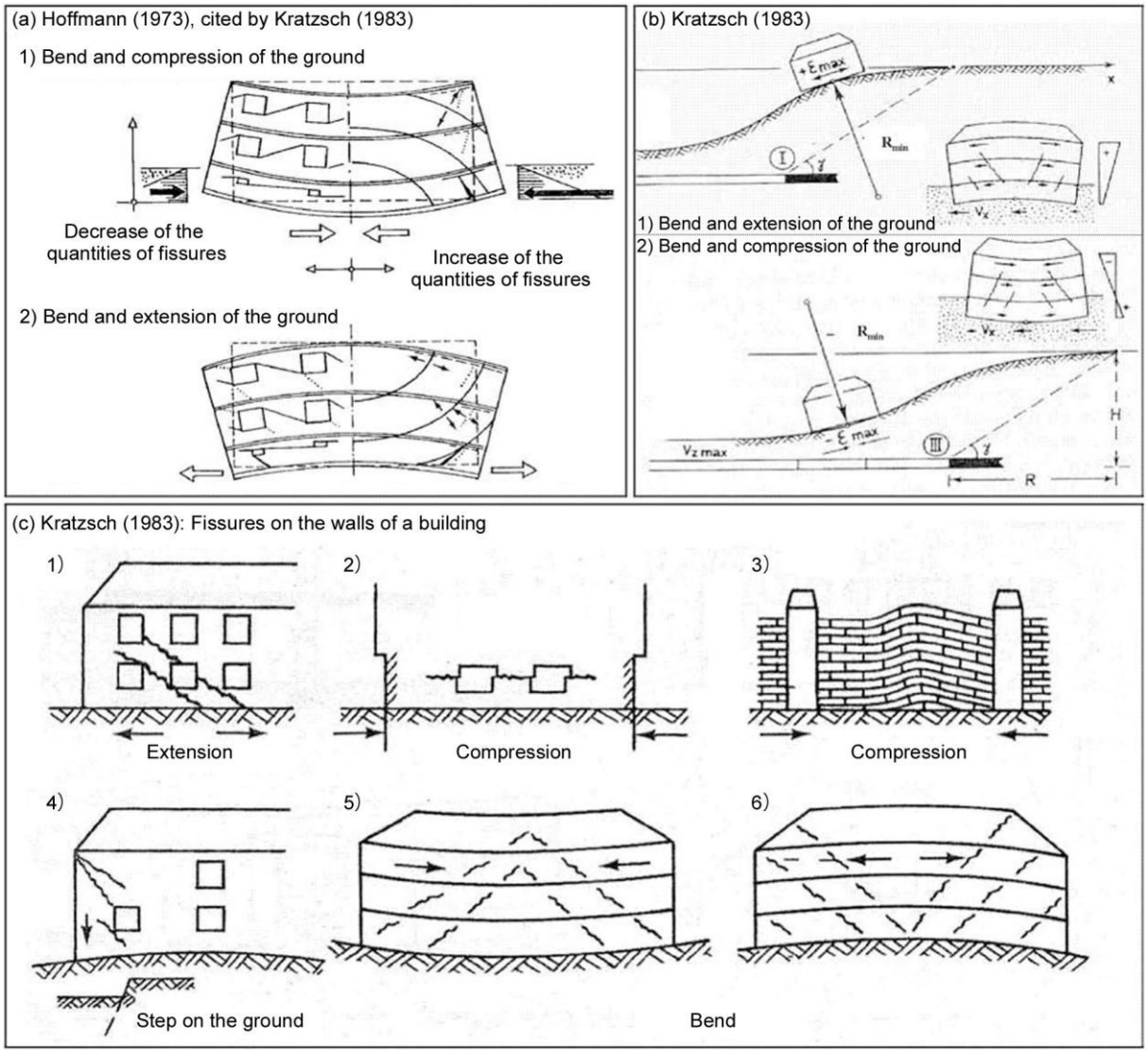

Figure 7. Behavior of a building influenced by both horizontal strain and curvature (Kratzsch 1983): (a) & (b) multi-influence of horizontal strain and curvature; (c) single influence of horizontal strain (c-1 to c-3) and curvature (c-4 to c-5)

(1) Figure 7(c) summarizes the damages caused by the single influence of horizontal strain or curvature. As in Figure 7(c-1) to Figure 7(c-3), extension and compression of the building (also of the ground surface) are caused by horizontal strain; as in Figure 7(c-4) to Figure 7(c-6), bend (concave or convex) of the building (also of the ground surface) is caused by curvature. Fissures can be caused by either of them. Particularly, we note that the fissures caused by compression of the ground are horizontal, as in Figure 7(c-2), while other fissures are all inclined.

(2) The locations and directions of the fissures on the building caused by the multi-influence of the curvature and horizontal strain, as shown in Figure 7(a) and Figure 7(b), are similar to that just caused by the curvature, as shown in Figure 7(c-5) and Figure 7(c-6).

(3) At the bottom of the building, the effects of horizontal strain and curvature are opposite.

In the compressive zone of subsidence (refer to Figure 1), the stress diagram in Figure 7(b-2) suggests that the effect of curvature is greater than that of horizontal strain (because, at the building's bottom in this case, the stress caused by curvature is tensile, the stress caused by horizontal strain is compressive, and the stress in Figure 7(b-2) is tensile, which is the accumulation of the former two); the bottom of the building is lengthened and suffers from tensile stress, as shown in Figure 7(a-1) and Figure 7(b-2), respectively. In the tensile zone of subsidence, the bottom of the building is not lengthened and suffers from tensile stress (the effect of curvature is less than that of horizontal strain in this case).

(4) Given that a structure is generally less resistant to tensile stress than to compressive stress (according to the material properties), the damage of buildings in the tensile zone of subsidence should be more serious than that in the compressive zone.

1.2.2 Building damage evaluation

The assessment of building damage in mining subsidence areas can be performed using three types of methods: empirical, analytical, and numerical. The numerical method, specifically the finite element method (FEM), is also the method used in the following chapters of this thesis.

1.2.2.1 Methods of building damage evaluation

Methods for evaluating the building damage in mining subsidence areas have been developed in many countries (England, USA, Poland, South Africa...). Most methods are empirical, based on the observed building damage data, and there are also some methods based on mechanical calculations (Deck 2002). The majority of the methods use the horizontal strain to assess the damage extent of building (Saeidi 2012).

The empirical methods can be very simple, such as the method used by Skempton and MacDonald (1956), which is the simplest and comprises only the threshold values of the ground displacements, and the method used by NCB (1975), which is the most famous but considers only one parameter (the length) to describe a building; they can also be very detailed, as the method of Kwiatek (1998), which considers 15 parameters to depict a building. The methods of Yu *et al*. (1988) and Dzegniuk *et al.* (1997) consider a medium number of parameters. When using the empirical methods, simple ones are imprecise, while detailed ones are too complicated to implement.

Analytical methods are based on modeling the building by a beam with the stiffness of the material (Boscardin and Cording 1989, and Burland 1995). The influence of the subsidence is employed as the imposed displacements to the structure, and then the maximum strain and stress in the structure can be calculated in order to derive the damage extent.

Numerical methods are used mostly for the prediction of ground movements (Coulthard and Dutton 1998, Melis *et al*. 2002), the study of soil-structure interaction, and assessment of the transmitted ground movement (Selby 1999, Burd *et al*. 2000, Son and Cording 2005, Franzius *et al*. 2006). Very few studies, however, address the question of the building damage assessment with numerical methods (Abdallah *et al.* 2008, Saeidi 2010). Some researchers, such as Papadrakakis *et al*. 1996, Nakamura *et al*. 2007, Nakamura *et al*. 2008, Jankowski

2009, Nakamura *et al*. 2010, Helmerich *et al*. 2012, Domede *et al*. 2013, used existing FEM softwares to study the damages of individual structures (buildings, bridges...) with very detailed constructions.

Although our method is a numerical method, as it employs beam system to study the buildings in a large scale (a city for instance), its solving process is similar to that of the analytical method.

1.2.2.2 The analytical method

There are several analytical methods for assessing the building damage. Most of these methods (Boscardin and Cording 1989, Burland 1995, Boone 1996, and 2001, and Finno *et al*. 2005) consider the building as a beam on the use of beam theory (Timoshenko 1955). The evaluation process can be seen in Figure 8 and described as follows: firstly, a beam with appropriate dimensions and the load of self weight is chosen to stand for the building; then, the horizontal strain and curvature are applied onto the beam to simulate the subsidence influence; analytical calculation is used to compute the maximum principal strains in the structure, which will later be compared to the structural damage criterion to determine the level of damage.

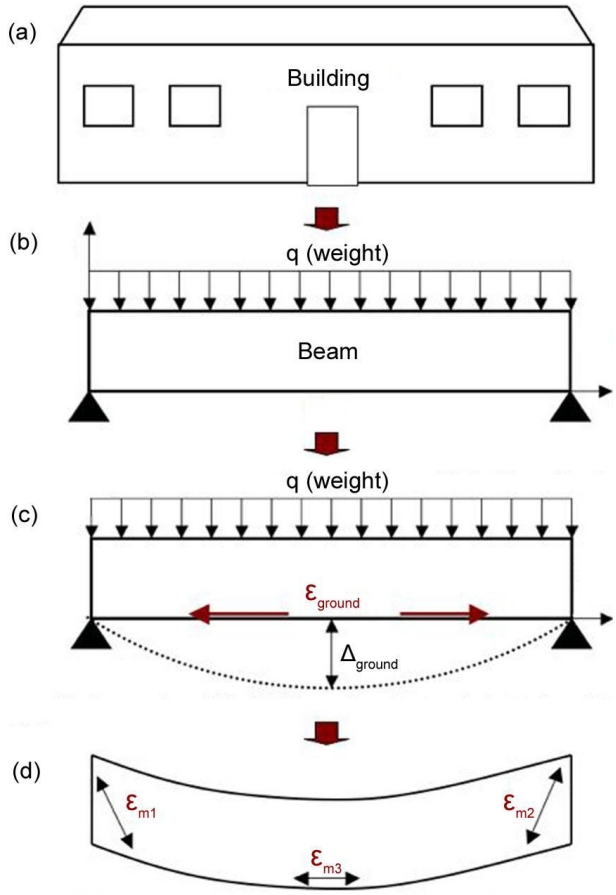

Figure 8. Principles of the analytical methods for the evaluation of the building damage (Saeidi 2010): (a) a building; (b) using a beam to perform the building and considering its self weight; (c) taking the curvature (Δ_{ground}) and horizontal strain (ε_{ground}) into account; (d) computing the maximum strains (ε_{m1}, ε_{m2}, and ε_{m3})

A comparison between the existing analytical methods, leads to the following remarks.

(1) These methods consider two types of loads to simulate the self weight of the building: concentrated load and uniform distributed load. Methods of Burland and Wroth (1974) and Boscardin and Cording (1989) consider the concentrated load in calculation, while Methods of Boone (1996) and Finno *et al*. (2005) consider the distributed load, which is more realistic in practice.

(2) Boscardin and Cording (1989) suggest a parameter of distortion angle to model the effect of curvature, while the others consider a parameter of deflection.

(3) These methods consider different types of buildings. Methods of Burland (1995) and Bosardin and Cording (1989) consider masonry buildings, which are modeled by beams with rectangular cross section. The method of Boone (1996) considers three types of structures that are masonry structure, simple frame structure of reinforced concrete and simple frame structure of steel. The method of Finno *et al*. (2005) considers frame structures with multi-floors.

(4) The location of the neutral axis is an issue discussed in these literatures. In the convex area, Burland and Wroth (1974), Boscardin and Cording (1989), and Finno *et al*. (2005) consider that the neutral axis is probably at the bottom of the beam. Boone (1996) considers that the neutral axis is located at the center of the beam.

Later, in section 3, we will develop a new method to evaluate the building damage caused by mining subsidence. Our method is more complete than the others: different frame structure models (with the dimensions according to the real buildings), different materials, different cross sections (for different types of elements in structures), and different initial loads can be taken into account for different types of buildings (as the real case study illustrated in section 4). Of course, this method also depends on the precision of the investigation data as the other methods. Rough data call simple simulations. But, at least, it provides a possible way to perform a delicate calculation. Otherwise, due to the use of the frame model regarding to the building's shape, we can employ the vertical subsidence and horizontal displacement directly to the supports of the model. Therefore, the computation of horizontal strain and curvature are no more necessary. Then, by using the displacement method, which is equivalent to the finite element method, the internal forces and displacements over the structure can be obtained, that means the damage evaluation is not only based on a single parameter (strain or curvature for instance).

Chapter 2: Improving the influence function method to take ground topographic variations into account in mining subsidence prediction

Chapitre 2: Amélioration de la méthode des fonctions d'influence pour prendre en compte les variations topographiques du sol dans la détermination des cuvettes d'affaissement

Abstract of chapter 2

The influence function method is widely used in subsidence computation. The original method is well adapted for predicting subsidence induced by the extraction of a horizontal stratiform layer from an underground mine beneath a flat surface, but provides improper results when the surface is not flat. Some typical influence functions, the principle of the original influence function method, and the characteristics of the subsidence under a flat surface are illustrated first.

Real-world mining conditions are too complicated to separate topographic influence from influences caused by other factors. Therefore, the present work intends to make use of simplified numerical simulations to analyze the topography influence only: one continuous stratum of rock formation above the mined layer is considered without taking into account any discontinuity through the system that could affect the transmission of movement from the mined zone to the surface; the top surface condition is also simplified by using a global slope over the whole mining zone. Under such simplified mining conditions, the subsidence characteristics changed by topography can be studied.

By studying the characteristics of element mining subsidence using numerical simulations, two new asymmetrical influence functions are suggested to compute the vertical and horizontal element subsidence, respectively. The new influence functions are based on the probability density functions of normal distributions corrected by complementary error functions. Their parameters can be described by the surface dip angle and mean mining depth, meaning that the new influence functions take topographic variations into account. After that, displacements, including vertical and horizontal, at every surface point can be computed by the standard summation method. Finally, full-scale subsidence is achieved by summing all the points' displacements.

The improved influence function method can take the known maximum subsidence values and influence angles obtained from field data into account to enhance the computational precision. Several numerical simulations and two field subsidence cases, respectively from France and China, were studied and showed that compared to the original influence function method, the new method better simulates subsidence, especially in terms of horizontal displacement.

Résumé du chapitre 2

La méthode des fonctions d'influence est largement utilisée dans le calcul des affaissements miniers. La méthode originale est bien adaptée à la prédiction de l'affaissement induit par l'extraction d'une couche horizontale d'une mine souterraine située sous une surface plane, mais fournit des résultats incorrects lorsque la surface n'est pas plane. Une première partie présente quelques fonctions d'influence usuelles, le principe originel de la méthode des fonctions de d'influence et les caractéristiques de l'affaissement pour une topographie plane.

Les conditions d'exploitation réelles sont généralement trop compliquées pour séparer l'influence topographique de l'influence d'autres facteurs. Néanmoins, par le biais de modélisations numériques simplifiées, nous pouvons analyser l'influence de la topographie seulement. C'est ce que nous faisons en utilisant des modèles comportant une seule formation rocheuse au dessus d'une couche exploitée horizontale et dans lesquels la topographie est constituée d'une pente constante. Dans de telles conditions d'exploitation simplifiées, la manière dont les caractéristiques de l'affaissement sont affectées par la topographie peut être étudiée.

Ainsi, deux nouvelles fonctions d'influence asymétriques sont suggérées pour calculer le déplacement vertical et horizontal. Elles sont basées sur des fonctions de densité de probabilité normales corrigées par des fonctions d'erreur complémentaires. Leurs paramètres peuvent être reliés à l'angle d'inclinaison de la surface et la profondeur moyenne de l'exploitation minière, ce qui permet à ces nouvelles fonctions d'influence de prendre en compte les variations topographiques. Après cela, les déplacements verticaux et horizontaux à chaque point de surface peuvent être calculées par la méthode de superposition standard et la cuvette d'affaissement à grande échelle peut être calculée.

La méthode ainsi améliorée requiert la connaissance ou l'estimation de l'affaissement maximal attendu ainsi que des angles d'influence qui peuvent être obtenus à partir de données de terrain. Plusieurs simulations numériques et deux cas test, respectivement en France et en Chine, ont été étudiés et montrent l'amélioration obtenue par rapport à la méthode des fonctions d'influence originale, notamment en termes de déplacements horizontaux.

2.1 The influence function method

2.1.1 A widely used method

Many mathematical functions have been adopted as influence functions. The most widely used functions are listed in Table 2 (Whittaker and Reddish 1989, He *et al*. 1991, Saeidi *et al*. 2013). Most of them are exponential functions. The first is the probability density function of a multivariate normal distribution when the correlation coefficient equals zero.

The integration of these influence functions must equal or approximately equal 1 over influence radius (*R*) region. The relationships between this radius, the influence angle (φ) and the mining depth (*H*) can be described as in Equation 1 and Figure 9. The influence angle or the influence radius is used to quantitatively define the range or the border of the subsidence zone. They are usually known in each studied region through past subsidence events analysis.

Table 2. Some influence functions used in subsidence prediction

Author	User (Year)	Influence function	Remark
Knothe	Knothe (1953,1957) Zenc (1969) Whittaker and Reddish (1989)	$\frac{1}{R^2}e^{-\pi\frac{r^2}{R^2}}$	
Bayer	Bayer (1945) Niemczyk (1949) Whittaker and Reddish (1989)	$\frac{3}{\pi R^2}[1-(\frac{r}{R})^2]^2$	
Sann	Sann (1949) Brauner (1973)	$\frac{2}{\pi^{3/2}Rr}e^{-4(\frac{r}{R})^2}$	
Litwiniszyn	Litwiniszyn (1957) Sroka A.Hejmanowski (2006) Liu Baochen and Liao Guohua (1965)	$\frac{n}{R^2}e^{-n\pi(\frac{r}{R})^2}$	With *n* =1 or *n* =2, in relation to strata conditions
	Kochmanski (1959)	$\frac{7}{R^2}e^{-6.65\frac{r}{R}}$	
	Ehrhardt and Sauer (1961)	$\frac{4.6}{\pi R^2}e^{-4.6(\frac{r}{R})^2}$	
Reddish	Reddish *et al*. (1994)	$\frac{1-v}{\pi}\frac{D}{(r^2+D^2)^{3/2}}$	*D*: depth of the mining object *v*: Poisson ratio of overburden
Sheorey	Sheorey *et al*. (2000)	$\frac{0.5352}{R^2}[1+\cos\frac{\pi r}{R}]$	

$$R = H\tan(\varphi) \qquad \text{Equation 1}$$

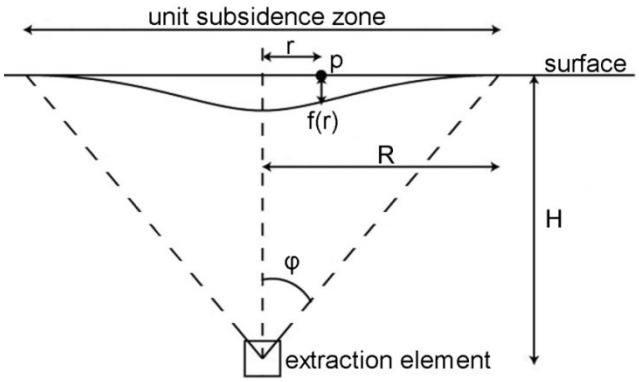

Figure 9. The influence function (f(r), can be any one of the influence functions listed in Table 2) of the extraction of a mining element (the vertical displacement is magnified compared to the relative distance between the surface and the extraction zone)

2.1.2 Principles of the influence function method

Notably, for the classical influence function method, the influence function is used to simulate vertical subsidence (also called vertical displacement) induced by the extraction of a horizontal stratiform underground mining layer (or part of it). Other movements and deformations, including horizontal displacement, horizontal strain, slope and curvature, are derived from vertical subsidence.

The influence function simulates the vertical subsidence of several surface points due to one elementary mining zone. Theoretically, these points can extend infinitely, but in practice, a value is set as the border to simplify and speed the calculation. The final full-scale vertical subsidence basin can be calculated as the superposition of all the elementary subsidence due to all excavated mining elements. The procedure can be explained as follows (Deck 2002, Saeidi *et al*. 2013):

(1) The subsidence caused by an extraction element

Figure 9 illustrates the influence zone caused by an extraction element. The element can be considered as an infinitesimal integral element or an element with a unit area for numerical integration. The influence zone, or unit subsidence zone, depends on the influence function used (f(*r*) in Figure 9). Once the influence function is determined, the vertical subsidence of every surface point is only related to the horizontal distance between the extraction element and the surface point (*r*). Usually, we can set a threshold value as the border of subsidence (e.g. 0.01 m). The influence radius (*R*), which is defined as the horizontal distance between the mining element and the subsidence border, and the influence angle (*φ*), which is another way to determine the position of the subsidence border, are related to each other according to Equation 1. Both of them vary according to morphologies and properties of the overlying strata and are usually known in the studied mining regions, from past events back-analysis.

(2) Full-scale vertical mining subsidence basin

As Figure 10 shows, for calculating the subsidence of a polygonal shaped underground

mining zone, we first rasterize the polygon into a grid of small size squared or rectangle zones where several properties are defined (i.e. depth, influence angle, and maximum subsidence value). The vertical subsidence due to each of these grid zones, which are considered as extraction elements, is then calculated using the influence function of each grid zone. Finally, at all surface points, the elementary vertical displacements are added according to the superposition principle.

By employing this approach repeatedly, the final full-scale vertical subsidence basin can be estimated. For practical reasons, we do not calculate the subsidence of all the surface points. Instead, we divide the surface into a regular grid and calculate the subsidence at the grid intersection points and interpolate this over the entire area.

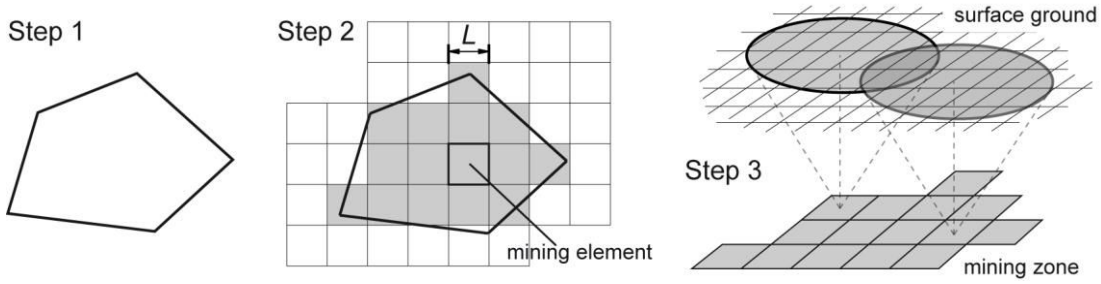

Figure 10. Calculation of a full-scale mining subsidence basin (Step 1: Definition of the mining polygon; Step 2: Rasterization and discretization of the mining polygon; Definition of the properties of every grid mesh; Step 3: Discretization of the surface; Calculation of the influence on surface grid meshes)

The rasterization and discretization of the mining polygon and the surface do not need to have the same mesh size. The mesh density of the mine polygon affects the computational accuracy of every surface point's subsidence; however, this is not true for the surface mesh density. Some trials that we carried out using field data from the iron mines in Lorraine, the primary mining region in the east of France, showed that, to ensure computational accuracy, the mesh length of the mine polygon (*L*, as in Figure 10) should be smaller than a third of the tangent of the influence angle (φ) times the mining depth (*H*), as in Equation 2. If the mesh length is greater than this threshold value, the results are sensitive to the mesh size that is not desirable.

$$L < \frac{H \tan(\varphi)}{3} \qquad \text{Equation 2}$$

If smooth subsidence contours are required, the mesh density of the surface can be increased.

In 2D cases, the same principles apply, but the superposition method is easier to implement, provided that the influence functions can be integrated mathematically or numerically.

(3) The other movements and deformations

After obtaining the vertical subsidence, the slope can be calculated as the first derivative of the vertical subsidence, and the curvature can be calculated as the first derivative of the slope. Both the slope and curvature can be calculated for any two perpendicular directions in 3D cases.

When the ground surface is flat, the horizontal displacement is known to be similar in shape to the slope. This subsidence feature was firstly observed in field measurements by Knothe (1959), and then was used into the influence function method (Golosinski *et al*. 1996, Saeidi *et al*. 2013). Therefore, the horizontal displacement can be calculated as the slope times a coefficient (to be defined from field data). Finally, the horizontal strain is calculated as the first derivative of the horizontal displacement. The horizontal displacement and strain are computed in any two perpendicular directions in 3D cases, similar to the slope and curvature.

2.1.3 Characteristics of subsidence in flat terrain due to horizontal underground mining

Referring to Figure 11, the shape of subsidence curves due to horizontal underground mining in a flat terrain can be summarized as follows:

(1) Symmetry

The vertical subsidence, horizontal strain and curvature are symmetrical about the vertical line, which passes through the center of the extraction zone. The horizontal displacement and slope are point symmetrical about the surface point above the mining center.

(2) Similarity

The slope and horizontal displacement are similar as mentioned earlier. Therefore, the horizontal displacement can be computed from the slope, for flat surfaces. The same feature applies to the curvature and the horizontal strain, both being a derivative of the former quantities.

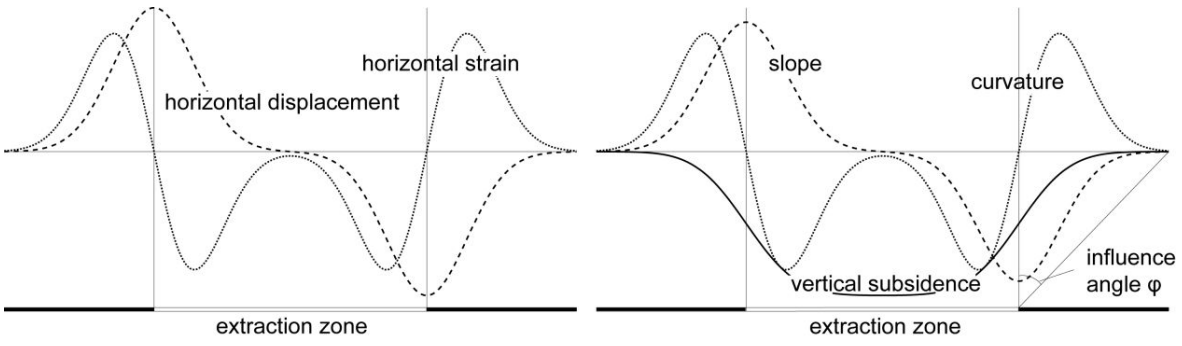

Figure 11. Subsidence curves when excavating a flat mine under a flat surface (vertical scale is magnified compared to the horizontal)

2.2 Topography influence on subsidence

2.2.1 Data sources

Real-world mining conditions are complicated and subsidence characteristics are practically influenced by ground and surface conditions. That makes it difficult to separate topography influences from influences caused by other factors. While, many authors, such as Fougeron *et al*. 2005, Deck *et al*. 2010 and Xu *et al*. 2013, have studied mining influence through numerical simulations, the present work uses simplified numerical simulations to analyze the topography influence only, avoiding the effects of other factors.

2.2.1.1 Simplify the mining conditions

(1) Simplify the overlying strata

How subsidence is affected by topography is a complex problem. There are many types of rocks, and their relative or absolute characteristics may affect the subsidence intensity and profile. For studying the relationship between subsidence and topography, we only considered the case of one continuous stratum of rock formation above the mined layer without taking into account any discontinuity through the system that could affect the transmission of movement from the mined zone to the surface.

(2) Simplify the surface shape

For testing purposes, the surface condition is simplified. The problem is complicated if the dip angle and dip direction of the surface vary (e.g. a hilly ground surface). Therefore, we checked the new implemented method against a simple topographic variation of the ground, i.e. a global slope over the whole mined area. A global slope means that the surface is dipping in one direction, at one angle. Later, the subsidence under the condition of varying surface slope will also be studied to verify the achievements.

The simplification of the overlying strata and surface conditions must be considered before complicated configurations can be approached.

2.2.1.2 Numerical simulation models

Using the surface and overlying stratum conditions described above, the subsidence laws are determined from a finite difference modeling calculation (FLAC 2D).

The numerical simulation models are similar to the model illustrated in Figure 12. They consist of three strata: one horizontal floor, one horizontal ore body (part of which will be mined), and one roof with variable global dip angle. All strata are isotropic and have the properties mentioned in Table 3. Properties for the ore body and floor come from iron mines in Lorraine (Fougeron *et al*. 2005). For the roof, the Young's modulus has been divided by 1000 to increase the subsidence while keeping the material elastic. Reducing the Young's modulus is not a problem because we are interested in the shape of the vertical subsidence and horizontal displacement more than their magnitudes (which are then adjusted to fit field data). The properties used here to generate a subsidence profile approximately correspond

to an influence angle of 45° when the surface is flat. The profile shape can be adjusted to any field influence angle.

In all our numerical simulation models, the horizontal displacement is prevented on both the left and right sides, the vertical displacement is fixed at the bottom, and the top is free. Initial stress field corresponding to gravity loading is given at the start.

Before excavation, the model is solved to achieve equilibrium (we consider the maximum velocity less than 10^{-7} m as balance). This phase leads to a little adjustment of the given initial stress field. Then all displacements and rotations (which are actually very small) are reset to zero so that the next phase exhibits the displacements induced by the mining excavation only. After that, part of the ore body is excavated and the model is solved until a new equilibrium is reached. Then, the displacements of the top surface are exported for analysis. For each model, the computational time, which depends on the size of the model and the performance of the computer, is around 10 - 30 minutes.

These calculations must be understood as a tool for designing a new influence function, not as a tool to study directly the subsidence of any particular geometry. Moreover, only 2D calculations are used here but the resulting influence function will operate in 3D on almost any kind of surface with varying topography. Therefore, the computational effort is expected to be far less than using 3D numerical models, especially when making some sensitivity studies or back analysis.

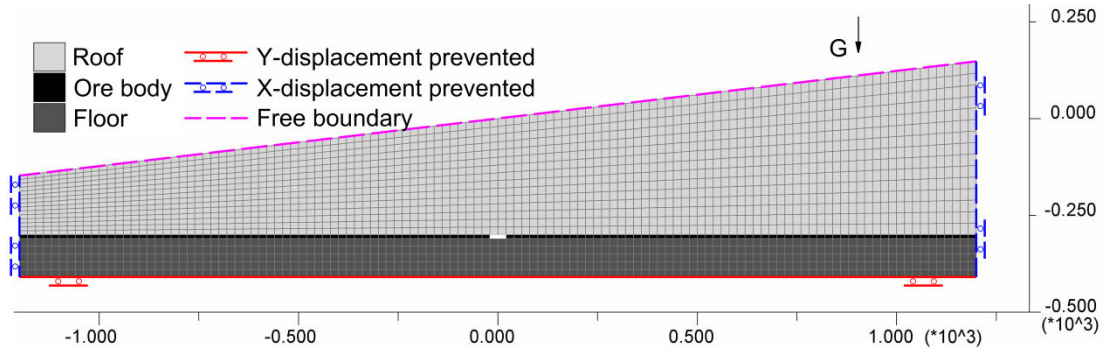

Figure 12. Numerical simulation model (FLAC 2D) with a surface slope of 10° and mean depth of 300 m

Table 3. The physical and mechanical characteristics used in the model

Stratum	Volumic Mass	Young's modulus (E)	Poisson Ratio (υ)
Roof	2500 kg/m^3	16.4 MPa	0.3
Ore body	2500 kg/m^3	7.8 GPa	0.3
Floor	2500 kg/m^3	6.0 GPa	0.3

2.2.2 Characteristics of the subsidence changed by the topography

Several models were set up to study the characteristics of the subsidence under simplified model conditions and rock properties when the surface is not flat. Here, three of these models are chosen to illustrate the results.

For comparison, the models are the same with different surface angles and mean depths. The length of the model is 2400 m. The extraction zone is 400 m long, 5 m thick and located in the middle of the ore body. The mean mining depth, which is the elevation difference between the center of the extraction zone and the surface point above it, is 400 or 500 m so that the subsidence remains subcritical (i.e. do not reach its maximum value). The surface dip angle is 0° or 15°, and the surface dips to the negative direction of the x-axis.

The subsidence data (as listed in Table 39 in Annex 1) are achieved by three numerical calculations with FLAC 2D. Generally, we can monitor the positions of surface points before and after mining, then the vertical and horizontal subsidence data can be derived as the differences of them.

Figure 13 shows the variation of the vertical subsidence, horizontal displacement, slope and horizontal strain at the ground surface for different surface dip angles and mean mining depths. The vertical and horizontal subsidence curves in Figure 13(a) are obtained directly by the subsidence data (in Table 39). The slope and the horizontal strain in Figure 13(b) are respectively computed as the derivative of the vertical subsidence and the horizontal displacement; they are often concerned in mining damage studies (for example, damage assessment of building upon a mine). The maximum and minimum values of these subsidence curves are listed in Table 4.

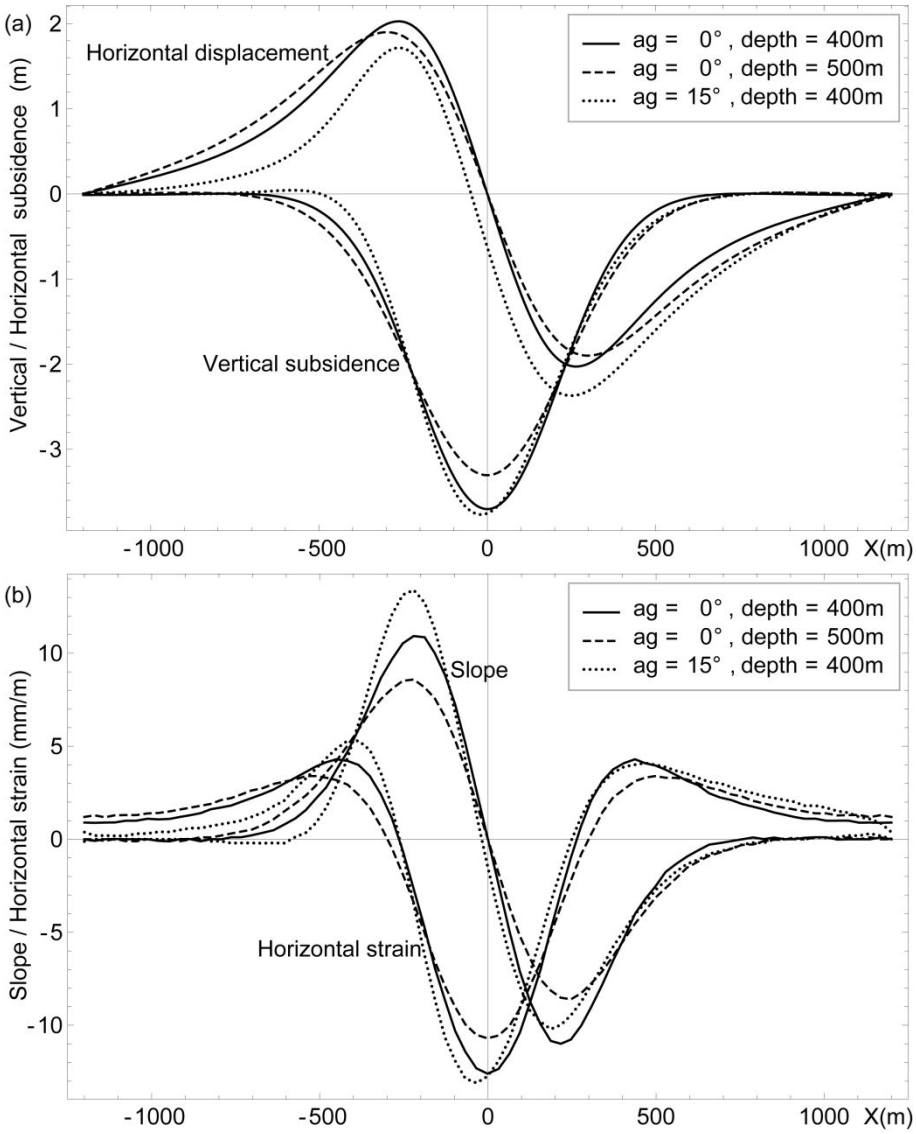

Figure 13. Variation of subsidence with surface dip angle and mean depth got by numerical simulations: (a) Comparison of vertical and horizontal subsidence; (b) Comparison of horizontal strain and slope

Table 4. The maximum and minimum values of subsidence (x-position of the given values are also indicated)

Subsidence			angle=0° depth=400m		angle=0° depth=500m		angle=15° depth=400m	
			value	x	value	x	value	x
Vertical subsidence (m)	max		3.70	0	3.31	0	3.77	-19
Horizontal displacement (m)	max		2.03	-263	1.90	-299	1.72	-263
	min		-2.03	263	-1.90	299	-2.37	249
Slope (mm/m)	max		11.02	-210	8.61	-235	13.45	-240
	min		-11.02	210	-8.61	235	-10.21	185
Horizontal strain (mm/m)	max	x+	4.32	453	3.42	505	4.11	445
		x-	4.32	-453	3.42	-505	5.41	-395
	min		-12.63	0	-10.72	0	-13.12	-35

Under the simplified conditions mentioned above, subsidence changes due to topography can be described as follows:

(1) As the surface angle increases, the influence range decreases downward (left side of Figure 13), but increases upward. By contrast, this range increases on both left and right sides as the depth increases.

(2) As the surface angle increases, the maximum value of the vertical subsidence slightly increases, and the location of the maximum subsidence point moves downward. The slope, which can be considered as the change rate or the derivative of the vertical subsidence, varies more prominently. The positive maximum value of the slope increases by 22% in the surface downward direction, and its negative maximum value decreases by 7% in the upward direction. By contrast, the maximum slope decreases by a same value on both left and right sides as the depth increases.

(3) As the surface angle increases, the maximum value of the positive horizontal displacement decreases by 15% (within this study, positive horizontal displacement means a move in the surface upward direction), and the negative horizontal displacement increases by 17% on the opposite side (downward). The point where the horizontal displacement equals 0 moves from the center of the mining zone (when surface angle is 0°) to the surface downward direction. The horizontal strain, which can be considered as the change rate or the derivative of the horizontal displacement, has its positive maximum value (tensile stress) increased by 25% in the surface downward direction and decreased by 5% in the opposite direction, while its negative maximum value (compressive stress zone) increases by 4% around the center of the surface. By contrast, when only the depth increases, the changes of the horizontal displacement and strain appear symmetrical.

(4) The vertical subsidence, horizontal displacement, slope and horizontal strain become asymmetrical when the surface is not flat.

(5) Because the horizontal displacement and the slope are not similar anymore as the surface angle rises (horizontal displacement decreases but slope increases in the surface downward direction, horizontal displacement increases but slope decreases in the surface upward direction), the horizontal displacement can no longer be computed from the slope when using influence function method.

2.3 Improving the influence function method

The improvements presented in this section are based on the results of the previously described simplified numerical simulations. They have been introduced into a subsidence computation code developed in our laboratory (Deck 2002, Saeidi *et al*. 2009, 2010 and 2013).

As indicated above, the influence functions are used to simulate element subsidence. By studying the characteristics of element mining subsidence using numerical simulations, we tried to find new asymmetrical influence functions to describe element subsidence, wherein the surface angle and mean depth are used as parameters to integrate topography into the influence function method.

2.3.1 Element mining subsidence

With the simplified surface shape and given rock properties, a small part of the ore body is mined to compute the element subsidence. As mentioned above, the numerical models are the same, but the surface angle and mean depth vary for each. The element mining zone is always located in the center of the ore body, and the top surface slopes to the left side in each model.

To understand the characteristics of element subsidence, two series of simulations were performed: one with varying surface slope angle and a fixed mean mining depth (Figure 14), the other with varying mean mining depth and a fixed surface slope angle (Figure 15).

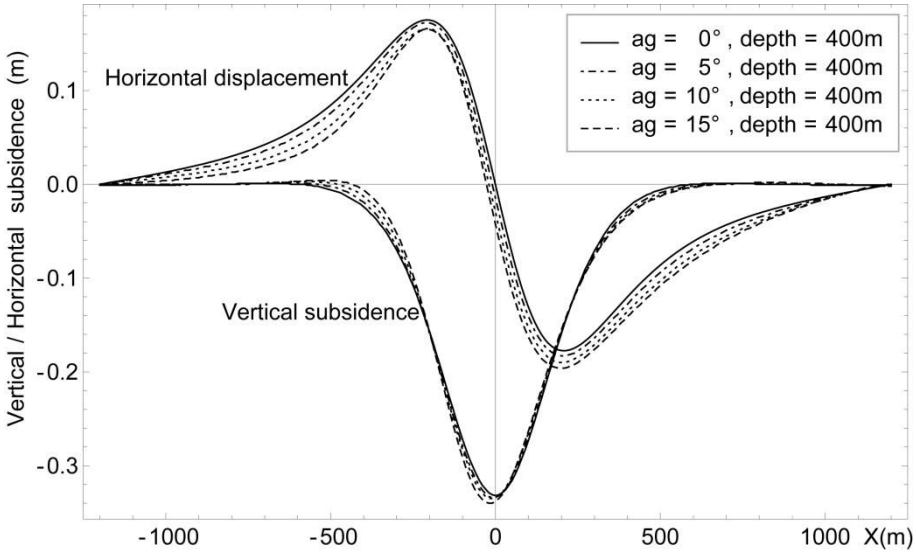

Figure 14. Variation of element subsidence with surface slope angle obtained by numerical simulations

Figure 14 illustrates several things. By increasing the surface angle, the vertical subsidence increases, and the maximum subsidence point slightly moves downward. The positive horizontal displacement (where surface points move in the upward direction of the surface) decreases, meanwhile the absolute value of the negative horizontal displacement increases. The area between the positive horizontal displacement and the x-axis becomes smaller than the area between the negative horizontal displacement and the x-axis (when the surface angle equals 0°, they are the same), which means that there is more negative horizontal displacement in the upper part of the model than positive horizontal displacement in the lower part. The intersection point of the horizontal displacement and x-axis moves in the negative direction of the x-axis.

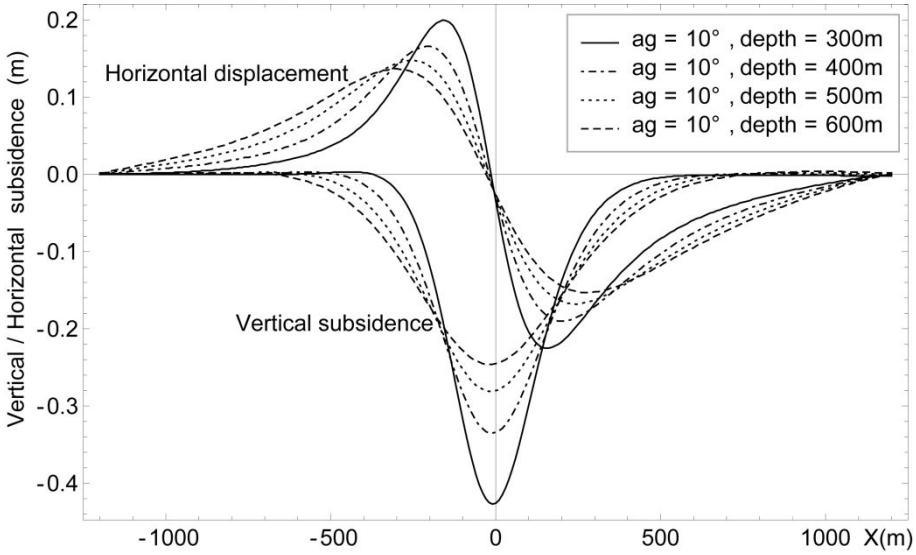

Figure 15. Variation of element subsidence with mean mining depth obtained by numerical simulations

Figure 15 illustrates that with increasing mean depth, the vertical subsidence decreases. Both the positive and absolute negative values of the horizontal displacement decrease, while the influence range increases.

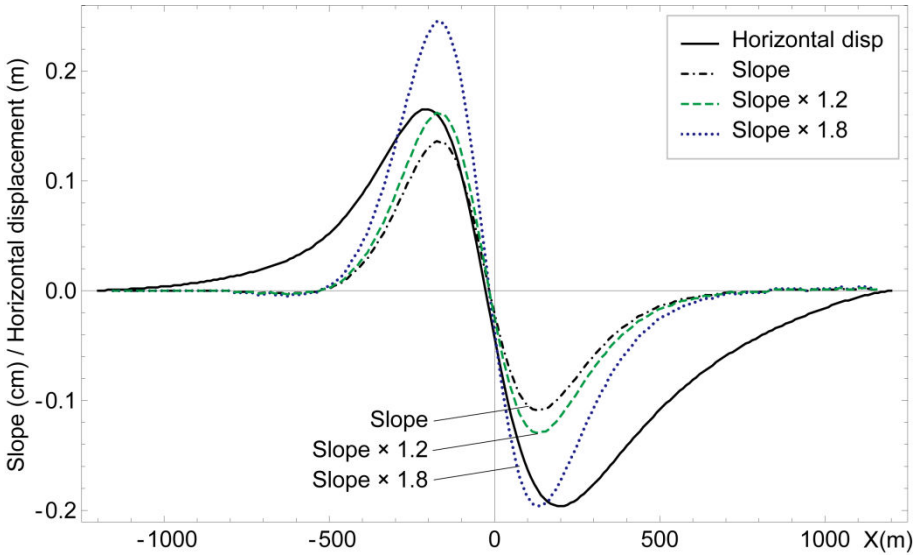

Figure 16. Comparison of slope and horizontal displacement (surface angle = 15°, mean depth = 400 m)

When the surface angle is not 0°, the horizontal displacement is no longer similar to the slope, as shown in Figure 16. The slope in this figure was computed as the derivative of the vertical subsidence. No matter how the slope is magnified, it cannot fit both sides of the horizontal displacement together. More precisely, the slope times 1.2 (the dashed curve in Figure 16) can fit the maximum value of horizontal displacement, but cannot match the

minimum value; or the slope times 1.8 (the dotted curve in Figure 16) can fit the minimum value of horizontal displacement, but exceed the maximum value in the other direction. This observation means that the horizontal displacement cannot be computed from the slope times a factor, so that we need two new influence functions to fit both the vertical and horizontal displacements.

2.3.2 Asymmetrical influence function

The first influence function mentioned in Table 2 is based on the probability density function (PDF) of a multivariate normal distribution while the traditional form of the PDF of a normal distribution can be described as in Equation 3. This function and its derivative can generally match the vertical and horizontal element mining subsidence. But due to their characteristics, their plots will always be symmetrical, regardless of how the parameters are chosen. Therefore, without refinement, they are not suitable for element mining subsidence in the cases of non-flat ground surface.

We used a complementary error function, as in Equation 4, to shift the basic PDF of a normal distribution and its derivative, to make them asymmetrical, so that they can be used as the influence function for the calculation of the vertical and horizontal displacements for non-flat surfaces. After that, they should be multiplied by a factor (*sm*), to enlarge their value.

To accurately represent element subsidence, several parameters should be calibrated. The new asymmetrical influence functions are described in Equation 5 and Equation 6. Equation 5 is used for vertical displacement. It is the PDF of a normal distribution times a complementary error function, also known as a skewed normal distribution. Equation 6 is used for horizontal displacement, it is the derivative of the PDF of a normal distribution times a complementary error function.

$$G(x) = \frac{1}{\sqrt{2\pi}\sigma} \mathrm{e}^{-\frac{(x-\mu)^2}{2\sigma^2}} \qquad \text{Equation 3}$$

$$erfc(x) = \frac{2}{\sqrt{\pi}} \int_x^{\infty} e^{-t^2} dt \qquad \text{Equation 4}$$

$$infv(x) = sm_1\, G(x)\, erfc\left[-\frac{\alpha_1(x-\mu_1)}{\sqrt{2}\sigma_1}\right] = \frac{sm_1}{\sqrt{2\pi}\sigma_1} \mathrm{e}^{-\frac{(x-\mu_1)^2}{2\sigma_1^2}} erfc\left[-\frac{\alpha_1(x-\mu_1)}{\sqrt{2}\sigma_1}\right]$$

Equation 5

$$infh(x) = sm_2\, G'(x)\, erfc\left[-\frac{\alpha_2(x-\mu_2)}{\sqrt{2}\sigma_2}\right] = \frac{sm_2(x-\mu_2)}{\sqrt{2\pi}\sigma_2^3} \mathrm{e}^{-\frac{(x-\mu_2)^2}{2\sigma_2^2}} erfc\left[-\frac{\alpha_2(x-\mu_2)}{\sqrt{2}\sigma_2}\right]$$

Equation 6

Using *infv* and *infh* to fit the vertical and horizontal element displacement obtained from numerical simulations, part of the parameters of these two functions under different surface angles and mean depths are listed in Table 5. They have been obtained using non-linear fitting with the Levenberg-Marquardt method in *Mathematica*™.

Table 5. Parameters of the influence functions

Surface angle(°)	Mean depth(m)	sm_1	μ_1	σ_1	α_1	sm_2	μ_2	σ_2	α_2
0	100	-116.6	0.0	48.2	0.000	-8160.9	0.0	68.6	0.000
0	200	-137.9	0.0	91.7	0.000	-21218.3	0.0	134.6	0.000
0	300	-137.8	0.0	132.1	0.000	-34779.6	0.0	199.5	0.000
0	400	-138.4	0.0	169.3	0.000	-49205.0	0.0	259.2	0.000
0	500	-139.0	0.0	203.0	0.000	-62094.6	0.0	308.9	0.000
0	600	-140.2	0.0	233.6	0.000	-72768.9	0.0	348.0	0.000
5	200	-138.4	-65.6	116.8	1.181	-21285.2	-2.3	134.9	0.078
5	300	-138.2	-92.0	165.7	1.119	-34815.9	-4.6	199.7	0.080
5	400	-139.1	-114.3	208.5	1.053	-49204.1	-7.3	258.7	0.073
5	500	-139.7	-131.9	245.8	0.983	-62102.5	-10.9	308.0	0.069
5	600	-141.0	-144.3	276.6	0.901	-72846.9	-14.5	346.8	0.062
10	300	-138.1	-107.5	179.5	1.522	-34874.1	-9.3	200.6	0.167
10	400	-138.6	-134.1	224.4	1.416	-48731.1	-15.2	258.2	0.159
10	500	-139.1	-155.9	261.4	1.293	-61222.0	-20.7	305.8	0.133
10	600	-140.0	-171.2	290.8	1.152	-71639.7	-26.2	343.8	0.107
15	400	-138.6	-144.9	233.0	1.709	-48115.1	-20.3	256.0	0.220
15	500	-138.5	-169.5	270.1	1.548	-59800.7	-28.5	301.5	0.190
15	600	-139.1	-187.9	298.1	1.361	-70181.5	-35.5	338.2	0.148

By plotting these parameters versus depth and angle as in Figure 17, we can then fit them to simple functions (Equation 7 to Equation 14) so that they can be defined for any depth and angle in the studied range. When the surface angle is 0°, μ and α should always be 0 to keep the two influence functions symmetrical. In that case, σ_1 can also be computed from the influence angle (φ) and the mining depth (H) as in Equation 15.

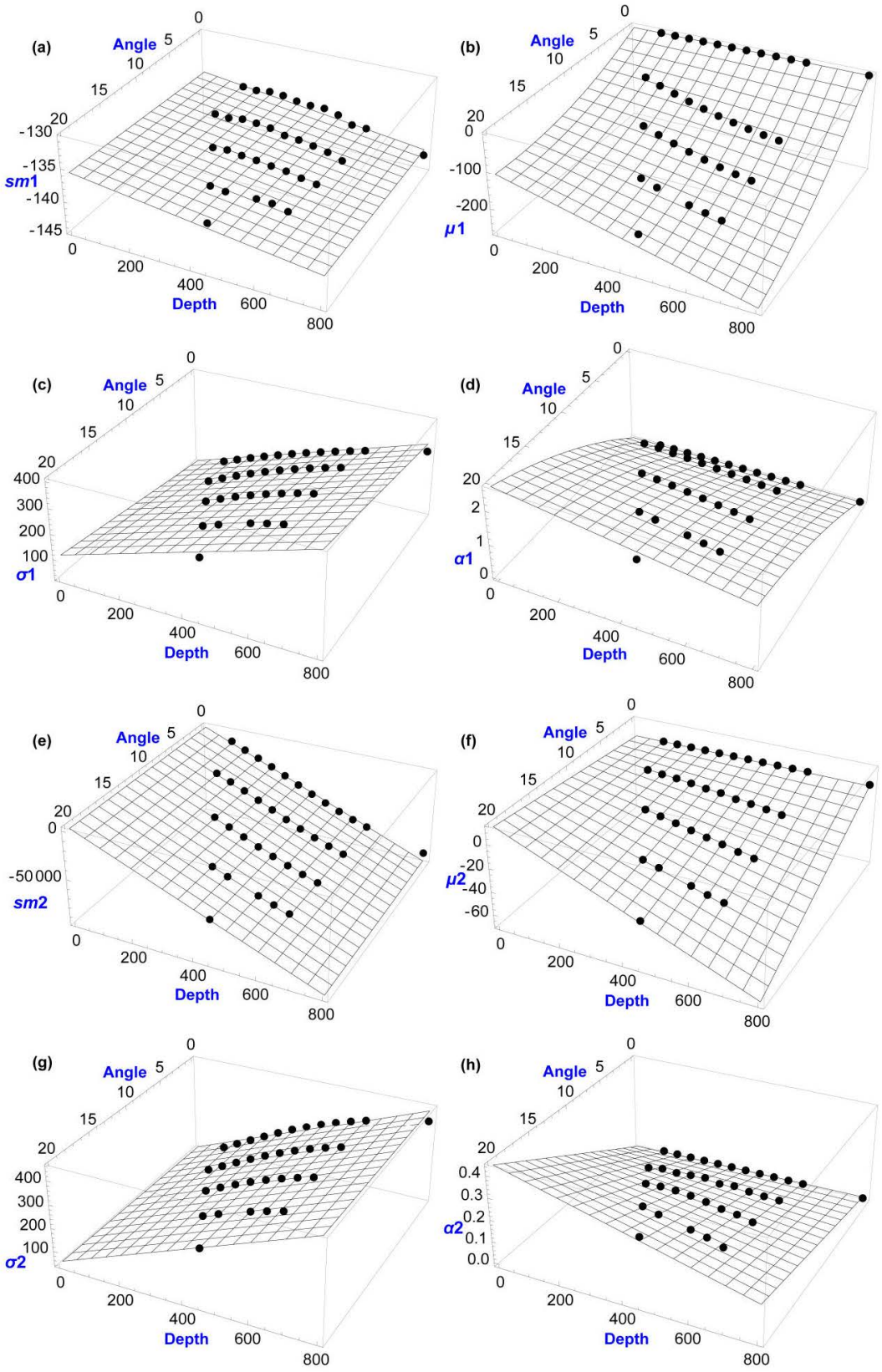

Figure 17. The relationships between parameters of new asymmetrical influence functions and surface angle and mean depth: (a)~(d) are the fittings of the parameters of infv in Equation 5, the fitting results are shown in Equation 7 ~ Equation 10; (e)~(h) are the fittings of the parameters of infh in Equation 6, the fitting results are shown in Equation 11 ~ Equation 14

$$sm_1 = -136.73 + 0.050\ ag - 0.0059\ H \quad \text{Equation 7}$$

$$\mu_1 = -12.26\ ag + 0.34\ ag^2 - 0.0099\ ag\ H \quad \text{Equation 8}$$

$$\sigma_1 = 4.78\ ag + 0.41\ H \quad \text{Equation 9}$$

$$\alpha_1 = 0.19\ ag - 0.0026\ ag^2 - 0.000060\ ag\ H \quad \text{Equation 10}$$

$$sm_2 = 1953.82 - 23.20\ ag - 123.21\ H \quad \text{Equation 11}$$

$$\mu_2 = 0.68\ ag - 0.0053\ ag\ H \quad \text{Equation 12}$$

$$\sigma_2 = 1.02\ ag + 0.59\ H \quad \text{Equation 13}$$

$$\alpha_2 = 0.022\ ag - 0.000017\ ag\ H \quad \text{Equation 14}$$

$$\sigma_1 = H\ \tan(\varphi)/\sqrt{2\pi} \ \text{(ag=0)} \quad \text{Equation 15}$$

Asymmetrical influence functions (both *infv* and *infh*), which represent element subsidence, can be calculated under any surface angle and mean depth. Figure 18 shows the comparison between element subsidence from numerical simulations, the original symmetrical, and the new asymmetrical influence functions for randomly chosen cases. Figure 19 illustrates the differences between numerical simulations and the original or improved influence function method. The sum of the squares of the differences between the results of the numerical simulation and the original influence function method or the improved influence function method can be found in Table 6 (the distance between two neighboring sample points is 10 m). Figure 18, Figure 19 and Table 6 illustrate that the new asymmetrical influence functions fit better than the original symmetrical functions as long as the surface angle grows.

To make Figure 18, Figure 19 and Table 6 understandable, please note that: “Simulation” means the numerical simulation results; “Sym_inf” means the original method using the symmetrical influence functions; “Asym_inf” means the improved method using the asymmetrical influence functions; “Simulation – Sym_inf” means the difference of subsidence between the numerical simulation results and the original method using the symmetrical influence functions; “Simulation – Asym_inf” means the difference of subsidence between the numerical simulation results and the improved method using the asymmetrical influence functions; “(V)” means the vertical subsidence; “(H)” means the horizontal displacement.

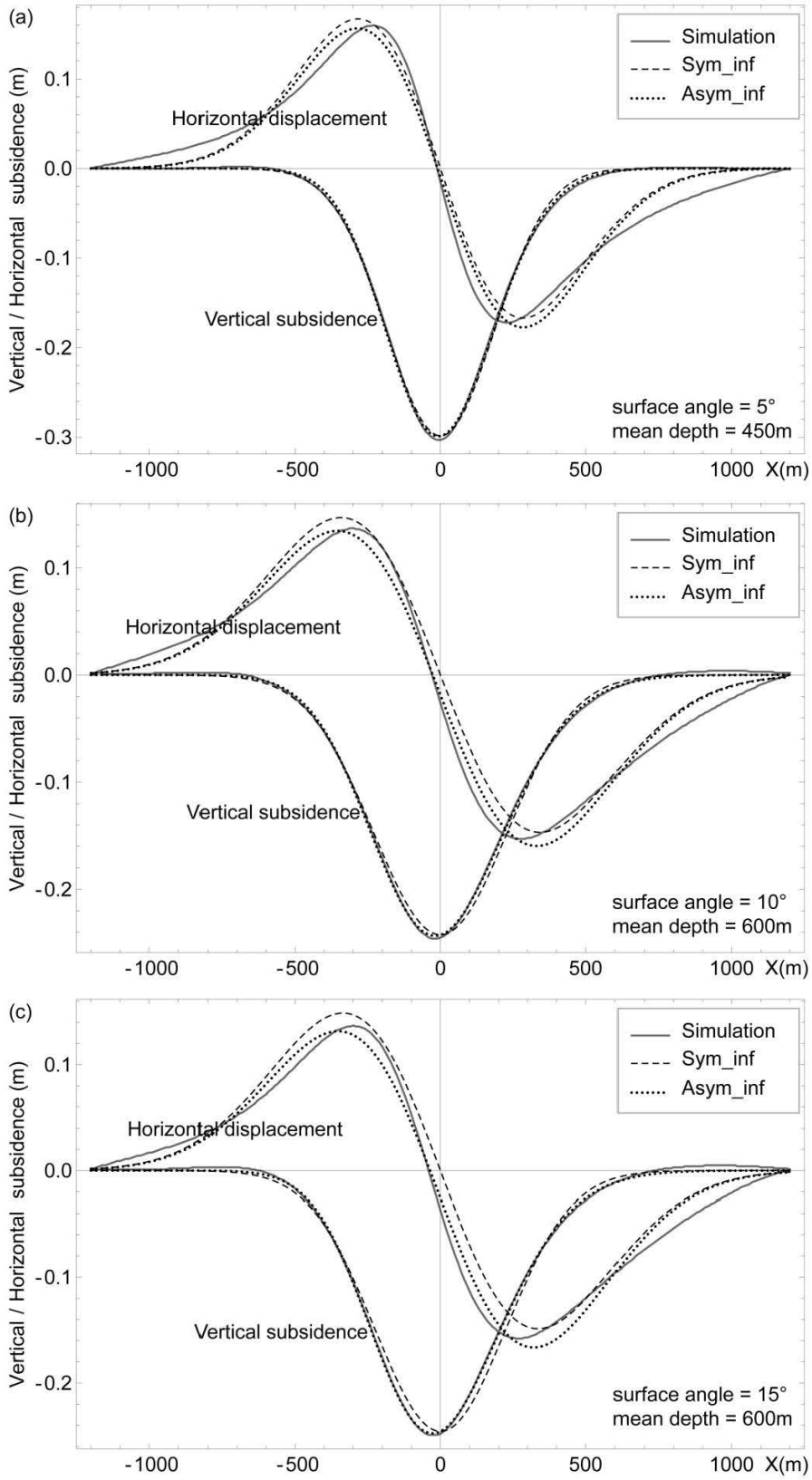

Figure 18. Element subsidence comparison (numerical simulation, original symmetrical influence function method and new asymmetrical influence function method): (a) when surface angle is 5°, mean depth is 450 m; (b) when surface angle is 10°, mean depth is 600 m; (c) when surface angle is 15°, mean depth is 600 m

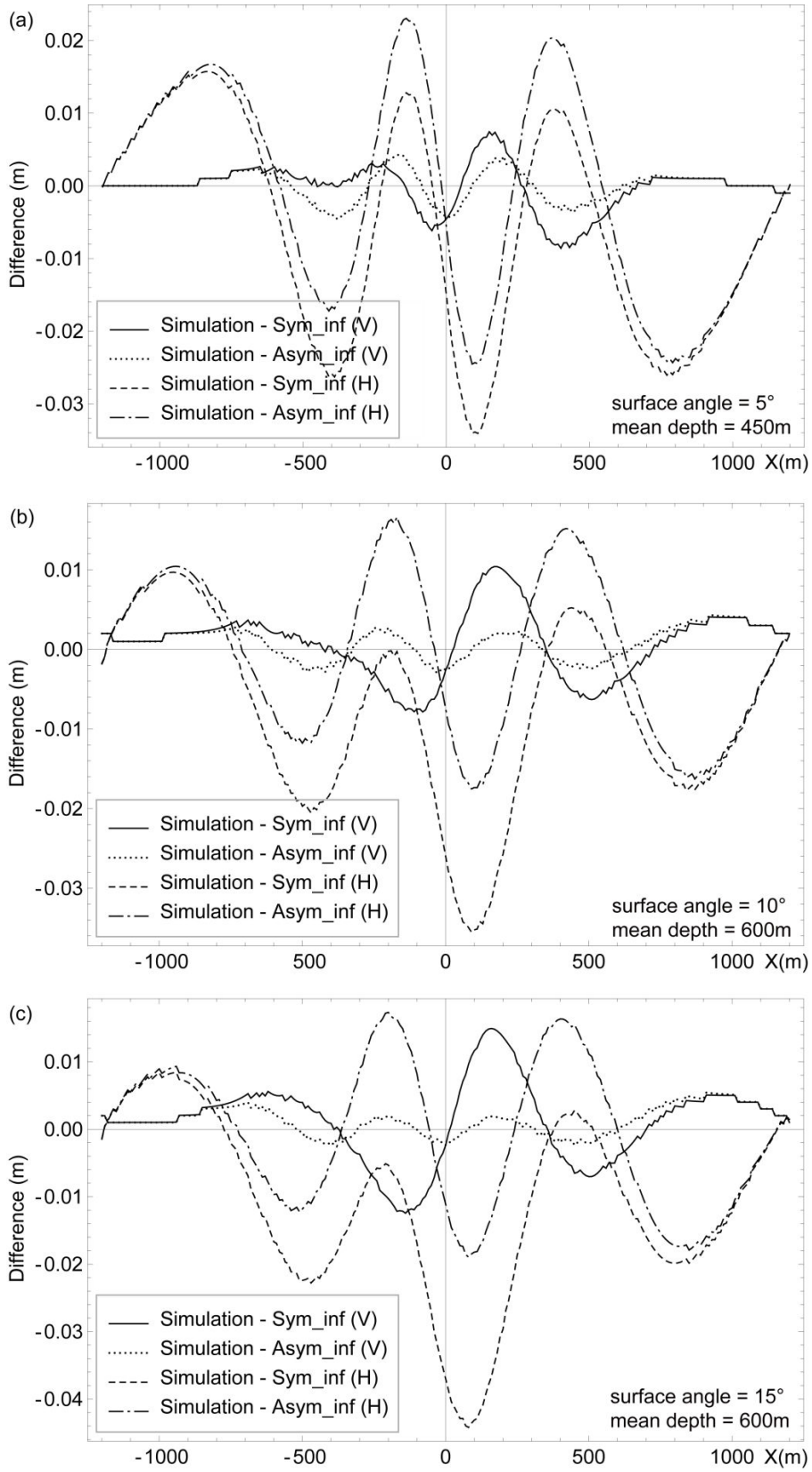

Figure 19. Differences in element subsidence computation (numerical simulation minus original symmetrical influence function method and numerical simulation minus new asymmetrical influence function method): (a) when surface angle is 5°, mean depth is 450m; (b) when surface angle is 10°, mean depth is 600m; (c) when surface angle is 15°, mean depth is 600m

Table 6. The sum of the squares of the differences between the numerical simulation results and the original symmetrical or improved asymmetrical influence function method results (element subsidence); Bold values are the best results and all correspond to asymmetrical influence function

The sum of squares	ag=5°, H=450m (Figure 18(a))	ag=10°, H=600m (Figure 18(b))	ag=15°, H=600m (Figure 18(c))
Simulation - Sym_inf(V)	0.0023	0.0042	0.0085
Simulation - Asym_inf(V)	**0.0010**	**0.0011**	**0.0014**
Simulation - Sym_inf(H)	0.0615	0.0477	0.0716
Simulation - Asym_inf(H)	**0.0510**	**0.0243**	**0.0271**

2.3.3 Full-scale subsidence

Following the principles of the influence function method, the new asymmetrical influence functions can be used to account for both vertical and horizontal displacements of every surface point induced by any extraction zone unit.

At any surface point, the asymmetrical influence function to be used for a given element mining zone, must be defined regarding the surface angle and mean depth. When the surface is undulant, as in Figure 20, the surface angle and mean depth of every surface point vary. Taking P1 in Figure 20 as an example, we can consider L1, which is the tangent of the surface at P1, as the hypothetical calculative surface, then use surface angle ag1 and mean depth H1 to account for the subsidence at this point induced by the excavation element under consideration, as we did when the surface has a constant slope.

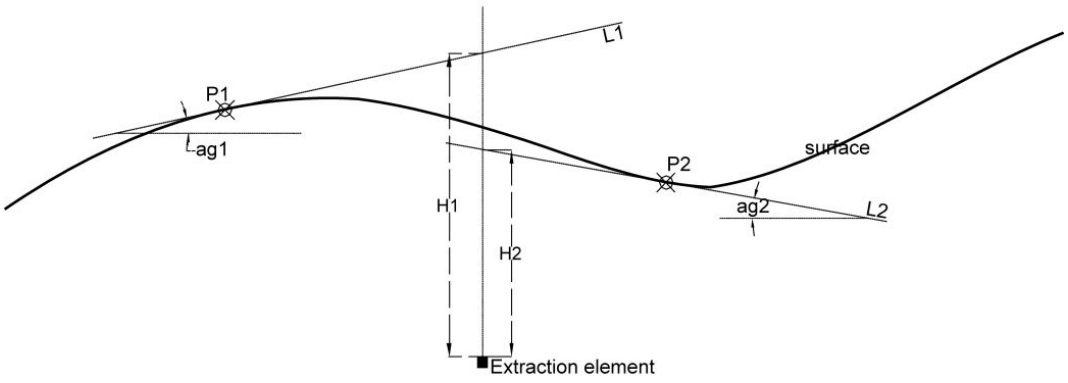

Figure 20. The surface angle and mining depth when surface angles vary

After that, displacements at every surface point due to mining can be computed by the summation or integration method. Finally, full-scale subsidence is achieved by summing all the points' displacements. We have programmed these procedures into *Mathematica™*.

Figure 21 and Figure 22 show full-scale subsidence comparisons between the original

influence function method, the improved influence function method and the numerical simulation when the surface has a unique global slope angle. Figure 23 provides the same comparison when the surface angle varies and Figure 24 concerns the case of a multi-layered roof. The legends in these figures have the same meanings as in Figure 18. In Figure 21, the subsidence is subcritical, while in Figure 22 and Figure 24 it is critical and in Figure 23 it is supercritical (i.e. flat zone in the middle).

These four figures show that both the original and improved methods provide a good estimate of the vertical subsidence, but the improved method looks better than the original in the surface upward direction (right side of Figure 21, Figure 22 and Figure 24). As aforementioned, when the surface is inclined, the location of the maximum subsidence point moves to the downward direction of surface, and the improved method is better than the original one from this point of view. For example, in Figure 21, the x-coordinates of the maximum vertical subsidence points obtained by the numerical simulation, the improved and original methods are respectively -35, -40 and -5; in Figure 22, these coordinates are -9.4, -10 and -2; and in Figure 24, they are -15, -21 and -6. Regarding the horizontal displacements, the improved method fits much better than the original for the maximum value, the influence range, or the position of the intersection point of the subsidence curve and the x-axis. Table 7, which lists the sum of the squares of the differences between the results of the numerical simulation and the original influence function method or the improved influence function method (the distance between two neighboring sample points is 10 m), also proves that the improved method is more relevant than the original, especially in the horizontal displacement computation.

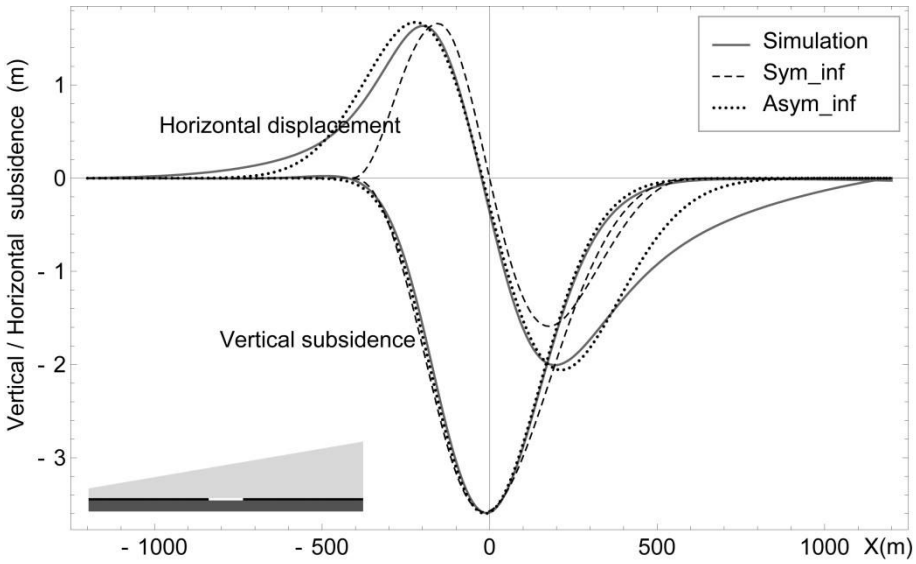

Figure 21. Comparison of the methods in the case of subcritical full-scale subsidence (surface angle = 10°, mean depth = 300 m, length of mining zone = 300 m)

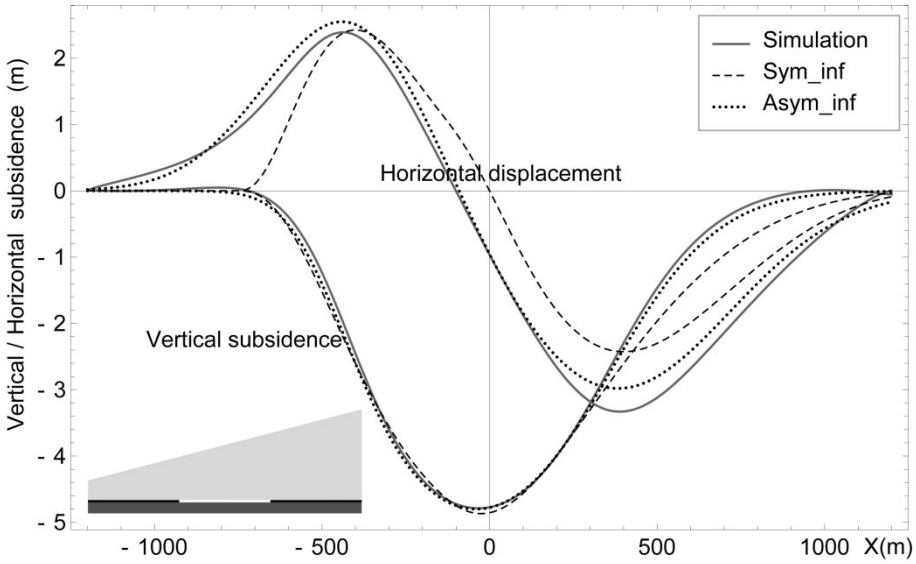

Figure 22. Comparison of the methods in the case of critical full-scale subsidence (surface angle = 15°, mean depth = 500 m, length of mining zone = 800 m)

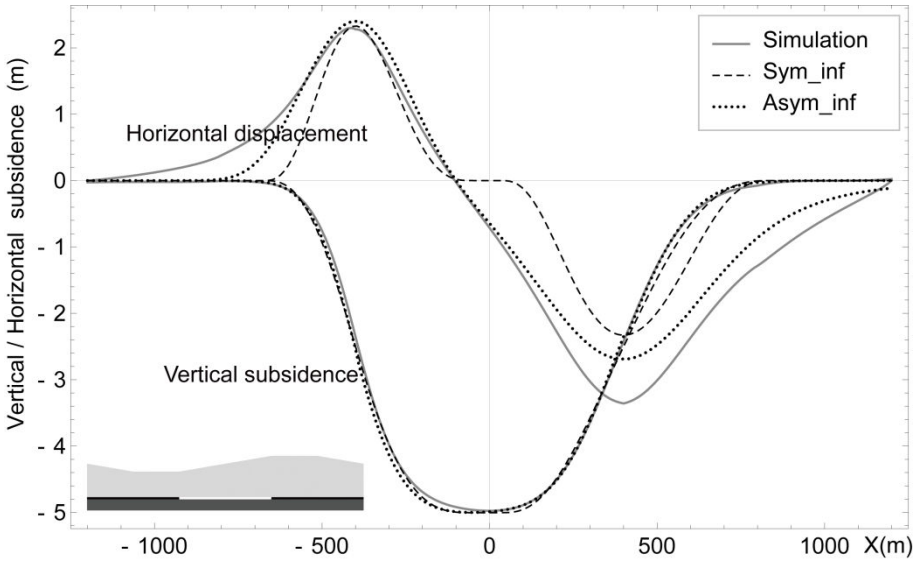

Figure 23. Comparison of the methods in the case of supercritical full-scale subsidence (varied angle, mean depth = 300 m, length of mining zone = 800 m)

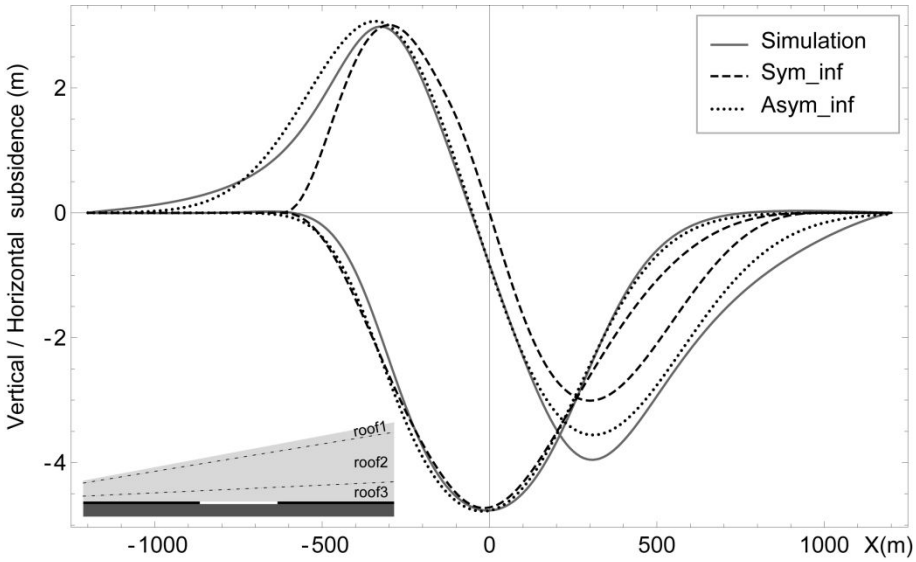

Figure 24. Comparison of the methods in the case of critical full-scale subsidence (surface angle = 11°, mean depth = 400 m, length of mining zone = 600 m; multi-layered roof, the Young modules of roof1, roof2 and roof3 are 5.0, 13.0 and 30.6 MPa, the mean thicknesses of roof1, roof2 and roof3 are 50, 250 and 100 m)

Table 7. The sum of the squares of the differences between the numerical simulation results and the original symmetrical or improved asymmetrical influence function method results (full-scale subsidence); Bold values are the best results and all correspond to asymmetrical influence function

The sum of squares	ag=10°, H=300m m_zone=300m (Figure 21)	ag=15°, H=500m m_zone=800m (Figure 22)	varied angle, H=300m m_zone=800m (Figure 23)	ag=11°, H=400m m_zone=600m (with 3 roofs) (Figure 24)
Simulation - Sym_inf(V)	2.56	15.32	1.47	9.66
Simulation - Asym_inf(V)	**0.36**	**1.64**	**1.10**	**3.48**
Simulation - Sym_inf(H)	40.69	96.29	150.14	103.72
Simulation - Asym_inf(H)	**6.87**	**8.60**	**23.53**	**12.26**

2.4 The usage of the developed code

2.4.1 Corrections from field data

In practice, some factors obtained by surveying data of local subsidence events can be taken into account to optimize the quality of subsidence calculation. Usually, the maximum subsidence values (vertical and horizontal) and the influence angle can be considered as the adjusting factors (input data for our code). They can be estimated from past nearby subsidence events, in other words, they are known values for a given mining area.

We can magnify or minify the vertical and horizontal subsidence obtained by our improved

influence function method to match the previously mentioned expected maximum values. For horizontal displacement, either the positive or negative maximum values can be considered. During this process, the vertical and horizontal subsidence at every point should respectively be multiplied by a uniform magnification factor so that the shapes of the subsidence curves remain unchanged.

Regarding the influence angle, it can be used to compute σ_1 as in Equation 15 when surface is flat. Solving simultaneous Equation 9 and Equation 15 under the condition of ag = 0° can provide a new coefficient of H (in Equation 9), which is related to the influence angle, then σ_1 can be redefined as in Equation 16. A similar adjusting process can be carried out for the influence angle of the horizontal displacement, as shown in Equation 17.

$$\begin{cases}\sigma_1 = 4.78 \times 0 + t1\ H \\ \sigma_1 = H\ \tan(\varphi_v)/\sqrt{2\pi}\end{cases} => \ \sigma_1 = 4.78\ ag + \frac{\tan(\varphi_v)}{\sqrt{2\pi}} H \qquad \text{Equation 16}$$

$$\begin{cases}\sigma_2 = 1.02 \times 0 + t2\ H \\ \sigma_2 = H\ \tan(\varphi_h)/\sqrt{2\pi}\end{cases} => \ \sigma_2 = 1.02\ ag + \frac{\tan(\varphi_h)}{\sqrt{2\pi}} H \qquad \text{Equation 17}$$

where φ_v is the influence angle for vertical displacement and φ_h is the influence angle for horizontal displacement

As in Equation 16 and Equation 17, we suggest two influence angles (φ_v and φ_h) for the calculations of σ_1 (related to vertical subsidence) and σ_2 (related to horizontal displacement), respectively. In practice, as φ_h may be unknown, σ_2 also can be calculated from φ_v. Here, we try to provide a possibility to make more precise computation of the horizontal displacement when its influence angle (φ_h) is known (derived from past or nearby subsidence events for instance).

2.4.2 The methodology of the developed code

In the previous sections of this chapter, we introduced the principles of the influence function method, and improved them by taking into account the new asymmetrical influence functions of both vertical subsidence and horizontal displacement in order to better take ground topographic variations into account. This improvement has been then implemented in a code programmed into *Mathematica™*.

To use this code, the ground surface data, extraction zone data and some other parameters should be organized following a specified form and then input to the code. As in Figure 25, the ground surface data and the extraction zone data are coordinates information. They are used to define the topography of the surface and the shape of the mining zone. The additional input parameters should include the maximum values and the influence angles of the vertical and horizontal subsidence, and the discretization of the extraction zone. As aforementioned in Equation 2, the mesh length of the mining element should be smaller than a threshold to avoid the sensitivity of the results to the mesh sizes.

Our code can take all the input data into account, and then the calculated subsidence data, which contain vertical and horizontal subsidence, are output into two separate lists. After that, as a post-processing work, the subsidence charts and other subsidence factors, including slope (the derivative of vertical subsidence), curvature (the derivative of slope) and

horizontal strain (the derivative of horizontal displacement) can also be computed in *Mathematica™*.

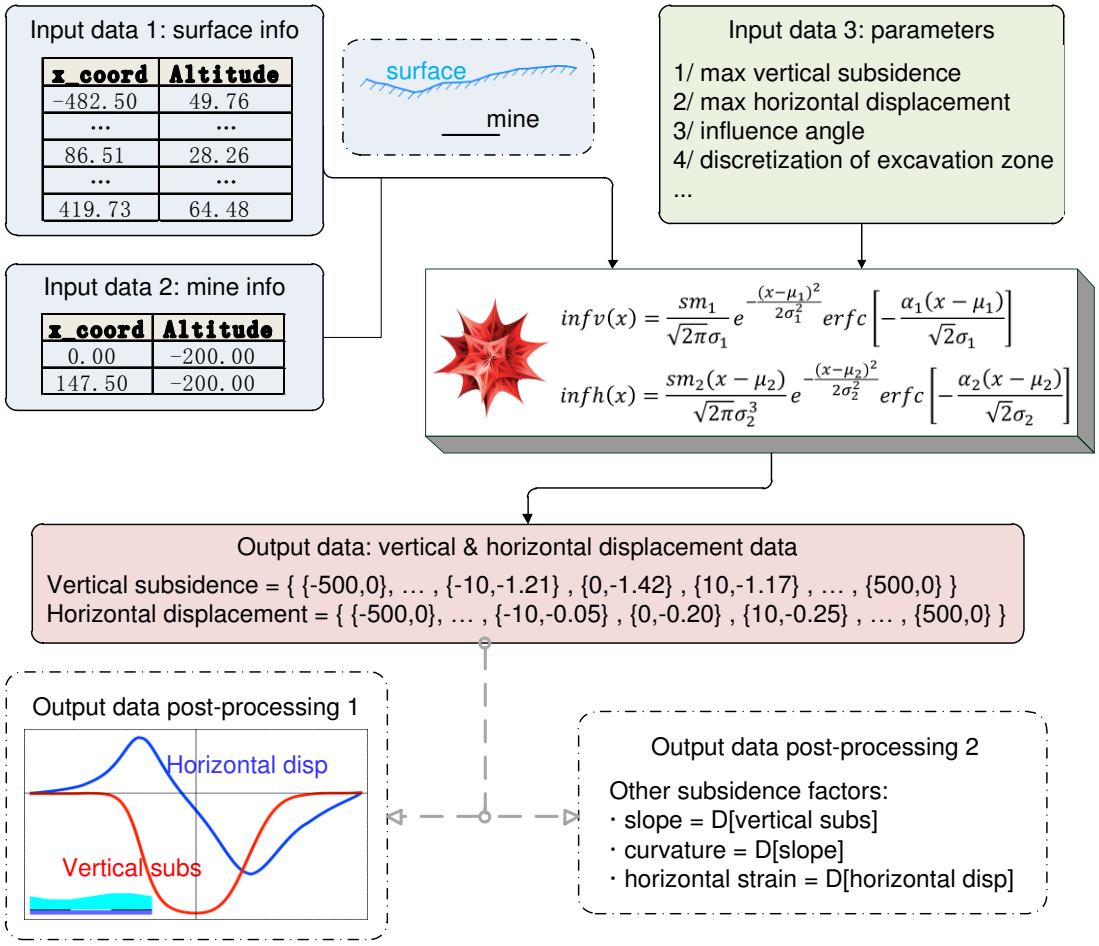

Figure 25. The usage process diagram of the developed code

2.5 Application cases

2.5.1 Case study 1

In the iron mines of Lorraine, the room and pillar mining method is widely used and several subsidence events appeared either during the excavation or after the mines have been abandoned. From 2009 to 2011, our laboratory did some studies about an iron mine in Angevillers (a small city in the north of Lorraine) where a slow subsidence process has been recorded. The ground surface is slightly inclined to the west; its coordinates are listed in Table 40 in Annex 2 and shown in Figure 26. Measured vertical subsidence (listed in Table 41 in Annex 2) and the two likely collapsed mining zones (their coordinates are listed in Table 42 in Annex 2) are also shown in Figure 26. The subsidence is subcritical and the maximum vertical displacement values over the two zones are 0.5 m and 0.3 m at present. The influence angle is about 30°. The mean depth of the mine is around 160 m. These are the

only parameters available for this case study.

Introducing the original symmetrical and our new asymmetrical influence function methods in 3D and taking the field conditions into account lead to the vertical subsidence results given in Table 43 and Table 44 in Annex 2. The vertical subsidence iso-contours are given in Figure 26. It can be noticed that the asymmetrical function provides results closer to the observed values in terms of the location of the maximum subsidence and all subsidence iso-contours which all shift to the downward direction of the ground surface (left side of Figure 26). This behavior is clearer on the left side of mzone1, where the surface elevation contours are closer to each other (which means a deeper surface angle), than on the right side of mzone2. This calculation confirms the role of the topography on the distribution of subsidence that the original influence function does not properly take into account.

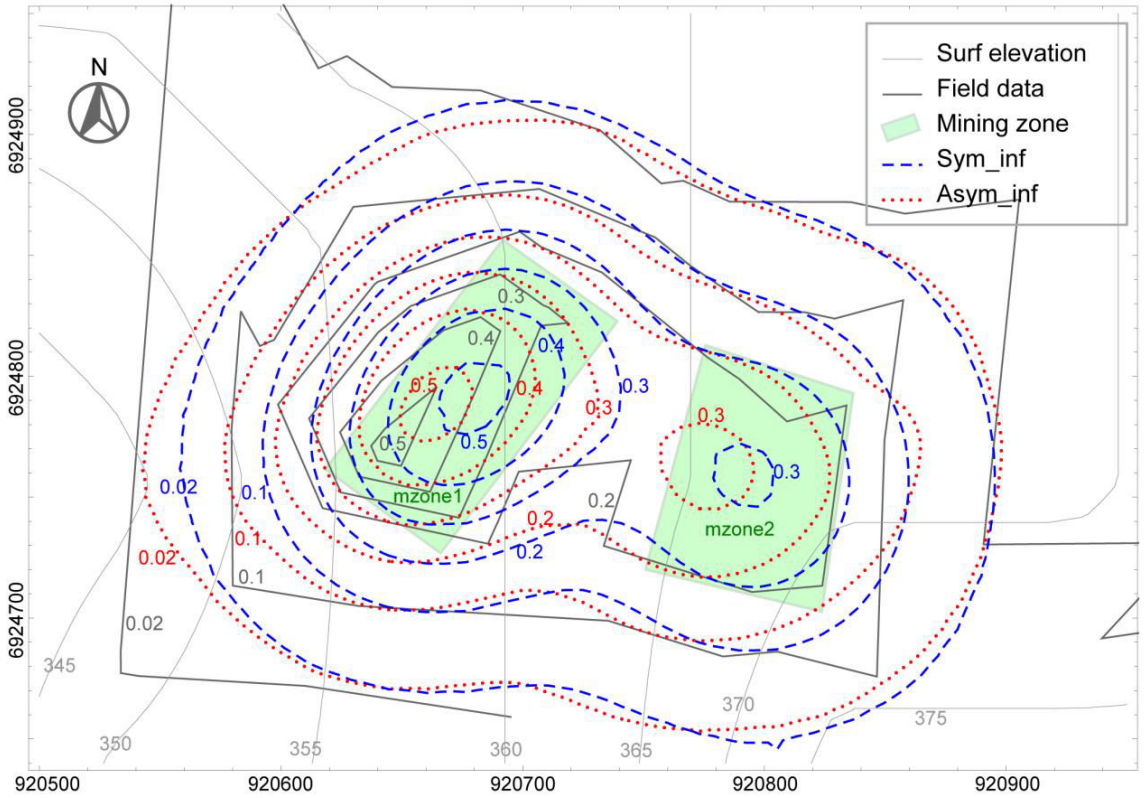

Figure 26. Comparison between the measured vertical subsidence (Angevillers, France) and the computed subsidence either from the original or the new influence function method (unit of subsidence: m)

2.5.2 Case study 2

Using our improved influence function method, and taking into account the maximum subsidence values and influence angles, the subsidence of a transverse section of the #2307 working face, which is a fully mechanized caving coal mine working face in Jincheng city of China, is computed and shown in Figure 27. The subsidence got by field surveying and

subsidence calculated by the original as well as the new influence function methods are plotted in the same figure for comparison, and they can also be found in Table 47, Table 48 and Table 49 in Annex 2. Table 45 and Table 46 in Annex 2 list the coordinates of the ground surface and the #2307 working face. The elevation of the ground surface over this working face is around 880 - 940 m; the transverse length of the working face is 147.5 m, the mean mining depth is around 230 m, the mean thickness is 6.7 m, and the dip angle is 1.5°; the measured maximum vertical and horizontal subsidence values are 2.64 m and +0.57/-0.85 m (maximum values of the horizontal displacement upon the two sides of the mining zone; in this case, the positive maximum value is given as an input for the improved method), the mean influence angles for the vertical and horizontal displacements are 25° and 40° (Song *et al*. 2007). These are the only parameters available for this case study.

Regarding the measured field subsidence, Figure 27 shows that it is asymmetrical. The maximum vertical subsidence is shifted to the surface downward direction and the negative horizontal displacement is clearly greater than the positive. Figure 27 also shows the subsidence computed from the original influence function method, still being symmetrical. By contrast, the subsidence computed with the improved influence function method globally better fits the field data. The Table 8, which lists the sum of the squares of the differences between the subsidence given by the field data and the original influence function method or the improved influence function method (the distance between two neighboring sample points is 10 m), also proves that the new method is better than the original, especially in the horizontal displacement computation.

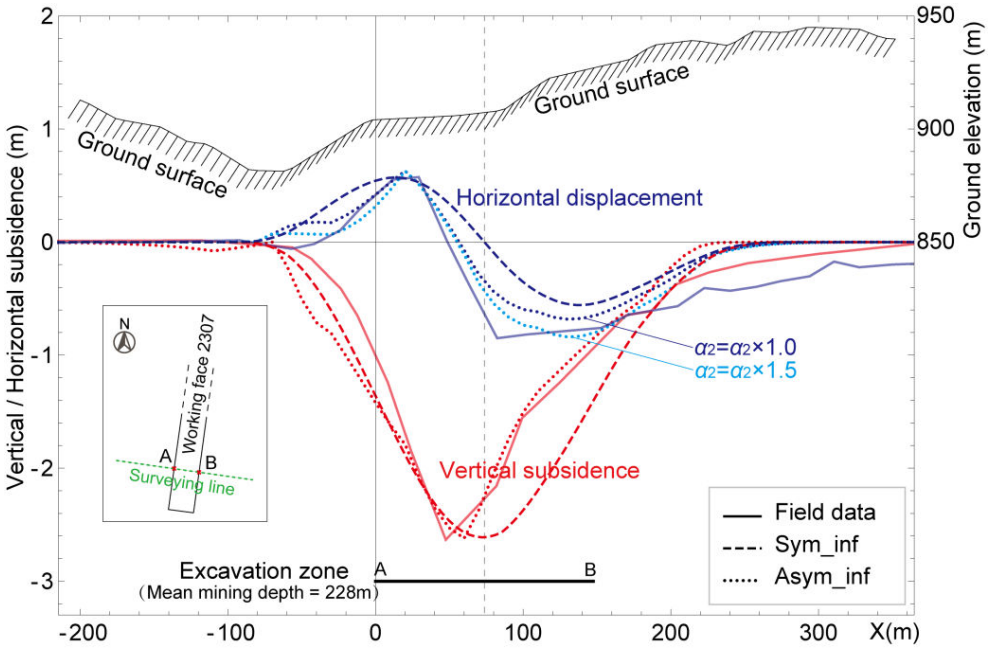

Figure 27. Comparison between the measured vertical and horizontal subsidence (Jincheng, China) and the computed subsidence either from the original or the new influence function method

Table 8. The sum of the squares of the differences between the field data and the original symmetrical or improved symmetrical influence function method results (case study 2); Bold values are the best results and all correspond to asymmetrical influence function

The sum of squares	In the calculation range (-300 ≤ x ≤ 350)	In the mining range (0 ≤ x ≤ 175.5)
Field data - Sym_inf(V)	4.43	3.79
Field data - Asym_inf(V)	**2.14**	**0.41**
Field data - Sym_inf(H)	4.22	2.32
Field data - Asym_inf(H) ($\alpha_2 = \alpha_2 \times 1.0$)	**1.84**	**0.54**
Field data - Asym_inf(H) ($\alpha_2 = \alpha_2 \times 1.5$)	**1.49**	**0.22**

In this calculation using the new influence function method, the positive maximum horizontal displacement is set to a known constant value depending on the field data, but the negative part of the horizontal displacement curve is still higher than expected as shown in Figure 27, although it is closer to the measured curve than the one given by the original method. By studying the new asymmetrical influence function method, we found that the increase of the parameter α_2 can enlarge the difference between positive and negative horizontal displacement. Therefore, the horizontal displacement can be recalculated using α_2 times 1.5 (1.5 is obtained by testing) instead of the original α_2. As shown in Figure 27, the recalculated horizontal displacement curve (data can be found in Table 49) fits better than the original one without magnifying α_2 (also refer to Table 8).

Moreover, some other parameters can also be adjusted to improve the computational precision: α_1 has an effect on shifting the vertical subsidence (the asymmetry slightly increases as α_1 is increased); μ_1 and μ_2 can let the vertical and horizontal subsidence curves make a move along the surface dip direction (move to the surface upward direction as μ increases) without changing the shape. But the quantitative value of the magnification factor is unknown without a feedback from field data as the magnification of α_2 in case study 2. Once such adjustment is carried out in a particular mine or mine area, it can be used for nearby mining zones where geological and excavation conditions are similar.

As seen before, our new asymmetrical influence function method can be used to improve mining subsidence prediction work under non-horizontal surfaces. However, if only the vertical subsidence is concerned, this improved method does not provide prominent added value. Given that most damage due to subsidence comes from the horizontal strain of the ground, which can be computed as the derivative of the horizontal displacement, the new method looks more appropriate for most cases, when it is used to analyze the consequence of subsidence on surface assets.

2.6 Conclusions

In this chapter, we proposed some improvements to the original influence function method to take the topography influence on subsidence due to horizontal underground mining into

account.

The original influence function method is well adapted for predicting subsidence induced by the extraction of horizontal stratiform layer from an underground mine beneath a flat surface, but provides improper results when the surface is not flat. Therefore, new asymmetrical influence functions have been suggested to compute the vertical and horizontal element subsidence. They are based on the probability density functions of normal distributions corrected by complementary error functions. The parameters of these asymmetrical influence functions can be described by the surface dip angle and mean mining depth, meaning that the new influence functions take topographic variations into account. Full-scale subsidence can then be computed using the new functions according to a standard summation method.

This improved influence function method can take the known expected maximum subsidence and influence angle obtained from field data into account. Some other parameters can also be adjusted from surveying subsidence data to enhance the computational precision.

Several numerical simulations and two field subsidence cases were studied and showed that compared to the original influence function method, the new method better simulates subsidence, especially in terms of horizontal displacement.

This developed subsidence computation code does not consider inclined mining zones, which has been already studied by other researchers. The influence of an inclined mining zone on subsidence could be taken into account according to the achievements of these studies.

The parameters of the new asymmetrical influence functions were obtained by numerical simulations using adjusted rock properties from Lorraine region (France); they may also be used in other regions by applying the local expected maximum subsidence values and influence angles. Moreover, if the parameter fittings could be redone before using this method in other regions, the subsidence results would probably be effective.

Chapter 3: Introducing structural mechanics into building damage assessment under mining subsidence

Chapitre 3: La mécanique des structures au service de l'évaluation des dommages aux bâtiments en zone d'affaissement minier

Abstract of chapter 3

This chapter aims at studying the mechanical behavior of civilian houses, which are normally non-high-rise timber, masonry and concrete buildings, at a large scale (a city for instance) to provide some preliminary estimates of the damages due to mining subsidence. As our required precision is not necessarily high, it is commonly believed that plane (2D) models, which have the advantages of easy computer programming and fast calculation compared to making use of 3D models, can be used to solve real-world 3D structural problems.

In the present research, two plane framed structural models, which are set up in the vertical sections passing through the principal inertia axes of a building's projective polygon, are used to simulate a real-world 3D building.

The matrix displacement method is used in this research. Some modifications are made to this method to take full advantage of the capabilities of *Mathematica*™. Structural models, which are simplified from the real structure, are firstly prepared by digitizing the model into node and element lists. Then the force-displacement relations of an element are introduced in a traditional way. After that, in order to organize the force-displacement relations of the entire structural model, we skip the step of organizing the structure stiffness matrix by directly solving a set of equations composed of the force equilibrium conditions in global coordinate system at each node. Finally, the internal forces and displacements over the structural model can be solved. Our method was proved credible by the comparison of results with two other commercial softwares.

The grades of the building damage can be determined according to the computed internal forces over the structure, including the axial forces, shear forces, and bending moments, through the use of criteria, which indicate the relationships between each damage grade and its corresponding value ranges of forces. The damage extent can be decided from one of the internal forces and its corresponding criterion, from any two of them and their corresponding criteria, or from all of the three and their criteria. Using our code, the damage evaluations can be intuitively presented on the deformed structure by colored lines, which are used to distinguish different grades. Kinematic structure damage evaluations are also available in this code.

Practically speaking, the scope of the method developed in this chapter is more general than assessing building damage induced by mining subsidence. It can be used also for studying damage due to arbitrary external forces and displacements.

Résumé du chapitre 3

Ce chapitre vise à présenter une méthode de modélisation du comportement mécanique d'habitations civiles à une grande échelle (une ville par exemple) afin de fournir une estimation préliminaire des dommages induits par un affaissement minier. Comme la précision requise n'est pas nécessairement élevée, il est communément admis que des modèles 2D, qui ont l'avantage de la programmation facile et du calcul rapide, peuvent être utilisés pour résoudre des problèmes structuraux 3D.

Dans le présent chapitre, deux modèles structurels plans sont mis en place dans des sections verticales passant par les axes principaux d'inertie du polygone de projection horizontale d'un bâtiment. Ils sont utilisés pour simuler un bâtiment 3D du monde réel.

La méthode matricielle des déplacements est alors utilisée. Quelques modifications sont apportées à cette méthode pour tenir compte des avantages de Mathematica™. Les modèles structurels, simplication de la structure réelle, sont d'abord préparés par la discrétisation du modèle en listes de nœuds et d'éléments. Ensuite, les relations force-déplacement d'un élément sont introduites de façon traditionnelle. Après cela, en vue d'organiser les relations force-déplacement de l'ensemble du modèle structurel, nous sautons l'étape de l'organisation de la matrice de rigidité de la structure en résolvant directement un ensemble d'équations composées des conditions d'équilibre des forces dans le système de coordonnées global à chaque noeud. Enfin, les forces internes et les déplacements dans le modèle structurel peuvent être résolus. Notre méthode a été vérifiée par des comparaisons avec deux logiciels commerciaux.

Les niveaux de dégradation du bâtiment modélisé peuvent être déterminées à partir des forces internes calculées dans la structure : forces axiales, forces de cisaillement et moments de flexion, grâce à l'utilisation de critères associant des plages de valeurs de ces forces aux différents niveaux de dommages. L'étendue des dommages peut être appréciée à partir de l'une des forces internes et son critère correspondant, ou à partir de deux d'entre elles et de leurs critères correspondants, ou de toutes les trois et leurs critères. Grâce au code développé, les dommages peuvent être intuitivement présentés sur la structure déformée par des lignes colorées utilisées pour distinguer les différents niveaux de dommage. La cinématique des dommages de la structure est également disponible.

En pratique, la portée de la méthode développée dans ce chapitre est plus grande que l'évaluation des dommages de construction induites par un affaissement minier. Elle peut également être utilisée pour étudier les dommages dus à des forces externes et des déplacements arbitraires.

3.1 Plane framed structural model

3.1.1 The choice of the plane framed model

Many types of structures exist in civil engineering projects, and this study focuses on traditional civilian houses, which are normally non-high-rise timber, masonry and concrete buildings.

It is commonly believed that plane (2D) models can be used to solve real-world 3D structural problems, and there are already a lot of structure studies (Boone 1996, Ren *et al*. 1999, Bentz *et al*. 2000, Franzius *et al*. 2004, Finno *et al*. 2005, Milani *et al*. 2009, Mohr *et al*. 2010, El-Sayed *et al*. 2011, Stromberg *et al*. 2012, Akhaveissy *et al*. 2013, Masoero *et al*. 2013, Goh *et al*. 2014, Hamid *et al*. 2014, Reyes-Salazar *et al*. 2014) based on plane models, which have the obvious advantages of easy computer programming and fast calculation compared to making use of 3D models. But, also indicated by these studies, it is clear that a plane model cannot fully represent shapes and properties of a real structure, and the achieved displacements and forces (also strains and stresses) in such a model can only approximately stand for these quantities in the real world.

In the present research, we suggest to use plane framed structural models, which are the most often used types of models, to simulate 3D civilian houses. For each building, two framed models are considered, and their establishment can be stated as follows. First, the considered building is projected to a horizontal plane to construct a polygon, which can present the outline sketch of the building. Two principal axes of inertia of the polygon passing through the centroid point can always be found, as the red lines in Figure 28; they are definitely orthogonal to one another guaranteed by mathematical theories. Then two plane framed structural models can be set up in the spatial vertical sections through the lines of the principal axes of inertia of the polygon. Given that, our will is to study the mechanical behaviors of the civilian houses at a large scale (a city for instance including hundreds or thousands of such houses) to provide some preliminary estimates of the damages (due to mining subsidence in our case) all over the studied zone, the required precision is not necessarily high. Therefore, employing plane models to study the structural mechanical problems is an easy and efficient way for us, at least, as a first attempt to provide a damage estimate at such a large scale. The adequacy of this approach can be further proved by future work. Therefore, this chapter will mainly discuss the calculation methods of the plane framed structures.

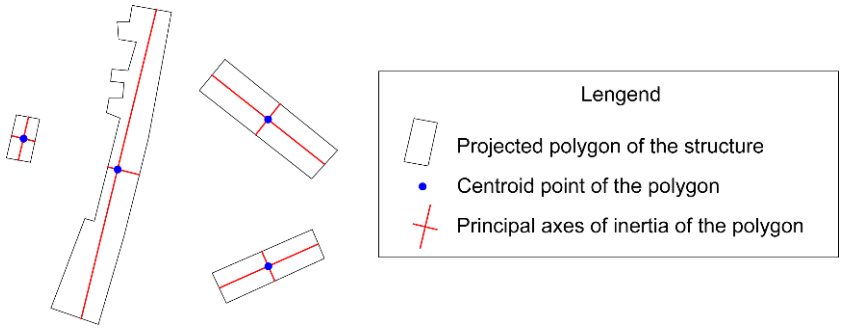

Figure 28. Principal axes of inertia of the projected polygons of the structures in a horizontal plane (top view), i.e. the chosen sections where the plane models are built

The structures in civil engineering are mainly made of materials such as steel, concrete, bricks, stone, timber, and so on. In order to simplify the statements in this chapter, the materials used in a structure are assumed to be continuous, homogeneous, isotropic, perfectly elastic or plastic in analysis. This assumption will have some degrees of approximation comparing with the practical conditions. In fact, our method and structural model can take different materials into account, which will be discussed in the real case study (chapter 4).

3.1.2 Structural model and its components

Real structures are usually too complex to perform an analysis in their original real states. A structural model involved in calculation should be a simplified representation of the real structure for the purpose of analysis or computation by neglecting some less important details. That is, the definition of the structural model is the foundation of structural analysis.

In practice, a structural model is not unchangeable. For instance, a more precise structural model should be developed for an important structure; while a less precise structural model should be used for an unimportant structure. Furthermore, in schematic design stage we can develop a rough model for a structure; while in technical design stage we can select a more precise model for the same structure. For hand-oriented methods, the simplest models of structures should be used; while for computer-oriented methods, complex models of structures might be selected. In other words, the simplification of structures, i.e. the selection of structural models, should be done according to the practical requirements and the computational conditions.

Here, the symbols and shapes of the components of a structural model, i.e. the elements, joints, and supports, are standardized for unifying the expressions in this thesis. Note that, in the present research, JOINT is defined as the connection between two or several structural elements, while SUPPORT is the connection between the structure and its foundation. When referring to a structural model, both of them can be termed as NODE, which is a mathematical point without any dimensional attribute. Hereinafter, we will normally use NODE to express the joint and the support, when it is not strictly necessary to distinguish between them. In the current section, because we are going to introduce the components of

the structural model, the names of JOINT and SUPPORT must be used separately.

(1) Element of a structure

When studying a plane framed structure, the selected structural model can be represented by a line diagram, as in Figure 29. On this diagram, each element (also can be named member, beam, or bar) of the structure is represented by a line which coincides with its centroidal axis; the length of each element is represented by the distance between nodes to which the element is attached; the position of the loads acting upon elements is also transmitted along their centroidal axes. This approach is only suitable for a framed structure. In Figure 29, there are 6 elements in total, which are named as E1 – E6.

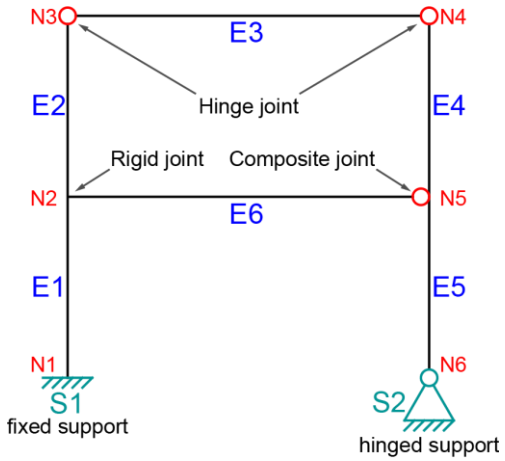

Figure 29. A plane framed structural model with 6 elements (E1 – E6), 6 nodes, including 4 joints (N2 – N5), and 2 supports (S1 and S2, i.e. N1 and N6)

(2) Joint of a structure

The connections between elements of a structure are commonly termed as joints. Two types of joints are usually used:

a) Rigid joint

A rigid joint prevents both relative translations and rotations of the element ends connected to it, which means that all element ends connected to a rigid joint have the same translation and rotation. In other words, the original angles between the elements intersecting at a rigid joint are maintained after the structure has deformed under the action of loads. Such joints are capable of transmitting forces as well as moments between the connected elements. Rigid joints are usually represented by filled points at the intersections of elements on the line diagram of the structure. As shown in Figure 29, N2 is a rigid joint. After the action of arbitrary loads, both the translations and the rotations of E1, E2, and E6 at N2 must be the same.

b) Hinge joint

A hinge joint, also named flexible joint, prevents only relative translations of element ends connected to it. All element ends connected to a hinge joint have the same translation but may have different rotations. Such joints are capable of transmitting forces but not moments between the connected elements. Hinge joints are usually depicted by hollow points at the intersections of elements on the line diagram of the structure. As shown in Figure 29, N3 and N4 are two hinge joints. Taking N3 as example, after the action of arbitrary loads, the translations of E2 and E3 at the end N3 must be the same; but, the angle between E2 and E3 might be not the same as before, due to the rotations of E2 and E3 at N3 can be different.

As shown in Figure 29, N5 is a special composite joint. It can be considered that E4 and E5 are connected to a rigid joint at N5, while E6 and E4, also E6 and E5, are connected to a hinge joint at N5. So, the translations of E4, E5 and E6 and the rotations of E4 and E5 at N5 must be the same after the action of arbitrary loads; while E6 can have a relative rotation regarding E4 and E5.

(3) Support of a structure

Supports are used to attach structures to their foundations (usually to the earth, or sometimes to other bodies), thereby restricting the movements of the structures under the action of applied loads. The supports prevent the movements by providing opposing forces of the applied loads to keep the structures at equilibrium. A support that prevents translation of the structure in a particular direction exerts a reaction force on the structure in that direction. Similarly, a support that prevents rotation of the structure about a particular axis exerts a reaction couple on the structure about that axis. The types of supports commonly used for plane structures are grouped into 4 categories, as shown in Figure 30.

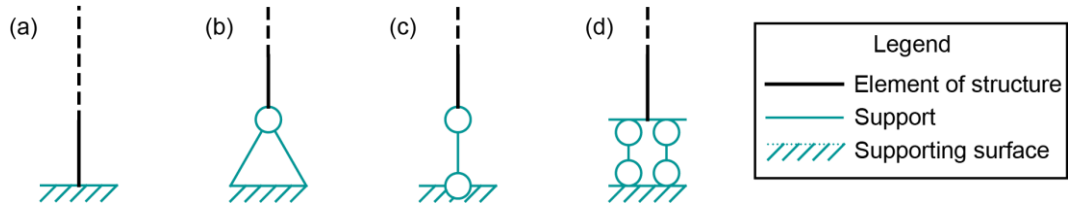

Figure 30. The commonly used supports: (a) fixed support; (b) hinged support; (c) roller support; (d) directional support

a) Fixed support

The fixed support, whose simplified model is shown in Figure 30(a), prevents both relative translation and rotation between structure and its foundation. So, as aforementioned, the reactions consist of a force acting in any direction and a couple of moment, and the magnitudes of the reactions can be arbitrary values as long as the support can bear. In analysis, this force is usually represented by two perpendicular force components with unknown magnitudes. The support S1 in Figure 29 is a fixed support. It can provide the reactions of two force components (in this case, we prefer to set them in the directions along

E1 and perpendicular to E1) and a couple of moment for the element E1 when necessary. So E1 is completely immovable at its end N1.

b) Hinged support

The hinged support, whose simplified model is shown in Figure 30(b), prevents translation in any direction. So the reaction force may act in any direction, and is usually represented by two perpendicular force components with unknown magnitudes. Therefore, the support S2 in Figure 29 is a hinged support, and it can provide two force components (in this case, we prefer to set them in the directions along E5 and perpendicular to E5) for the element E5 to restraint its translation when necessary. So at N6, the translation of E5 is fixed, but the rotation of E5 is allowed.

c) Roller support

The roller support, whose simplified model is shown in Figure 30(c), prevents translation and provides reaction force perpendicular to the supporting surface. This reaction force may be directed either into or away from the structure, and its magnitude is unknown.

d) Directional support

The directional support (or double-link support), whose simplified model is shown in Figure 30(d), restricts all relative movement between structure and its foundation but slides along its supporting surface. So the reactions consist of a force perpendicular to the supporting surface and a couple of moment. The magnitudes of the reactions are unknown.

3.2 The choice of the matrix displacement method

Generally, structures are statically indeterminate in practice. The force method and the displacement method are two classical methods used for the analysis of statically indeterminate structures and they can also be used for statically determinate structures. However, the analysis of a large quantity of structures by using these hand-oriented methods can be quite time consuming. Benefitting from the availability of modern computer technologies, the analysis of structures is routinely performed today on computers using software based on matrix methods. The matrix structural analysis uses the principle of classical structural mechanics to formulate the analytical procedure of a structure by matrix algebra, and then solves the algebraic equations by a computer with the purpose of achieving the structure's reactions, i.e. internal forces and displacements (or stresses and strains). Although both the force and the displacement methods can be expressed in a matrix form, the displacement method is more systematic and can be more easily implemented on computers. Thus, most of the computer programs for structural analysis are based on the displacement method, which is also the method we chose to study and apply to our researches.

The fundamental principle of the matrix displacement method is identical to that of the classical displacement method. Matrix methods do not involve any new fundamental principles, but the relationships of equilibrium, compatibility, and element

force-displacement relations are now expressed in the form of matrix equations, so that the numerical calculations can be efficiently performed on a computer. Like the displacement method, a structure is also considered to be an assemblage of straight elements (usually appear as beams) connected at their ends to nodes in the matrix displacement method. An element, or termed a member, is defined as a part of the structure for which the element force-displacement relations to be employed in the analysis are valid in matrix algebraic form. By assembling the force-displacement relations of the elements under the equilibrium and compatibility conditions, the force-displacement relations of the entire structure can be generated.

Analyzing problems involved in structural mechanics can be classified into statically determinate and statically indeterminate problems. The former could be solved only by means of force equilibrium conditions, while the latter could be determined by satisfying all of the following three types of fundamental conditions (Bao and Gong, 2006):

(1) Force equilibrium conditions

The entire structure or part of it must be balanced under the action of forces. The force here is the generalized concept, including couples.

(2) Compatibility conditions (or geometrical conditions) of displacements

The continuity of a structure must be maintained after the structure has deformed under the action of the loads applied on it. That is, there are no overlap and gap existing in the materials composing the structure, and meanwhile the deformation and displacement of the structure should satisfy the restraint conditions provided by the joints and supports.

(3) Constitutive equation conditions

These are the constitutive equations linking stress to strain or forces to displacements in a structure. These equations have been solved in material mechanics.

3.3 Principle of the matrix displacement method for the analysis of a plane framed structure

In this section, we explain how to prepare a structural model and organize the node and element lists, which are two input data of our code developed into *Mathematica*™, for digitizing a structural model. Then, the establishment of force-displacement relations of elements and the development of force-displacement relations of the structure are introduced. By these relations, the internal forces and displacements over the structure can be computed.

3.3.1 Preparation of a structural model and the input data lists

3.3.1.1 Preparation of a structural model

In the matrix displacement method, the structure can be represented as a model using a line diagram, on which all the elements and nodes are identified by numbers. On this model, the

local and global coordinate systems, and the displacements and forces of the element ends (or nodes) should be indicated as a preparation for the further computations.

(1) Discretization of a structure

Before proceeding with other analyses and computations, the structure must be discretized into elements and nodes.

An element is defined as a part of the structure for which the element force-displacement relations to be used in the analysis are valid in matrix algebraic form. In other words, given the displacements of the two ends of an element, one should be able to determine the forces (including the moments) at its ends by using the force-displacement relations expressed in a matrix form.

As aforementioned, a node is defined as a structural part with infinitesimal size to which the element ends are connected, including both the connections between the elements (joints) and the connections between the structure and its foundation (supports). That is, the nodes of a structure should include all the ends of the elements.

Taking Figure 31(a) as example, it is a structural model with 6 elements and 6 nodes (including 4 joints and 2 supports). First of all, the numbers (i.e. ID) of the elements (E1~E6) and the nodes (N1~N6) should be appointed, as shown in Figure 31(b). In this research, we name the element as En (n is a number), and the nodes as Nn (n is a number).

Moreover, for each element, the node IDs of the two ends should be recorded, and as the inherent properties of the element, the flexural rigidity EI and the axial rigidity EA must be indicated for further calculations. Here, E is the Young's modulus (or tensile modulus, or elastic modulus); I is the cross-section inertia moment; A is the cross-section area. Note that, these quantities are the element properties regarding only the shape and material of the element itself. They have relationship with neither the displacements nor the loads.

By the way, the two supports in this figure are denoted as S1 (the left fixed support) and S2 (the right hinged support).

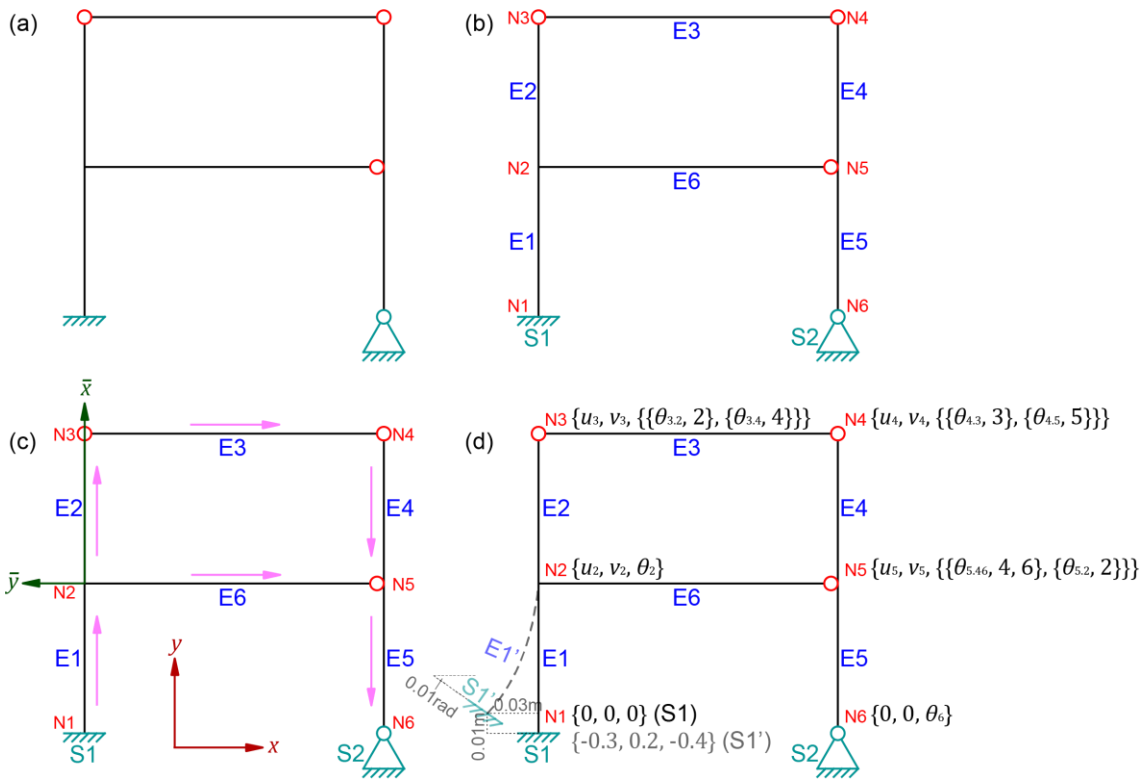

Figure 31. Preparation of a structural model: (a) the line diagram of a structure; (b) the discretization of the structure, the elements and nodes are identified by numbers; (c) the global and local coordinate systems; (d) the displacements at the nodes (in global coordinate system, the displacements of S1 and the deformation of E1 are magnified), the units of u, v, and θ are m, m, and rad, respectively.

(2) Global and local coordinate systems

In the matrix displacement method, the overall geometry and behavior of the structure are described with reference to a global (or structural) coordinate system, which is a standard right-handed Cartesian coordinate system, with the x axis to the right and the y axis up, the anticlockwise rotation is positive. The origin of this coordinate system is arbitrary, theoretically. The global coordinate system can be seen in Figure 31(c).

Because it is usually convenient to derive the basic force-displacement relations in terms of the forces and displacements in the directions along and perpendicular to elements, a local (or element) coordinate system is defined for each element of the structure. The origin of the local coordinate system for an element may be arbitrarily located at one of the ends of the element, with the $\bar{x}$ axis directed along the centroidal axis of the element to the other end. Then the $\bar{y}$ axis can be gotten by rotating the $\bar{x}$ axis 90° anticlockwise, the anticlockwise rotation is positive in this system.

Here, we use the symbols with the bars over them (e.g. $\bar{x}$ and $\bar{y}$) to identify the associated physical quantities defined in local coordinate system to distinguish the quantities defined in global system (e.g. x and y). Hereinafter, for the displacements and forces, the bars over the symbols have the same meaning.

In Figure 31(c), the positive direction of the $\bar{x}$ axis for each element is indicated by drawing an arrow along each element. For example, this figure illustrates that the origin of the local coordinate system for element E2 is located at its end N2, with the $\bar{x}$ axis directed from N2 to N3, and with the $\bar{y}$ axis directed to the left side of the model. The local coordinate system of element E2 can be seen in In Figure 31(c).

(3) Node displacement list in global coordinate system

The unknown displacements of a structure are the independent node displacements (translations and rotations) that are necessary to specify the deformed shape of the structure when subjected to an arbitrary loading. In the calculation, we should specify the displacements at both two ends of the elements, and then the displacements can be used to calculate the forces at the ends by taking the force-displacement relations into account. Due to the fact that many elements have overlapped ends, as an input data, we can give the displacements of the structure nodes instead of the displacements of element ends to avoid such redundant data. And the displacements of the nodes also include some known displacements at the supports.

In the present work, we set u as the unknown horizontal displacement of a node, which is considered as positive when in the positive direction of the x axis; v as the unknown vertical displacement of a node, which is considered as positive when in the positive direction of the y axis; θ as the unknown rotational angle of the elements at a node, which is considered as positive when anticlockwise. These symbols without the bars over them are all in global coordinate system.

As Figure 31(d) illustrates, we can see that node N1, which is attached to the fixed support S1, can neither translate nor rotate; therefore, it has a known displacement list as $\{0, 0, 0\}$ (the units of u, v, and θ are m, m, and rad, similarly hereinafter unless otherwise stated). But sometimes, the support may move. As in this figure, S1 moves from the original position to S1' by translating to the left side 0.03 m, translating up 0.01 m, and rotating clockwise 0.01 rad (in the figure, the displacements of S1 and the corresponding deformations of E1 are magnified for display). Using the same sign conventions as the unknown displacements, under this situation, the known displacement list at N1 should be $\{-0.03, 0.01, -0.01\}$. Since node N2 of the frame is not attached to a support, three displacements, which include the translations in the x and y directions, respectively, and the rotation, are needed to completely specify its deformed position. As N2 is a rigid joint, the translations and rotation of the connected elements E1, E2 and E6 are the same, so its node unknown displacement list is $\{u_2, v_2, \theta_2\}$. Because N3 and N4 are hinge joint, which means the elements connected to them have the same translations but different rotations, the unknown displacement list of N3 is $\left\{u_3, v_3, \{\{\theta_{3.2}, 2\}, \{\theta_{3.4}, 4\}\}\right\}$. The rotation angle of the displacement list of N3 is a list, which means the rotation angles of the connected elements (E2 and E3) are not the same (more than one angle). In this case, $\{\theta_{3.2}, 2\}$ (the numbers 2 and 3 in this list are the node IDs) means the rotation angle of the element E2 (with the ends N3 and N2) is supposed to be $\theta_{3.2}$ at the end N3; while $\{\theta_{3.4}, 4\}$ means the rotation angle of the element E3 (with the

ends N3 and N4) is $\theta_{3.4}$ at the end N3. The unknown displacement lists of N4 and N5 are similar to N3. But for N5, we noticed that it is a composite node, the translations of its connected elements E4, E5 and E6 are the same, as well as the rotations of E4 and E5; but the rotation of E6 can be different from E4 or E5. So, two rotation angles should be indicated although three elements are connected to N5. Finally, N6 is attached to the hinged supports, its displacement list is $\{0, 0, \theta_6\}$, which means the element connected to N6 can rotate only. The displacement lists of all the nodes are printed in Table 9 and Figure 31(d).

Table 9. The node displacement lists

Position	The displacement list	Type of node
N1	$\{0, 0, 0\}$	Rigid support, if S1 does not move
	$\{-0.03, 0.01, -0.01\}$	Rigid support, if S1 moves to S1'
N2	$\{u_2, v_2, \theta_2\}$	Rigid joint
N3	$\left\{u_3, v_3, \{\{\theta_{3.2}, 2\}, \{\theta_{3.4}, 4\}\}\right\}$	Hinge joint
N4	$\left\{u_4, v_4, \{\{\theta_{4.3}, 3\}, \{\theta_{4.5}, 5\}\}\right\}$	Hinge joint
N5	$\left\{u_5, v_5, \{\{\theta_{5.46}, 4, 6\}, \{\theta_{5.2}, 2\}\}\right\}$	Composite joint: hinge + rigid
N6	$\{0, 0, \theta_6\}$	Hinged support
Remark: the units of u, v, and θ are m, m, and rad		

(4) Element end displacement and force vectors in local coordinate system

Figure 32 shows an arbitrary element of a structure. Three displacements, including translations in the $\bar{x}$ and $\bar{y}$ directions and rotation, are needed to specify the deformed position of each end of the element. Thus this element has a total of six unknown end displacements. As shown in Figure 32, the element end displacements are denoted by $\bar{u}_i$, $\bar{v}_i$, $\bar{\theta}_i$ at the end Ni and $\bar{u}_j$, $\bar{v}_j$, $\bar{\theta}_j$ at the end Nj, and the corresponding element end forces are denoted by $\bar{X}_i$, $\bar{Y}_i$, $\bar{M}_i$ and $\bar{X}_j$, $\bar{Y}_j$, $\bar{M}_j$. Note that these end displacements and forces are defined relatively to the local coordinate system of the element. The translations and forces are considered as positive when in the positive directions of the local $\bar{x}$ and $\bar{y}$ axes, and the rotations and moments are considered as positive when anticlockwise.

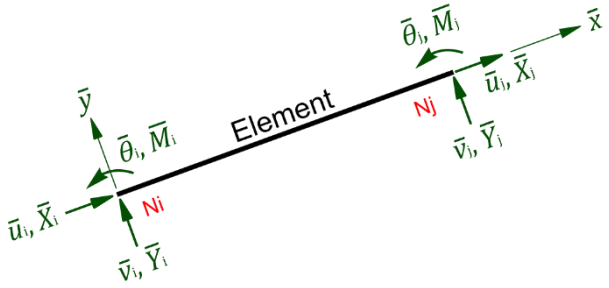

Figure 32. Displacements and forces at two ends of an element in local coordinate system (the end displacements and forces are positive in the directions of the arrows)

In the matrix displacement method, the six element end displacements and six element end forces should be arranged in a matrix form before further calculations. The element end displacement vector and the element end force vector can be written as in Equation 18 and Equation 19, respectively, in which, the orders of displacements and forces are not commutative.

$$\overline{\boldsymbol{\Delta}}^e = \begin{bmatrix} \bar{u}_i \\ \bar{v}_i \\ \bar{\theta}_i \\ \bar{u}_j \\ \bar{v}_j \\ \bar{\theta}_j \end{bmatrix} \qquad \text{Equation 18}$$

$$\overline{\boldsymbol{F}}^e = \begin{bmatrix} \bar{X}_i \\ \bar{Y}_i \\ \bar{M}_i \\ \bar{X}_j \\ \bar{Y}_j \\ \bar{M}_j \end{bmatrix} \qquad \text{Equation 19}$$

The bars over the displacement and force symbols identify that the associated physical quantities are defined in local coordinates. The bold characters mean that the associated quantities are matrices (or vectors). The characters with the superscript e mean that the associated quantities are defined for an element.

3.3.1.2 Preparation of the input data lists

The node list and element list are two input data in our computer code, which can be used to compose a unique structural model, and should include the information of the external loads and support displacements.

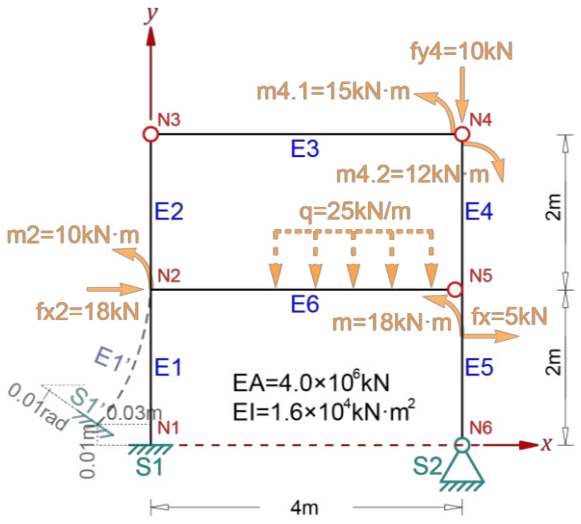

Figure 33. Composing a structural model (the displacements of S1 and the deformation of E1 are magnified)

3.3.1.2.1 Load on a structure

The internal forces and displacements of a structure are the reactions of the external loads and structural support displacements (both or either). So, it is necessary to inform the external loads as a part of the input data in the structural analysis.

In framed structures, the loads can be simplified into concentrated loads and distributed loads according to their distributions. As in Figure 33, q is a distributed load (q means in a unit length, the magnitude of the load is q); fx2, m2, fy4, m4.1, m4.2, fx, and m are concentrated loads. These external loads should be known values, so the above symbols can be arbitrary, and it is not necessary to standardize them.

In another way, the external loads on a structure can be classified as node load and element load according to their acting positions. Obviously, only concentrated load can be node load (fx2, m2, fy4, m4.1, and m4.2); however, both concentrated (fx and m) and distributed (q) loads can perform on an element.

We consider the positive external loads are in the positive directions of the axes of the global coordinate system, while the anticlockwise moments are positive too. Then the loads acting on the structure can be organized as lists.

(1) Node load

The loads at a node are comprised of three forces: the force in x direction, the force in y direction, and the moment. As in Figure 33, at node N2, the load list should be $\{18, 0, 10\}$ (when the units of the quantities are uniform, they can be omitted when composing the input data, here, the units of the force in x direction, the force in y direction, and the moment are kN, kN, and kN·m, similarly hereinafter unless otherwise stated).

Specially, for a hinge joint, the moment should be applied at the element end(s) but not directly at the joint, although they are seemingly coincident in the model. For example, refer

to Figure 33, at N4, the moment m4.1 is acting at the end N4 of the element E3 (not at the joint), the moment m4.2 is acting at the end N4 of the element E4. So, the load list at N4 is $\{0,-10,\{\{15,3\},\{-12,5\}\}\}$. The number 3 and 5 in the internal brackets are the IDs of nodes, they compose an element with N4 on which the moments 15 kN·m and –12 kN·m are acting, respectively.

When we analyze the displacements at the supports, we found that some of them are known, which means the supports can provide restrains in the relative directions. That is, the unknown forces can possibly appear at the supports. For instance, at node N1 connected with a fixed support S1 (E1 and S1 have no or the same translations and rotation), the load list should be $\{\mathrm{fx1},\mathrm{fy1},\mathrm{m1}\}$; at N6, the load list should be $\{\mathrm{fx6},\mathrm{fy6},0\}$ where only the translations are restrained.

(2) Element load

Comparing to the node loads, when talking about the loads acting on an element, we should indicate their acting positions regarding the element. This position is a relative position about the element (i.e. if there is a distributed load acting on the whole element, the position is from 0 to 1). Taking Figure 33 as example, the distributed load acting on E6 (from 0.4×4m to 0.9×4m, if E6 starting at N2) can be informed as $\{\{0.4,0.9\},\{0,-25,0\}\}$, and the concentrated loads on E5 (at 0.3×2m, if E5 starting at N5) can be listed as $\{\{0.3\},\{5,0,18\}\}$.

All the load lists are printed in Table 10.

Table 10. The load lists

Position		The load list	Remark
Node	N1	$\{\mathrm{fx1},\mathrm{fy1},\mathrm{m1}\}$	Rigid support
	N2	$\{18,0,10\}$	
	N3	$\{0,0,0\}$	
	N4	$\{0,-10,\{\{15,3\},\{-12,5\}\}\}$	2 moments acting at a hinge joint
	N5	$\{0,0,0\}$	
	N6	$\{\mathrm{fx6},\mathrm{fy6},0\}$	Hinged support
Element	E5	$\{\{0.3\},\{5,0,18\}\}$	
	E6	$\{\{0.4,0.9\},\{0,-25,0\}\}$	
Remark: the units of the force in x direction, the force in y direction, and the moment are kN, kN, and kN·m			

3.3.1.2.2 Node and element lists

The node and element lists, which are the two input data for our code, should include the complete information about the structural model. That means, only depending on these two lists, we can rebuild the structural model. So, the node list must include the node ID, the

coordinates (x and y) of each node in the global coordinate system, and the node displacement list (including support displacements) while the element list contains the node IDs of two ends, the flexural rigidity EI and axial rigidity EA of the element. The external loads must be added into these two lists too, if any.

So, we defined the typical node list and element list for a structure as in Equation 20 and Equation 21.

$$\begin{Bmatrix} \{1,\{x_1,y_1\},\{node\ displacement\ list\}_1,\{node\ load\ list\}_1\}, \\ \{2,\{x_2,y_2\},\{node\ displacement\ list\}_2,\{node\ load\ list\}_2\}, \\ \cdots \\ \{n,\{x_n,y_n\},\{node\ displacement\ list\}_n,\{node\ load\ list\}_n\} \end{Bmatrix} \quad \text{Equation 20}$$

$$\begin{Bmatrix} \{IDi_1,IDj_1,EA_1,EI_1,\{element\ load\ list\ if\ any\}_1\}, \\ \{IDi_2,IDj_2,EA_2,EI_2,\{element\ load\ list\ if\ any\}_2\}, \\ \cdots \\ \{IDi_m,IDj_m,EA_m,EI_m,\{element\ load\ list\ if\ any\}_m\} \end{Bmatrix} \quad \text{Equation 21}$$

In Equation 20, the nodes should be ordered as the sequence of their IDs. For each node, its displacement list and load list must be indicated. By contrast, in Equation 21, the element load list only should be specified when any external force is acting on the corresponding element.

Also taking Figure 33 as example, the node list and element list are as follows:

$$nodelist = \begin{Bmatrix} \{1, & \{0,0\}, & \{-0.03,0.01,-0.01\}, & \{\mathrm{fx1},\mathrm{fy1},\mathrm{m1}\} & \}, \\ \{2, & \{0,2\}, & \{u_2,v_2,\theta_2\}, & \{18,0,10\} & \}, \\ \{3, & \{0,4\}, & \{u_3,v_3,\{\{\theta_{3.2},2\},\{\theta_{3.4},4\}\}\}, & \{0,0,0\} & \}, \\ \{4, & \{4,4\}, & \{u_4,v_4,\{\{\theta_{4.3},3\},\{\theta_{4.5},5\}\}\}, & \{0,-10,\{\{15,3\},\{-12,5\}\}\} & \}, \\ \{5, & \{4,2\}, & \{u_5,v_5,\{\{\theta_{5.46},4,6\},\{\theta_{5.2},2\}\}\}, & \{0,0,0\} & \}, \\ \{6, & \{4,0\}, & \{0,0,\theta_6\}, & \{\mathrm{fx6},\mathrm{fy6},0\} & \} \end{Bmatrix} \quad \text{Equation 22}$$

$$elementlist = \begin{Bmatrix} \{1,2,4000000,16000 & & \}, \\ \{2,3,4000000,16000 & & \}, \\ \{3,4,4000000,16000 & & \}, \\ \{4,5,4000000,16000 & & \}, \\ \{5,6,4000000,16000, & \{\{0.3\},\{5,0,18\}\} & \}, \\ \{2,5,4000000,16000, & \{\{0.4,0.9\},\{0,-25,0\}\} & \} \end{Bmatrix} \quad \text{Equation 23}$$

In these two lists, the red numbers are the IDs of the nodes; the green values are known displacements and loads; the blue symbols are unknown displacements and loads, which can be solved by studying the relationships between the forces and displacements; the orange values are the relative positions of the element forces regarding the elements.

3.3.2 Force-displacement relations of an element (mainly after Bao and Gong 2006, Leet *et al*. 2011)

In the matrix displacement method of analysis, the unknown displacements and forces of an element or a structure are determined by solving a system of simultaneous equations, which can be expressed in a matrix form as in Equation 24.

$$\boldsymbol{F} = \boldsymbol{k}\boldsymbol{\Delta} \qquad \text{Equation 24}$$

In which $\boldsymbol{\Delta}$ denotes the unknown displacement vector; $\boldsymbol{F}$ represents the external loads vector at the nodes; and $\boldsymbol{k}$ is named the stiffness matrix. The bold characters mean that the associated quantities are matrices.

For an element, we usually discuss the stiffness matrix in a local (element) and a global (structure) coordinate system, respectively, which will be described in this section. The element stiffness matrix is used to express the forces at the ends of the element as functions of the element end displacements. Note that the terms forces and displacements are in the general sense to include moments and rotations.

3.3.2.1 Element stiffness matrix in local coordinate system

(1) Stiffness matrix for a general element

Our objective is to determine the relationships between the element end forces and end displacements in a local coordinate system. If we neglect the coupling influence between axial deformation and bending deformation, the stiffness relationships pertinent to axial deformation and those pertinent to bending deformation can be derived separately as follows.

a) The relationships between the element end axial displacements and axial forces can be presented as in Equation 25.

$$\left.\begin{aligned} \overline{X}_i &= \frac{EA}{L}(\overline{u}_i - \overline{u}_j) \\ \overline{X}_j &= -\frac{EA}{L}(\overline{u}_i - \overline{u}_j) \end{aligned}\right\} \qquad \text{Equation 25}$$

b) The relationships between the element end transverse displacements (perpendicular to the axial one), rotation angles, shear forces, and bending moments can be presented as in Equation 26.

$$\left.\begin{aligned} \overline{Y}_i &= \frac{12EI}{L^3}\overline{v}_i + \frac{6EI}{L^2}\overline{\theta}_i - \frac{12EI}{L^3}\overline{v}_j + \frac{6EI}{L^2}\overline{\theta}_j \\ \overline{M}_i &= \frac{6EI}{L^2}\overline{v}_i + \frac{4EI}{L}\overline{\theta}_i - \frac{6EI}{L^2}\overline{v}_j + \frac{2EI}{L}\overline{\theta}_j \\ \overline{Y}_j &= -\frac{12EI}{L^3}\overline{v}_i - \frac{6EI}{L^2}\overline{\theta}_i + \frac{12EI}{L^3}\overline{v}_j - \frac{6EI}{L^2}\overline{\theta}_j \\ \overline{M}_j &= \frac{6EI}{L^2}\overline{v}_i + \frac{2EI}{L}\overline{\theta}_i - \frac{6EI}{L^2}\overline{v}_j + \frac{4EI}{L}\overline{\theta}_j \end{aligned}\right\} \qquad \text{Equation 26}$$

The element end displacements ($\overline{u}_i,\ \overline{v}_i,\ \overline{\theta}_i,\ \overline{u}_j,\ \overline{v}_j,\ \overline{\theta}_j$) and forces ($\overline{X}_i,\ \overline{Y}_i,\ \overline{M}_i,\ \overline{X}_j,\ \overline{Y}_j,\ \overline{M}_j$) in local coordinate system have been introduced in Equation 18 and Equation 19, and their positive directions are as the arrows shown in Figure 32. To establish the stiffness relationships for an element, three quantities of the element should be taken into account. They are: element length L (can be determined by the coordinates of the two ends), and the aforementioned flexural rigidity EI and axial rigidity EA.

c) Element force-displacement relations and element stiffness matrix

Combining Equation 25 and Equation 26, we can write them in a matrix form as in Equation 27, which presents the relationships between the element end displacements and forces.

$$\begin{bmatrix} \bar{X}_i \\ \bar{Y}_i \\ \bar{M}_i \\ \bar{X}_j \\ \bar{Y}_j \\ \bar{M}_j \end{bmatrix} = \begin{bmatrix} \frac{EA}{L} & 0 & 0 & -\frac{EA}{L} & 0 & 0 \\ 0 & \frac{12EI}{L^3} & \frac{6EI}{L^2} & 0 & -\frac{12EI}{L^3} & \frac{6EI}{L^2} \\ 0 & \frac{6EI}{L^2} & \frac{4EI}{L} & 0 & -\frac{6EI}{L^2} & \frac{2EI}{L} \\ -\frac{EA}{L} & 0 & 0 & \frac{EA}{L} & 0 & 0 \\ 0 & -\frac{12EI}{L^3} & -\frac{6EI}{L^2} & 0 & \frac{12EI}{L^3} & -\frac{6EI}{L^2} \\ 0 & \frac{6EI}{L^2} & \frac{2EI}{L} & 0 & -\frac{6EI}{L^2} & \frac{4EI}{L} \end{bmatrix} \begin{bmatrix} \bar{u}_i \\ \bar{v}_i \\ \bar{\theta}_i \\ \bar{u}_j \\ \bar{v}_j \\ \bar{\theta}_j \end{bmatrix} \quad \text{Equation 27}$$

Then the equation above can be written as in Equation 28. It is the stiffness equations in local coordinates for a general element.

$$\overline{\boldsymbol{F}}^e = \overline{\boldsymbol{k}}^e \overline{\boldsymbol{\Delta}}^e \quad \text{Equation 28}$$

In Equation 28, $\overline{\boldsymbol{k}}^e$ is referred to the element (or local) stiffness matrix, which is a 6×6 square matrix (refer to Equation 27). The element stiffness matrix $\overline{\boldsymbol{k}}^e$ is a symmetrical matrix. It is also singular as $\left|\overline{\boldsymbol{k}}^e\right| = 0$. So, there exists no inverse matrix. In other words, by Equation 28, the end forces $\overline{\boldsymbol{F}}^e$ of the element can be uniquely determined by the given end displacements $\overline{\boldsymbol{\Delta}}^e$. But under the action of a given end forces $\overline{\boldsymbol{F}}^e$, the end displacements $\overline{\boldsymbol{\Delta}}^e$ cannot be uniquely determined.

(2) Possible simplifications of the element stiffness matrix in some cases

Sometimes, one or some of the end displacement of an element is designated or small enough to be neglected. So the relationships between the displacements and forces in Equation 27 can be simplified. For instance, the axial deformation effect may be neglected in the analysis of rigid frames in some analyses. For this kind of special element, the element stiffness matrix $\overline{\boldsymbol{k}}^e$ can be simplified by removing the first and forth rows and columns, and the first and forth elements can be removed from the displacement vector $\overline{\boldsymbol{\Delta}}^e$ and the force vector $\overline{\boldsymbol{F}}^e$. Another case, for trusses, the element is subjected to only axial forces, thus only two displacements ($\bar{u}_i$ and $\bar{u}_j$) need to be taken into consideration. That means Equation 25 may be more efficient for trusses.

These simplifications are very useful in manual computations, but complicate the situations in programming a code with slightly or none accelerating the computing speed. Therefore, we will not pay attention to these simplifications anymore.

3.3.2.2 Element stiffness matrix in global coordinate system

For a structure, its elements are oriented in different directions. Thusly, it becomes necessary to transform the stiffness relations for each element from the local (element) coordinate system (denoted by $\bar{x}\bar{y}$) to a global (structure) coordinate system (denoted by xy).

(1) Element transformation matrix of coordinates

Considering an arbitrary general element shown in Figure 34, the orientation of the element with respect to the global xy coordinate system is defined by an angle α measured anticlockwise from the positive direction of the global x axis to the positive direction of the local $\bar{x}$ axis. The stiffness matrix in local coordinate system, which is valid for the element end displacements and forces in Figure 34(a), has been deduced in the previous section. Now, we want to express this local stiffness matrix in the global coordinate system as in Figure 34(b). Thus, a transformation matrix of coordinates has been introduced.

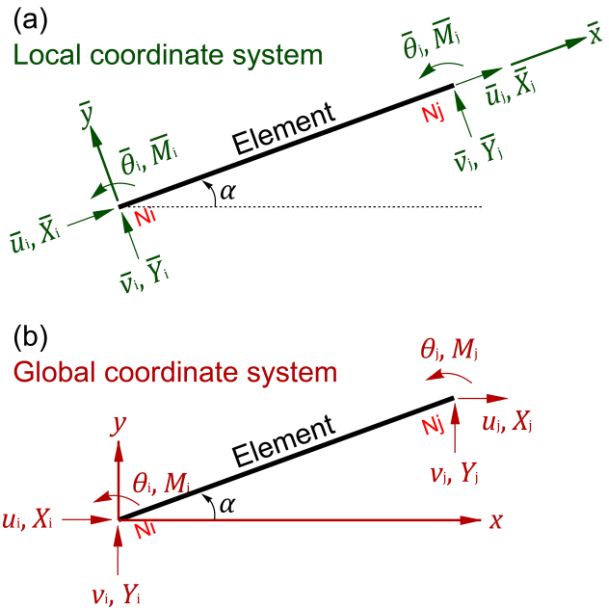

Figure 34. From a local to a global coordinate system: (a) the element end displacements and forces in local coordinate system; (b) the element end displacements and forces in global coordinate system

By considering the projection of forces shown in Figure 34, we can find the relations between the end forces in the global coordinate system and those in the local coordinate system as in Equation 29.

$$\left.\begin{aligned} \bar{X}_i &= X_i \cos\alpha + Y_i \sin\alpha \\ \bar{Y}_i &= -X_i \sin\alpha + Y_i \cos\alpha \\ \bar{M}_i &= M_i \\ \bar{X}_j &= X_j \cos\alpha + Y_j \sin\alpha \\ \bar{Y}_j &= -X_j \sin\alpha + Y_j \cos\alpha \\ \bar{M}_j &= M_j \end{aligned}\right\} \qquad \text{Equation 29}$$

The equations above can be rewritten in a matrix form as in Equation 30, or symbolically as in Equation 31, which is the transformation of end forces from global to local coordinate system. $\boldsymbol{T}$ in Equation 31 is the transformation matrix of coordinates (from global to local), or called rotation matrix.

$$\begin{bmatrix} \bar{X}_i \\ \bar{Y}_i \\ \bar{M}_i \\ \bar{X}_j \\ \bar{Y}_j \\ \bar{M}_j \end{bmatrix} = \begin{bmatrix} \cos\alpha & \sin\alpha & 0 & 0 & 0 & 0 \\ -\sin\alpha & \cos\alpha & 0 & 0 & 0 & 0 \\ 0 & 0 & 1 & 0 & 0 & 0 \\ 0 & 0 & 0 & \cos\alpha & \sin\alpha & 0 \\ 0 & 0 & 0 & -\sin\alpha & \cos\alpha & 0 \\ 0 & 0 & 0 & 0 & 0 & 1 \end{bmatrix} \begin{bmatrix} X_i \\ Y_i \\ M_i \\ X_j \\ Y_j \\ M_j \end{bmatrix} \quad \text{Equation 30}$$

$$\bar{\boldsymbol{F}}^e = \boldsymbol{T}\boldsymbol{F}^e \quad \text{Equation 31}$$

Similarly, the reverse operation can be expressed as Equation 32 and Equation 33, in which the transformation matrix $\boldsymbol{T}^T$ can determine the transformation of element end forces from local to global coordinate system.

$$\begin{bmatrix} X_i \\ Y_i \\ M_i \\ X_j \\ Y_j \\ M_j \end{bmatrix} = \begin{bmatrix} \cos\alpha & -\sin\alpha & 0 & 0 & 0 & 0 \\ \sin\alpha & \cos\alpha & 0 & 0 & 0 & 0 \\ 0 & 0 & 1 & 0 & 0 & 0 \\ 0 & 0 & 0 & \cos\alpha & -\sin\alpha & 0 \\ 0 & 0 & 0 & \sin\alpha & \cos\alpha & 0 \\ 0 & 0 & 0 & 0 & 0 & 1 \end{bmatrix} \begin{bmatrix} \bar{X}_i \\ \bar{Y}_i \\ \bar{M}_i \\ \bar{X}_j \\ \bar{Y}_j \\ \bar{M}_j \end{bmatrix} \quad \text{Equation 32}$$

$$\boldsymbol{F}^e = \boldsymbol{T}^T\bar{\boldsymbol{F}}^e \quad \text{Equation 33}$$

Like end forces, Equation 34 and Equation 35 are the transformations of element end displacements from global to local, and from local to global coordinate system, respectively.

$$\bar{\boldsymbol{\Delta}}^e = \boldsymbol{T}\boldsymbol{\Delta}^e \quad \text{Equation 34}$$

$$\boldsymbol{\Delta}^e = \boldsymbol{T}^T\bar{\boldsymbol{\Delta}}^e \quad \text{Equation 35}$$

We recognized that, $\boldsymbol{T}$ is a orthogonal matrix, that is

$$\boldsymbol{T}\boldsymbol{T}^T = \boldsymbol{T}^T\boldsymbol{T} = \boldsymbol{I} \quad \text{Equation 36}$$

In which, $\boldsymbol{I}$ is an unit matrix with the same order as that of $\boldsymbol{T}$.

(2) Element stiffness matrix in global coordinate system

By using the element stiffness relations in local coordinates and the transformation relations of coordinates, we can now develop the elements stiffness relations in global coordinates as follows.

Substituting Equation 31 and Equation 34 into Equation 28 (the stiffness relation of an element in local coordinate system), we obtain Equation 37.

$$\boldsymbol{T}\boldsymbol{F}^e = \bar{\boldsymbol{k}}^e\boldsymbol{T}\boldsymbol{\Delta}^e \quad \text{Equation 37}$$

Pre-multiplying $\boldsymbol{T}^T$ to the both two sides of Equation 37, and in the meanwhile considering Equation 36, we obtain Equation 38.

$$\boldsymbol{F}^e = \boldsymbol{T}^T\bar{\boldsymbol{k}}^e\boldsymbol{T}\boldsymbol{\Delta}^e \quad \text{Equation 38}$$

Introducing a new parameter $\boldsymbol{k}^e$ as shown in Equation 39, which is used to replace the coefficient matrix before $\boldsymbol{\Delta}^e$ in Equation 38, Equation 38 can be reformed as in Equation 40.

$$\boldsymbol{k}^e = \boldsymbol{T}^T\bar{\boldsymbol{k}}^e\boldsymbol{T} \quad \text{Equation 39}$$

$$\boldsymbol{F}^e = \boldsymbol{k}^e\boldsymbol{\Delta}^e \quad \text{Equation 40}$$

Equation 39 is the transformation relation of the element stiffness matrices in local ($\bar{\boldsymbol{k}}^e$) and

global ($\boldsymbol{k}^e$) coordinate systems, in which, $\boldsymbol{k}^e$ is referred to as the element stiffness matrix in the global coordinate system, and it is a symmetrical and singular matrix as $\overline{\boldsymbol{k}}^e$.

Equation 40 defines the relations between the element end forces and end displacements in global coordinates.

3.3.3 Force-displacement relations of the structure

Normally, as the next step, we should use the achieved element stiffness matrices in the global coordinate system to organize a so called structure stiffness matrix, which can be used to associate all elements' end forces with their end displacements, then the unknown element end displacements and forces can be obtained.

Since the software *Mathematica*™ used in this study has the powerful capacity in solving mathematical problems, we will skip the step of organizing the structure stiffness matrix by directly solving an equation set composed of the force equilibrium conditions in global coordinate system at each node.

3.3.3.1 Solving a structure without element loads

We consider a structure without element loads as a basic shape, for which the solving processes of getting the unknown displacements and forces are gathered as follows, and can refer to Figure 35. The solving processes take into account both the structural model and the element force-displacement relations of each element provided by the previous work.

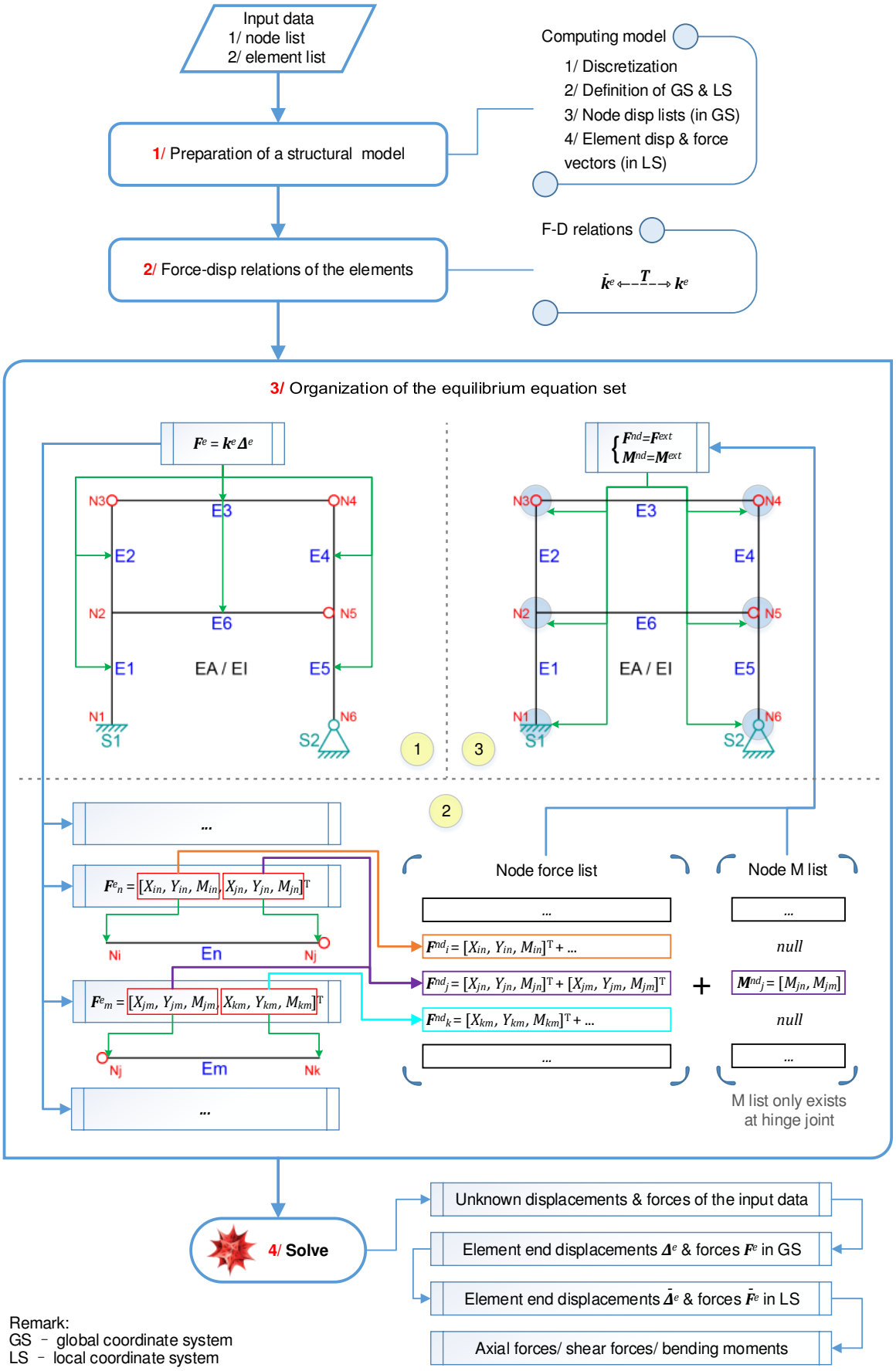

Figure 35. The solving processes of a structure without element loads

(1) According to the prepared displacement lists in the input node data (the third column of Equation 20), we can arrange the element end displacement vectors ($\boldsymbol{\Delta}^e$) in the global coordinate system for all elements (like Equation 18, but without bars over the symbols). In these vectors, both known and unknown displacements exist. Using the element force-displacement relations as in Equation 40, the element end force vectors $\boldsymbol{F}^e$ with six end forces in each (like Equation 19, but without bars over the symbols) can be represented by $\boldsymbol{k}^e\boldsymbol{\Delta}^e$.

(2) In $\boldsymbol{F}^e$, who is a 6×1 vector, the first three elements belong to the starting end of an element and are re-stored in a new node force list $\boldsymbol{F}^{nd}$; the same thing should be done to the last three elements belong to the ending end of the element. Normally, more than one element connect to a node, so, the forces from different elements should be superposed when we consider the aggregated node force $\boldsymbol{F}^{nd}$.

(3) At every node, the computed node forces $\boldsymbol{F}^{nd}$ from displacements should equal the external node loads $\boldsymbol{F}^{ext}$ acting on this node (from the forth column of Equation 20), as in Equation 41, to keep the entire structure balanced.

Specially, if a node is a hinged joint, in order to keep that the solutions of Equation 41 are unique, we must store an additional moment list in the second step, which includes the end moments of all elements at this node, and then let it equal a list of relative external moments offered by the node load list, as in Equation 42.

$$\boldsymbol{F}^{nd} = \boldsymbol{F}^{ext} \qquad \text{Equation 41}$$

$$\boldsymbol{M}^{nd} = \boldsymbol{M}^{ext} \qquad \text{Equation 42}$$

(4) Combining Equation 41 and Equation 42, we can organize an equilibrium equation set, which can be solved in *Mathematica*™ to get the afore-assumed displacements and forces. Then, the unknown displacements and forces in $\boldsymbol{\Delta}^e$ and $\boldsymbol{F}^e$ can be replaced by their relative values. Till now, the element end displacements and forces in the global coordinate system are all known values. Then, using the transformation matrix $\boldsymbol{T}$, the element end displacements and forces in the local coordinate system can also be conveniently worked out. Generally, the axial forces, shear forces, and bending moments are interesting in studies, and they can be got from the local element end forces by only modifying their plus-minus signs according to Equation 43.

$$\begin{bmatrix} \text{axial force}_i \\ \text{shear force}_i \\ \text{bending moment}_i \\ \text{axial force}_j \\ \text{shear force}_j \\ \text{bending moment}_j \end{bmatrix} = \begin{bmatrix} -\bar{X}_i \\ \bar{Y}_i \\ -\bar{M}_i \\ \bar{X}_j \\ -\bar{Y}_j \\ \bar{M}_j \end{bmatrix} \qquad \text{Equation 43}$$

In which, the relationships between the element end forces in the local coordinate system and the axial forces, shear forces, and bending moments are derived from the definitions of the directions of these physical quantities, whose positive directions are as the arrows shown in Figure 36.

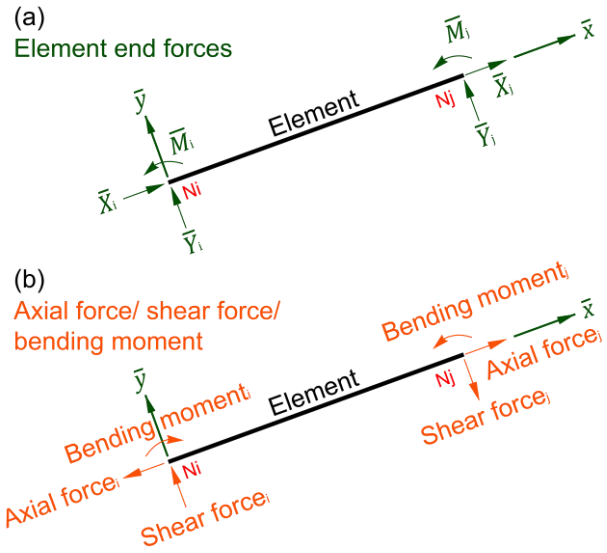

Figure 36. Transformation relations of the element end forces in the local coordinate system and the axial forces, shear forces, and bending moments: (a) the element end displacements in the local coordinate system; (b) the axial forces, shear forces, and bending moments at the ends of an element

3.3.3.2 Solving a structure with element loads

Replacing the element loads by their equivalent element end loads is a traditional way to solve a structure subjected to element loads. But this method should enumerate all types of (at least the most usually used types) equivalent node loads regarding the element loads, and it cannot deal with the element loads out of the given database, for example, a load changing irregularly along the centroidal axis of an element can never been studied in this way.

Instead of using this method, we insert rigid nodes (joints) to the elements according to the positions of element loads to avoid the work of enumeration and to improve the applicability of our method.

For a concentrated element force, as the continuous red arrow (marked as F) in Figure 37, a rigid node should be inserted at exactly where the force is applied (marked as a blue cross). Then the original element will be separated into two elements connected to this inserted node, in the meanwhile, the element concentrated force is transformed to a common node force.

For an arbitrary distributed force, as the irregularly red line (marked as q(x)) in Figure 37, several concentrated forces (marked as F1 to F5) are introduced to play a similar role (discretization of the distributed force). First, the effective range of this distributed force should be divided to several portions with the same length along the element. At the same time, the force is separated to several segmented distributed forces according to the portions. The more portions are defined, the more precise results will be achieved later. Then, at the center of each portion, a concentrated force is used to substitute for the segmented

distributed force. If the length of the portion is small enough, the mean values of the segmented distributed forces can be set as the magnitudes of the concentrated forces. So that, an arbitrary element distributed force is replaced by several element forces, which can be transferred to common node forces by inserting the rigid nodes.

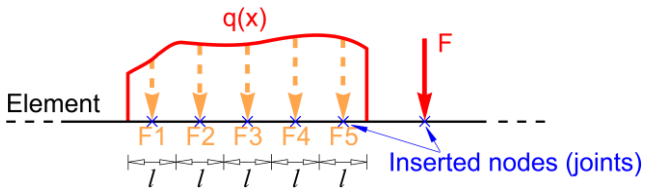

Figure 37. The transformations of element loads

Now, the structure with element loads can be managed as the structure with only node loads, and then be solved following the way indicated in Figure 35.

3.3.4 Output data

After the computation, the displacements and forces of the structure can be output as data tables and figures.

Taking the simple structure in Figure 33 as example, we will exhibit the output data. The structure is a plane framed structure with six nodes, six elements, and two supports. If we have five node forces, two element concentrated forces, and one element distributed force, and compel the support S1 to move slightly as in Figure 33 (all these information are organized in Equation 22 and Equation 23), deformations and internal forces will emerge over the structure, which can be computed by the matrix displacement method.

Table 11 and Table 12 contain the element end displacements and forces in the global coordinate system; while Table 13 and Table 14 are the same two quantities but in the local coordinate system. As aforementioned, the axial forces, shear forces, and bending moments at the ends of the element have the same values but different signs compared to the end forces in their local coordinate system, and they are more interesting in practice, so we print them in Table 15. In fact, the internal forces and displacements at any positions of the structure (means not only at the ends of the elements) can be computed by discretizing the elements and inserting nodes, which uses the same solution of solving the structure with the distributed element loads.

The curves of the axial force, shear force, and bending moment over the structure can be found in Figure 38(a), (b), and (c), respectively. The displacements in the global coordinate system can also well represent the structural deformations as in Figure 38(d).

Table 11. Element end displacements in the global coordinate system

	Ni	Nj	$\bar{u}_i$ (m)	$\bar{v}_i$ (m)	$\bar{\theta}_i$ (rad)	$\bar{u}_j$ (m)	$\bar{v}_j$ (m)	$\bar{\theta}_j$ (rad)
E1	1	2	-0.030	0.010	-0.010	-0.012	0.010	-0.005
E2	2	3	-0.012	0.010	-0.005	-0.009	0.010	0.000
E3	3	4	-0.009	0.010	-0.003	-0.009	0.000	-0.001
E4	4	5	-0.009	0.000	-0.004	-0.012	0.000	0.002
E5	5	6	-0.012	0.000	0.002	0.000	0.000	0.008
E6	2	5	-0.012	0.010	-0.005	-0.012	0.000	0.000

Table 12. Element end forces in the global coordinate system

	Ni	Nj	X_i (kN)	Y_i (kN)	M_i (kN·m)	X_j (kN)	Y_j (kN)	M_j (kN·m)
E1	1	2	-59.700	20.011	22.043	59.700	-20.011	97.356
E2	2	3	41.200	3.750	-82.399	-41.200	-3.750	0.000
E3	3	4	41.200	3.750	0.000	-41.200	-3.750	15.000
E4	4	5	41.200	-6.250	-12.000	-41.200	6.250	94.399
E5	5	6	-41.700	-39.989	-94.399	36.700	39.989	0.000
E6	2	5	-82.899	16.261	-4.957	82.899	33.739	0.000

Table 13. Element end displacements in the local coordinate system

	Ni	Nj	u_i (m)	v_i (m)	θ_i (rad)	u_j (m)	v_j (m)	θ_j (rad)
E1	1	2	0.010	0.030	-0.010	0.010	0.012	-0.005
E2	2	3	0.010	0.012	-0.005	0.010	0.009	0.000
E3	3	4	-0.009	0.010	-0.003	-0.009	0.000	-0.001
E4	4	5	0.000	-0.009	-0.004	0.000	-0.012	0.002
E5	5	6	0.000	-0.012	0.002	0.000	0.000	0.008
E6	2	5	-0.012	0.010	-0.005	-0.012	0.000	0.000

Table 14. Element end forces in the local coordinate system

	Ni	Nj	X_i (kN)	Y_i (kN)	M_i (kN·m)	X_j (kN)	Y_j (kN)	M_j (kN·m)
E1	1	2	20.011	-59.700	22.043	20.011	-59.700	-97.356
E2	2	3	-3.750	-41.200	82.399	-3.750	-41.200	0.000
E3	3	4	41.200	-3.750	0.000	41.200	-3.750	-15.000
E4	4	5	-6.250	41.200	12.000	-6.250	41.200	94.399
E5	5	6	39.989	41.700	-94.399	39.989	36.700	0.000
E6	2	5	82.899	16.261	4.957	82.899	-33.739	0.000

Table 15. Axial forces, shear forces, and bending moments at the element ends

	Ni	Nj	Axial force$_i$ (kN)	Shear force$_i$ (kN)	Bending moment$_i$ (kN·m)	Axial force$_j$ (kN)	Shear force$_j$ (kN)	Bending moment$_j$ (kN·m)
E1	1	2	-20.011	59.700	-22.043	-20.011	59.700	97.356
E2	2	3	-3.750	-41.200	82.399	-3.750	-41.200	0.000
E3	3	4	-41.200	3.750	0.000	-41.200	3.750	15.000
E4	4	5	-6.250	41.200	12.000	-6.250	41.200	94.399
E5	5	6	-39.989	-41.700	94.399	-39.989	-36.700	0.000
E6	2	5	82.899	16.261	4.957	82.899	-33.739	0.000

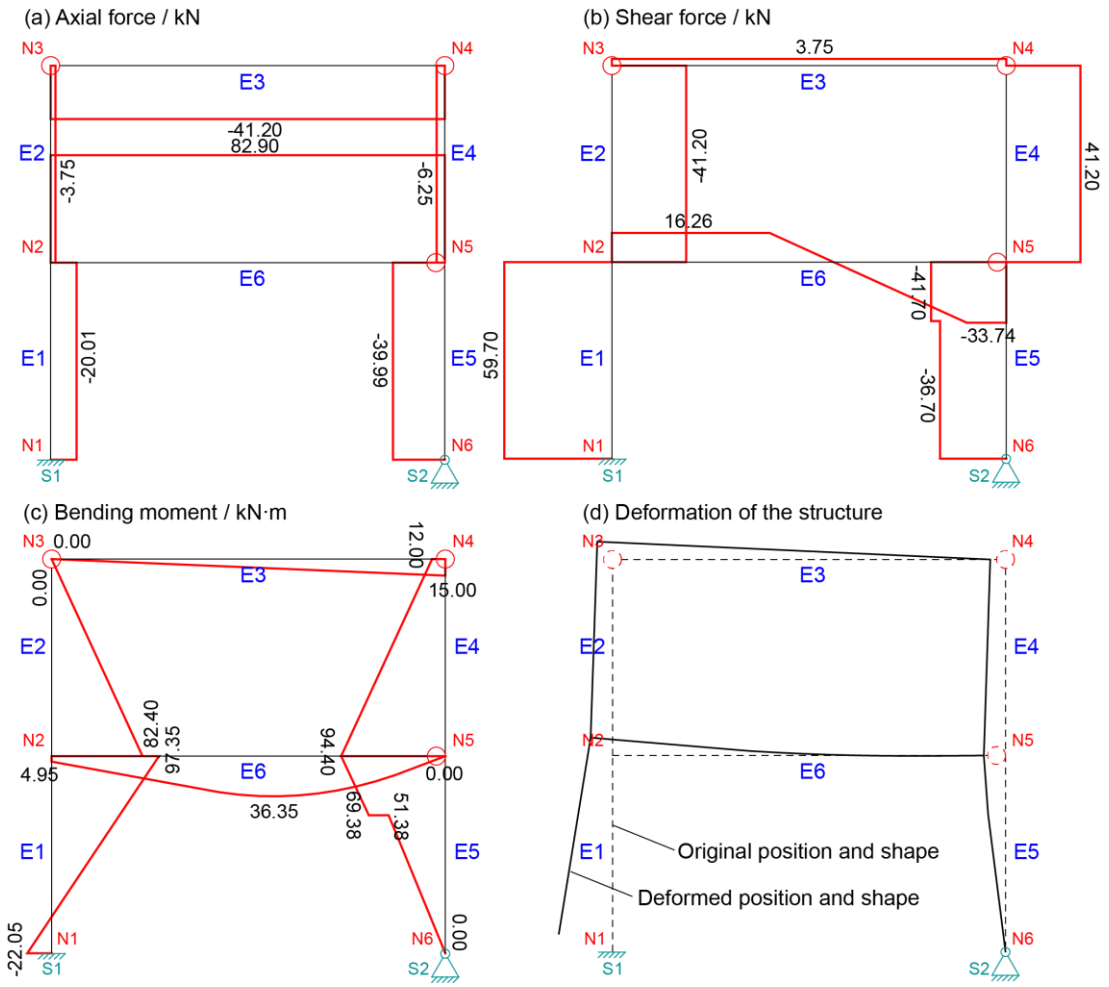

Figure 38. Some interesting output data (the structural model, external loads and support displacements can refer to Figure 33, Equation 22, and Equation 23): (a) the axial force diagram; (b) the shear force diagram; (c) the bending moment diagram; (d) the deformations of the structure (they are magnified compared to the size of the structure)

3.3.5 Verification

For verifying the validity of our developed computer code, we use some existing softwares to solve the same structure as in Figure 33, and then to compare the results with those achieved in the last section.

(1) Comparison 1: with *Autodesk® Robot™ Structural Analysis*

The software *Autodesk® Robot™ Structural Analysis* is a finite element code, which is widely used by engineers and researchers. It can be used for modeling, analyzing and designing various types of structures (*Autodesk robot structural analysis metric getting started guide*, Autodesk).

Taking the structural shape, the external forces, and the support displacements in Figure 33 into account, *Robot™ Structural Analysis* can provide the result diagrams of the internal forces and displacements as in Figure 39. By comparing Figure 39 with Figure 38, which is achieved by our code in the last section, we can conclude that the results got by these two softwares (codes) are the same.

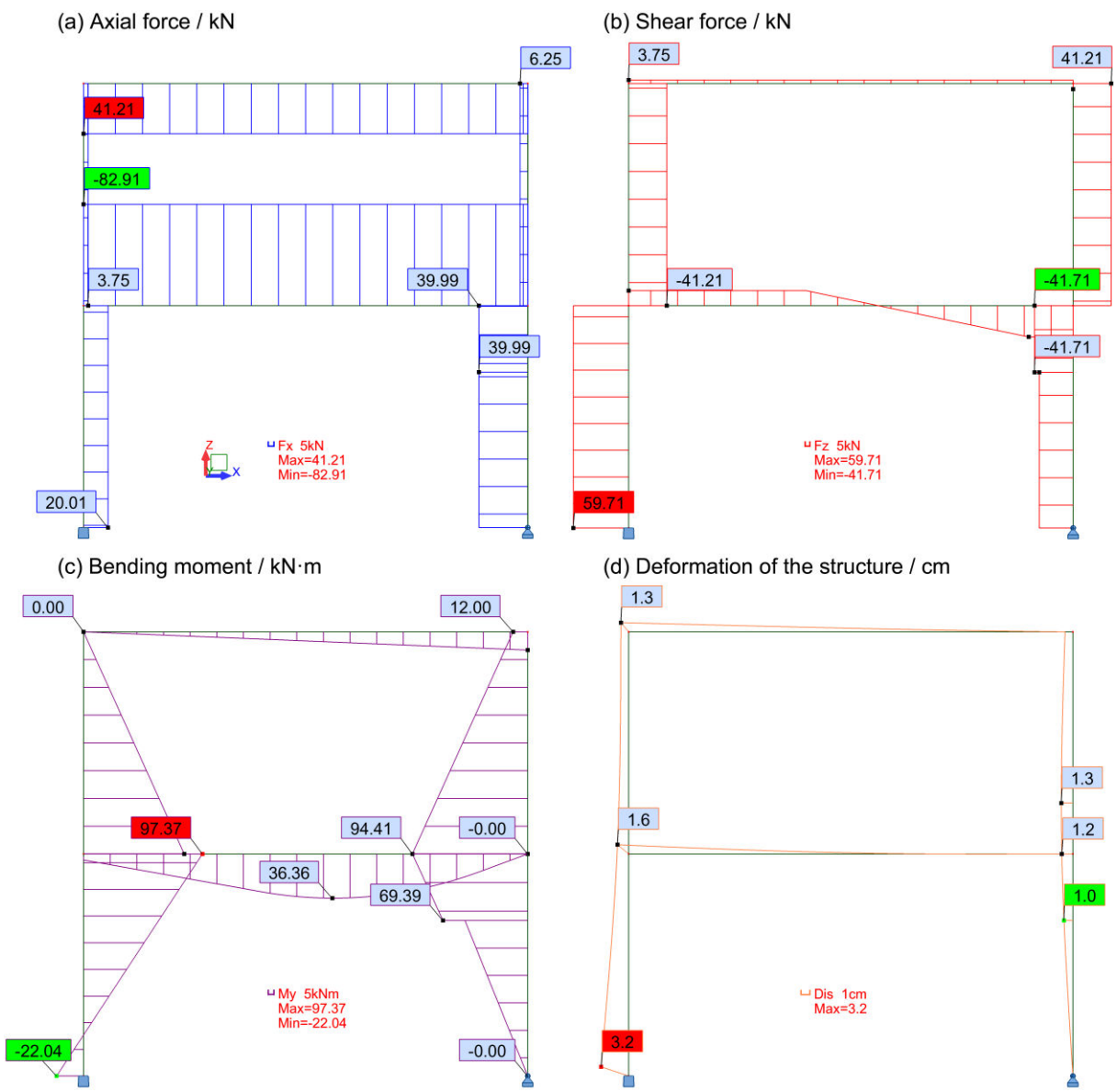

Figure 39. Comparison 1: the internal forces and displacements got by Robot™ Structural Analysis software (the structural model, external loads and support displacements can refer to Figure 33): (a) the axial force diagram; (b) the shear force diagram; (c) the bending moment diagram; (d) the deformations of the structure (they are magnified compared to the size of the structure)

(2) Comparison 2: with *SM Solver*

The software *SM Solver* (Structural Mechanics Solver) is developed by the Department of Civil Engineering of Tsinghua University (China), using the finite element method (Yuan 1993) to solve structure problems. It has been employed in some researches (Li *et al*. 2014, Wang *et al*. 2004, Yuan *et al*. 2006 and 2008), and has been proved creditable.

The input data for *SM Solver* are organized according to Figure 33, and then the results diagrams of the internal forces and displacements are plotted as in Figure 40. We consider that they are the same as those got by our computer code.

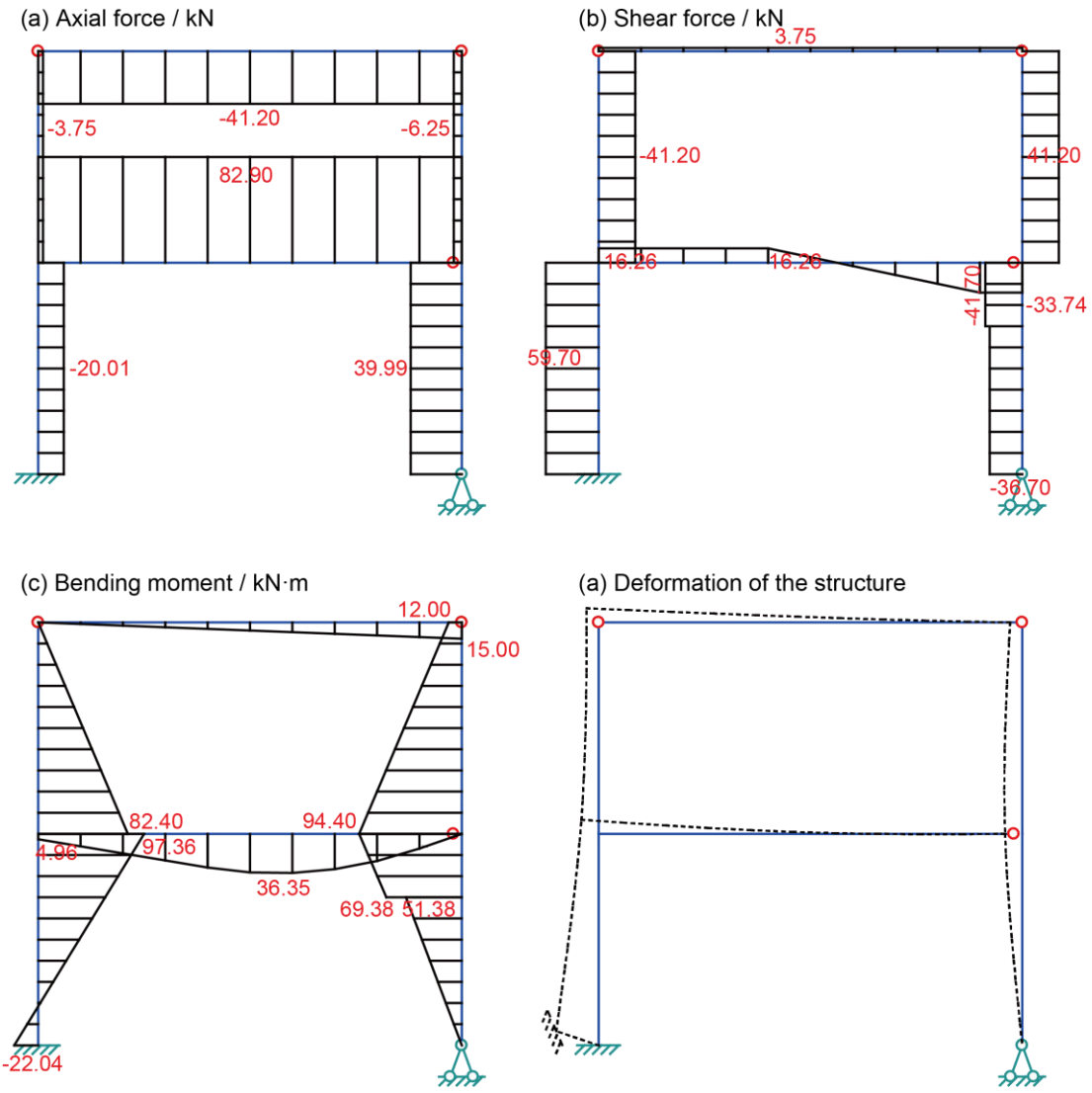

Figure 40. Comparison 2: the internal forces and displacements got by SM Solver software (the structural model, external loads and support displacements can refer to Figure 33): (a) the axial force diagram; (b) the shear force diagram; (c) the bending moment diagram; (d) the deformations of the structure (they are magnified compared to the size of the structure)

By the above mentioned two comparisons, we proved our developed computer code can provide the same results as existing softwares. That is, our code turns out to be correct.

3.4 Building damage evaluation

3.4.1 Building damage evaluation depending on the internal forces

In this research, we are going to consider that the grades of the building damage can be determined according to the internal forces over the structure, including the axial forces, shear forces, and bending moments, through the use of criteria to indicate the relationships

between each damage grade and its corresponding value range of forces. The used criterion might be an acknowledged technical one or a local experiential one, and is commonly different for the axial forces, the shear forces, and the bending moments. Specially, the positive and negative values of the axial forces, which mean tensile and compressive forces, usually should have different value ranges for a grade. When the internal forces over the structure are achieved by the matrix displacement method, they can be compared with the criteria to judge which value range they belong to, then the damage grade of the structure (or each element of the structure, or even each point of the structure) can be determined. It can be noted that the damage grade can be decided from one of the internal forces and its corresponding criterion, or from any two of them and their corresponding criteria, or from all of the three and their criteria.

Using the simple structure in Figure 33 as an example, in the meanwhile, taking both the displacements of the support S1 and the external loads acting on the structure into account, the values and curves of the internal forces are shown in the last section, as in Table 15 and Figure 38. We assume the damage grade criteria for the axial force and the bending moment are as in Table 16.

Note that, these criteria are just assumptions for this example, in order to well distinguish the grades and to explain the grading process. In fact, the criteria can be more complete with the value ranges defined for each or each kind of structural element. In the next chapter, the building damage evaluation in Joeuf will use different criteria for the walls, first floors, and other floors of the buildings.

Table 16. The criteria of damage grades (only for the structure in Figure 33)

Damage grade	Axial force (kN)		Bending moment (kN·m)	Measures
	Compressive force	Tensile force		
1	< 20	< 2	< 10	None
2	20 – 40	2 – 4	10 – 20	Pay attention
3	40 – 80	4 – 8	20 – 40	Minor repair
4	> 80	> 8	> 40	Heavy repair
Remark: the values of forces are absolute values; the positive axial force is tensile force; the negative axial force is compressive force				

By the comparison between the computed internal forces over the structure (as in Table 15 and Figure 38) and the damage grade criteria (as in Table 16), the damage evaluation results depending on the axial force and bending moment over the structure are shown in Figure 41. The damage evaluation results are plotted on the deformed structure using colored continuous lines. More details can be stated as follows:

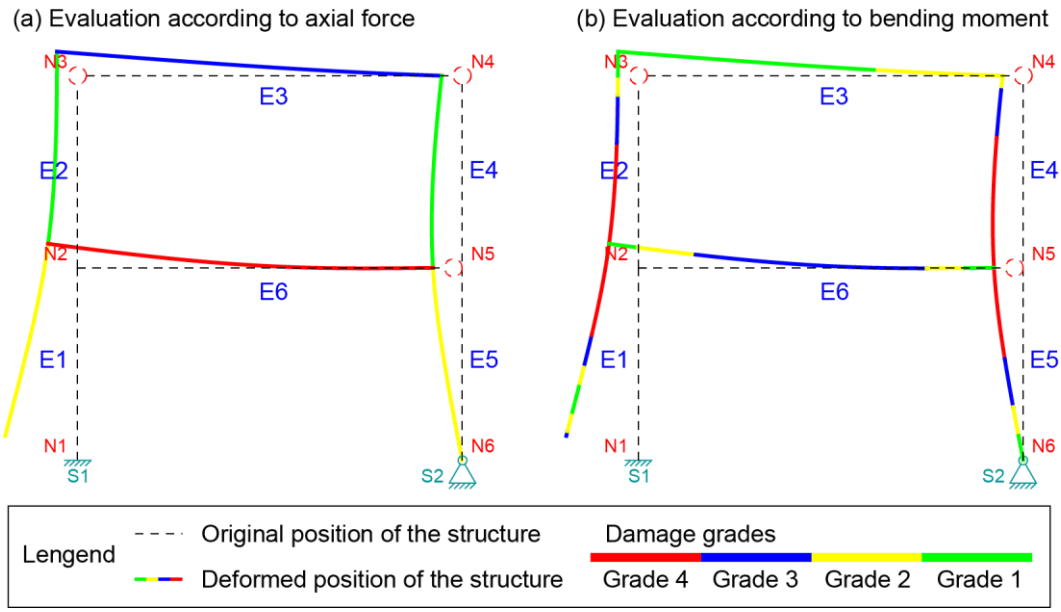

Figure 41. Damage evaluation results along the deformed shape of a structure (the structural model, external loads and support displacements can refer to Figure 33, Equation 22, and Equation 23; the deformations of the structure are magnified compared to the size of the structure): (a) the damage evaluation result according to the axial force over the structure; (b) the damage evaluation result according to the bending moment over the structure

(1) Only according to the axial force

The maximum tensile axial force (82.90 kN) appears in the element E6, which is a horizontal beam, the damage extent reaches grade 4 (because the force is greater than 8 kN in this element); also a noticeable compressive axial force (–41.20 kN) in grade 3 (40 – 80 kN) appears in the top beam (i.e. the element E3). That means, for E3 and E6, some damage can be expected and repair work can be necessary as mentioned in the last column of Table 16. In this case, we can find that the damage caused by tensile force far exceeds grade 4, while the compressive force damage is still in grade 3. This phenomenon can be attributed to the value ranges used for the tensile force that are much more sensitive than those for the compressive force. As in practice, we usually pay more attention to the tensile force than the compressive one in structures.

(2) Only according to the bending moment

The bending moments are more complex to interpret than the axial forces because they vary along the elements. In the studied structure, around nodes N2 and N5, which interconnect the vertical element E1, E2 and E4, E5, respectively, the maximum bending moment can be found, and the damage possibly reaches grade 4. More specifically, in the elements E2, E4, and E5, the damage grade decreases along the element from N2 and N5 to the top of the structure or to the support; but in the element E1, due to the bending moment which firstly decreases from 97.35 kN·m to 0, then increases again to –22.05 kN·m, the damage grade also changes from grade 4 to grade 1, then to grade 3 from the top to the bottom. Moreover,

a damage in grade 3 also appears in the element E6. So, according to the bending moment, almost all the structure, excluding the top beam E3, should be repaired.

(3) According to a multi-judgment based on the axial force and bending moment

As aforementioned, the damage grade judgment can depend on more than one internal force. When the damage grades obtained from different forces are not the same, the higher grade can be selected. For instance, when considering only the axial force, the damage grade of the element E3 is grade 3; while considering the bending moment, it is grade 2; so, the damage grade of E3 can be considered as 3 when taking both the axial force and the bending moment into consideration. Then, according to the previous analyses, all the structure should be repaired due to the fact that the lowest damage grade of the elements is grade 3.

Furthermore, if the criterion of the shear force for this structure is known, the damage grade also can be determined by the multi-judgment of all of the three forces.

3.4.2 Kinematic analysis

Because subsidence phenomena, which are the focus of this thesis, have some kinematic aspects (for instance, a structure may be subjected to varying loads and displacements before reaching a stable state after the subsidence has ended), it is interesting to take varying external loads and support displacements into account in the structure damage analysis. The present section deals with this problem by considering varying support displacements as an example.

Taking the structure with the marked external loads in Figure 33 as an example, we assume the support S1 moves from its original position to S1' by four stages, and the displacements of S1 at every stage are presented by linear functions as in Equation 44. Although the dynamic subsidence functions (i.e. subsidence – time functions) should be non-linear in practice (Cui *et al*. 2001, Lian *et al*. 2011), we provide here a possible way to solve such issues but not deal with a real case, as the dynamic subsidence problem is not a topic of this thesis.

$$\begin{gathered} DispAtS1(n) = \{u1(n), v1(n), \theta1(n)\} \\ u1(n) = -7.5\,n \\ v1(n) = 2.5\,n \\ \theta1(n) = -2.5\,n \\ (n = 0, 1, 2, 3, 4) \end{gathered} \qquad \text{Equation 44}$$

In which, n is the variable of the stage serial number. It also can be considered as a time variable. Here, the units of u, v, and θ are mm, mm, and rad/1000, respectively. At Stage 0, the support S1 is located at its original position without any displacements, i.e. the internal forces and displacements are caused only by the external loads at this moment; at stage 4, the support S1 arrives at the its final position S1'.

Using the function $DispAtS1(n)$ in Equation 44 instead of the original support displacements ($\{-0.03, 0.01, -0.01\}$, as in Figure 33 and Equation 22), the kinematic damage evaluations of the structure can be carried out in *Mathematica*™. Due to the restriction of plotting and displaying animations, the diagram of each stage is output as a

substitution.

Figure 42 and Figure 43 are two kinematic damage evaluation results according to the axial force and bending moment over the structure, respectively. Note that different value ranges (as in Table 16) are considered for the compressive force (negative axial force) and tensile force (positive axial force) in Figure 42. These two figures can intuitively illustrate the developing processes of the damage grade in the structure, then help people to decide when and where the necessary measures must be implemented. Otherwise, in some cases, the support S1 might move to S1' first, then back to its original position (or anywhere else). Under such circumstance, if we use the static analysis, the damage evaluation figures might be the same as Figure 42(a) and Figure 43(a), then the wrong conclusion of only slight damage to the structure will be drawn. By contrast, while using the kinematic analysis, the high damage grade can easily be noticed. If the mechanical strength of the structure is overpassed when the support moves to the position S1', for instance, some fissures or cracks emerge in the structure, the internal forces cannot be calculated any more during the support return to its original position, and the final damage diagrams will never match the forms as in Figure 42(a) and Figure 43(a). In other words, the conclusion made by the static analysis is possibly incorrect.

Moreover, if we want to pay close attention to some points of the structure, the kinematic analysis can help us to study the variations of the internal forces, as shown in Figure 44 and Figure 45. These two figures illustrate that, in the course of the movement of the support S1, the absolute values of the axial force at the midpoints of the element E3 (compressive force) and E6 (tensile force) rise evidently, while the values of the bending moment at the midpoints of the element E1, E2, E4, and E5 increase. We can also notice that the bending moment at the midpoint of the element E1 has different signs at stage 0 and stage 4, which means the bending direction of E1 is changed during the moving process of the support (refer to shape of E1 in Figure 42(a) and (e), or in Figure 43(a) and (e)). Also, the bending direction of E5 is changed, but not as obviously as E1.

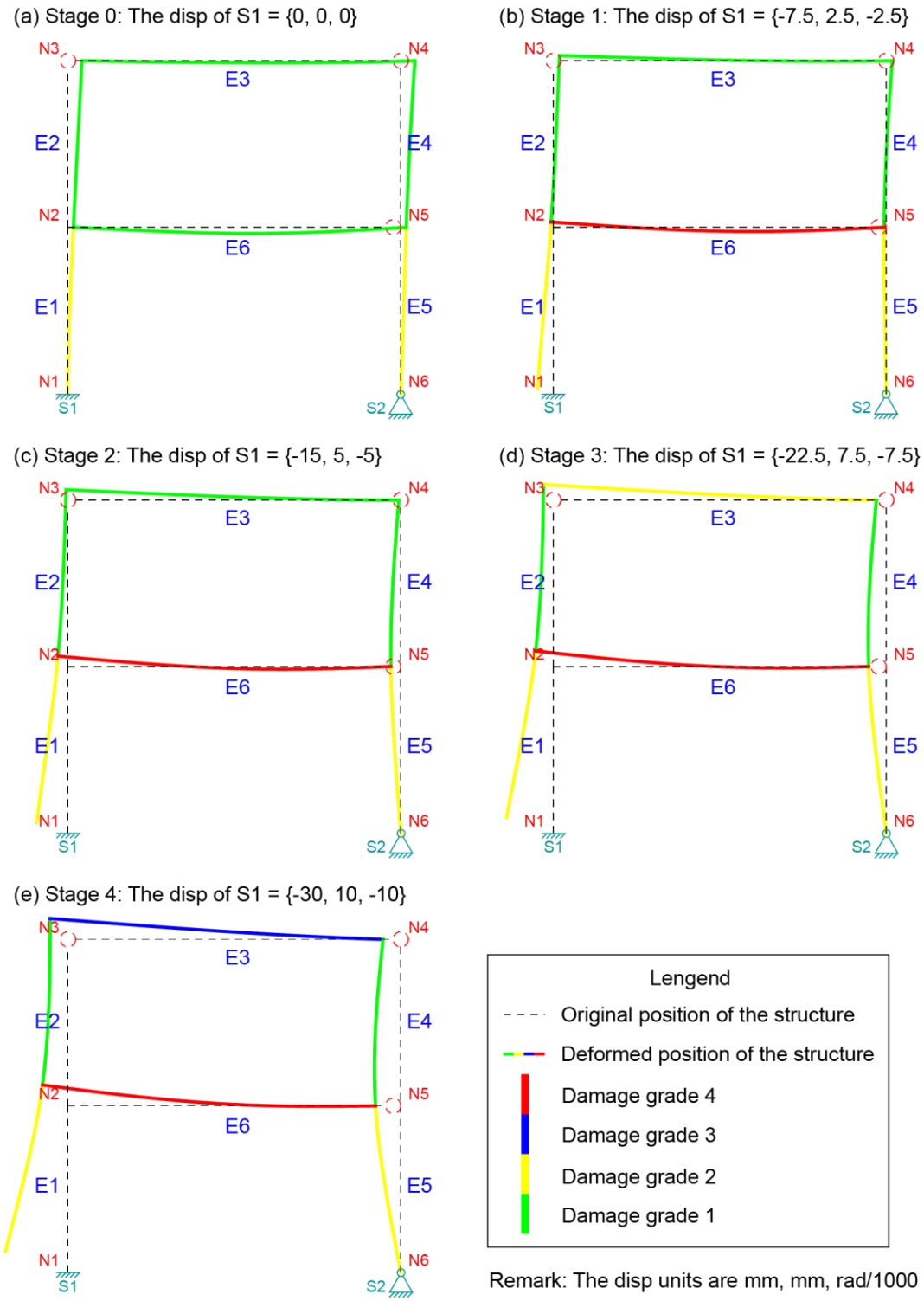

Figure 42. Kinematic damage evaluation results according to the axial force over the structure (the structural model and external loads can refer to Figure 33, Equation 22, and Equation 23; the displacements of the support S1 are the functions of the stage serial number as in Equation 44; the deformations of the structure are magnified compared to the size of the structure)

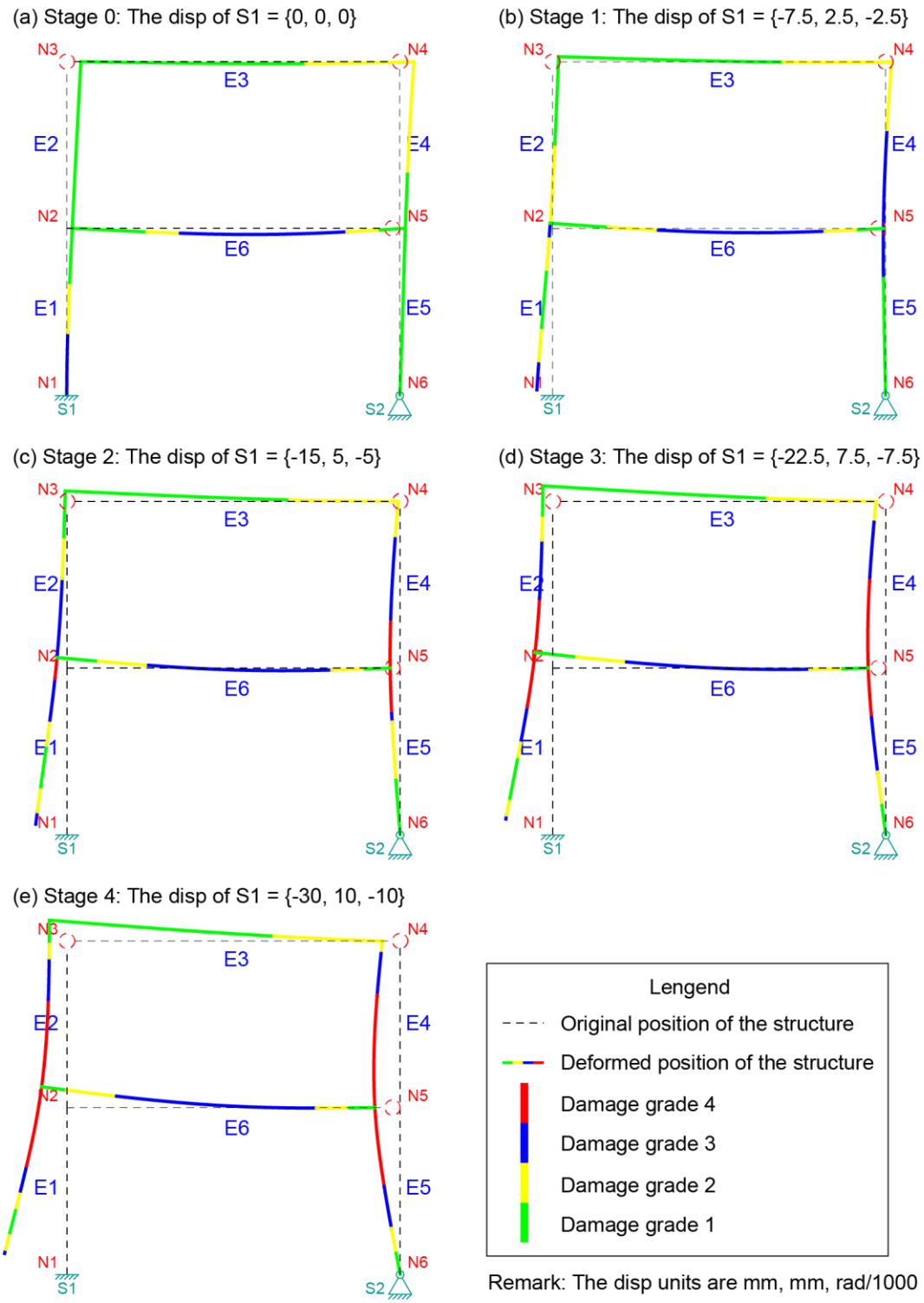

Figure 43. Kinematic damage evaluation results according to the bending moment over the structure (refer to the statements in the brackets of Figure 42)

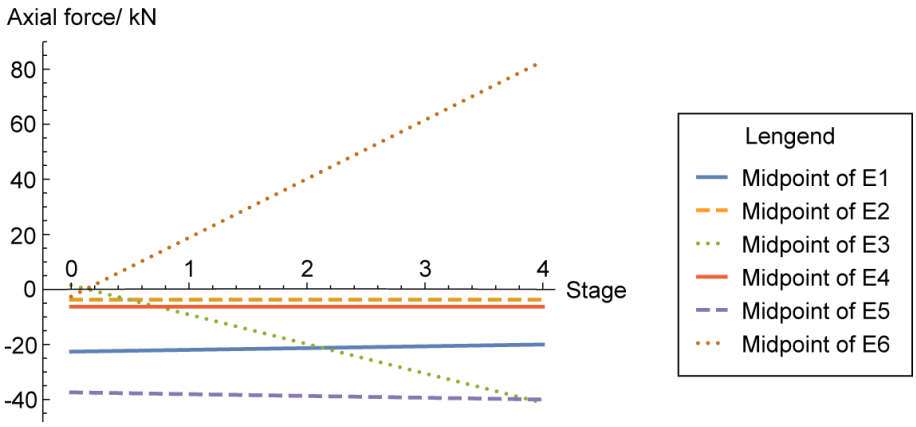

Figure 44. Variations of the axial forces of several interesting points on the structure (refer to the statements in the brackets of Figure 42)

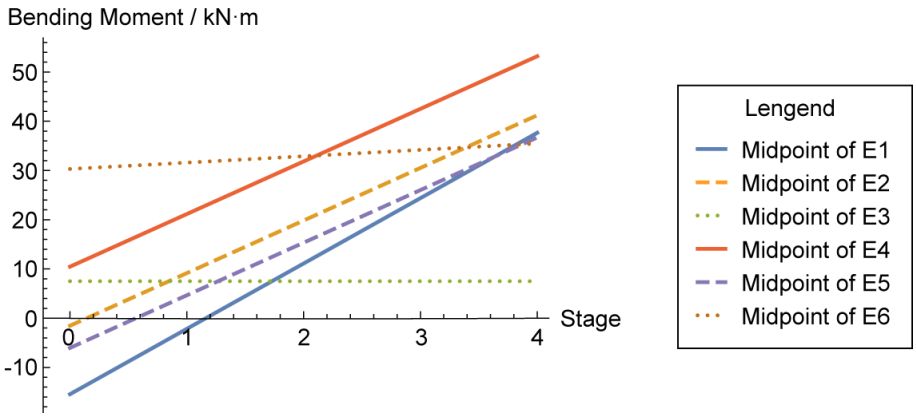

Figure 45. Variations of the bending moments of several interesting points on the structure (refer to the statements in the brackets of Figure 42)

3.5 Conclusions

The work presented in this chapter focuses on traditional civilian houses, which are normally non-high-rise timber, masonry and concrete buildings, and uses plane framed models to solve real-world 3D structural problems by the matrix displacement method.

For each building, two plane framed structural models can be set up in the vertical sections through the principal axes of inertia of a polygon, which presents the projected outline sketch of the building in a horizontal plane.

The matrix displacement method can then be used to compute the internal forces and displacements over these models as we implemented the method into a specific code within *Mathematica*™. First, structural models, which are simplifications of the real structures, should be prepared by digitizing the model into node and element lists. In this step, the nodes and elements are marked by numbers, the global (structure) and local (element)

coordinate systems are defined, and the known and unknown node displacements (including the support displacements) and the external forces are arranged. Then the force-displacement relations of an element are introduced in a traditional way. In the local coordinate system, the element end force vector is related to the element end displacement vector through an element stiffness matrix; a transformation matrix of coordinates is used to express this relationship in the global coordinate system. After that, the force-displacement relations of the entire structural model are organized in our own way as the software *Mathematica*™ used in this study has the powerful capacity in solving such mathematical problems. We skip the step of organizing the structure stiffness matrix by directly solving a set of equations composed of the force equilibrium conditions in global coordinate system at each node, then the unknown forces and displacements can be solved. Finally, after the internal forces and displacements over a structure are all carried out, we provide the tables and figures as the output data to present them.

The grades of the building damage can then be determined according to the achieved internal forces over the structure and the criteria. The damage extent can be decided from one of the internal forces and its corresponding criterion, from any two of them and their corresponding criteria, or from all of the three and their criteria. In our code, the damage evaluations can be intuitively presented on the deformed structure by colored lines, which are used to distinguish different grades. Kinematic structure damage evaluations are also available in this code.

In the following chapter, we are going to focus on large scale assessment of building damage. The method and code presented in this chapter are going to be used to compute the effects of mining subsidence on all the interesting buildings of a city, each of them being represented by two perpendicular frame structure models such as those previously presented.

Soil-structure interactions, which are very important to building damage assessment, have not been considered up to now in the developed code. In our laboratory, they were studied by Deck (2010) and could be taken into account later by introducing the soil rigidity in the models or changing the subsidence inputs to take them into account.

Non-linear strain-stress relationships were also not considered in the plane frame structural model in this study. Therefore, the internal forces might be incorrect when plasticity appears in the models, especially, for the masonry buildings. This limitation could also be improved in a further work.

Chapter 4: Case study – damage evaluation of Joeuf city due to mining subsidence

Chapitre 4: Etude de cas – évaluation des dommages potentiels dans la ville de Joeuf

Abstract of chapter 4

In this chapter, by using the improved methods of subsidence computation (presented in chapter 2) and building damage evaluation (presented in chapter 3), a real case application is performed in the city of Joeuf, which is located above the iron-ore field in Lorraine (France) and lies in a valley. There are more than 1500 Buildings and more than 7000 inhabitants in Joeuf city. Mining subsidence is the major hazard to this city.

Under Joeuf city, six mining zones (polygons) in two iron layers (the layer gray and layer S2-S3) have been abandoned. Taking the topography and mining data into account, and considering the local maximum subsidence value and influence angle, we can compute the subsidence expected at Joeuf. During calculation, the six mining polygons are input into our developed code respectively to compute the subsidence induced by each polygon. Then the subsidence at any position induced by the collapse of any single polygon or the arbitrary combinations of polygons (by using the superposition principle) can be determined.

According to the investigations in Joeuf, five sets (two models for each) of typical structural models are selected to simulate the shapes of the buildings. Then, the element properties (including the flexural rigidity EI and axial rigidity EA) and initial loads are defined for different elements (standing for walls, first floor, and the other floors) of different types of buildings. Assembling the typical models, the element properties, and the initial loads, the complete structural models (without the influence of mining subsidence at present) can be organized for representing the buildings in Joeuf. A longitudinal model and a transverse model are considered for each building.

The computed subsidence is then employed into the prepared structural models as support displacements to calculate the internal forces. Comparing the internal forces with damage criteria, the damage grades of all the buildings in Joeuf can be assessed. According to the axial forces and bending moments over the structures, 19%, 23%, and 37% of the buildings are in high danger under the subsidence caused by the collapse of the layer gray, the layer S2-S3, and both the undermined layers, respectively. Comparison between an existing method and the method presented in this research shows that our method can provide credible results of building damage evaluation.

Résumé du chapitre 4

Dans ce chapitre, en utilisant les méthodes de calcul d'affaissement (présenté dans le chapitre 2) et du calcul de dommages aux bâtiments (présenté dans le chapitre 3), une application est effectuée dans la ville de Joeuf, qui est située au-dessus d'une zone d'extraction minière et se trouve dans une vallée. Plus de 1 500 bâtiments composent cette ville habitée de plus de 7000 personnes. L'affaissement minier est l'aléa principal auquel est exposé cette ville.

Sous Joeuf, six zones ont été exploitées en deux couches (couche grise et couche S2-S3). Prenant les données topographiques et minières en compte, et compte tenu de la valeur de l'affaissement maximum local attendue et de l'angle d'influence dans cette région, nous pouvons calculer l'affaissement prévisionnel à Joeuf. Lors du calcul, plusieurs combinaisons d'effondrement des zones minières peuvent être envisagées.

Selon les données relatives aux bâtiments de la ville de Joeuf, cinq ensembles de modèles structurels typiques (deux modèles pour chaque) sont choisis pour les simuler. Les propriétés des éléments de structure (la rigidité en flexion EI et la rigidité axiale EA) ainsi que les charges initiales sont définies (pour les murs, le premier étage, et les autres étages) pour les différents types de bâtiments, de même que les assemblages d'éléments relativement à la géométrie des ouvrages. Un modèle longitudinal et un modèle transversal sont considérés pour chaque bâtiment.

L'affaissement calculé est ensuite utilisé dans les modèles structurels en tant que déplacements imposés aux éléments support afin de calculer les forces internes. En comparant les forces internes avec des critères de dommages, les niveaux de dommages de tous les bâtiments de Joeuf peuvent être évalués. Selon les forces axiales et les moments fléchissant sur les structures, 19%, 23%, et 37% des bâtiments sont en danger élevé en vertu de l'affaissement causé par l'effondrement de la couche grise, la couche S2-S3, ou des deux couches, respectivement. Une comparaison avec une méthode existante montre également que la nouvelle méthode fournit des résultats crédibles.

4.1 Overview of the city of Joeuf

The city of Joeuf is located above the iron-ore field in Lorraine (France); its position is marked as in Figure 46. There are more than 1500 Buildings and more than 7000 inhabitants in this city. The aerial view of the main part of Joeuf city can be seen in Figure 47, and the digitization of the buildings is plotted in Figure 48. Note that, the small unimportant constructions (for example, garages, garden sheds, etc.) are not of interest, and have been removed when digitizing. The construction dates of most of the existing buildings in Joeuf are between 1870 and 1930. Many districts are workers' housing estates with a similar building type. The majority of buildings are masonry made with one or two floors; few of them are more recent buildings with concrete materials and a global better quality.

According to the study of Al Heib (2002), iron mines were exploited under the city. In case of subsidence, the maximum vertical subsidence has been estimated to be up to 2 m. The subsidence issue is the major hazard to the city of Joeuf.

Figure 46. The position of the city of Joeuf

Figure 47. Aerial view of the city of Joeuf

Figure 48. Digitization of the buildings of Joeuf

4.2 Modelling of the mining subsidence in Joeuf

As mentioned in chapter 2, which introduces the improved influence function method for calculating the subsidence caused by underground excavation under a non-flat surface, the mining zone data and the ground surface data must be prepared before the subsidence computation and some parameters should also be provided such as the maximum subsidence values and influence angles.

4.2.1 The topography in Joeuf

The topography data of Joeuf city have been obtained from the web site of IGN[1] (l'Institut Géographique National). In view of the range of the iron mines that is wider than the range of Joeuf city, and meanwhile considering the requirement of the subsidence calculation (subsidence range is wider than mining range), we extracted all the topography data in a rectangular range, which satisfies the limitation of the x and y coordinates in Equation 45, as the preparation work. Finally, 22196 points were selected; 50 sample points of those are listed in Table 17.

$$865200 < x < 869000$$
$$174100 < y < 178600$$

Equation 45

[1] www.ign.fr

Table 17. The coordinates of the ground surface (part) over the iron mines in Joeuf

Point ID	X	Y	Z	Point ID	X	Y	Z
1	866683.1	173980.1	240.0	26	868236.5	176408.7	200.0
2	867937.0	174051.5	250.0	27	866359.9	176464.7	210.0
3	866382.9	174064.4	245.0	28	867376.8	176468.8	182.5
4	868480.8	174191.8	265.0	29	866066.6	176674.3	250.0
5	867764.5	174210.8	235.0	30	866821.5	176705.2	205.0
6	865386.9	174303.6	215.0	31	868679.0	176813.7	190.0
7	868816.2	174464.9	285.0	32	867085.8	176926.4	220.0
8	869169.1	174515.4	300.0	33	867298.2	177006.9	185.0
9	868910.7	174667.2	285.0	34	865357.8	177071.4	260.0
10	866562.8	174886.6	225.0	35	865455.0	177134.0	250.0
11	866290.3	174968.0	220.0	36	865866.0	177289.6	225.0
12	866037.3	175121.5	210.0	37	868066.2	177518.7	175.0
13	868890.8	175160.0	280.0	38	868104.5	177570.1	190.0
14	865100.9	175228.5	200.0	39	868477.8	177584.5	225.0
15	866279.0	175308.8	195.0	40	865669.5	177586.3	215.0
16	866161.7	175324.8	200.0	41	865563.5	177797.4	240.0
17	867362.6	175347.7	235.0	42	865733.8	177927.5	270.0
18	867411.2	175456.6	230.0	43	865169.8	177990.9	265.0
19	868806.1	175589.5	275.0	44	868235.0	178003.7	195.0
20	867423.2	175613.9	225.0	45	865231.5	178068.1	225.0
21	865318.0	175645.4	230.0	46	865322.4	178151.9	220.0
22	865842.9	175922.8	195.0	47	868952.6	178269.2	175.0
23	868281.8	176242.2	225.0	48	868950.8	178500.6	180.0
24	866049.0	176291.7	235.0	49	867359.1	178618.2	290.0
25	867624.1	176340.9	205.0	50	868810.6	178660.5	200.0

The achieved topography data are plotted in Figure 49 into red points. In subsidence calculation, the topography data should cover the whole computational range, i.e. the elevations of any random points in the range should be known when necessary, so an interpolation function, fitted from these topography data, is used to describe the elevations of the surface ground. Then the 2D topography iso-contours can be computed from this interpolation function (or from the original topography data) as shown in Figure 49 where the buildings of Joeuf city have also been reported. The city part is re-plotted in Figure 50 for better display of our studied objects. Generally speaking, the elevation of the main part of the city is between 170 and 240 m. According to the same data, the 3D topography model is plotted in Figure 51, in which it is clear that Joeuf city lies in a valley, which is named Orne. The lengths in the z-axis in Figure 51 are magnified compared to the lengths in the x-axis or the y-axis, so that the steep areas around the city are actually much less sharp

than they appear in the figure (refer to Figure 47).

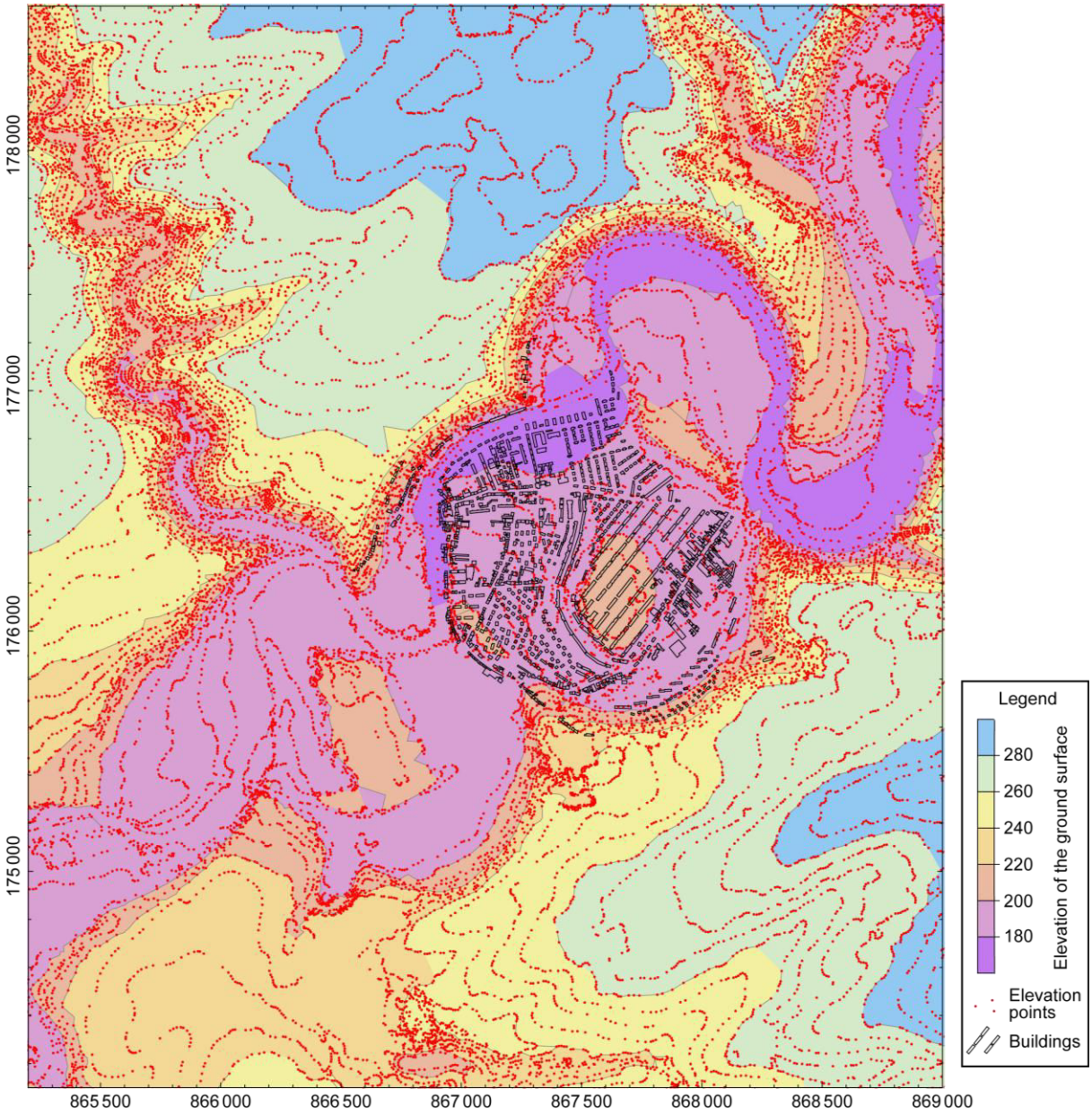

Figure 49. The superposition of the 2D topography iso-contours, the elevation points, and the buildings of Joeuf

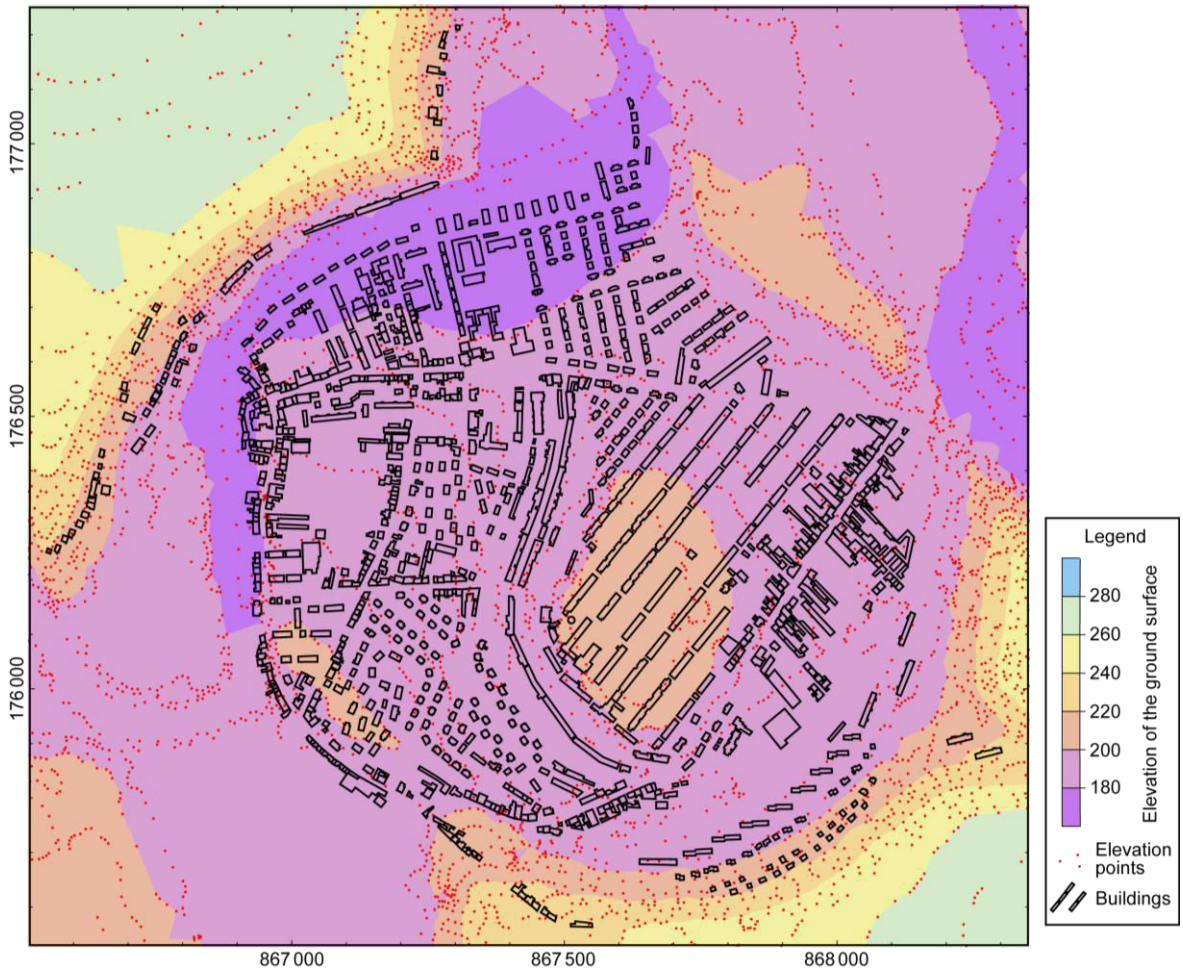

Figure 50. The enlarged detail of the part of Joeuf city in Figure 49

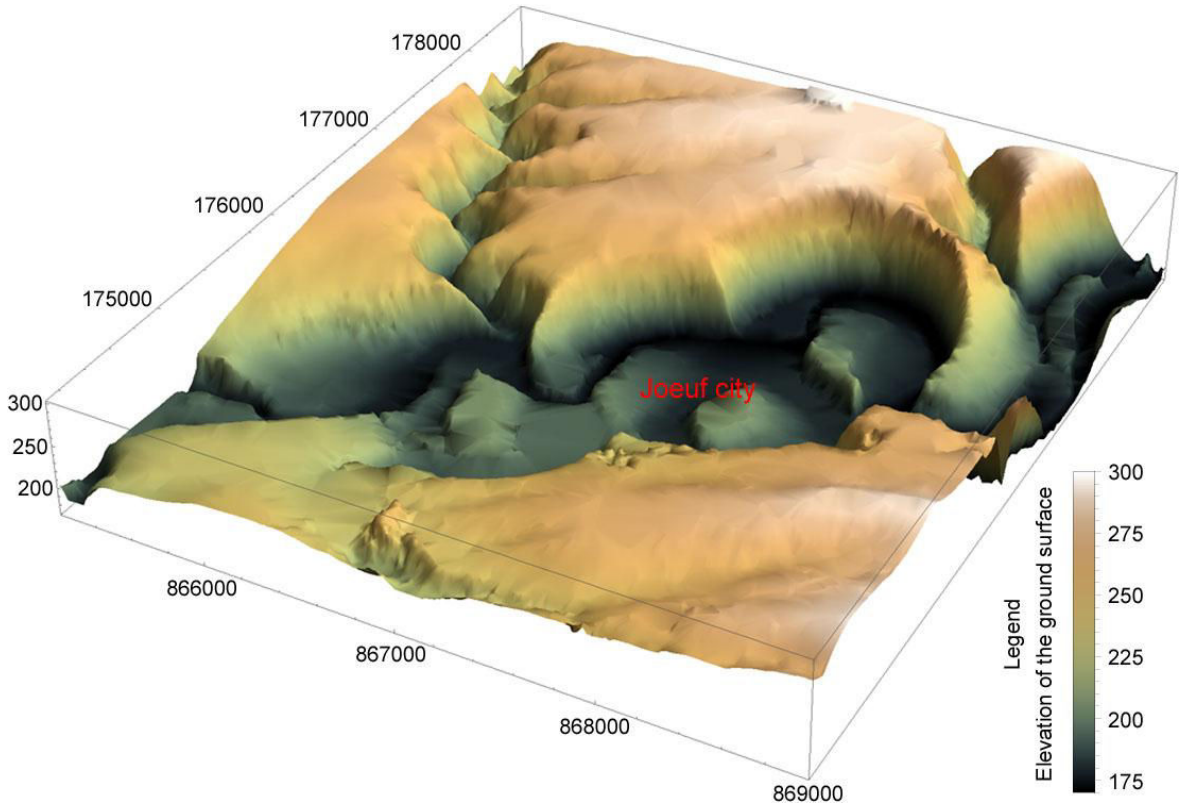

Figure 51. 3D model of the topography (the length of the z axis is magnified compared to the length of the x/y axes)

4.2.2 The iron mines under Joeuf

The excavated iron mines in/around the city of Joeuf, consist of four underground layers, as shown in the vertical section diagram of Figure 52. From the bottom to the top, they are the layer brown, the layer gray and the layer S2 and S3. We only consider the layer Gray and the multi-layer S2-S3 in this study.

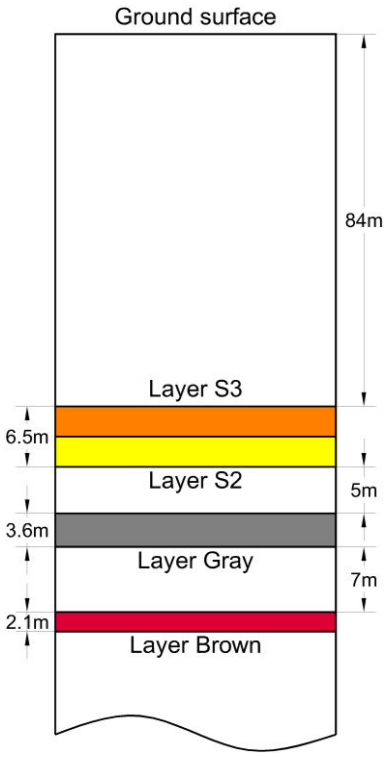

Figure 52. Typical vertical section of the mines in Joeuf

The mining thickness of the layer brown is 2.1 m. It was little exploited (exploitation rate of 21%) and is separated from the layer gray by an interlayer with a thickness of approximately 7 m. According to the study of Saeidi (2010), it can be considered as a stable layer in the analysis of the hazard. In other words, the layer brown will not be taken into account in the following subsidence computation. The mining thickness of the layer gray is 3.6 m, its exploitation rate is 35%. The layer S2 and S3 were exploited together with a mining thickness of 6.5 m. The exploitation rate of these two layers is around 45%. The thickness of the interlayer between the layer S2-S3 and the layer gray is 5 m.

Due to the slope of the iron layers, and the varying ground surface, the mining depths are not the same everywhere. The minimum and the maximum values are 44 m and 163 m (Al Heib 2002, GEODERIS 2009). Most of the buildings of Joeuf, which we pay close attention to, are located in the valley of Orne, where the mining depth is generally the lowest nearby. The mean depths of the layer gray and of the layer S2-S3 are around 95 m and 84 m under the buildings (also can refer to Figure 52).

The mining plans of the layer gray and the multi-layer S2-S3 are plotted in Figure 53 and Figure 54. As Saeidi mentioned in his study (2010), layers S2 and S3 were exploited in a complicated way, and the mining plans for them are slightly different; whereas, the layer S3 is more critical regarding the scenarios of rupture within the mine. Therefore, we can choose to only take into account the mining polygons of the layer S3, which can also be considered as the mining positions of the layers S2, to play the role of the mining zones (mining polygons) subjected to a possible rupture of the multi-layer S2-S3. Note that, in the subsidence

calculation, we must employ the total mining thickness of these two layers, i.e. the thickness of the layer S2-S3, which is 6.5 m.

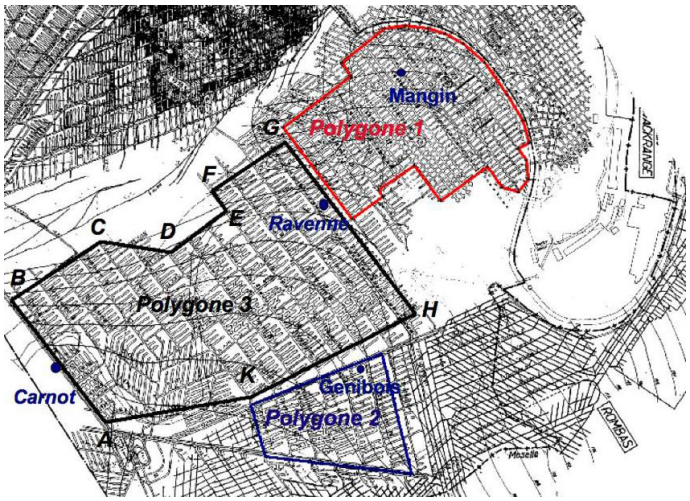

Figure 53. The layer gray and three mining polygons: Polygon 1 – Polygon 3

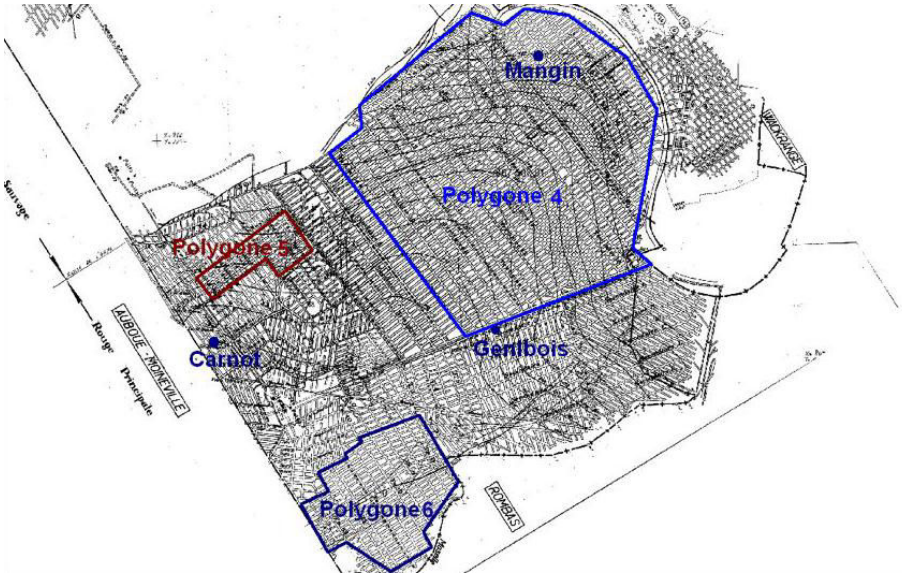

Figure 54. The layer S2-S3 and three mining polygons: Polygon 4 – Polygon 6

Following Saeidi's way, the chosen mining polygons of the layer gray and the layer S2-S3 are shown as in Figure 53 and Figure 54. The superposition and the relative positions of all the six polygons of the layer gray and the layer S2-S3 can be seen in Figure 55, and the coordinates of the vertexes of the six polygons are listed in Table 18 – Table 23, which will be later taken into account in our subsidence computation code as the input data.

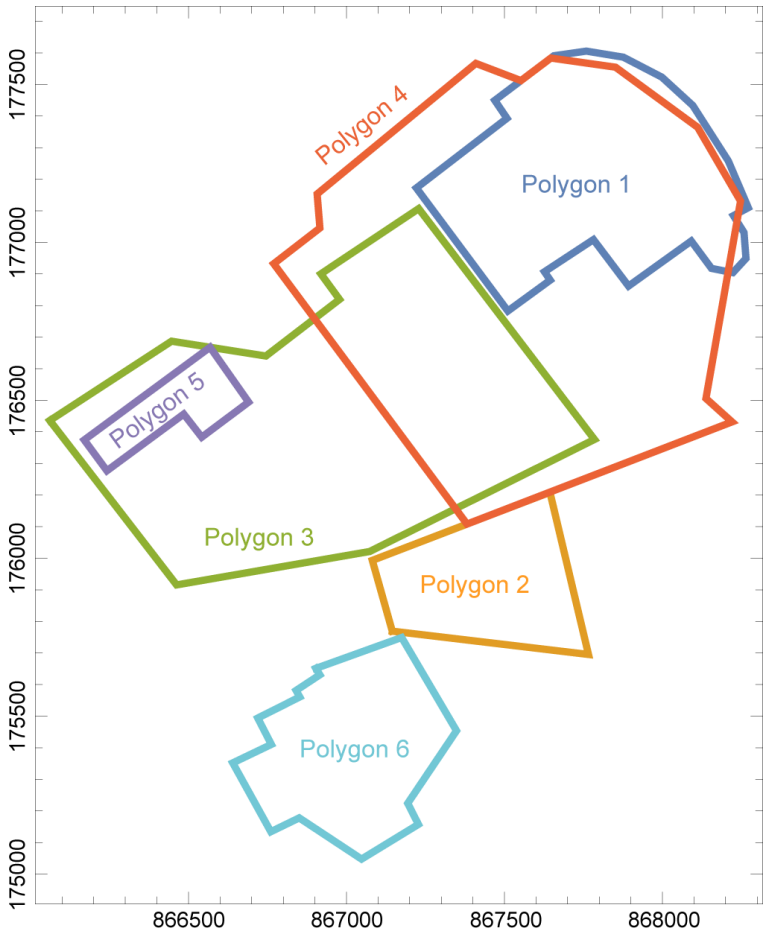

Figure 55. The superposition of the mining polygons of the layer gray (Polygon 1 – Polygon 3) and the layer S2-S3 (Polygon 4 – Polygon 6)

Table 18. The coordinates of the polygon 1 of the layer gray

Point ID	X	Y	Depth (m)	Point ID	X	Y	Depth (m)
1-1	867221	177172	95	1-12	868258	177031	95
1-2	867508	177393	95	1-13	868264	176949	95
1-3	867469	177450	95	1-14	868223	176904	95
1-4	867657	177591	95	1-15	868155	176918	95
1-5	867759	177606	95	1-16	868091	177004	95
1-6	867876	177587	95	1-17	867893	176862	95
1-7	867998	177523	95	1-18	867782	177009	95
1-8	868096	177434	95	1-19	867627	176907	95
1-9	868209	177258	95	1-20	867645	176881	95
1-10	868272	177110	95	1-21	867511	176783	95
1-11	868225	177085	95				

Table 19. The coordinates of the polygon 2 of the layer gray

Point ID	X	Y	Depth (m)	Point ID	X	Y	Depth (m)
2-1	867145	175769	95	2-3	867644	176209	95
2-2	867082	175993	95	2-4	867766	175695	95

Table 20. The coordinates of the polygon 3 of the layer gray

Point ID	X	Y	Depth (m)	Point ID	X	Y	Depth (m)
3-1	866061	176436	95	3-6	867229	177107	95
3-2	866446	176687	95	3-7	867785	176376	95
3-3	866745	176640	95	3-8	867074	176021	95
3-4	866978	176820	95	3-9	866462	175916	95
3-5	866919	176900	95				

Table 21. The coordinates of the polygon 4 of the layer S2-S3

Point ID	X	Y	Depth (m)	Point ID	X	Y	Depth (m)
4-1	866770	176933	84	4-7	867852	177555	84
4-2	866916	177046	84	4-8	868112	177364	84
4-3	866907	177153	84	4-9	868247	177131	84
4-4	867410	177567	84	4-10	868138	176506	84
4-5	867552	177512	84	4-11	868220	176432	84
4-6	867647	177584	84	4-12	867382	176108	84

Table 22. The coordinates of the polygon 5 of the layer S2-S3

Point ID	X	Y	Depth (m)	Point ID	X	Y	Depth (m)
5-1	866170	176375	84	5-4	866542	176383	84
5-2	866568	176668	84	5-5	866485	176457	84
5-3	866690	176494	84	5-6	866242	176277	84

Table 23. The coordinates of the polygon 6 of the layer S2-S3

Point ID	X	Y	Depth (m)	Point ID	X	Y	Depth (m)
6-1	866903	175651	84	6-8	866761	175134	84
6-2	867175	175749	84	6-9	866640	175352	84
6-3	867348	175454	84	6-10	866762	175411	84
6-4	867194	175224	84	6-11	866719	175494	84
6-5	867228	175157	84	6-12	866852	175561	84
6-6	867048	175048	84	6-13	866841	175581	84
6-7	866851	175178	84	6-14	866916	175631	84

For comparison, the mining polygons and the buildings of Joeuf city are plotted in the same figure with the topography, as in Figure 56. From this figure, we confirm that the mining range is wider than the city range as aforementioned, and the selected range of the surface ground data will be enough for subsidence computation.

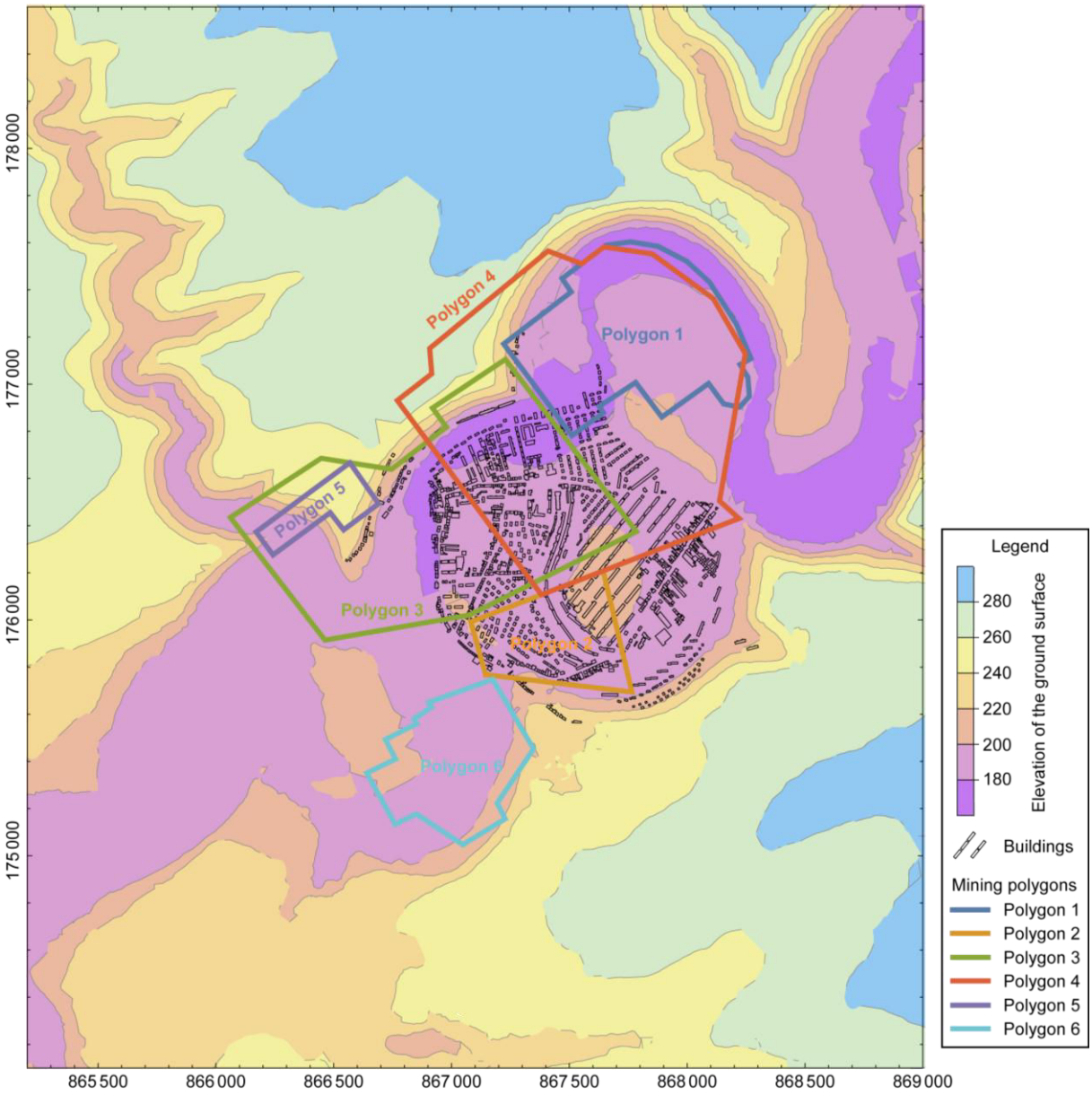

Figure 56. The superposition of the mining polygons, the buildings of Joeuf, and the topography

4.2.3 Mining subsidence computation

4.2.3.1 Preparation of the input data

The input data, mainly including the topography and mining polygon data, should be organized as lists for our developed subsidence computation code in *Mathematica*™, which

has been introduced in chapter 2 and by Cai *et al*. (2014). These data lists must contain the complete coordinate information, which can be used to represent the original shape of the topography and mining polygons. Some parameters, such as maximum subsidence values and influence angles, are also needed by our computer code in order to optimize the computational precision.

(1) Preparation of the topography data

The surveying work is usually restricted by field conditions; we cannot get all the coordinate data for every expected surface point. Therefore, as in Figure 49 and Figure 50, the projections of the achieved topographic points appear scattered. Although they can be used as the input data in our computer code, the precision of the subsidence results in the point-sparse range might be worse than in the point-dense range, because the subsidence results are only output at the points indicated by the input topography data list. Thus, we commonly use an interpolation function fitted from the observed surface data to manage a topography list, in which the points can cover the calculation range and the distances between any two neighboring points are uniform in a horizontal plane. The managed topography data list for Joeuf case is plotted in Figure 57. It should be organized as {{tx1, ty1, tz1}, {tx2, ty2, tz2} …}, in which the difference between tx1 and tx2 equals the difference between tx2 and tx3 (or ty1 and ty2 …). tz1 (or tz2 …) is the ground elevation. Furthermore, for some noticeable areas, the point density can be intensified when necessary.

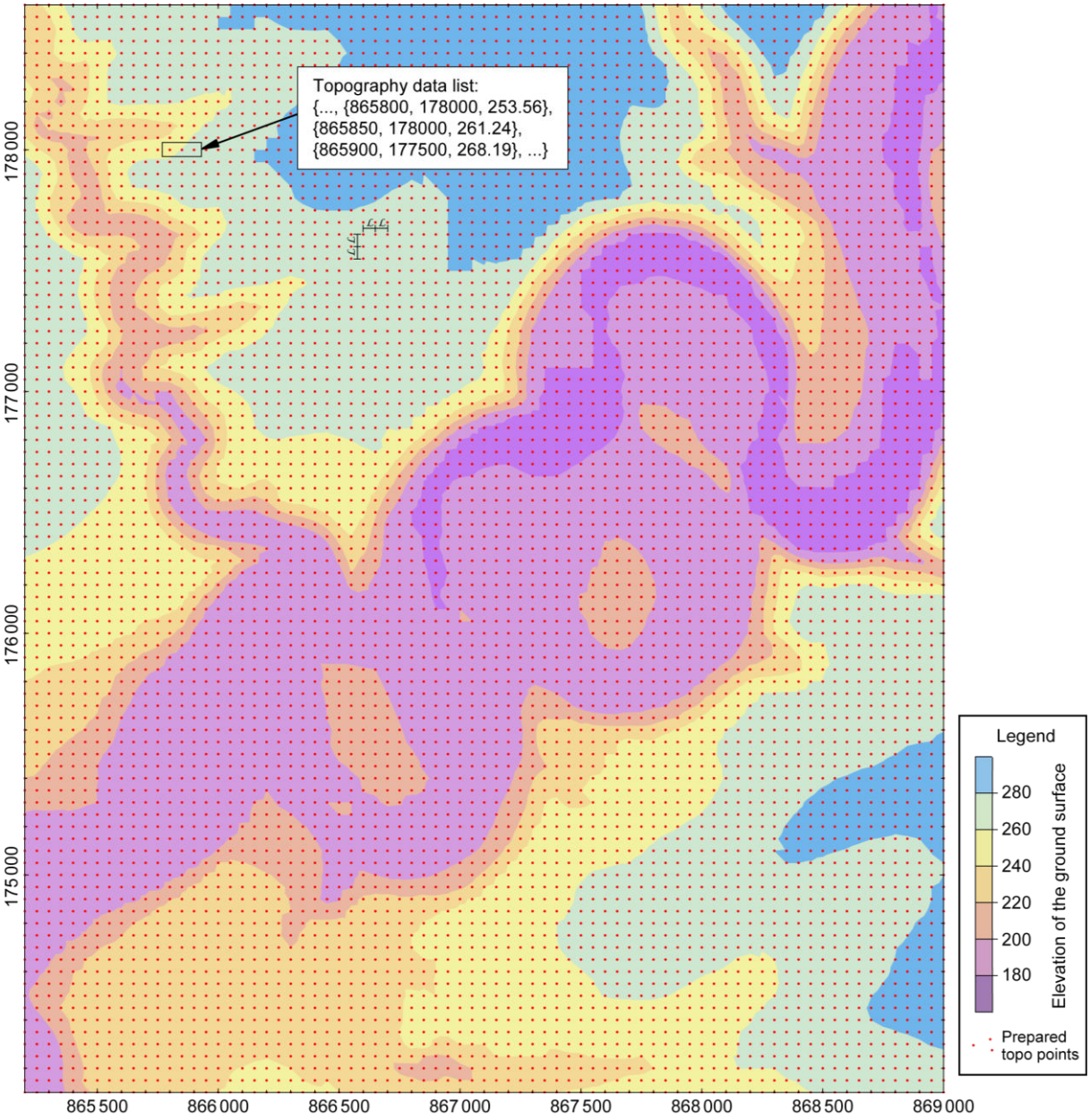

Figure 57. Preparation of the topography data at the equidistant points in the calculation range

(2) Preparation of the mining polygon data

Given the principles of the influence function method, the final subsidence at a surface point is the superposition of the subsidence caused by each mining element (refer to chapter 2). Therefore, we discretize the six mining polygons under Joeuf city into several mining elements as in Figure 58 (for Polygon 1 – Polygon 3 in the layer gray) and Figure 59 (for Polygon 4 – Polygon 6 in the layer S2-S3), in which the colored points stand for the centroids of the mining elements. A mining element can be considered as a square, its geometric center locates exactly at the discretized point, and its side length equals the horizontal distance between two neighboring points. In Figure 58 and Figure 59, some of the mining elements are marked as examples. The input data list for one mining polygon should be

organized as {{mx1, my1, mz1}, {mx2, my2, mz2} …}, whose form is the same as for the topography data list. The points in this list distribute equidistantly in a horizontal plane and must full fill the corresponding mining polygon; the z coordinates are the elevations of these points.

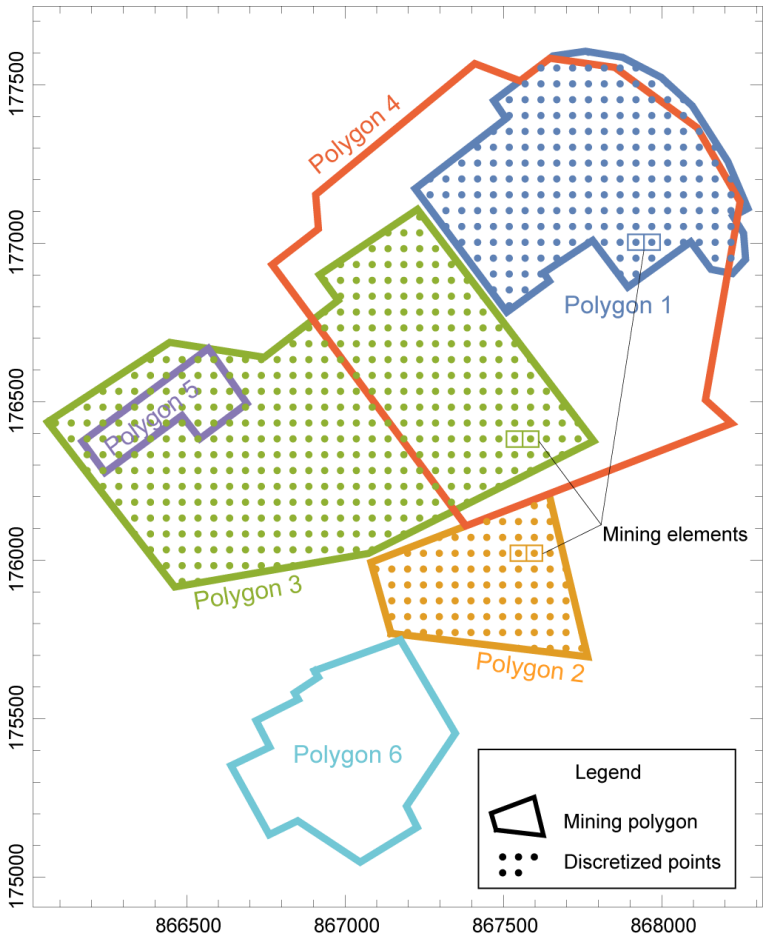

Figure 58. Discretization of the mining polygons (Polygon 1 – Polygon 3) of the layer gray

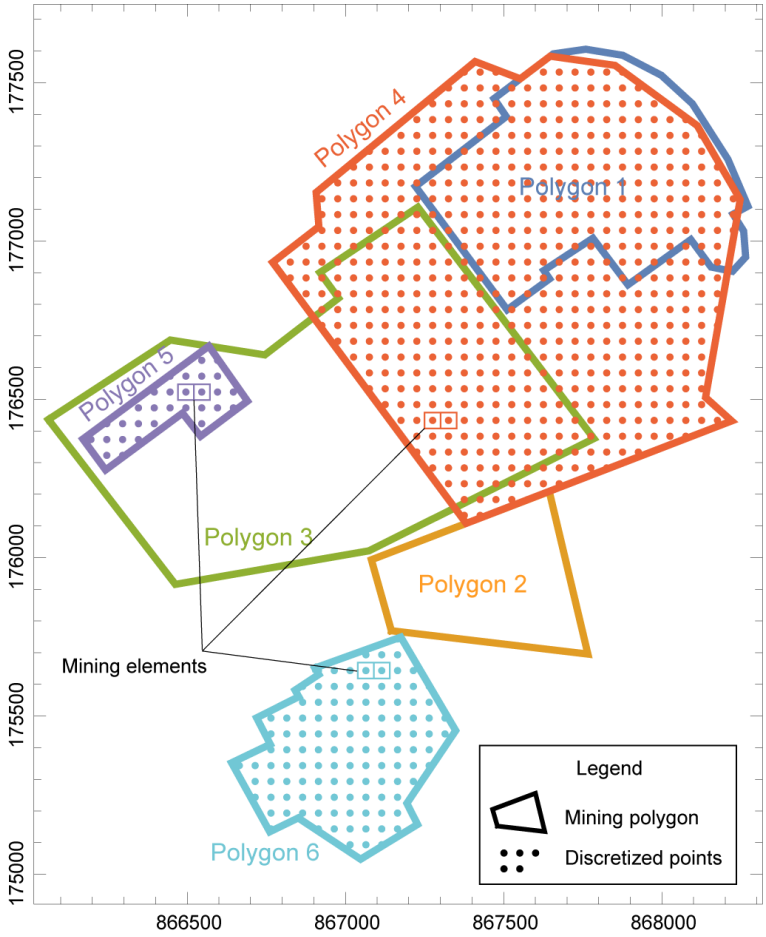

Figure 59. Discretization of the mining polygons (Polygon 4 – Polygon 6) of the layer S2-S3

(3) Corrections from field data

As mentioned in chapter 2, in practice, some factors, usually the maximum subsidence value and the influence angle, can be taken into account to optimize the quality of subsidence calculation. These two factors can be estimated from past nearby subsidence events, in other words, they are known values for a given mining area.

According to the field work carried out in the iron mines in Lorraine (Al Heib *et al*. 2003, 2008, Cai *et al*. 2014, Saeidi 2010), the observed influence angles are about 25 – 40°. In the following subsidence computation, we set the influence angle as 35°.

Considering the shallow mining depths (as in Figure 52), and the sizes of the mining polygons (as in Figure 55), the subsidence in this area is supposed to be critical. In this case, Equation 46 can be used to calculate the maximum vertical subsidence (Al Heib 2003).

$$S_{max} = 0.5\,\tau\,T \qquad \text{Equation 46}$$

In which, S_{max} is the maximum vertical subsidence by the collapse of a mining polygon; τ is the exploitation rate; T is the mining thickness.

The main characteristics of the layer gray and the layer S2-S3 are listed in Table 24, including the mining depth, the exploitation rate, and the mining thickness. Then the maximum

vertical subsidence values of these two layers obtained from these characteristics according to Equation 46 are output in the same table.

Table 24. Main characteristics of the layer gray and the layer S2-S3 and the expected maximum vertical subsidence values of these two layers

Layer	Mining Depth	Exploitation rate (%)	Mining thickness (m)	S_{max} (m)
Layer gray	95	35%	3.6	0.63
Layer S2-S3	84	45%	6.5	1.46

4.2.3.2 Subsidence computation

Taking into account all the prepared topography and mining polygon data, and considering the local maximum subsidence and influence angle, subsidence computation can be carried out with our computer program and the results are output as a list including the position information (x and y coordinates) and the corresponding subsidence values (the vertical subsidence, the horizontal displacement in x direction, and the horizontal displacement in y direction). In order to provide the subsidence everywhere in the computational range, we usually use three interpolation functions, by fitting the subsidence result lists, to describe the vertical and horizontal (in x and y directions) subsidence.

During calculation, the determined six mining polygons are input into the code respectively to compute the subsidence induced by each polygon, so that the subsidence results at any demanded position caused by any polygon or the arbitrary combinations of the polygons (by using the superposition principle) can be worked out. Six calculation scenarios are listed as in Table 25.

In fact, the subsidence caused by each layer and the superposition of the two layers might be the most interesting and useful data for the building damage assessment. Therefore, three exhibition scenarios were adopted as shown in Table 25. The vertical and horizontal subsidence iso-contours caused by the layer gray (i.e. Polygon 1, 2, and 3), by the layer S2-S3 (i.e. Polygon 4, 5, and 6), and by the two layers together are plotted in Figure 60 – Figure 68, with the buildings of Joeuf city. The final maximum vertical subsidence value is 2.08 m, and other maximum and minimum subsidence values of these three exhibition scenarios are listed in Table 26. Of course, the subsidence results induced by each single polygon or any polygons' group can also be output as iso-contours diagrams or lists when necessary.

Table 25. The calculation and exhibition scenarios of the subsidence computation in Joeuf

Scenario	Involved polygons					
Calculation scenario	Polygon 1	Polygon 2	Polygon 3	Polygon 4	Polygon 5	Polygon 6
Exhibition scenario	Polygon 1, 2, and 3 (layer gray)			Polygon 4, 5, and 6 (layer S2-S3)		
	Polygon 1 – 6					

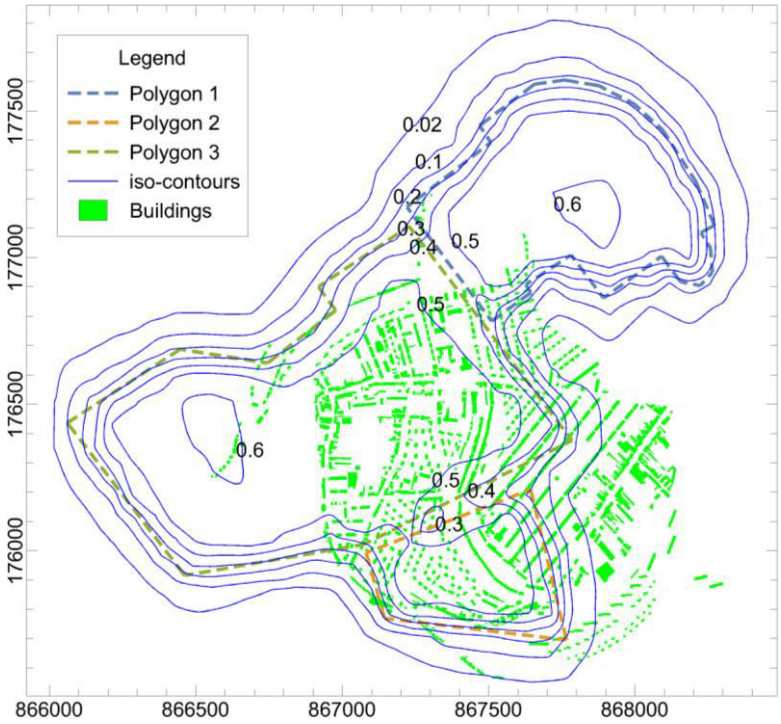

Figure 60. Vertical subsidence iso-contours caused by the excavation of the layer gray (i.e. Polygon 1 – Polygon 3)

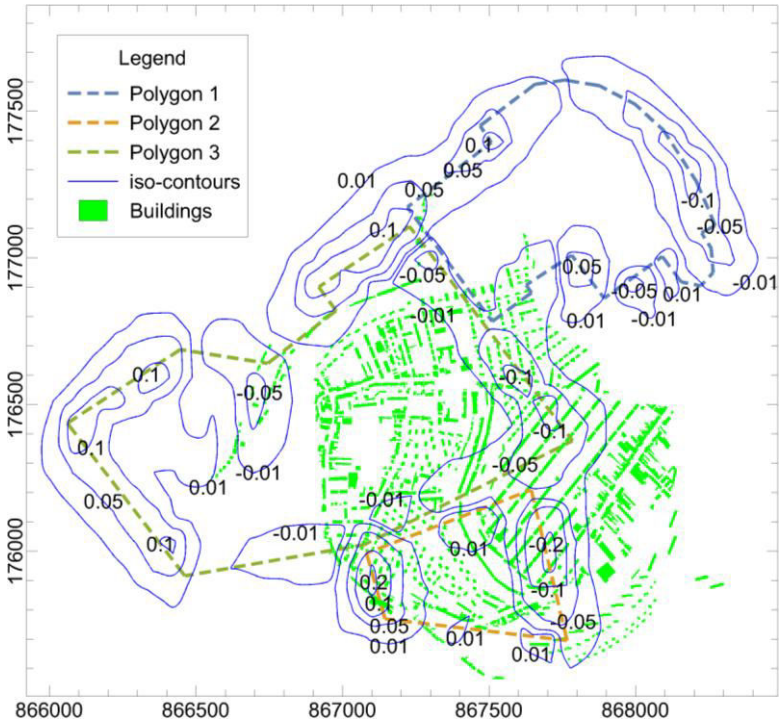

Figure 61. Horizontal displacement (in x direction) iso-contours caused by the excavation of the layer gray (i.e. Polygon 1 – Polygon 3)

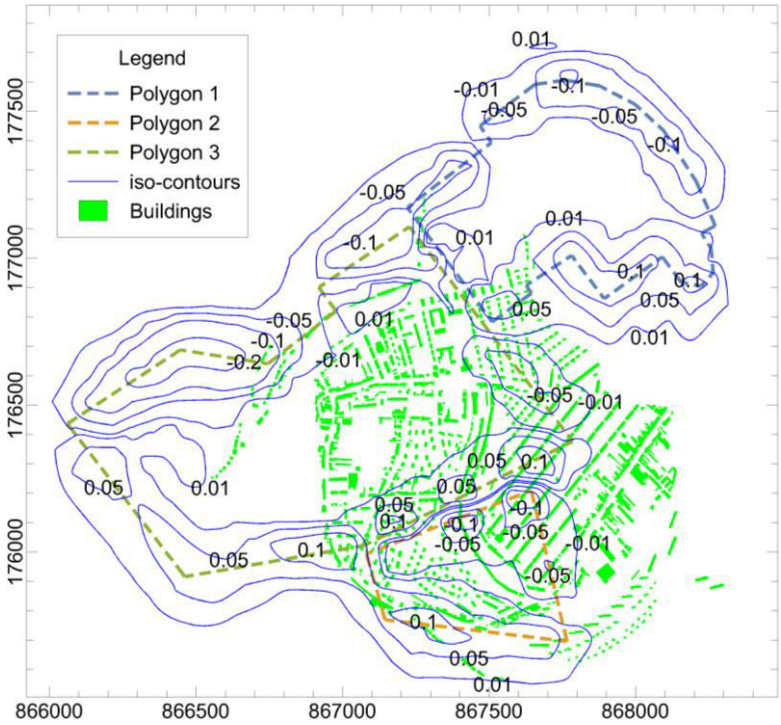

Figure 62. Horizontal displacement (in y direction) iso-contours caused by the excavation of the layer gray (i.e. Polygon 1 – Polygon 3)

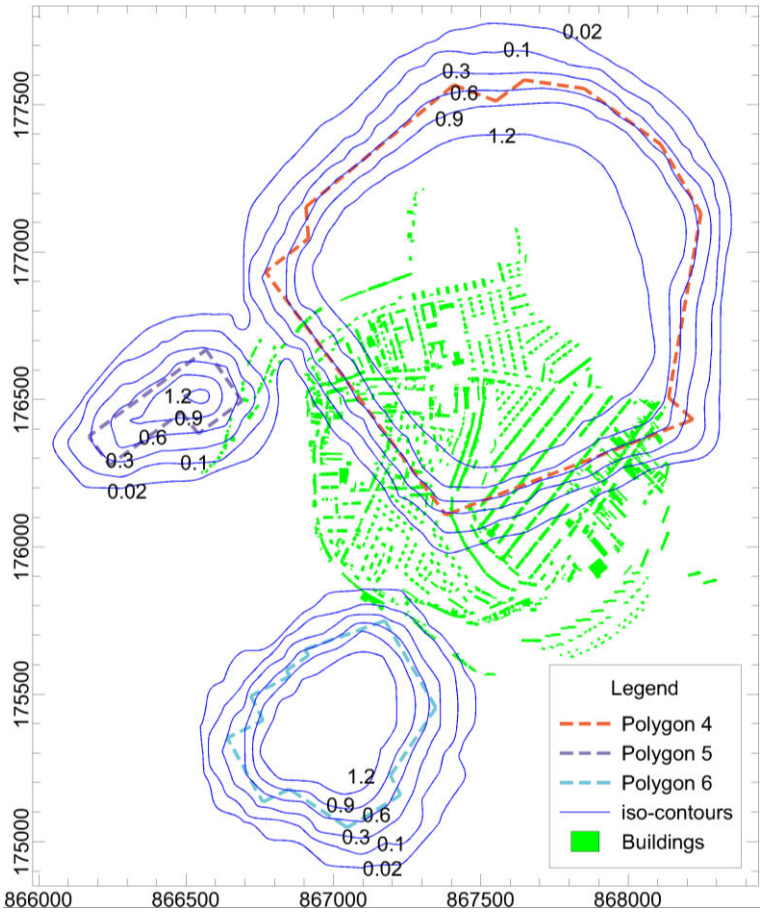

Figure 63. Vertical subsidence iso-contours caused by the excavation of the layer S2-S3 (i.e. Polygon 4 – Polygon 6)

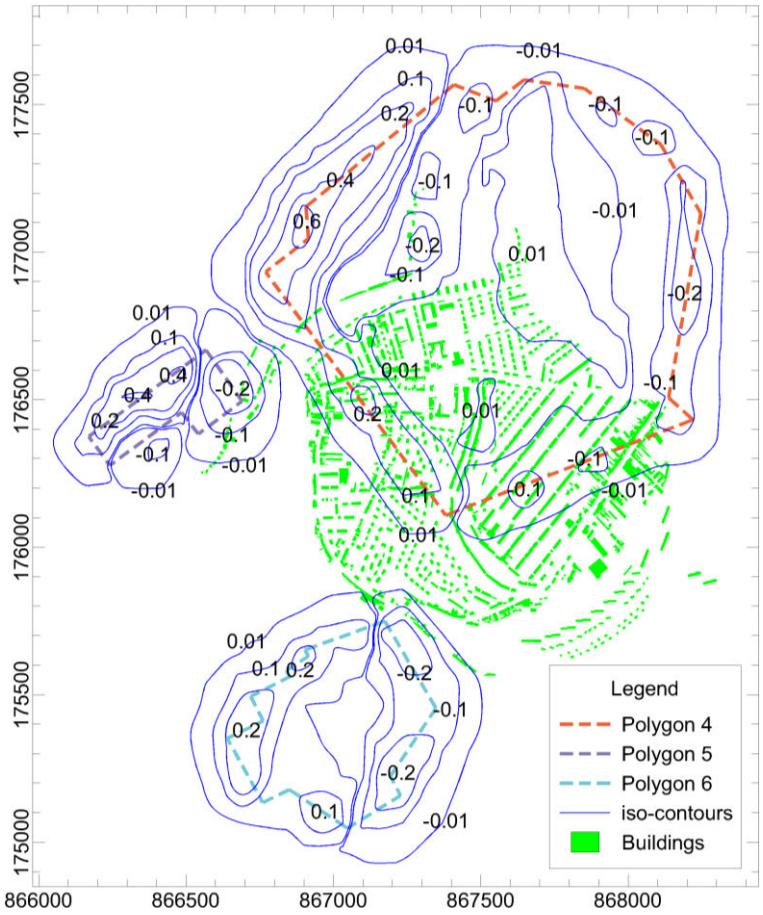

Figure 64. Horizontal displacement (in x direction) iso-contours caused by the excavation of the layer S2-S3 (i.e. Polygon 4 – Polygon 6)

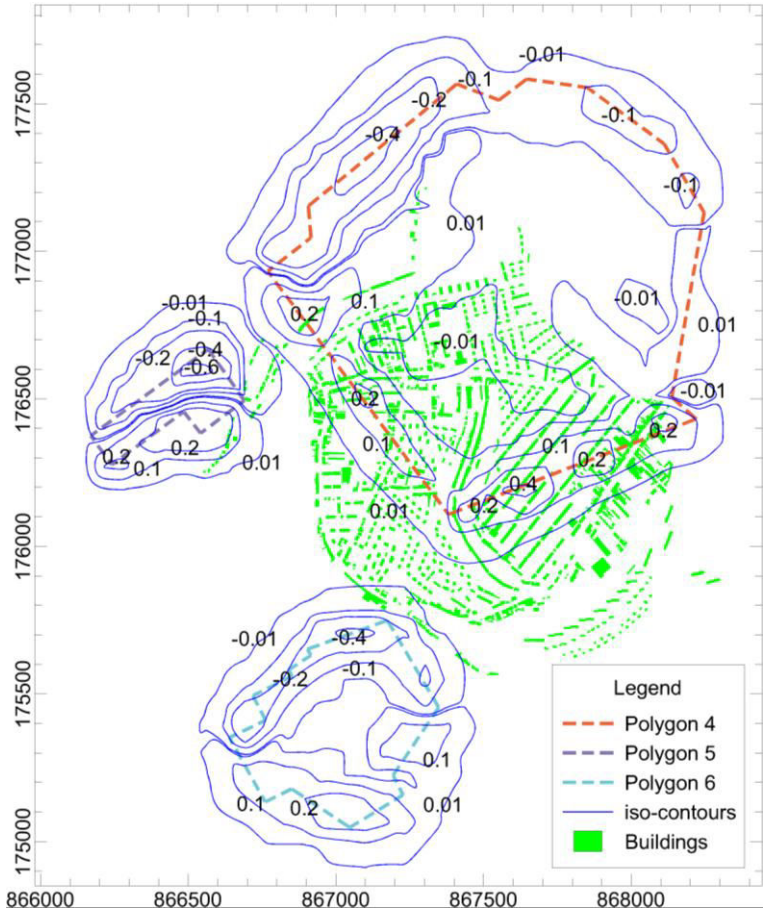

Figure 65. Horizontal displacement (in y direction) iso-contours caused by the excavation of the layer S2-S3 (i.e. Polygon 4 – Polygon 6)

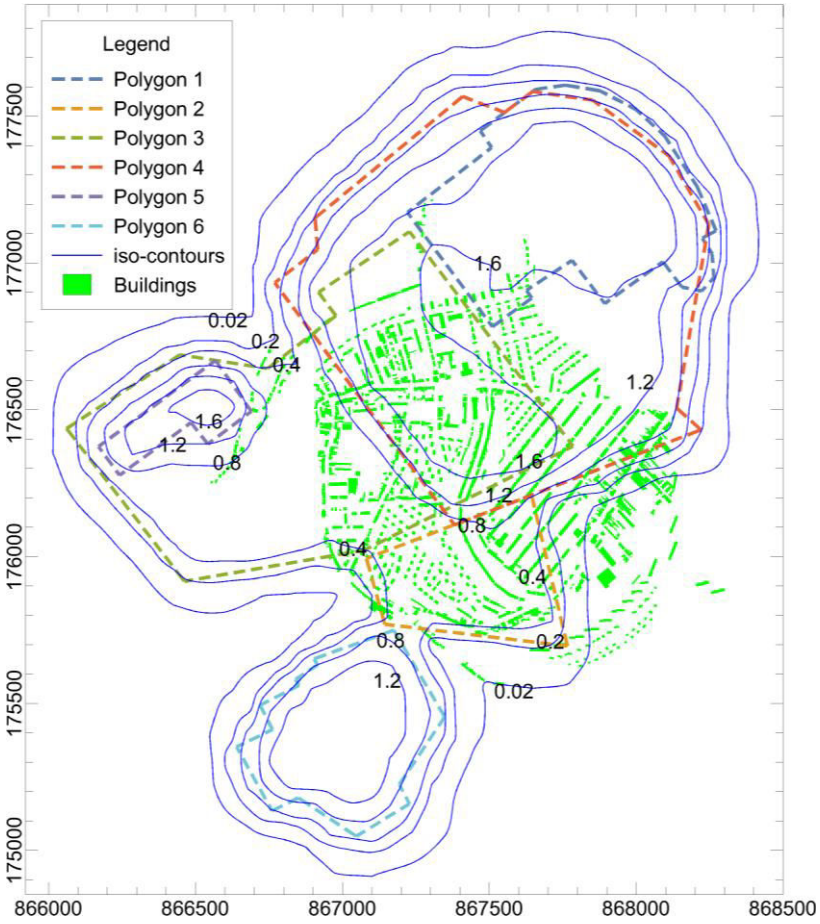

Figure 66. Vertical subsidence iso-contours caused by the excavation of the iron mines under Joeuf city (i.e. layer gray and layer S2-S3, Polygon 1 – Polygon 6)

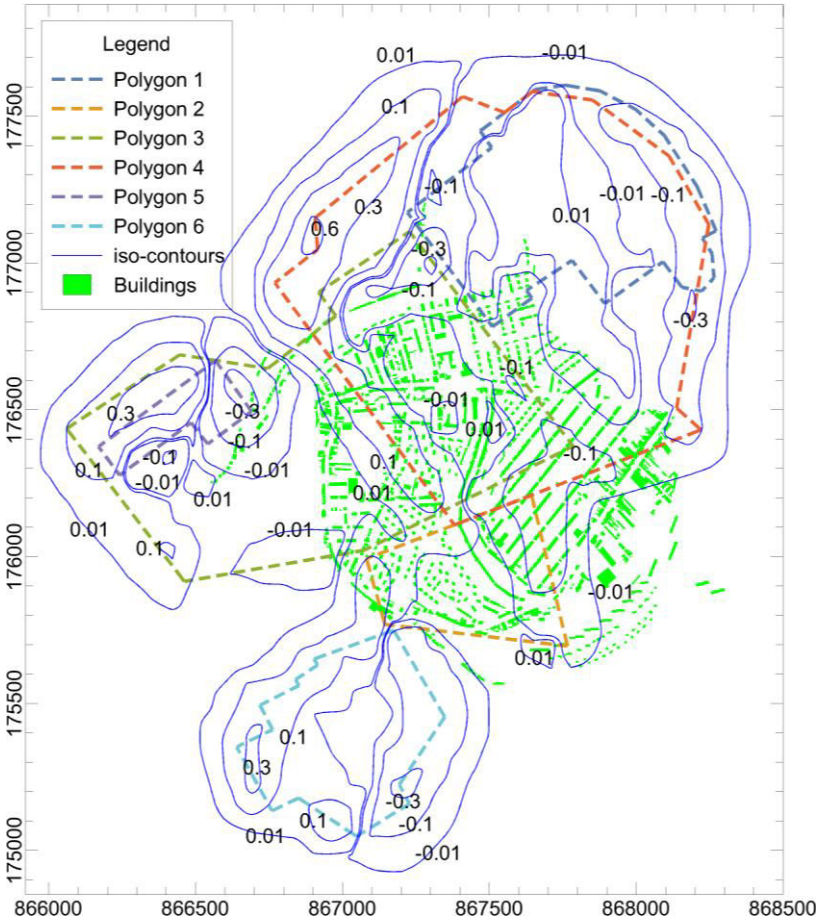

Figure 67. Horizontal displacement (in x direction) iso-contours caused by the excavation of the iron mines under Joeuf city (i.e. layer gray and layer S2-S3, Polygon 1 – Polygon 6)

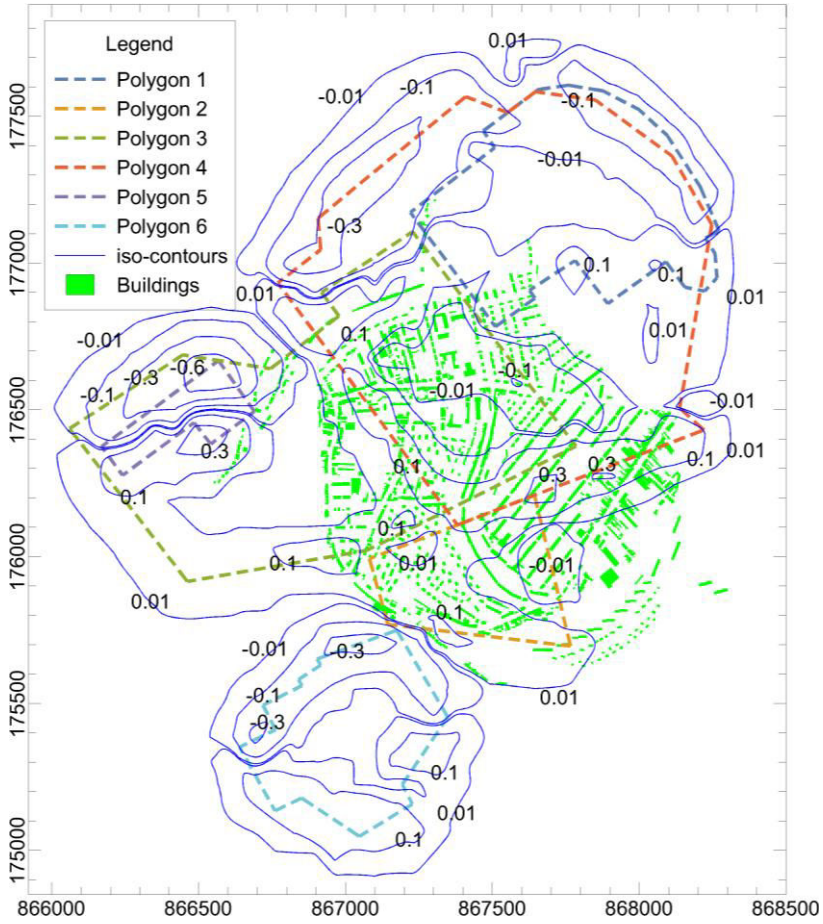

Figure 68. Horizontal displacement (in y direction) iso-contours caused by the excavation of the iron mines under Joeuf city (i.e. layer gray and layer S2-S3, Polygon 1 – Polygon 6)

Table 26. The maximum and minimum subsidence values caused by the excavation of the iron mines under Joeuf city

Subsidence	Layer gray		Layer S2-S3		Layer gray & S2-S3	
	Min	Max	Min	Max	Min	Max
Vertical subsidence (m)	0.63		1.46		2.08	
Horizontal displacement in x direction (m)	-0.29	0.27	-0.54	0.88	-0.54	0.88
Horizontal displacement in y direction (m)	-0.35	0.28	-0.81	0.60	-0.94	0.57

4.3 Definition of structural models for the buildings in Joeuf

The buildings in a city are not always the same, and the resistances to damage capacities of the buildings are also different, thus employing a uniform structural model to play the role of all the buildings in a city is not acceptable.

By our investigations about the buildings in Joeuf, several typical model shapes and element properties are defined in this section, then considering the initial loads on the beams, the complete structural models (without the subsidence influence; subsidence will be taken into

account in the next section) can be assembled to simulate the buildings in Joeuf.

4.3.1 Investigations about the buildings in Joeuf

In the ferriferous basin regions in Lorraine, most of the buildings are workers' housing estates with similar characteristics and are constructed of masonry (Simonet 2001). The appearances and qualities of the buildings in Joeuf city are much related to the construction time. A fieldwork did by our laboratory (Saeidi 2010), in collaboration with the association C.P.H.J. (Cercle pour la Promotion de l'Histoire de Joeuf), divides the city into 15 zones, which are used to identify the construction eras of the buildings, as shown in Figure 69 and Table 27. By this investigation about the city, approximately 80% of the buildings' construction eras are clear.

Another detailed field investigation (Saeidi 2010) has been carried out in order to clarify the buildings' representations in each zone. Both the geometrical characteristics (height and length) and the structural properties (nature of floor, system of reinforcement, etc.) of the buildings were recorded and are presented in Figure 70 and Table 27.

Some photographs of the most common buildings are also exhibited in Figure 71. More building pictures can be seen in Figure 100 in Annex 4.

For now, the zones 1, 3, 4, 5, 6, 7, 10, and 11 have been well visited, additional work is still needed in zones 2, 8, 9, 12, 13, 14, and 15.

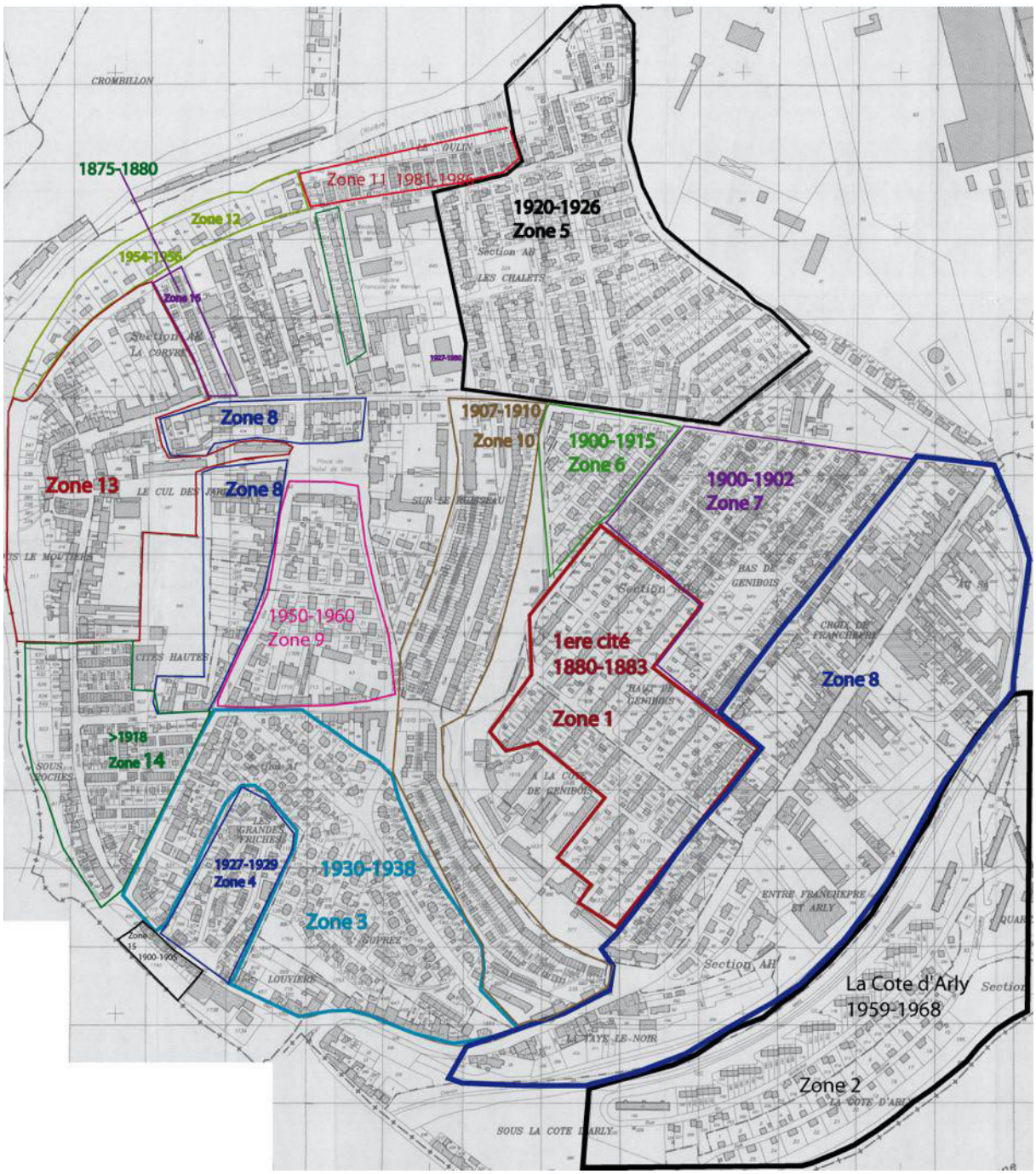

Figure 69. Map of Joeuf city with the zones according to the construction eras of the buildings

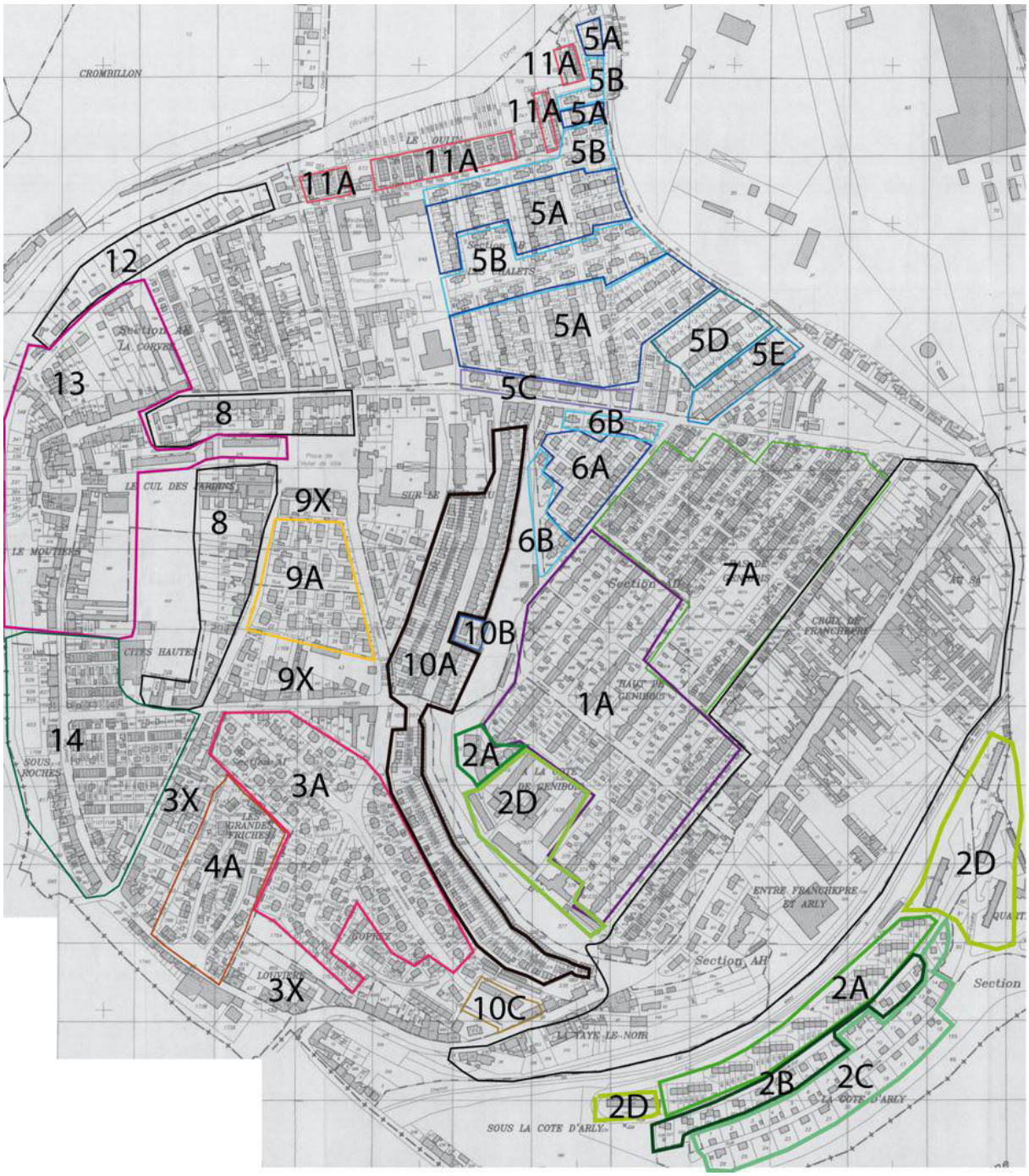

Figure 70. Map of Joeuf city with the zones according to the construction eras, the geometrical characteristics, and the structural properties of the buildings

Table 27. General characteristics of the buildings in Joeuf (the positions of the zones in this table can refer to Figure 69 and Figure 70)

Zone	Comments
Zone 1	Unreinforced masonry buildings built during 1880 to 1883 This zone is characterized by alternating principle buildings with two floors and Secondary buildings with one floor. Garages were built in front of some buildings.
Zone 2	Reinforced masonry (probably) buildings built during 1959 to 1968 In zone 2A, at least three houses are connected into on single building unit. Zone 2D consists of long reinforced concrete buildings.
Zone 3	Unreinforced masonry buildings built during 1930 to 1938, with a length of about 15 – 30 m
Zone 4	Unreinforced masonry buildings built during 1927 to 1929, with a length of about 15 – 30 m
Zone 5 and 6	Unreinforced masonry buildings built during 1920 to 1926 (zone 5) and 1900 to 1915 (zone 6), with a length of about 15 – 30 m and with two floors In these zones, unit buildings consist of two connected houses. The in-depth study in these zones allows us to distinguish them into several subzones (5A, 6A, 5B, 6B, and 5E) according to the differences in the shape and length of the buildings.
Zone 7	Unreinforced masonry buildings built during 1900 to 1902
Zone 8	The majority of the buildings are individual initiatives leading to extreme heterogeneity of form and structure.
Zone 9 and 12	The buildings in these zones are supposed to be reinforced masonry considering their construction eras (1950 – 1960 for zone 9 and 1954 – 1956 for zone 12)
Zone 10	Long building units with several connected houses of unreinforced masonry, built during 1907 to 1910
Zone 11	Reinforced masonry buildings built during 1981 to 1986, with a length of about 20 m
Zone 13	Historic center of the city consists of unreinforced masonry structures in many different forms.
Zones 14 and 15	The buildings in these zones are quite heterogeneous.

Unreinforced masonry building in zone 1

Reinforced masonry building in zone 2

Unreinforced masonry building in zone 3

Unreinforced masonry building in zone 10

Figure 71. Photographs of the most common buildings in Joeuf

In the following analyses, two simplifications are implemented:

(1) The small unimportant constructions (for example, garages, garden sheds, etc.) are not of interest and will be ignored.

(2) As illustrated in Figure 69, Figure 70, and Table 27, there are many connected houses in Joeuf. We will combine these connected houses together into single long buildings.

4.3.2 Standardization of structural models

Structural shape and elements' properties must be declared in the definition of a structural model. In this section, 5 sets (two models for each) of typical structural models are selected to simulate the shapes of the buildings. Then, the element properties (including the flexural rigidity EI and axial rigidity EA) and initial loads are defined. Assembling the typical models, the element properties, and the initial loads, the complete structural models (without the influence of mining subsidence at present) can be organized for representing the buildings in Joeuf.

In other cases, if detailed information (for example, the building design plans) can be obtained or more precise assessment is needed, the definition of the structural models can or should be more targeted.

4.3.2.1 Position of the structural models

As mentioned in chapter 3, we suggest to use two plane framed structural models to simulate one real 3D building. These two models should be set up in the spatial vertical sections through the two principal inertia axes of the polygon, which is used to represent the projective building outline in a horizontal plane; in addition, the two inertia axes are theoretically orthogonal and should both pass through the centroid point of the polygon, and their starting and ending points are the intersection points of the polygon and the inertia axes.

All the principal inertia axes of the buildings in Joeuf are plotted in Figure 72, using different colors to distinguish the longer ones (red) and the shorter ones (blue). The center part of the city, with the buildings of different orientations, different lengths, and different construction materials, is magnified and plotted also in Figure 72 for better display. As the magnified building No.621 in Figure 72, given the coordinates of the vertexes of the building, the starting and ending points of the two inertia axes are fixed and can be used to decide the positions of the structural models.

Figure 72. Selection of the axes where the structural models will be performed for each building: using the principal inertia axes of the building (passing through the centroid point of the building)

Furthermore, as in Figure 73, for an idealized cuboid building in 3D coordinate system (o-xyz), whose projection in a horizontal plane is a rectangle, the structural model in the spatial vertical section through the longer principal inertia axis is exactly the longitudinal section passing through the centroid of the real building, and the model in the vertical section through the shorter axis is the transverse section of the building. In Joeuf city, most of the projective polygons of the buildings are approximately rectangular. We think that the longitudinal and transverse sections of a building are quite suitable to represent the building's shape compared to other probable sections.

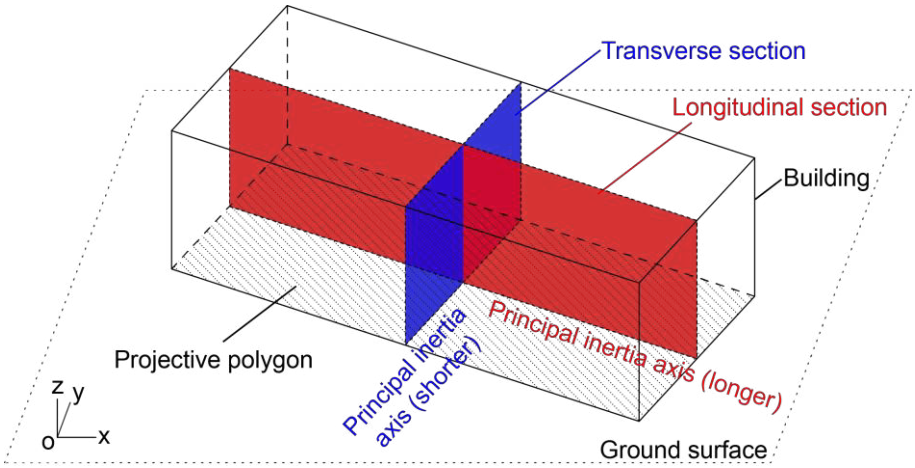

Figure 73. Two structural models are set up in the longitudinal and transverse sections of the building with an idealized cuboid shape

Other methods have also been considered in the preliminary work. For example, also considering two axes for one building, one is along the line from the subsidence center to the building centroid point, and the other is perpendicular to the former at the building centroid point, as in Figure 74. Their starting and ending points are the intersection points of the polygon and the axes. In Figure 74, we find a lot of axes are too short to provide the buildings' real shape, especially for the long buildings, and the axes more depend on the position of the subsidence center than the shapes of the buildings. Therefore, we rejected this method as not suitable for our further study.

Figure 74. Selection of the axes where the structural models will be performed for each building: using the axis from the building centroid point directing to the subsidence center and the axis perpendicular to the former at the building centroid (not suitable and rejected)

4.3.2.2 Typical structural models

As the amount of the buildings in Joeuf city is more than one thousand, it is a too heavy work to define the structural models for every building. Due to the fact that appearances of the buildings are not totally different from each other but are much related to the construction eras, and that the objective of this case study is the whole city but not a particular building (means that the precision is not necessarily high for each building), 5 sets of typical structural models were selected to simulate the shapes of the buildings.

4.3.2.2.1 Definition of the models

According to our investigations, the building appearances are much related to the

construction eras, i.e. the previously defined 15 zones in Joeuf city. By studying the shapes of the buildings in each zone and considering some simplifications, 5 sets of typical structural models can be selected to simulate the buildings in different zones. They are named TSM 1 to 5 as shown in Figure 75 to Figure 79, respectively. Each model set is composed of two typical plane framed structural models, including a longitudinal model and a transverse model (refer to Figure 75 to Figure 79), which are used to represent the building shapes in the longitudinal and transverse sections of the building (i.e. the vertical sections through the longer and the shorter principal inertia axes of the building' projective polygon), respectively.

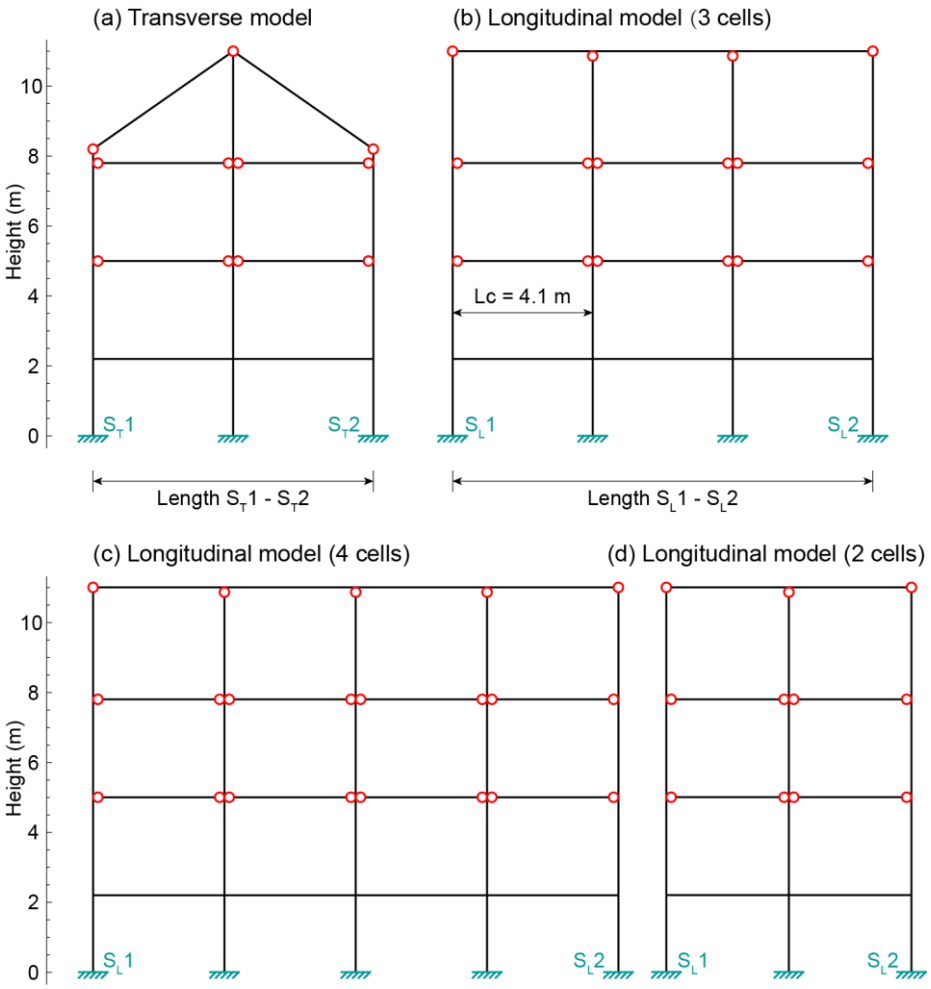

Figure 75. Typical structural model TSM 1: (a) transverse model; (b) longitudinal model with 3 cells on each floor (10.3 m < Length $S_L1 - S_L2$ < 14.3 m), standard length of each cell (Lc) is 4.1 m; (c) variant of longitudinal model with 4 cells (14.4 m < Length $S_L1 - S_L2$ < 18.4 m); (d) variant of longitudinal model with 2 cells (6.2 m < Length $S_L1 - S_L2$ < 10.2 m)

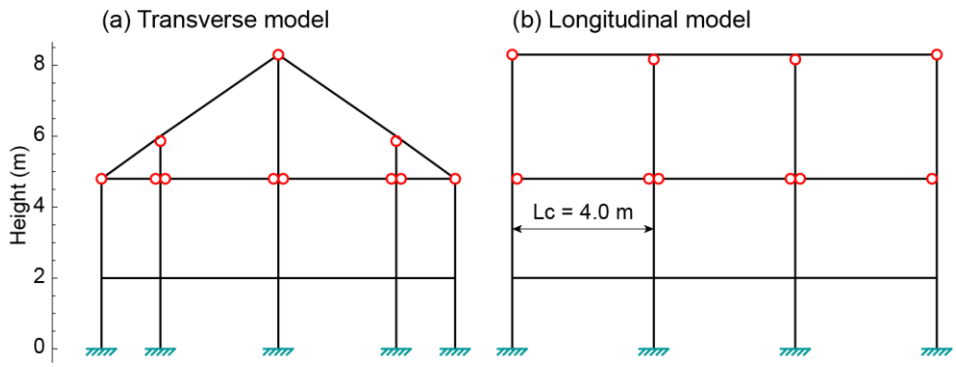

Figure 76. Typical structural model TSM 2: (a) transverse model; (b) longitudinal model (Lc = 4.0 m)

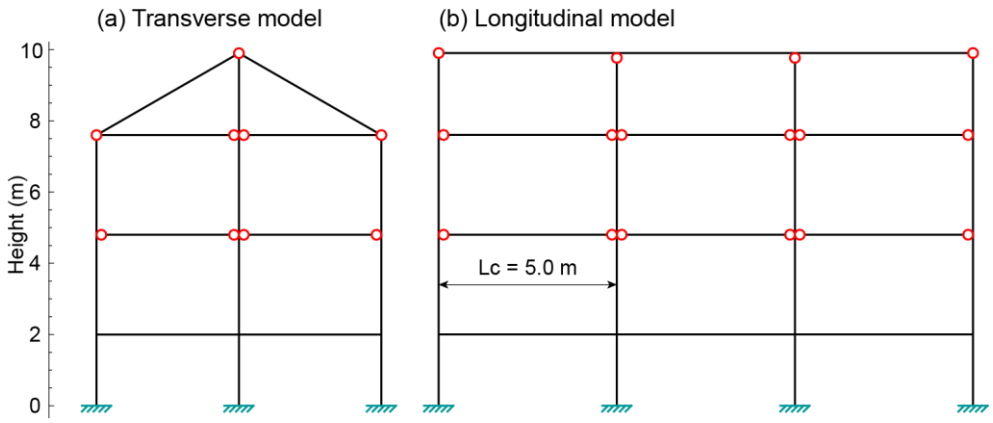

Figure 77. Typical structural model TSM 3: (a) transverse model; (b) longitudinal model (Lc = 5.0 m)

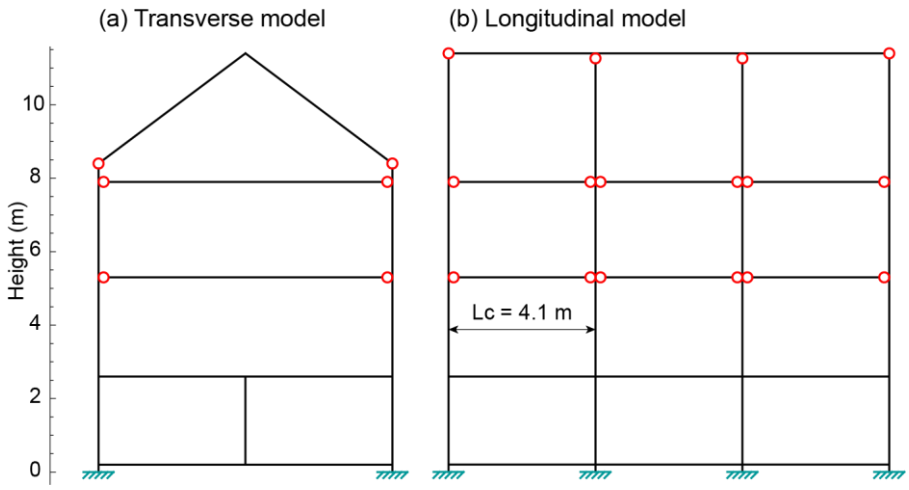

Figure 78. Typical structural model TSM 4: (a) transverse model; (b) longitudinal model (Lc = 4.1 m)

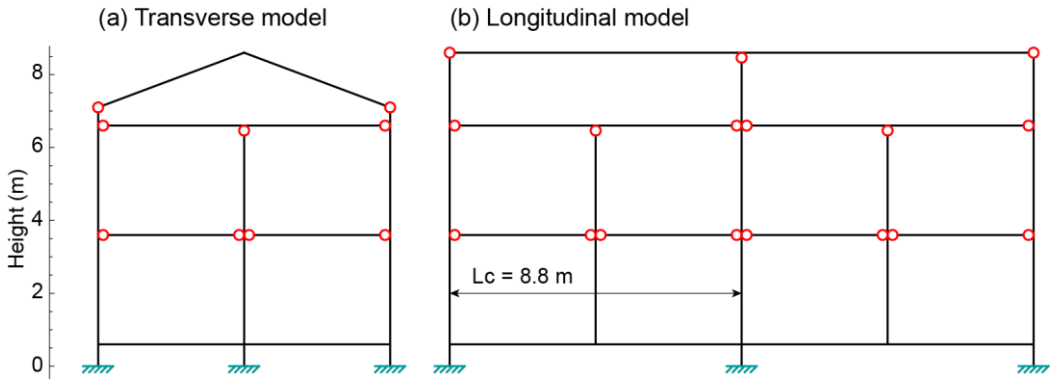

Figure 79. Typical structural model TSM 5: (a) transverse model; (b) longitudinal model (Lc = 8.8 m)

The dimensions of the typical structural models (TSM 1 to 5) are standardized as follows.

(1) The heights of the models

For each TSM model, the heights of its transverse and longitudinal models are given by investigations, as well as the heights of the floors of these two models. The heights can be described by the height-axes in Figure 75 to Figure 79.

(2) The lengths of the models

The lengths of the models are not fixed, they need to be adjusted according to the dimensions of their corresponding buildings.

Taking the model STM 1 in Figure 75 as example, the lengths between the starting support and the ending support of the transverse model (i.e. the length between S_T1 and S_T2 in Figure 75(a)) and the longitudinal model (i.e. the length between S_L1 and S_L2 in Figure 75(b)) are decided by the lengths of the shorter (the blue axes in Figure 72) and longer (the red axes in Figure 72) principal inertia axes of the corresponding building, respectively. Given the coordinates of the vertexes of each building's projective polygon, the lengths of the shorter and longer principal inertia axes, which equal the lengths of $S_T1 - S_T2$ and $S_L1 - S_L2$, can be achieved. Then, the shapes of the transverse and longitudinal models should be zoomed (only in length direction) to fit the lengths of $S_T1 - S_T2$ and $S_L1 - S_L2$.

Particularly, for a longitudinal model, which might be very long (depending on the length of the longer principal inertia axis of its corresponding building), only zooming the length of the model is sometimes unacceptable (the lengths of cells might be too long). Thus, standard lengths of the cells (Lc) of the longitudinal models are given in Figure 75 to Figure 79 (for STM 1 to 5, they are 4.1, 4.0, 5.0, 4.1, and 8.8 m, respectively), then the amount of the cells on each floor can be got as the ratio of the length $S_L1 - S_L2$ to Lc (round when the ratio is not an integer). For example, the standard cell length of TSM 1 is 4.1 m, when the length $S_L1 - S_L2$ is between 14.4 m (14.4/4.1=3.51) to 18.4 m (18.4/4.1=4.49), 4 cells should be considered on each floor, as shown in Figure 75(c); when the length $S_L1 - S_L2$ is between 6.2 m (6.2/4.1=1.51) to 10.2 m (10.2/4.1=2.49), 2 cells should be considered on each floor, as shown in Figure 75(d).

4.3.2.2.2 Distribution of the models

The links between our typical structural models and the afore-defined 15 zones can be summarized as in Table 28 and Figure 80. The buildings located out of these zones are assumed to have the similar shapes as the neighboring buildings, unless their shapes are clear by investigations.

For instance, model TSM 1 is used to represent the buildings in zones 1, 7, 8, 13, and 15 (as listed in Table 28), as shown with the green color in Figure 80 (besides the buildings out of the 15 defined zones).

Table 28. The relationship between typical structural models (TSM) and building zones

Model	Zone (construction era in brackets)
TSM 1	Zone 1 (1880 – 1883), zone 7 (1900 – 1902), zone 8 (unknown), zone 13 (very early), zone 15 (1875 – 1880)
TSM 2	Zone 3 (1930 – 1938), zone 4 (1927 – 1929)
TSM 3	Zone 5 (1920 – 1926), zone 6 (1900 – 1915), zone 14 (later than 1918)
TSM 4	Zone 10 (1907 – 1910)
TSM 5	Zone 2 (1959 – 1968), zone 9 (1950 – 1960), zone 11 (1981 – 1986), zone 12 (1954 – 1956)

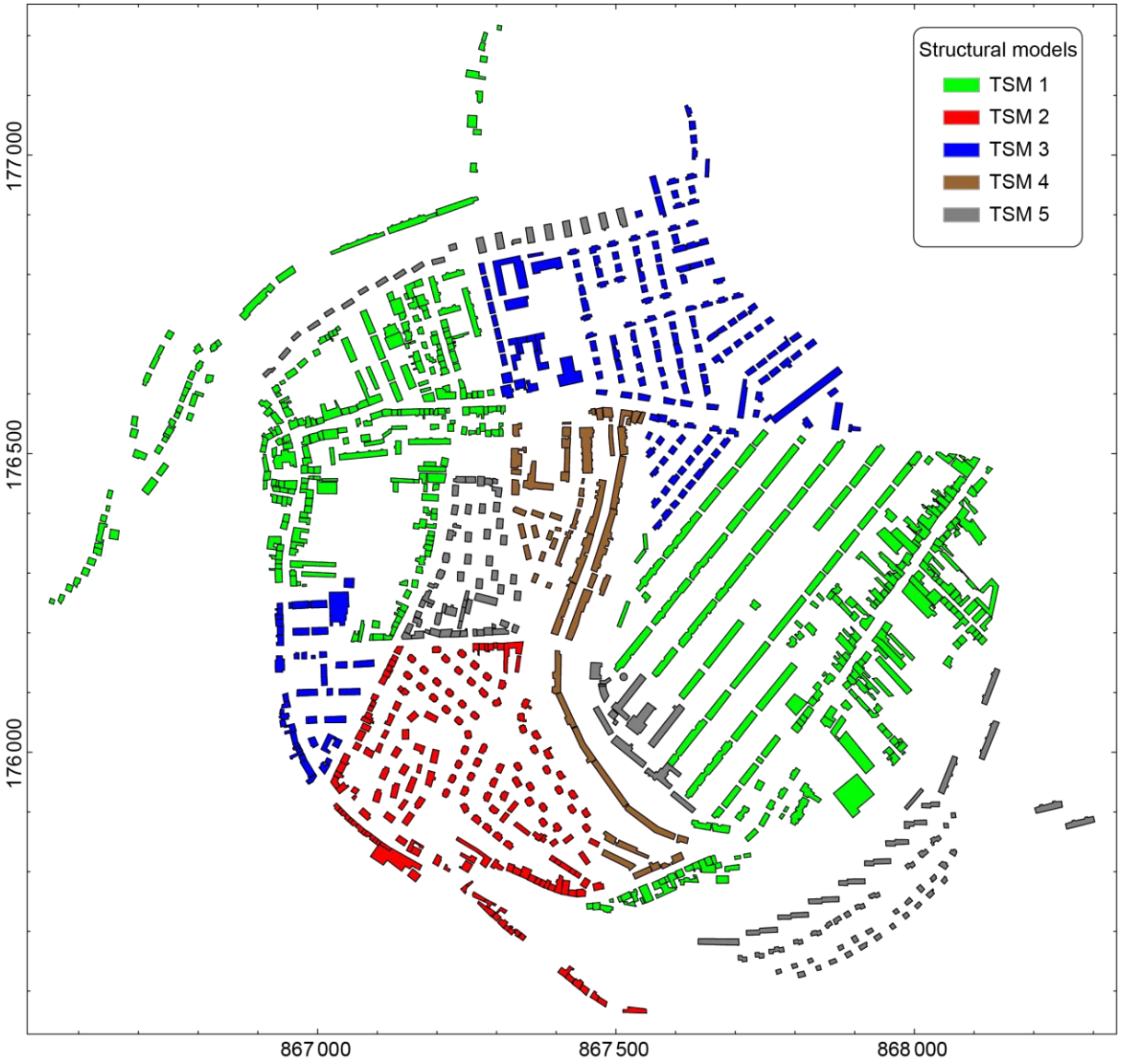

Figure 80. The distribution of the typical structural models (TSM) in Joeuf

4.3.2.3 Properties of the element

When constructing a structural model, except the shape, the flexural rigidity EI and axial rigidity EA are also necessary parameters for each element of the model, as aforementioned in chapter 3.

Decomposing the flexural rigidity and the axial rigidity, it can be found that the Young's modulus (E) is relative to the element material, while the moment of inertia (I) and the area (A) are the properties regarding only the cross section shape of the element. So, they will be introduced and standardized in this section, separately, as the preparation work for the future analyses.

4.3.2.3.1 Definition of building types

According to our investigations, the buildings with a similar shape (i.e. using the same TSM

model) might be different in their element properties (construction materials and cross section shapes). Therefore, on the basis of the investigations and considering the building typology in the mining subsidence area, which is firstly put forward by our laboratory (Saeidi *et al*. 2008, 2009, and 2010, refer to Annex 3), five types of buildings are defined in the city of Joeuf, as in Table 29 (detailed information in Annex 4), including two building types of unreinforced masonry buildings (MR1 and MR2), two types of reinforced masonry buildings (MC1 and MC2) and a type of reinforced concrete building (CF). The building types can be used to determine the element properties of the buildings, including the Young's modulus (E, depending on the used material), the inertia moment (I, depending on the cross section shape), and the area (A, depending on the cross section shape).

Table 29. Description of the 5 building types in Joeuf (the connected houses are combined)

Type name	Description
MR1	Unreinforced masonry buildings with high length (21 to 30 m), reinforced concrete floor (only for the 1st floor), and a little dismembered external shape with good symmetry of the bearing walls
MR2	Unreinforced masonry buildings with exceptional length (90 to 120 m), reinforced concrete floor (only for the 1st floor), and a little dismembered external shape with good symmetry of the bearing walls
MC1	Reinforced masonry buildings with medium length (11 to 20 m), reinforced concrete floor, and a little dismembered external shape with good symmetry of the bearing walls
MC2	Reinforced masonry buildings with high length (21 to 30 m), reinforced concrete floor, and a little dismembered external shape with good symmetry of the bearing walls
CF	Reinforced concrete buildings with exceptional length (60 to 90 m), reinforced concrete floor, and a simple external shape with good symmetry of the bearing walls
Remark: MR stands for unreinforced masonry building, MC stands for reinforced masonry building, and CF stands for reinforced concrete building.	

For defining the buildings' types in the zones that have not been well visited (zones 2, 8, 9, 12, 13, 14, and 15), hypotheses are made based on the construction eras, the sizes, and the photographs of the buildings. Furthermore, the buildings in zones 8, 13, 14, and 15 are quite heterogeneous and the majority of these buildings are supposed to be unreinforced masonry. For those areas, we assume the building types are MR1 or MR2 according to the building lengths (the full meanings of the types can be seen in Table 29).

Finally, all 1094 buildings (where connected houses are combined) in Joeuf are classified into 5 types, and they are plotted in Figure 81 by using different colors to distinguish their building types.

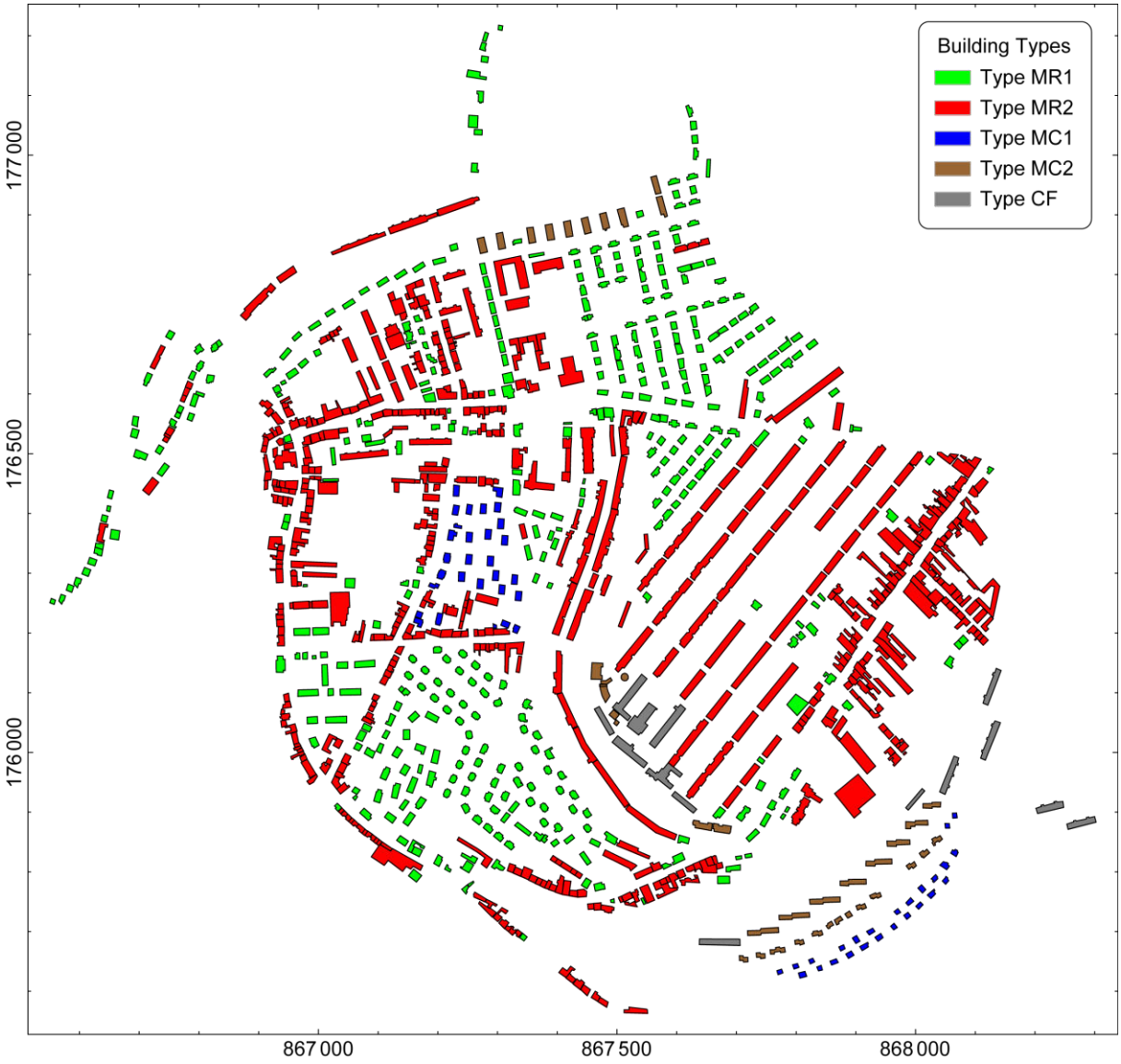

Figure 81. The distribution of the building types in Joeuf (about 25% of the types are hypothetic)

4.3.2.3.2 Elasticity moduli of the used materials

The modulus of elasticity (i.e. the Young's modulus E) is relative to the material used, and affects both the flexural rigidity and axial rigidity of an element. Therefore, we should indicate the Young's modulus for each material.

According to the in situ investigations implemented in Joeuf, there are four main materials used to construct the buildings, including timber, masonry, concrete, and steel.

In addition, two reinforced materials, including reinforced concrete and reinforced masonry, are taken into account. Reinforced concrete is always considered as an equivalent homogenous material for both the columns and beams of the structure; while reinforced masonry is considered as an equivalent homogenous material or composite material (simplified as a concrete slab with several I-shape steel beams at its bottom) for the

columns or beams, respectively, by using different young moduli.

On the basis of the investigated conditions of the buildings in Joeuf, in the meanwhile, referring to Wikipedia[1], and the studies of Bosiljkov *et al*. (2005), Felix (1999), Fiorelli *et al*. (2003), Fuente *et al*. (2010), Liu *et al*. (2008), and Zhao *et al*. (2010), the used young moduli of the single materials, equivalent homogenous materials, and composite material are gathered as in Table 30.

Table 30. The young moduli (E) for the materials

Material		Young module E (GPa)
Single material	Timber	11
	Masonry	5
	Concrete	25
	Steel	200
Equivalent homogeneous material	Reinforced masonry	10
	Reinforced concrete	25
Composite material	Reinforced masonry	25

4.3.2.3.3 Definition of typical cross sections and their properties

The moment of inertia (I) and the area (A) are the properties regarding only the cross section shape of the element itself.

From the investigations in Joeuf city, we found that the cross sections of the walls and floors of the buildings are various, and are normally depending on the building types that we already defined in Table 29. Standardization and simplification of the sections must be put forward before further analyses. According to the comprehensive consideration of the investigation work, two kinds of typical cross sections are defined for the vertical and horizontal beams of the structural models. The vertical beam is also called column here for better explanation.

(1) Rectangular cross section (Sr): for beam and column with single material or equivalent homogenous material

For columns, the rectangular cross section is always used; and this section type is also valid for the beams of the reinforced concrete (CF, as in Table 29) and unreinforced masonry (MR1 and MR2) buildings, except the beam simulating the first floor of the latter.

Referring to Figure 82, the neutral axis of the rectangular cross section is exactly its axis of symmetry, and the section area and moment of inertia can be easily calculated by Equation 47 and Equation 48, respectively.

[1] http://en.wikipedia.org/wiki/Young%27s_modulus

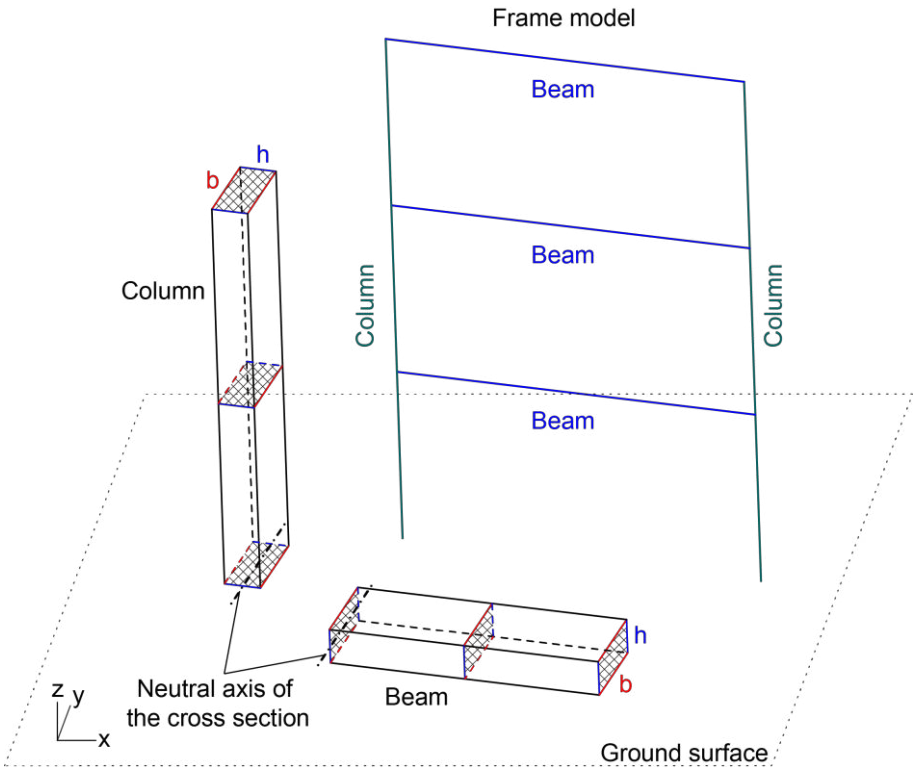

Figure 82. Typical rectangular cross sections of the column and beam of a plane frame model

$$A_r = bh \quad \text{Equation 47}$$

$$I_r = \frac{bh^3}{12} \quad \text{Equation 48}$$

Where A_r is the area of the rectangular cross section, I_r is the moment of inertia of the section, b is the length of the section side perpendicular to the structural plane, and h is the length of the section side parallel to the structural plane.

Use of Equation 48 should be under the hypothesis that no tensile crack occurs in the beam, which is questionable for masonry and concrete. This assumption is considered here since only a rough estimation of the stiffness is looking for. The exact calculation of the beam stiffness would require the exact value of reinforcement quantities and detailed calculation that are out of the scope of our investigation.

---- Sr for the columns

According to the investigation work, for the columns of the unreinforced masonry buildings (MR1 and MR2), h can be considered as 0.4 m; while for the reinforced masonry (MC1 and MC2) and reinforced concrete (CF) buildings, h is around 0.2 m. As we use the frame model to simulate the 3D buildings (the wall is simplified to a column), b is chosen to equal 1 m in order to normalize the frame structural model as an elementary slice of the real 3D building.

The young moduli (E) of the columns depend on the types of the buildings. For unreinforced masonry, reinforced masonry, and reinforced concrete buildings, 5 GPa, 10 GPa, and 25 GPa are considered, respectively.

---- Sr for the beams

The typical rectangular cross section of the beam, which is shown in Figure 83(b) and used for the reinforced concrete buildings (CF), has the same shape as its column section, i.e. with the size of 1 m $\times$ 0.2 m ($b \times h$), and use the equivalent homogenous material of reinforced concrete ($E =$ 25 GPa).

Furthermore, for the beams of the unreinforced masonry buildings (MR1 and MR2), except the one standing for first floor, the cross section, as shown in Figure 83(c), is more complex than the typical rectangular section. The cross section of such kind of beam between two columns (walls) of a structure is composed of a very thin slab, which will be neglected in the calculation of the area and inertia moment, and several equidistance ($d =$ 1.5 m) timber ($E =$ 11 GPa) sticks with the size of 0.15 m $\times$ 0.25 m ($a \times h$). So, we can consider the sub-section in the dashed frame of Figure 83(c) as a unit section, which can be used to reform the whole cross section by repetition. The area and inertia moment of the unit section can be calculated according to Equation 47 and Equation 48 (using a instead of b in this case), and then those properties of the whole section with the length of b can be expressed as in Equation 49 and Equation 50.

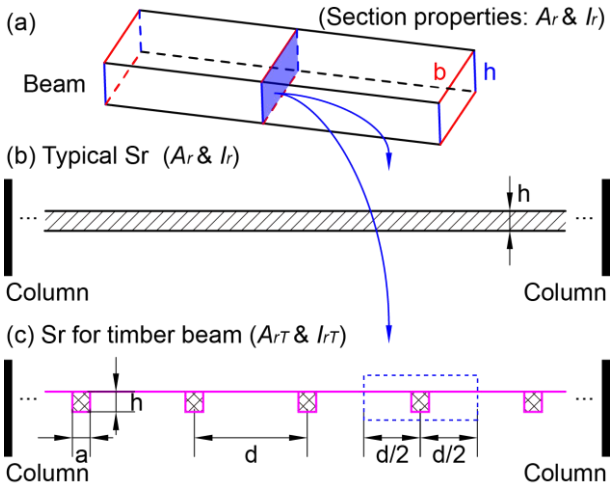

Figure 83. The rectangular cross section for a beam: (a) the cross section in a beam; (b) the typical rectangular cross section between two columns, used for the reinforce concrete buildings; (c) the special rectangular cross section between two columns, used for the unreinforced masonry buildings (ex. The 1st floor) with the marital of timber

$$A_{rT} = ah\frac{b}{d} \qquad \text{Equation 49}$$

$$I_{rT} = \frac{ah^3}{12}\frac{b}{d} \qquad \text{Equation 50}$$

Where A_{rT} and I_{rT} are the area and inertia moment of the timber rectangular cross section, as in Figure 83(c), with the length of b ($b =$ 1 m), d is the length of the unit cross

section ($d = 1.5$ m) or the distance between two timber sticks along the beam, a and h are the length and height of the timber stick ($a = 0.15$ m, $h = 0.25$ m).

(2) Composite cross section (Sc): for beam with composite material

The beam with composite cross section is employed for the floors of the reinforced masonry buildings (MC1 and MC2) and the first floor of the unreinforced masonry buildings (MR1 and MR2).

The cross section of such kind of beam between two columns (walls) is composed of a concrete slab and several equidistance I-shape steel beams as in Figure 84(b). Given that the whole cross section can be represented as the repetitions of the sub-section in the dashed frame, we can consider this sub-section as a unit section, and its diagram is magnified and plotted in Figure 84(c). Once the properties, including area and inertia moment, of the unit composite cross section are known, the properties of the cross section with the length of b can be expressed as in Equation 51 and Equation 52.

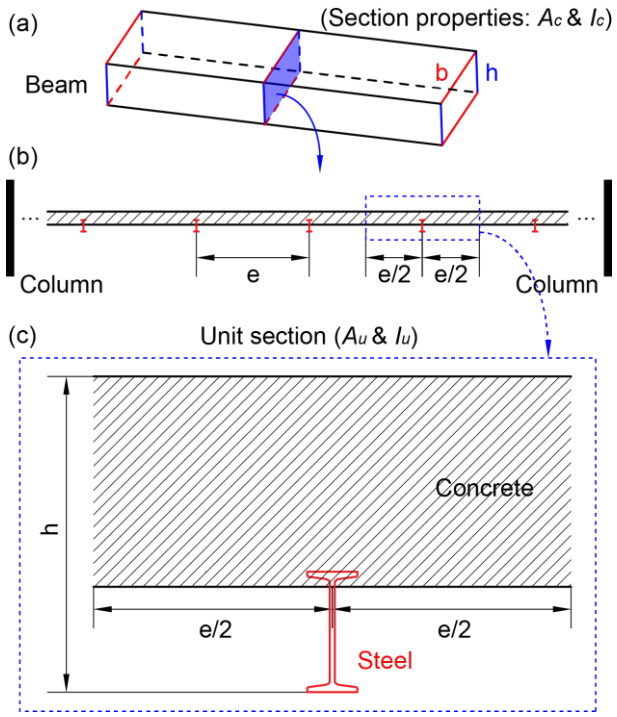

Figure 84. The composite cross section for a beam: (a) the cross section in a beam; (b) the composite cross section of the beam between two columns, used for the reinforced masonry buildings and the 1st floor of the unreinforced masonry buildings; (c) the chosen unit composite cross section

$$A_c = A_u \frac{b}{e} \qquad \text{Equation 51}$$

$$I_c = I_u \frac{b}{e} \qquad \text{Equation 52}$$

Where A_u and I_u are the area and inertia moment of the unit composite cross section as

in Figure 84(c), e is the length of the unit composite cross section (it equals 0.75 m according to the investigation) or the distance between two I-shape steel beams along the beam, A_c and I_c are the area and inertia moment of the composite cross section with the length of b ($b =$ 1 m).

Thus, the work turns to the section properties of the unit composite cross section, i.e. to determine A_u and I_u. In fact, the section shape in Figure 84(c) is still too complex to count its properties, as we don't know the length that the I-shape steel beams insert into the concrete slab. This section is then simplified to the shape as in Figure 85. The concrete part of the simplified section is a rectangle with the height of 0.1 m ($h_{c1} + h_{c2}$, by investigation); and the steel part is using a European standard section IPN 80, with the dimensions as shown in Figure 86, the area of 7.57×10^{-4} m^2 (A_{IPN80}) and the inertia moment of 77.8×10^{-8} m^4 (I_{IPN80}) refer to *Sections and Merchant Bars*, ArcelorMittal (the world's largest steel producer headquartered in Luxembourg). Considering elastic materials and that the cross-sections of the beam remain plane during bending, the position of the neutral axis z-z' of the unit composite cross section can be obtained when axial force equals zero (the neutral axis position is not fixed when axial force changes). As shown in Figure 85(c), the neutral axis z-z' is located in the concrete part, and is 5.98×10^{-2} m (h_{c2}) away from the interface between the concrete and the steel. Moreover, x1-x1' and x2-x2' in this figure are the gravity axes of the concrete part 1 (i.e. the concrete part in compression, above z-z') and the steel part of the section, and they are passing through the centroid point of each part, respectively.

The area and inertia moment of the unit composite cross section can be calculated by taking these properties of the concrete part and steel part into account, as in Equation 53 and Equation 54. The concrete part 2 (beneath z-z') will not be considered when calculating the inertia moment of the unit composite cross section, because it cannot provide any tensile stress when tensile strain occurs in it.

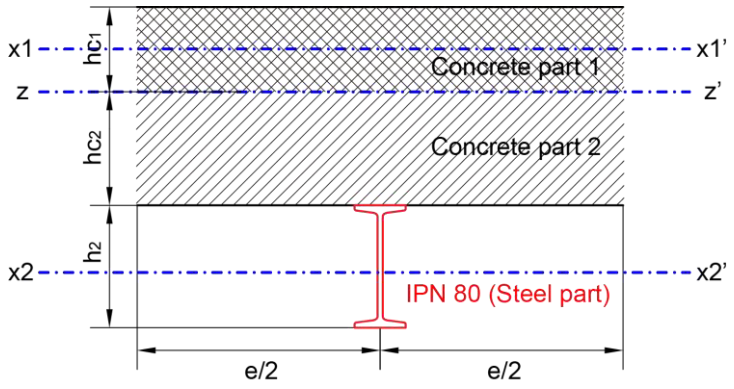

Figure 85. The simplified composite cross section for a beam and the neutral axes for the whole section (z-z'), for the concrete part 1 (x1-x1'), and for the steel part (x2-x2')

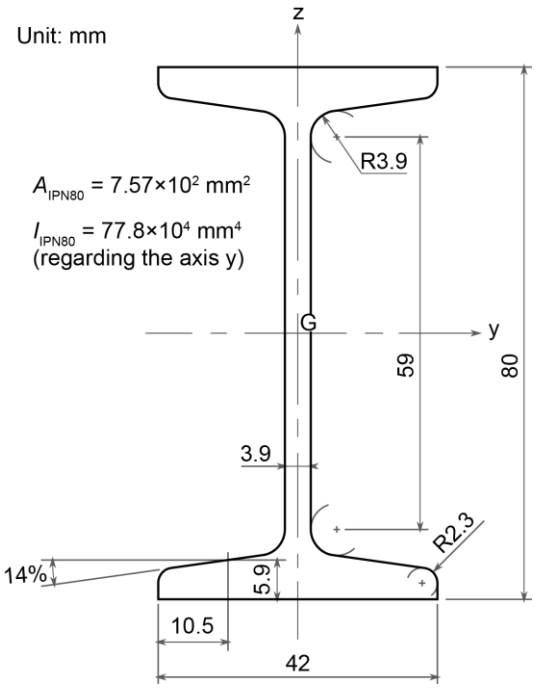

Figure 86. The European standard beam IPN 80

$$A_u = (A_{conc1} + A_{conc2}) + A_{st} \times \frac{E_{st}}{E_{conc}} \quad \text{Equation 53}$$

$$I_u = I_{conc1_z} + I_{st_z} \times \frac{E_{st}}{E_{conc}} \quad \text{Equation 54}$$

Where A_{conc1} and A_{conc2} are the areas of the concrete part 1 and part 2, A_{st} is the area of the steel part, I_{conc1_z} is the inertia moment of the concrete part 1 relative to the axis of z-z', I_{st_z} is the inertia moment of the steel part relative to the axis of z-z', E_{conc} and E_{st} are the young moduli of the concrete and steel (25 GPa and 200 GPa, respectively).

The concrete part 1 of the unit composite cross section is a rectangle, its area (A_{conc1}) and inertia moment relative to x1-x1' ($I_{conc1_{x1}}$) are easy to get by Equation 47 and Equation 48, respectively; A_{conc2} is also easy to calculate; and the area ($A_{st} = A_{IPN80} =$ 7.57×10^{-4} m^2) and inertia moment relative to x2-x2' ($I_{st_{x2}} = I_{IPN80} =$ 77.8×10^{-8} m^4) of the steel part are known values. Then, the inertia moments of the concrete part 1 and the steel part relative to their own neutral axes (i.e. $I_{conc1_{x1}}$ and $I_{st_{x2}}$) can be used to calculate their inertia moments relative to z-z' (i.e. I_{conc1_z} and I_{st_z}), which are demanded in Equation 54, by using parallel axis theorem.

In physics, the parallel axis theorem, also known as Huygens–Steiner theorem after Christiaan Huygens and Jakob Steiner, can be used to determine the mass moment of inertia of a rigid body or the area moment of inertia of a plane region (which is concerned in this section, also can be named second moment of area) about any axis, given the body's (or area's) moment of inertia about a parallel axis through the object's center of mass and the

perpendicular distance between the axes (Paul 1979, Kane and Levinson 2005, and Wikipedia[1]). Refer to Figure 87, the parallel axis theorem states as Equation 55 for a plane region D.

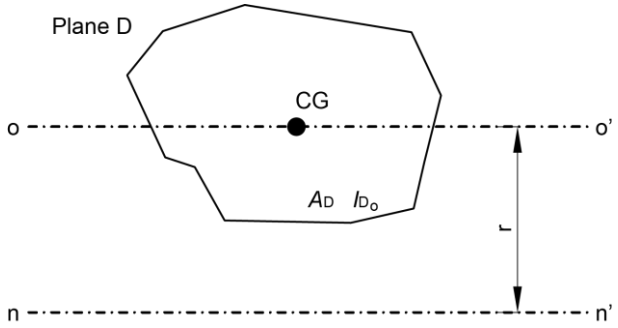

Figure 87. Parallel axis theorem

$$I_{D_n} = I_{D_o} + A_D r^2 \qquad \text{Equation 55}$$

Where I_{D_n} is the moment of inertia of the plane region D relative to the axis n-n', I_{D_o} is the moment of inertia of D with respect to its centroidal axis (the axis o-o'), A_D is the area of D, and r is the distance from the new axis n-n' to the centroid of D, refer to Figure 87. The centroid of D coincides with the center of gravity of a physical plate with the same shape that has uniform density.

Following the parallel axis theorem, the inertia moment of the concrete part 1 and steel part relative to the neutral axis of the whole section (i.e. z-z') can be calculated by Equation 56 and Equation 57, respectively.

$$I_{conc1_z} = I_{conc1_{x1}} + A_{conc1} \times \left(\frac{h_{c1}}{2}\right)^2 = \frac{e{h_{c1}}^3}{3} \qquad \text{Equation 56}$$

$$I_{st_z} = I_{st_{x2}} + A_{st} \times \left(\frac{h_2/2+h_{c2}}{2}\right)^2 = I_{IPN80} + A_{IPN80} \times \left(\frac{h_2/2+h_{c2}}{2}\right)^2 \qquad \text{Equation 57}$$

Where $I_{conc1_{x1}}$ is the inertia moment of the concrete part 1 relative to the axis of x1-x1', $I_{st_{x2}}$ is the inertia moment of the steel part relative to the axis of x2-x2', h_{c1} and h_2 are the heights of the concrete part 1 and the steel part, refer to Figure 85.

According to the investigations in Joeuf, we standardize the height of whole concrete part (i.e. $h_{c1} + h_{c2}$) as 0.1 m, and as aforementioned, h_{c2} equals 5.98×10^{-2} m, so h_{c1} equals 4.02×10^{-2} m; I_{IPN80}, A_{IPN80}, and h_2 are known values as 77.8×10^{-8} m^4, 7.57×10^{-4} m^2, and 0.08 m.

(3) Summary of the cross section properties

Summarizing the above mentioned two typical cross sections (the rectangular one Sr and the composite one Sc) and taking the investigated dimensions into account, we can calculate the

[1] http://en.wikipedia.org/wiki/Parallel_axis_theorem

areas and the moments of inertia of the cross sections for the columns and beams of different types of buildings, as shown in Table 31.

Table 31. The dimensions and properties of the cross sections for different buildings

Building type			Unreinforced masonry	Reinforced masonry	Reinforce concrete
			MR1 and MR2	MC1 and MC2	CF
Column	Section property	Type	Sr	Sr	Sr
		h (m)	0.40	0.20	0.20
		b (m)	1.00	1.00	1.00
		A (m^2)	0.40	0.20	0.20
		I (m^4)	5.33×10^{-3}	6.67×10^{-4}	6.67×10^{-4}
	E (Gpa)		5	10	25
Beam (1st floor)	Section property	Type	Sc	Sc	Sr
		h (m)	--	--	0.20
		h_{c1} (m)	4.02×10^{-2}	4.02×10^{-2}	--
		h_{c2} (m)	5.98×10^{-2}	5.98×10^{-2}	--
		h_2 (m)	0.08	0.08	--
		b (m)	1.00	1.00	1.00
		A (m^2)	0.108	0.108	0.20
		I (m^4)	5.01×10^{-5}	5.01×10^{-5}	6.67×10^{-4}
	E (Gpa)		25	25	25
Beam (ex. 1st floor)	Section property	Type	Sr (timber)	Sc	Sr
		h (m)	0.25	--	0.20
		h_{c1} (m)	--	4.02×10^{-2}	--
		h_{c2} (m)	--	5.98×10^{-2}	--
		h_2 (m)	--	0.08	--
		b (m)	1.00	1.00	1.00
		A (m^2)	0.025	0.108	0.20
		I (m^4)	1.30×10^{-4}	5.01×10^{-5}	6.67×10^{-4}
	E (Gpa)		11	25	25
Remark: for Sc, $e =$ 0.75 m; for Sr (timber), $d =$ 1.5 m, $a =$ 0.15 m; the meanings of the symbols can refer to Figure 82, Figure 83, and Figure 85.					

4.3.2.3.4 The element properties: flexural rigidity and axial rigidity

Considering the young moduli (E) of the materials (as in Table 30) and the moments of inertia (I) and areas (A) of the cross sections (as in Table 31), the properties of the elements, including the flexural rigidities EI and axial rigidities EA, which will be employed when constructing the structural models, can be achieved as in Table 32. For different building

types, the element properties are different.

Note that, the inertia moment values of the reinforced concrete columns and beams got by Equation 47 are over estimated (6.67×10^{-4} m^4 in Table 31), because its application supposes that no tensile crack appears in the section. Application of simple formulae from reinforced concrete design standards (BAEL), for a reinforcement of about 1% of steel, shows that a coefficient 2 can be considered. So, the flexural rigidities (EI) of the reinforced concrete (CF) elements in Table 32 should be calculated as 0.5 times the produce of the Young's modulus and inertia moment of reinforced concrete.

Table 32. The axial rigidities and flexural rigidities of the cross sections for different building types

Building type		Unreinforced masonry	Reinforced masonry	Reinforce concrete
		MR1 and MR2	MC1 and MC2	CF
Column	Section type	Sr	Sr	Sr
	EA (N)	2.00×10^{10}	2.00×10^{10}	5.00×10^{10}
	EI (N·m^2)	2.67×10^{8}	6.67×10^{7}	$0.5\times1.67\times10^{8}$
Beam (1st floor)	Section type	Sc	Sc	Sr
	EA (N)	2.70×10^{10}	2.70×10^{10}	5.00×10^{10}
	EI (N·m^2)	1.25×10^{7}	1.25×10^{7}	$0.5\times1.67\times10^{8}$
Beam (ex. 1st floor)	Section type	Sr (timber)	Sc	Sr
	EA (N)	2.75×10^{9}	2.70×10^{10}	5.00×10^{10}
	EI (N·m^2)	1.43×10^{7}	1.25×10^{7}	$0.5\times1.67\times10^{8}$

4.3.2.4 Initial loads on the beams

Two kinds of initial loads, including self weight and imposed force, are considered for the beams of the structural model, which are used to stand for the floors of the building. Usually, they can be defined as uniform distributed forces along the beams.

(1) Self weight

The self weights of the beams are decided by the densities of the materials and the shapes of the beams, that is, it is also depending on the building type. From Wikipedia[1], the densities of the materials are selected, as in Table 33. Then, for each beam, we can use its cross section, which has been introduced in the last section, and consider the length of 1 m (along the beam) to calculate the weight per meter, which is output in Table 33 and will be acted onto the beam as a distributed force. In calculation, the weight of the I-shape steel beams (IPN 80) of the composite section is a known value of 5.94 kg/m (*Sections and Merchant Bars*, ArcelorMittal).

(2) Imposed force

[1] http://en.wikipedia.org/wiki/Density

The imposed force includes the loads of furniture, people, etc. According to Eurocode 1 (EUROPEAN STANDARD EN 1991-1-1), the value of 2000 N/m is employed for all the beams.

Taking both the self weight and imposed force into account, the total initial loads acting on different types of beams (of different types of buildings) can be obtained and they are shown in Table 33.

Table 33. The initial loads on the beams

Building type		Unreinforced masonry	Reinforced masonry	Reinforce concrete
		MR1 and MR2	MC1 and MC2	CF
Beam (1st floor)	Section type	Sc	Sc	Sr
	Density (kg/m^3)	2400 (concrete part)	2400 (concrete part)	2500
	Self weight (N/m)	2479	2479	5000
	Imposed force (N/m)	2000	2000	2000
	Total load (N/m)	4479	4479	7000
Beam (ex. 1st floor)	Section type	Sr (timber)	Sc	Sr
	Density (kg/m^3)	700	2400 (concrete part)	2500
	Self weight (N/m)	175	2479	5000
	Imposed force (N/m)	2000	2000	2000
	Total load (N/m)	2175	4479	7000
Remark: the dimensions of the cross sections refer to last section; for roof, only self weight is considered; weight of IPN 80 is 5.94 kg/m.				

4.3.2.5 Organization of the structural model

Assembling the typical models, the element properties, and the initial loads, the complete structural models (without the influence of mining subsidence for now) can be organized for the buildings in Joeuf.

Taking the building No.621 (marked and magnified in Figure 72) as example, the process of organizing its structural models is described as follows.

(1) Shape definition

According to the distribution of structural models (as in Figure 80), the typical model STM 1 (as in Figure 75) is chosen. The lengths of S_T1 – S_T2 (transverse model) and S_L1 – S_L2 (longitudinal model) are 9.78 m and 20.94 m (decided by the coordinates of the vertexes of the building), respectively. Given the length of S_L1 – S_L2 and the standard cell length of the longitudinal model of STM 1 (Lc = 4.1 m), there are 5 cells on each floor.

(2) Element property definition

According to the distribution of building types (as in Figure 81), the building No.621 is an unreinforced masonry building (specifically, type MR1). Referring to Table 32, the flexural

rigidities (EI) of the columns, the beams standing for the 1st floor, and the beams standing for the other floors are 2.67×10^8 N·m^2, 1.25×10^7 N·m^2, and 1.43×10^7 N·m^2, respectively; the axial rigidities (EA) of those are 2.00×10^{10} N, 2.70×10^{10} N, and 2.75×10^9 N, respectively.

(3) Initial load definition

Because the building No.621 is an unreinforced masonry building, referring to Table 33, the initial loads on the beams standing for the 1st floor and the other floors are 4479 N/m and 2175 N/m, respectively. Specially, the initial load on the beams standing for the roof is 175 N/m.

Thus, the complete structural models of the building No.621 (before influenced by subsidence) are assembled and plotted as in Figure 88. The models of other buildings can be organized following the same process as the sample building.

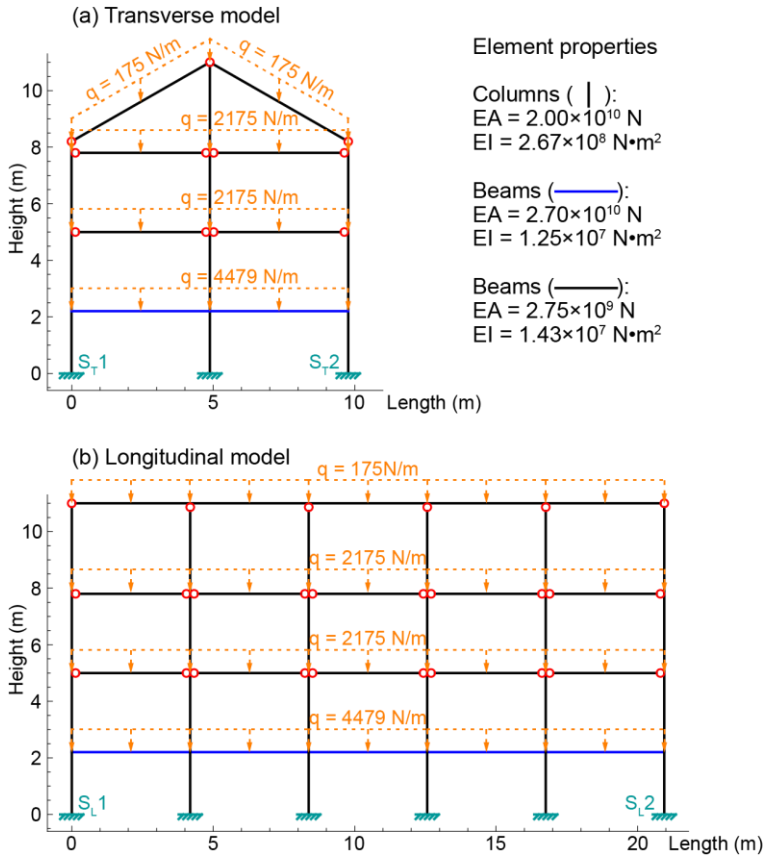

Figure 88. Organization of the structural models for a building (taking the building No.621 marked in Figure 72 as example), the structural shapes, element properties, and initial loads should be specified: (a) transverse model of the building No.621; (b) longitudinal model of the building No.621

4.4 Damage evaluation of the buildings in Joeuf due to mining subsidence

In this section, the computed mining subsidence (discussed in section 4.2) will be applied to

the defined structural models of the buildings (discussed in section 4.3) as support displacements to calculate the internal forces of the models. Then comparing the internal forces with damage criteria, the damage extent of the buildings in Joeuf can be assessed.

4.4.1 The structural models with the influence of subsidence

In mining areas, the buildings can be affected by subsidence. Because the ground surface is linked with the buildings' structural models through the supports, we decided to convert the computed subsidence data to the structural support displacements in order to simulate the mining influence on buildings. Then, using our developed code as described in chapter 3, the internal forces of the buildings can be determined.

(1) Subsidence at the supports

The mining subsidence caused by the excavation of the iron mines under Joeuf city has been determined, as in section 4.2. For now, the subsidence data are known values at any position of the ground surface in the computational range, which is much wider than the range of Joeuf city.

As mentioned in section 4.3, for each building, two structural models, including a longitudinal model and a transverse model with known shapes, element properties, and initial loads, are set up in the longitudinal and transverse sections (refer to Figure 89) of the building. Employing the positions (x and y coordinates) of the starting and ending supports of the structural models, which are provided by the principal inertia axes of the buildings, the subsidence acting at the supports can be extracted, including the vertical subsidence and the horizontal displacements in the x and y directions. Note that, the support positions and the subsidence factors are all defined in the 3D coordinate system o-xyz. We marked the subsidence at the starting and ending supports of the two models as in Figure 89(a), the subsidence at other probably existing supports (between the starting and ending supports in some cases) also can be extracted.

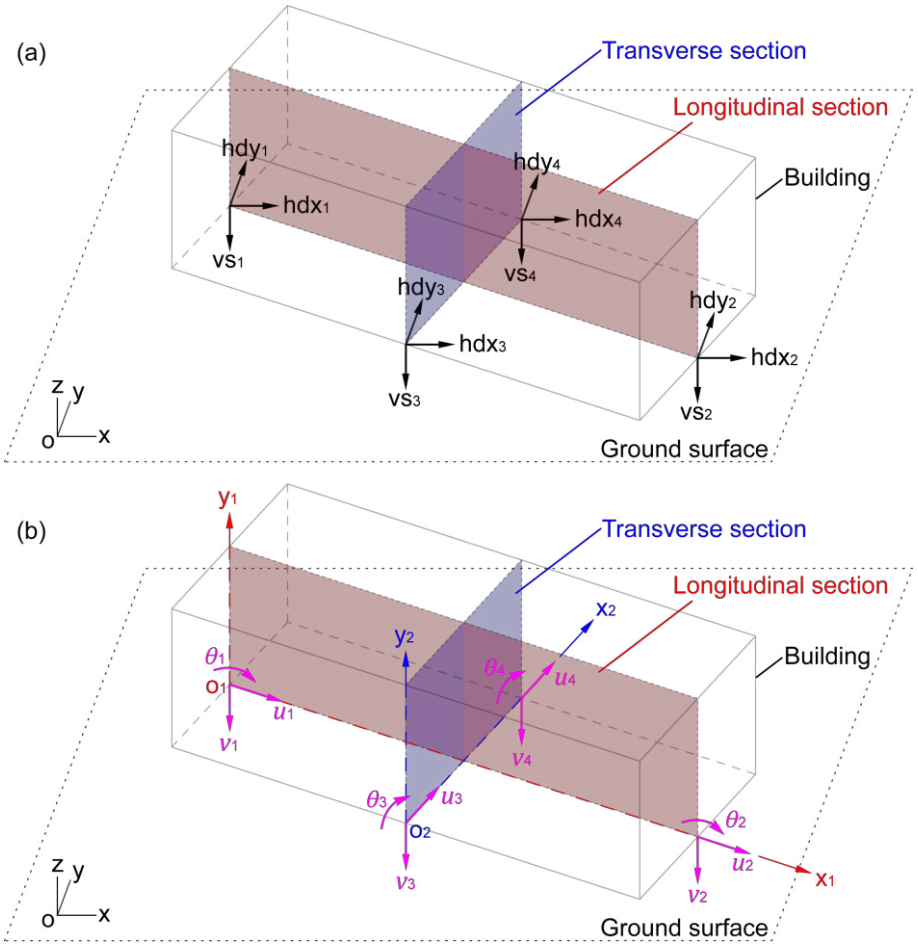

Figure 89. Transformation of the subsidence at the supports to the support displacements: (a) building with the subsidence at the supports; (b) building with the support displacements

(2) The support displacements

The support displacements must lie in the same planes of their corresponding structural models. They are defined in structural global coordinate systems, for example, the 2D coordinate systems o_1-x_1y_1 and o_2-x_2y_2 in Figure 89(b), which are used for the longitudinal or transverse structural models, respectively. The origin of a structural global coordinate system is located at the starting support of the model (with the minimum x coordinate), x axis is in the horizontal plane and from the origin to the ending support (with the maximum x coordinate), y axis is vertically up, the anticlockwise rotation is positive.

At each support, the support displacements (in 2D structural global coordinate system), which are composed of two translations (in the x and y directions) and a rotation, can be converted from the subsidence results (in 3D coordinate system o-xyz). As shown in Figure 89(b), the support translation in x direction (u) can be obtained by the geometrical relationship (in the horizontal plane o-xy) between the direction of the x axis of the structural global coordinate system and the two horizontal displacement vectors; the translation in y direction (v) always equals the vertical subsidence value, including the direction; and the rotation angle (θ) is the arc tangent value of the slope, which can be

computed as the first derivative of the vertical subsidence, considered as positive when anticlockwise. Since the subsidence data are known values at any position, the translations and rotation at each support can be obtained. Then, a list $\{u,\ v,\ \theta\}$ with the known values can be considered for the support subjected to subsidence.

In our method, only part of the horizontal displacements at one support is taken into account while constructing the structural model. For example, in Figure 89(a), there are two horizontal displacements (hdx1 and hdy1) acting at the left support of the model in the longitudinal section, and they can be decomposed into two orthogonal vectors, u_1 (in Figure 89(b)) and the other one, which is perpendicular to u_1 at o_1 in the horizontal plane (also is perpendicular to the plane o_1-x_1y_1 at o_1). But we do not take the latter into account, for the reason that the plane model cannot deal with the support displacement out of its plane, and the other model of this building (in the plane of o_2-x_2y_2) will mainly concern the translation in that direction.

4.4.2 The internal force criteria for building damage evaluation

By using our *Mathematica*™ code described in chapter 3, the building damage grades can be determined according to the internal forces over the structural models, which can be solved since the structural models with the subsidence influence are prepared, as well as their corresponding criteria. Shear force is less interesting in the frame structure models (Bao and Gong 2006, Leet et al. 2011). Thus, we consider the internal axial forces and bending moments to study the subsidence influence on the buildings. The criteria of the axial force and bending moment need to be specified.

(1) Allowed maximum axial force

The allowed maximum axial force acting on an element is defined as the strength of the material times the cross section area of the element. The positive (tensile) and negative (compressive) max values of the axial force should be considered respectively.

The compressive and tensile strengths of the masonry, concrete, and steel are listed as in Table 34. They come from the field investigation in Joeuf, and the strengths of masonry refer to Akira *et al*. (2014), Felix (1999), and Mosalam *et al*. (2009), the strengths of concrete refer to Akira *et al*. (2014), Nawy *et al*. (2008), and Lamond and Pielert (2006), and the strengths of steel refer to Akira *et al*. (2014), Nawy *et al*. (2008), and Philip *et al*. (1997).

Table 34. The compressive and tensile strengths of masonry, concrete, and steel

Material	Masonry	Concrete	Steel
Compressive strength (MPa)	15	30	--
Tensile strength (MPa)	1.5	3	200

As mentioned, the materials and cross sections of the elements (classified into 3 kinds, including beams standing for the first floors, beams standing for the other floors, and columns) of the unreinforced masonry, reinforced masonry, and reinforced concrete

buildings are different and known. Therefore, the allowed maximum axial forces are specified for different elements of different buildings as in Table 35. Specially, for the timber beams, we found in Joeuf that they are not really well fixed to the columns and can slightly move along the beam direction, so the axial forces will not be concerned in them, and their allowed maximum values are meaningless and not provided in Table 35.

Table 35. The allowed maximum compressive and tensile forces for different elements of different building types

Building type		Unreinforced masonry	Reinforced masonry	Reinforced concrete
		MR1 and MR2	MC1 and MC2	CF
Column	Type	Sr	Sr	Sr
	Compressive strength (MPa)	15	15	30
	Tensile strength (MPa)	1.5	1.5	3
	A (m^2)	0.40	0.20	0.20
	Fcmax (10^6 N)	6	3	6
	Ftmax (10^6 N)	0.6	0.3	0.6
Beam (1st floor)	Type	Sc	Sc	Sr
	Compressive strength (MPa)	30	30	30
	Tensile strength (MPa)	200	200	200
	A (m^2)	0.108	0.108	0.20
	Fcmax (10^6 N)	3.24	3.24	6
	Ftmax (10^6 N)	21.6	21.6	40
Beam (ex. 1st floor)	Type	Sr (timber)	Sc	Sr
	Compressive strength (MPa)	--	30	30
	Tensile strength (MPa)	--	200	200
	A (m^2)	0.025	0.108	0.20
	Fcmax (10^6 N)	--	3.24	6
	Ftmax (10^6 N)	--	21.6	40
Remark: Fcmax means the allowed maximum compressive force; Ftmax means the allowed maximum tensile force in an element				

(2) Allowed maximum bending moment

The computation of the allowed maximum bending moment is more complicated than that of axial force. In this research, we introduce an easier equivalent way to estimate it.

In one building, for a kind of structural element (columns, beams standing for the first floor, or beams standing for other floors), the maximum bending moment computed with only initial loads (i.e. without the support displacements due to subsidence) is multiplied by a safety factor to assess an equivalent allowed maximum bending moment. In other words,

allowed maximum bending moment = computed maximum bending moment (without subsidence) × safety factor. Therefore, the allowed maximum bending moments are different from a building to another as well as from one kind of element to another within the same building.

A safety factor of 2.0 (Burr and Cheatham 1995, and Wikipedia[1]), which is usually used for buildings in practice, is taken into account.

(3) The evaluation criteria

The criteria provided here are used to distinguish the damage grades according to the calculated internal forces. They may be not absolutely accurate and can be adjusted by research achievements or in situ data.

As illustrated in Table 36 (valid for both axial force and bending moment), the elements with the internal forces between 0.8 to 1.2 times the allowed maximum internal forces are considered as in a critical state between safe and dangerous. With lower forces, the elements are considered as safe; while with greater forces, they are supposed to in danger (of rupture). If the internal forces are 2 times higher than the critical values, we suppose the elements subjected to these internal forces are in high risk. The highest grade of all the elements in a structure will be recorded as the damage grade of the structure.

Axial force and bending moment can be used separately or together to assess the damage extent. For a building, when taking both of them into account and the damage extents got by them two are different, the highest grade should be considered for the building.

Table 36. The criteria of building damage evaluation depending on the allowed maximum internal forces (including axial force and bending moment)

Grade	Value range	State
1	< 0.8 × Fmax	Safe
2	0.8 × Fmax – 1.2 × Fmax	Critical state
3	1.2 × Fmax – 2.4 × Fmax	Probably risk
4	> 2.4 × Fmax	High risk
Remark: Fmax means the allowed maximum internal force (in a structure, it is not the same for different kinds of elements)		

4.4.3 Damage evaluation results in Joeuf

(1) Evaluation of building damage caused by the collapse of both the layer gray and S2-S3

Introducing the subsidence caused by the collapse of both the layer gray and layer S2-S3 (all the six mining polygons are collapsed, refer to Table 25, and the vertical and horizontal subsidence contours are plotted in Figure 66 to Figure 68) into the structural models as

[1] http://en.wikipedia.org/wiki/Factor_of_safety

support displacements, the internal forces over the structures can be calculated. Then comparing the computed internal forces to the defined damage grade criteria, the damage evaluation results can be assessed, as shown in Figure 90 and Figure 91, which are dependent on axial forces and bending moments, respectively. According to these two figures, the damage due to the bending moments looks more serious than that caused by axial forces. The statistics in Table 37 and the comparison in Figure 93, both regarding the building's proportion in each damage grade, also show that the number of buildings in damage grade 4 caused by bending moments are about twice of those caused by axial forces, and the safe buildings got by bending moments are about 2/3 of those got by axial forces.

Taking both the axial forces and the bending moments into account (for a building, the higher damage grade got by the axial forces or bending moments is chosen), the final damage evaluation result is shown in Figure 92. Finally, 34.74% of the buildings in Joeuf are almost certainly safe and 37.11% of the buildings are in high risk situation. Non-strictly speaking, the high risk buildings are mainly distributed in the areas where the subsidence contours are dense.

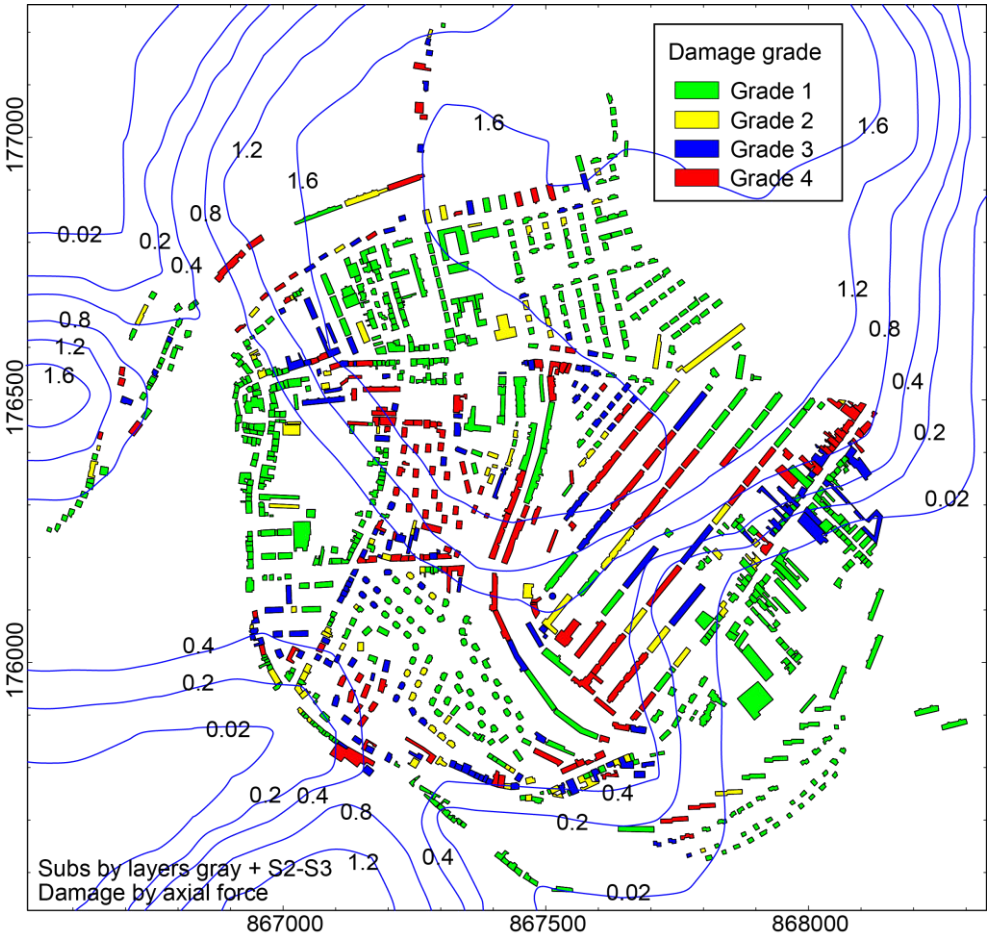

Figure 90. Evaluation of the building damage caused by mining subsidence due to the collapse of both the layer gray and layer S2-S3 (the vertical subsidence contours are plotted in the figure with the unit of meter) according to the axial forces in the buildings

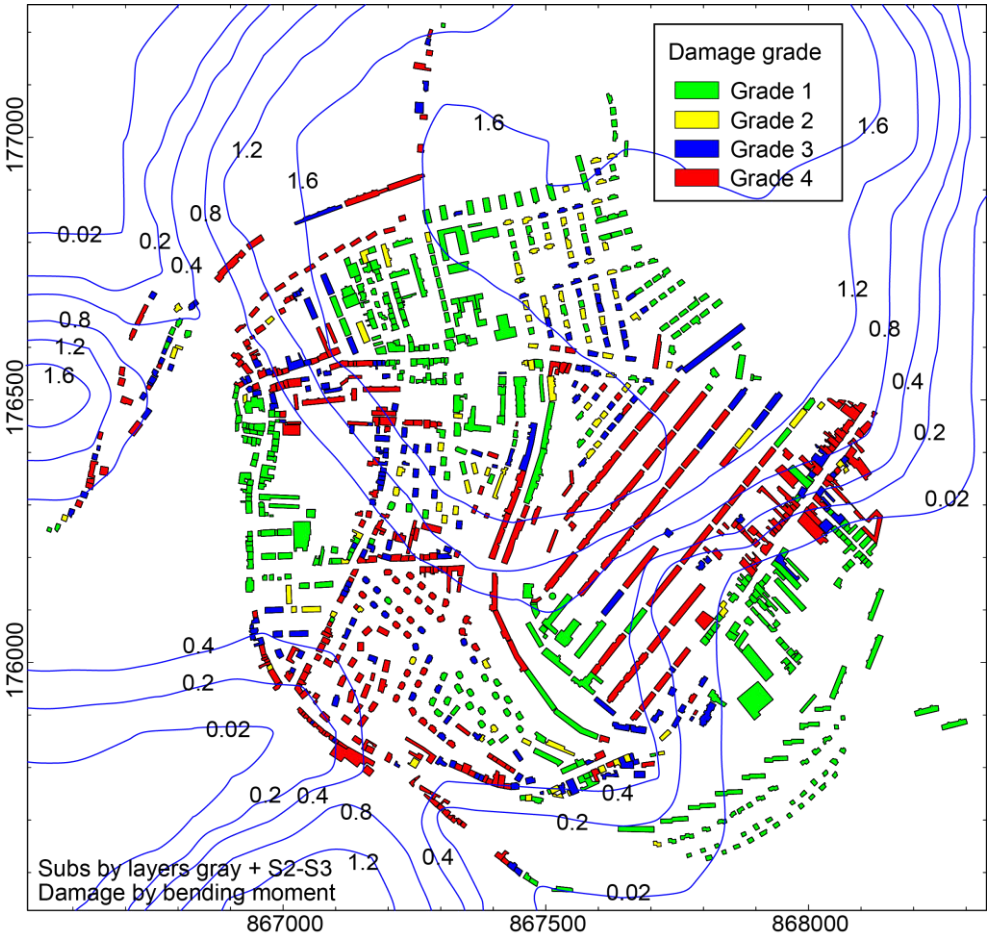

Figure 91. Evaluation of the building damage caused by mining subsidence due to the collapse of both the layer gray and layer S2-S3 (the vertical subsidence contours are plotted in the figure with the unit of meter) according to the bending moments in the buildings

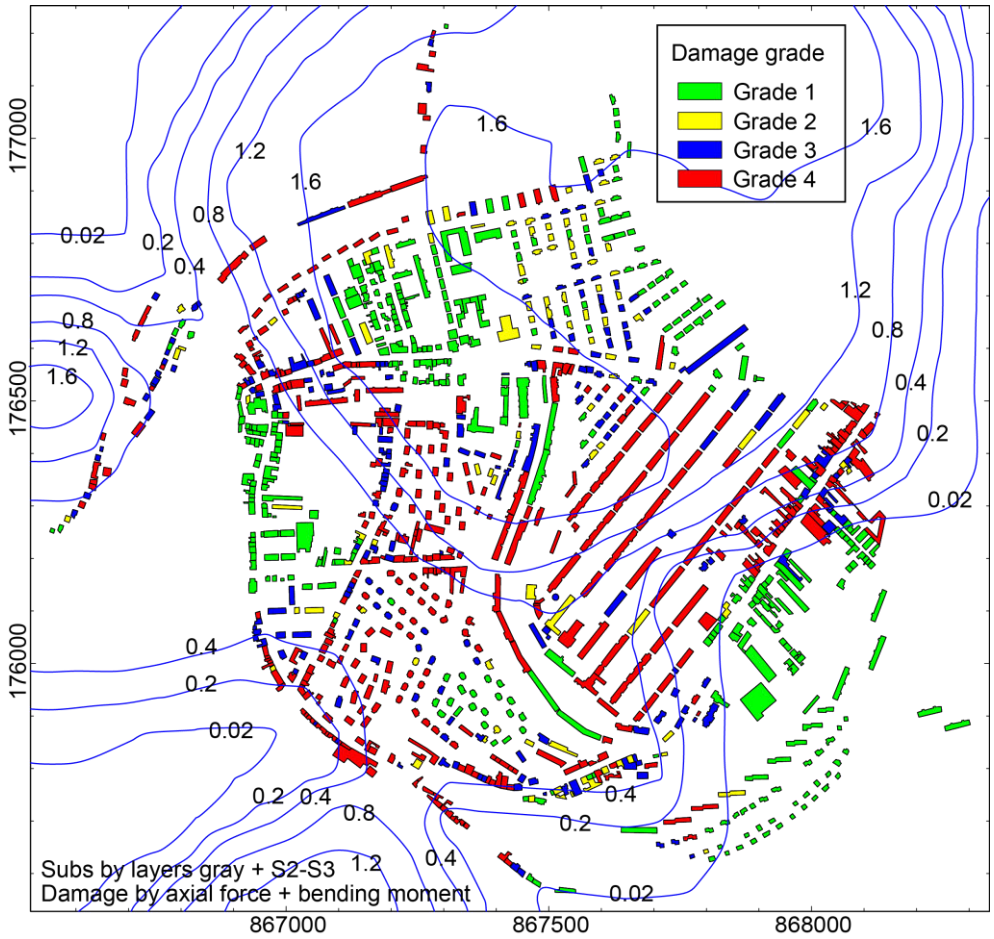

Figure 92. Evaluation of the building damage caused by mining subsidence due to the collapse of both the layer gray and layer S2-S3 (the vertical subsidence contours are plotted in the figure with the unit of meter) according to the axial forces and bending moments in the buildings

Table 37. Statistics of the proportion of the buildings in each damage grade due to the collapse of both the layer gray and layer S2-S3

Grade	Proportion of buildings in each damage grade (%)		
	According to axial force	According to bending moment	According to axial force & bending moment
1	61.06	39.12	34.74
2	8.96	8.69	8.59
3	14.35	19.56	19.56
4	15.63	32.63	37.11

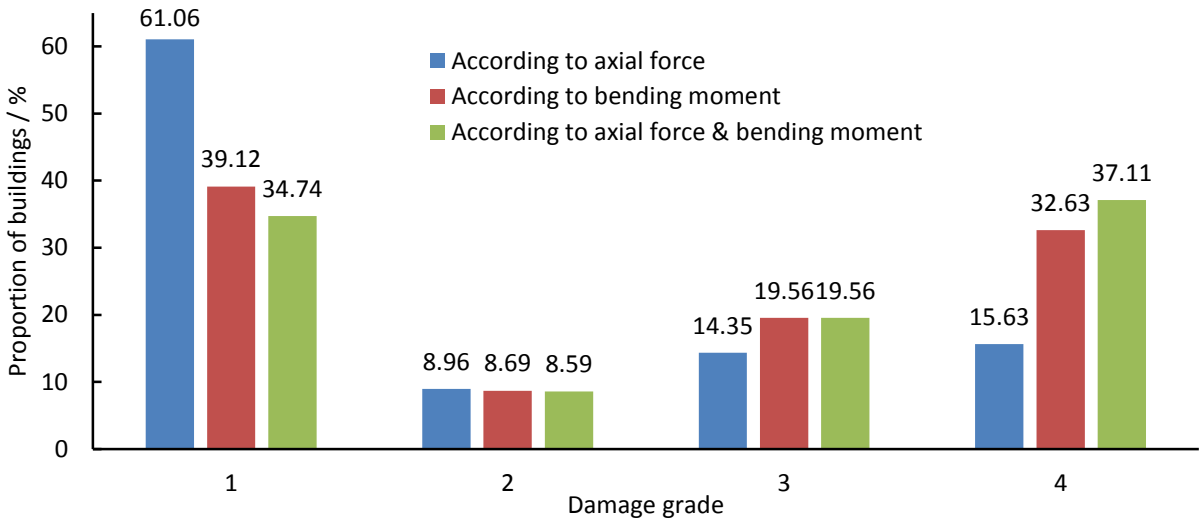

Figure 93. Comparison of the proportion of the buildings in each damage grade due to the collapse of both the layer gray and layer S2-S3

(2) Evaluation of building damage caused by the collapse of the layer gray or layer S2-S3

Using the same method of assessing the building damage caused by the multi-influence of the layer gray and layer S2-S3, the building damage grades caused separately by the collapse of any layer can also be obtained, as shown in Figure 94 (collapse of the layer gray, i.e. Polygon 1 – Polygon 3, refer to Table 25, and the vertical and horizontal subsidence contours are plotted in Figure 60 to Figure 62) and Figure 95 (collapse of the layer S2-S3, i.e. Polygon 4 – Polygon 6, refer to Table 25, and the vertical and horizontal subsidence contours are plotted in Figure 63 to Figure 65). These two figures are using the superposed results of damage grades deduced from the axial forces and bending moments. The statistics about the building's proportion in each damage grade due to the collapse of the layer gray or layer S2-S3 is listed in Table 38.

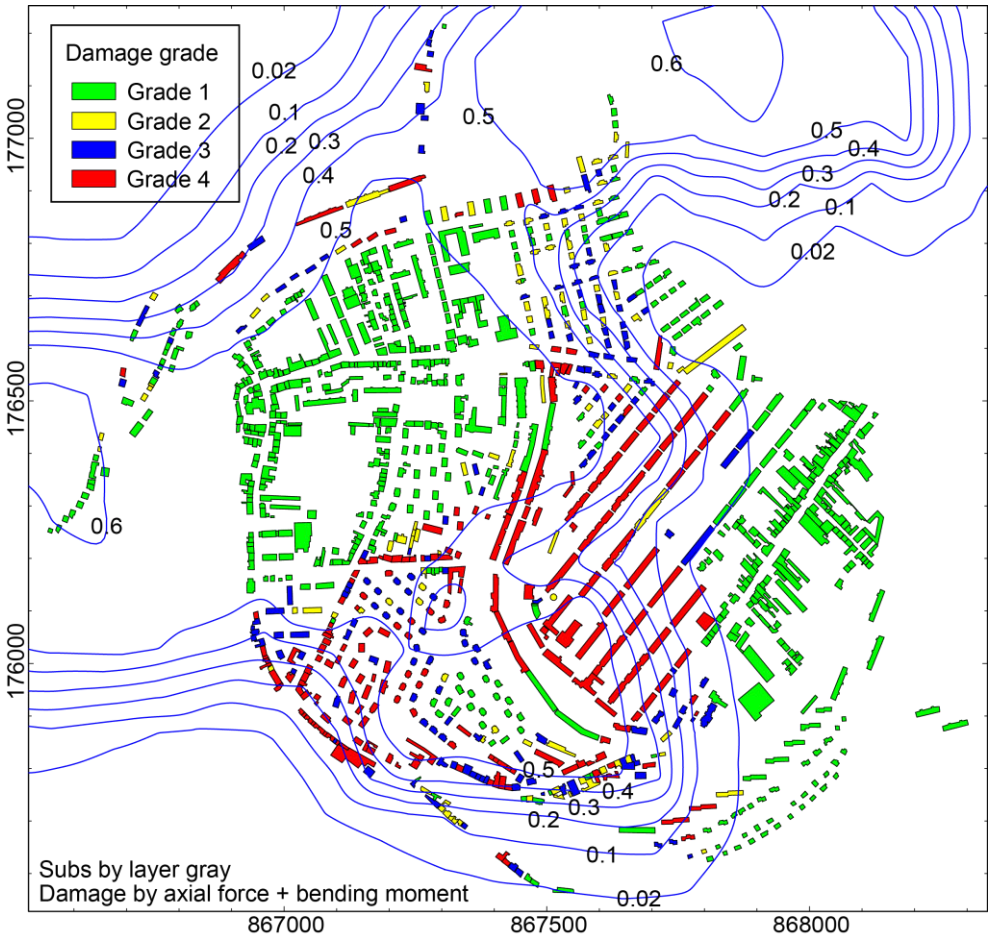

Figure 94. Evaluation of the building damage caused by mining subsidence due to the collapse of the layer gray (the vertical subsidence contours are plotted in the figure with the unit of meter) according to the axial forces and bending moments in the buildings

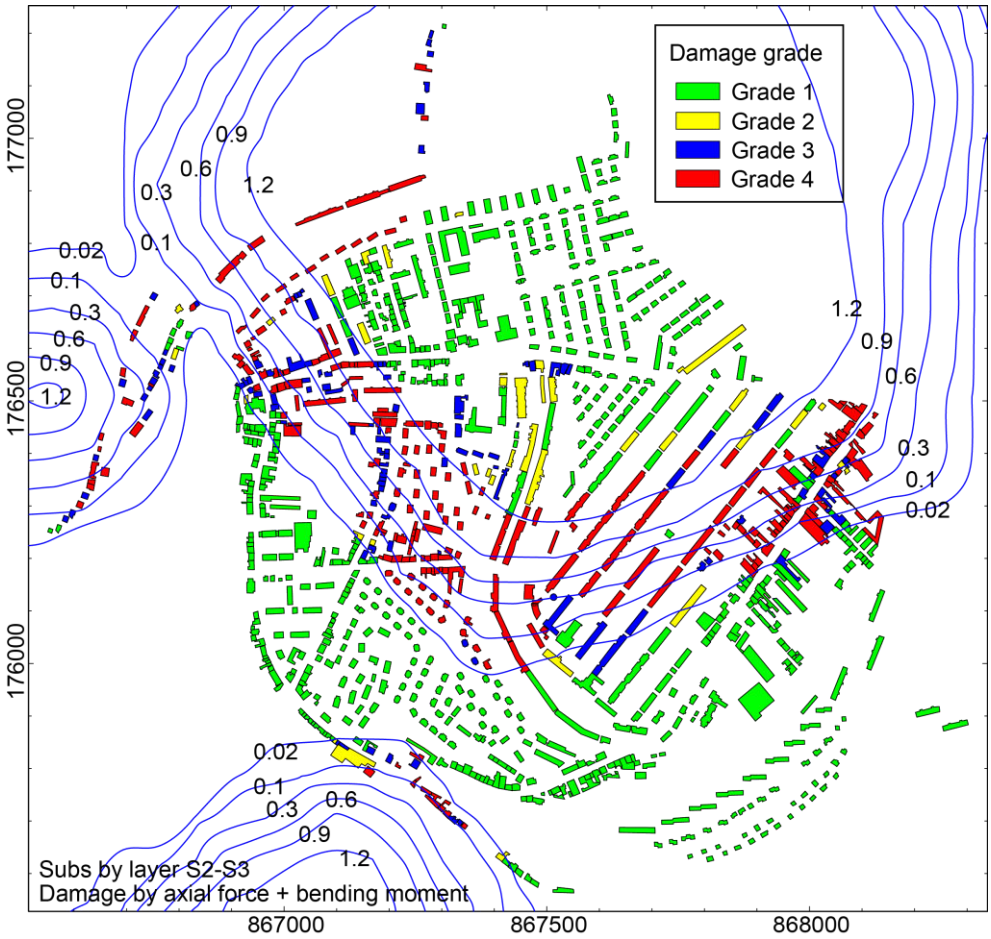

Figure 95. Evaluation of the building damage caused by mining subsidence due to the collapse of the layer S2-S3 (the vertical subsidence contours are plotted in the figure with the unit of meter) according to the axial forces and bending moments in the buildings

Table 38. Statistics of the proportion of the buildings in each damage grade due to the collapse of the layer gray or layer S2-S3

Layer	Grade	Proportion of buildings in each damage grade (%)		
		According to axial force	According to bending moment	According to axial force & bending moment
Gray	1	75.05	61.98	57.86
	2	7.22	8.59	9.14
	3	8.59	13.62	14.08
	4	9.14	15.81	18.92
S2-S3	1	77.33	64.26	60.97
	2	5.39	4.84	4.93
	3	7.22	11.43	11.52
	4	10.06	19.47	22.58

(3) Comparison with Saeidi's damage simulator

Saeidi *et al*. (2015) developed a building damage simulator, which can take subsidence intensity (mainly the horizontal strain, and also the curvature) on the structures into account. This damage simulator uses the vulnerability functions (Saeidi *et al*. 2009, and 2012), which are tangent hyperbolic functions as in Equation 58, to assess the building damage.

$$\mu_D(\varepsilon_H) = a_B[b_B + \tanh(c_B \times \varepsilon_H + d_B)] \quad \text{Equation 58}$$

Where μ_D is the damage mean value (between 0 and 1) for a value ε_H of the hazard intensity, and a_B, b_B, c_B, and d_B are four coefficients that must be determined for each building type.

Under the multi-influence of the layer gray and layer S2-S3 (horizontal strain and curvature can be derived from horizontal displacement and vertical subsidence), the building damage grades can be assessed by Saeidi's damage simulator and shown in Figure 96. The range of the damage mean value (0 to 1) is equally divided into 4 grades.

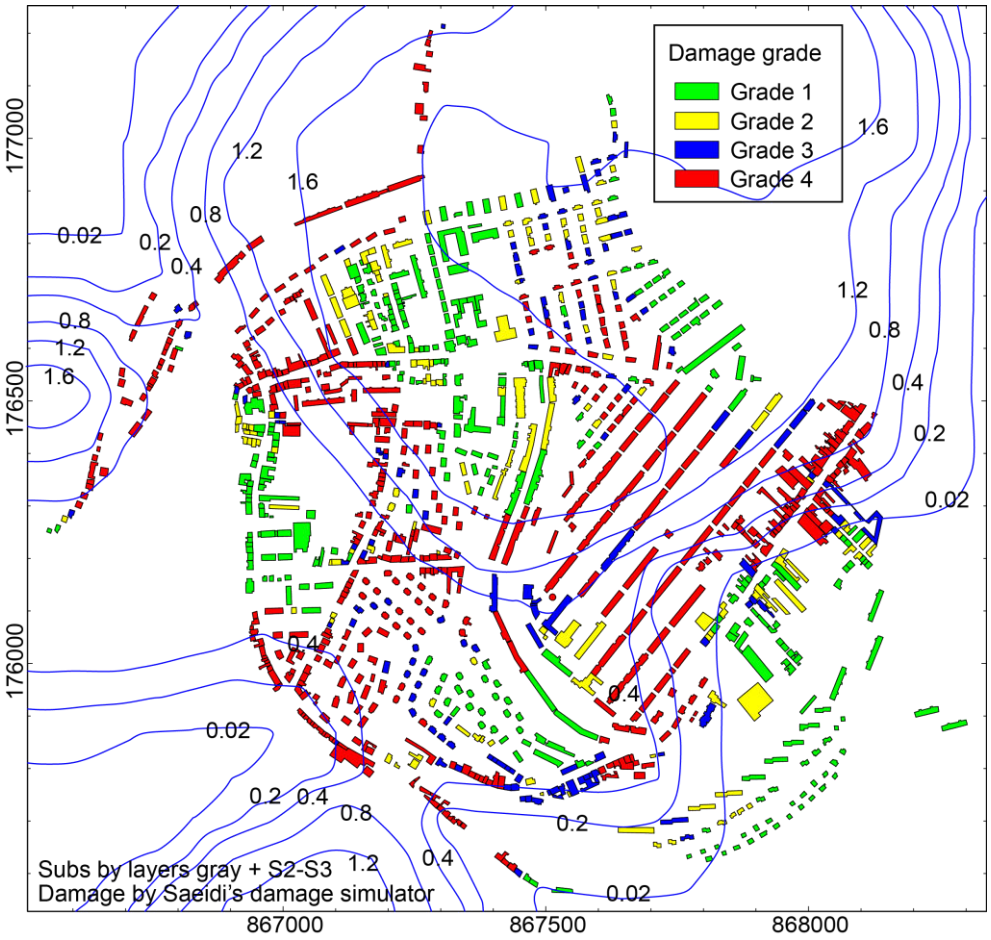

Figure 96. Using Saeidi's damage simulator to evaluate of the building damage caused by mining subsidence due to the collapse of the layer gray and layer S2-S3 (the vertical subsidence contours are plotted in the figure with the unit of meter)

Figure 97 illustrates the differences between the building damage grades as obtained from Saeidi's and our methods. The statistics about the differences are plotted in Figure 98. We can found that the building damage assessment results got by these two methods are similar: 60% of the buildings are in the same damage grades (difference equals 0); 30% of them are in the adjacent grades (difference equals 1 or -1).

Therefore, we consider that the method presented in this research can provide credible result of building damage evaluation.

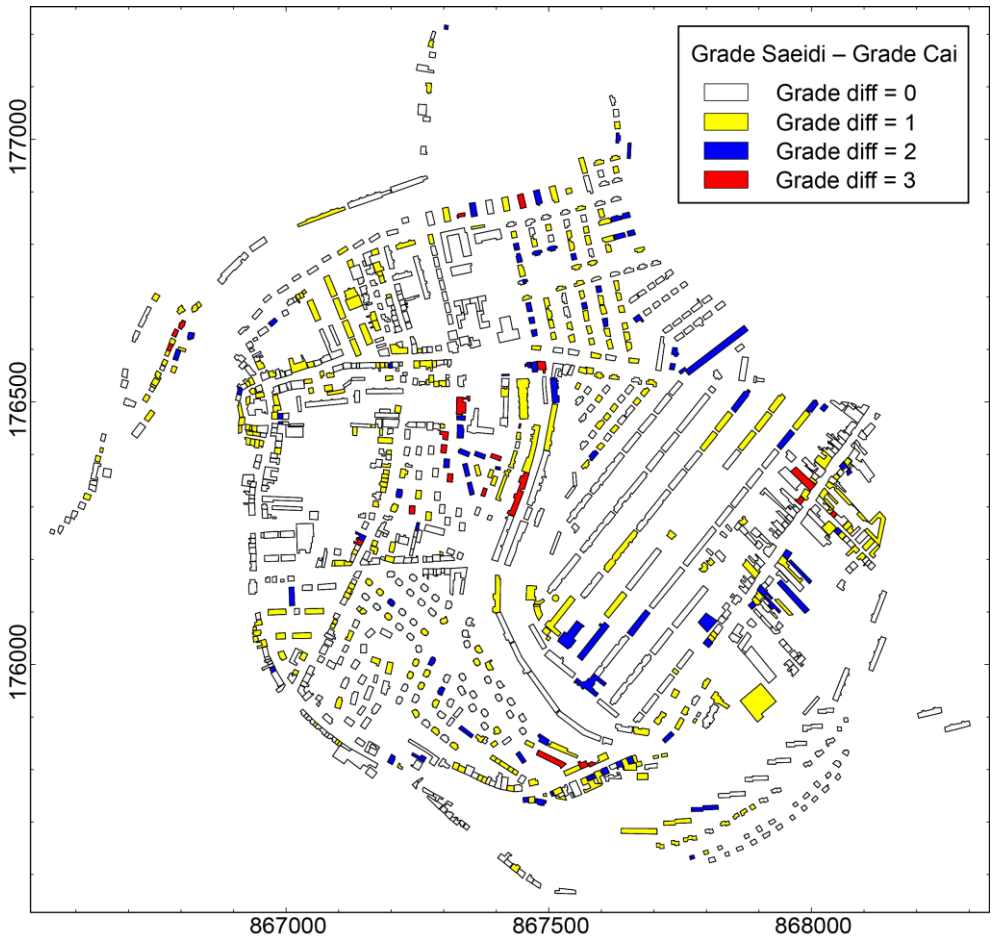

Figure 97. The differences between the building damage grades obtained by Saeidi's damage simulator and those obtained by the method presented in this research (the former minus the latter)

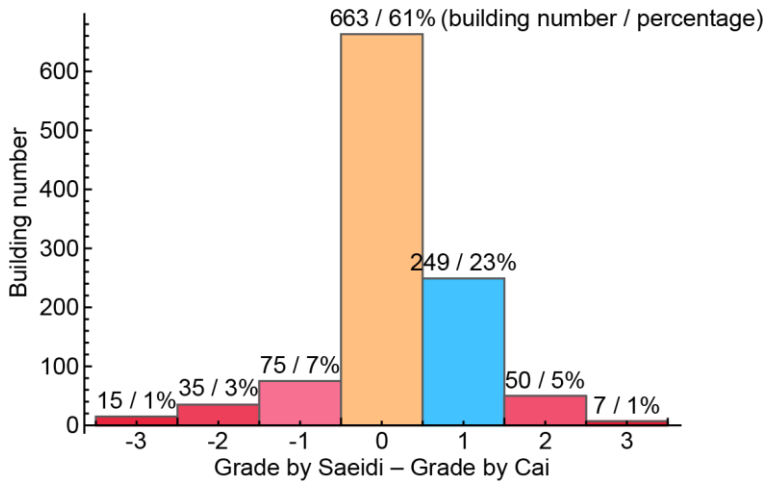

Figure 98. Distribution of the differences of building damage grades shown in Figure 97

4.5 Conclusions

The city of Joeuf is located above the iron-ore field in Lorraine (France). It has more than 1500 Buildings and more than 7000 inhabitants. The city lies in a valley with a non-flat ground surface. Under the city, at a depth of around 90 m, six mining zones (polygons) in two iron layers have been defined as potentially unstable. Taking the prepared topography and mining polygon data into account, and considering the local maximum subsidence and influence angle, we were able to compute the subsidence expected at Joeuf by the use of an improved influence function method that can take topographic variations into account as presented in chapter 2.

Investigating the buildings in Joeuf, several typical structural model shapes and element properties (including flexural rigidity and axial rigidity) were defined. Then considering the initial loads on the beams, complete structural models (without the influence of subsidence) could be assembled to simulate all the buildings. A longitudinal model and a transverse model were considered for each building.

Applying the computed mining subsidence to the defined structural models as support displacements, the internal forces could be calculated as discussed in chapter 3. Finally, the evaluations of building damage caused by subsidence were achieved through the comparison between the computed internal forces and predefined damage grade criteria. 34.74% of the buildings in Joeuf were found safe and 37.11% of them were found in relatively high danger due to the collapse of both the two iron layers. Comparison between an existing method and the method presented in this thesis showed that our method achieved similar results as the existing one.

General conclusions and perspectives

This research concerns the ground surface subsidence induced by underground exploitations, and the subsidence effects on buildings. In Lorraine, the abandoned extraction zones, which are supported by pillars after the excavation using the room and pillar method, caused several subsidence events. Particularly, since 1996, more than five hundred buildings have been affected by such events. The mining subsidence problems not only happened in Lorraine, but also in other regions of France and in other countries. Subsidence in a city induces the damage of buildings and might cause unexpected economical, environmental, social, and political chain reactions.

The objective of this thesis was to improve the methods for subsidence computation and building damage evaluation, then to develop the tools based on these methods to study the mining subsidence and building damage cases in Lorraine. The main achievements and results of this thesis are the following ones.

- Improvement of the influence function method

-- Summarized the influence function methods used in the mining subsidence computations.

The original influence function method is well adapted for predicting subsidence induced by the extraction of a horizontal stratiform layer from an underground mine beneath a flat surface, but provides improper results when the surface is not flat.

-- Studied the topography influence on the subsidence by numerical simulations.

Real-world mining conditions are too complicated to separate topography influence from influences caused by other factors. Simplified numerical simulations were studied to analyze the topography influence on subsidence only.

-- Put forward an improved influence function method, which uses new asymmetrical influence functions and can take the known maximum subsidence and influence angle into account, to simulate the mining subsidence induced by the extraction under a non-flat ground surface.

Two influence functions, based on the probability distribution function of a skew normal distribution, were selected to simulate the element vertical subsidence and horizontal displacement under non-flat surface. Their coefficients were fitted from simplified numerical simulations, and could be described in terms of surface dip angle and mean mining depth, meaning that the new influence functions took topographic variations into account. Full-scale subsidence was then computed using the new functions according to a standard summation method. Existing maximum subsidence and influence angle could be applied into the improved influence function method to enhance the computational precision.

-- Compared the subsidence results obtained by the improved influence function method with several numerical simulations and two field subsidence cases, then achieved the conclusion that this improved method can better simulate subsidence, especially in terms of horizontal displacement.

-- Limitations:

The developed subsidence computation code did not consider inclined mining zones, which has already been studied by other researchers.

The parameters of the new asymmetrical influence functions were obtained by numerical simulations using simplified ground conditions and properties of Lorraine region (France); they may also be used in other regions by applying the local maximum subsidence values and influence angles. But, if the parameter fittings can be redone before using this method in other regions, the subsidence results would be more accurate.

- Improvement of the building damage evaluation method

-- Proposed to use two plane framed structural models, which are set up in the vertical sections passing through the principal inertia axes of a building's projective polygon, to simulate a real-world 3D building.

-- Employed the matrix displacement method with some modifications to solve the internal forces and displacements over a structure, which is subjected to arbitrary external loads and support displacements. Our method was proved credible by the comparisons with two other commercial softwares.

Structural models, which were simplified from the real structure, were firstly prepared by digitizing the model into node and element lists. Then the force-displacement relations of an element were introduced using a traditional method. After that, in order to organize the force-displacement relations of the entire structural model, we skipped the step of organizing the structure stiffness matrix by directly solving a set of equations composed of the force equilibrium conditions in global coordinate system at each node. Finally, the internal forces and displacements over the structural model can be solved.

-- Put forward a new building damage evaluation method based on the mechanical properties of the structural model and the loading conditions, which were derived from the mining subsidence in this research. The subsidence, calculated by the asymmetrical influence function method presented above, was applied onto the structural model as support displacements. The extent of the building damage could be determined according to the achieved internal forces over the structure and their corresponding criteria.

This method can be used to assess the building damage caused by subsidence but not restricted to that. Furthermore, as this method is able to provide the internal forces over entire the structural model, it can also be used to estimate the damage extent of the elements even the points on a structure.

-- Limitations:

Soil-structure interactions, which are very important to building damage assessment (may significantly reduce the damage grades when taken into account), was not considered in the developed code. Then, a significant improvement for field applications would be to introduce it in either by considering extra elements at the base of each building to model the soil rigidity and its interaction with the building or by updating subsidence input values (reduce

factor) to take the presence and type of a building into account.

Non-linear strain-stress relationships were not considered in the plane frame structural model in this study. Therefore, the internal forces might be incorrect when plasticity appears in the models, especially, for the masonry buildings. This point could be very important if the kinematic of the subsidence phenomenon is intended to be taken into account for assessing the expected damages to the buildings

- Building damage evaluation in Joeuf city

-- Calculated the subsidence in Joeuf using our improved influence function method.

The city of Joeuf is located above the iron-ore field in Lorraine (France) and lies in a valley. Under the city, six mining zones (polygons) in two iron layers (the layer gray and layer S2-S3) have been abandoned. Taking the topography and mining data into account, and considering the local maximum subsidence and influence angle, we computed the subsidence expected at Joeuf.

-- Defined the structural models for the buildings (two models for each) in Joeuf with different model shapes, element properties, and initial loads.

According to the investigations in Joeuf, five sets (two models for each) of typical structural models were selected to simulate the shapes of the buildings. Then, the element properties (including the flexural rigidity EI and axial rigidity EA) and initial loads were defined for different elements of different types of buildings. Assembling the typical models, the element properties, and the initial loads, the complete structural models (without the influence of mining subsidence at present) were organized for representing the buildings in Joeuf.

-- The computed subsidence was employed into the models as support displacements to calculate the internal forces. Then comparing the internal forces with damage criteria, the damage grades of all the buildings in Joeuf were assessed. 37% of the buildings were found in high danger under the subsidence caused by the collapse of both the two undermined layers. Comparison between an existing method and the method presented in this research showed that our method could provide credible result of building damage evaluation.

- Perspectives

-- Regarding the influence function method, it would be interesting to take into account the inclined mining zones, which are commonly encountered in some other countries.

-- The building damage evaluation method is theoretically correct, but it is still interesting to compare the results obtained by this method with feedback analysis from damages actually observed after subsidence events.

-- Using 3D structural models should also provide more relevant results.

-- The soil-structure interactions could be taken into account in a future work.

-- The connections, i.e. the joints, in our structural model are all considered as well connected, that may be overestimated in the case study of Joeuf city, where the connections

in the old buildings cannot really offer the expected restrictions.

-- The influence of the discontinuities in the broken elements of a structure could be further discussed.

Conclusions générales et perspectives

Cette recherche porte sur les affaissements induits par les exploitations souterraines, et leurs conséquences sur les bâtiments. En Lorraine, les zones d'exploitation du minerai de fer qui se présentent sous la forme de chambres et piliers abandonnés, ont déjà causé plusieurs affaissements brutaux ou progressifs. En particulier, depuis 1996, plus de cinq cents édifices ont été touchés par de tels événements. De tels problèmes concernent également d'autres régions en France et dans le Monde et peuvent entraîner des conséquences économiques, environnementales, sociales et politiques inattendues.

L'objectif de cette thèse était d'améliorer les méthodes de calcul de l'affaissement du sol et des dommages aux bâtiments exposés, puis de développer des outils basés sur ces méthodes pour étudier les affaissements miniers et les dommages aux constructions en Lorraine ou ailleurs. Les principales réalisations et les principaux résultats de cette thèse sont les suivants :

- Amélioration de la méthode des fonctions d'influence

-- Synthèse des méthodes utilisant les fonctions d'influence dans le calcul des affaissements miniers.

La méthode des fonctions d'influence d'origine est bien adaptée pour prédire l'affaissement induit par l'extraction d'une couche stratiforme horizontale dans une mine souterraine sous une surface plane, mais fournit des résultats incorrects lorsque la surface du sol n'est pas plane.

-- Étude de l'influence de la topographie sur l'affaissement par des simulations numériques.

Les conditions d'exploitation du monde réel sont trop compliquées pour distinguer l'influence de la topographie des influences causées par d'autres facteurs. Des simulations numériques simplifiées nous ont permis d'analyser l'influence seule de la topographie sur l'affaissement.

-- Mis au point d'une méthode améliorée utilisant des fonctions d'influence asymétriques et pouvant prendre en compte l'affaissement maximal attendu et l'angle d'influence, pour simuler l'affaissement minier induit par l'extraction d'une couche sous une surface non plane.

Deux fonctions d'influence, basées sur des densités de probabilité d'une loi normale asymétrique, ont été élaborées pour simuler l'affaissement vertical et le déplacement horizontal élémentaire sous une surface non plane. Leurs coefficients ont été déterminés à partir de simulations numériques simplifiées, et peuvent être décrits en termes de pendage de la surface et de profondeur moyenne de l'exploitation minière. L'affaissement à grande échelle peut alors être calculé selon une méthode de superposition. La méthode permet alors de prendre en compte toutes les variations topographiques de la surface et elle peut prendre en compte la valeur de l'affaissement maximal attendu et l'angle d'influence si cette valeur est connue.

-- Comparaison des résultats obtenus avec plusieurs simulations numériques et deux cas d'affaissement réel, montrant l'amélioration significative de la méthode notamment en termes de déplacement horizontal.

- Amélioration de la méthode d'évaluation de l'endommagement des constructions

-- Proposition d'utiliser deux modèles structurels 2D dans les sections verticales passant par les axes principaux d'inertie du polygone de projection horizontale d'un bâtiment, pour simuler un bâtiment 3D du monde réel.

-- Emploi de la méthode matricielle des déplacements avec quelques modifications pour résoudre le système des forces internes et les déplacements dans une structure soumise à des charges externes et des déplacements arbitraires des fondations. La méthode a été vérifiée par comparaisons avec deux logiciels commerciaux.

Les modèles structurels, simplification de la structure réelle, sont d'abord préparés par discrétisation en noeuds et en éléments. Ensuite, les relations force-déplacement d'un élément sont introduites de manière traditionnelle. Après cela, nous sautons l'étape de l'organisation d'une matrice de rigidité de la structure en résolvant directement un ensemble d'équations composées des conditions d'équilibre des forces dans le système de coordonnées global. Enfin, les forces internes et les déplacements dans le modèle structurel peuvent être résolus.

-- Mise au point d'une nouvelle méthode d'évaluation des dommages de construction basée sur les propriétés mécaniques du modèle structurel et les conditions de chargement, ces dernières étant tirées du calcul de l'affaissement minier vu précédemment, avec les fonctions d'influence asymétriques. L'étendue des dommages peut alors être déterminée en fonction des forces internes obtenues dans la structure et la comparaison à des critères d'endommagement librement choisis.

Cette méthode peut être utilisée pour évaluer les dommages causés aux constructions lors d'un affaissement minier mais ne se limite pas à cela. En effet, comme la méthode est capable de fournir des forces internes sur la totalité du modèle de structure, elle peut également être utilisée pour estimer l'étendue des dommages même sur chacun des éléments des structures modélisées.

- Evaluation des dommages dans la ville de Joeuf

-- Calcul de l'affaissement à Joeuf en utilisant la méthode améliorée.

La ville de Joeuf est située au-dessus du gisement de minerai de fer et se trouve dans une vallée. Sous la ville, six zones (polygones) exploitées en deux couches ont été identifiés comme susceptibles de s'effondrer et de provoquer un affaissement. Prenant les données topographiques et minières en compte, et compte tenu de l'affaissement maximum et de l'angle de l'influence local, nous avons calculé l'affaissement attendu à Joeuf.

-- Définition des modèles structurels pour les bâtiments (deux modèles pour chaque) de la ville de Joeuf avec différentes formes de modèles, propriétés d'éléments et charges initiales.

Selon les données rassemblées sur les bâtiments de la ville de Joeuf, cinq ensembles (deux modèles pour chaque) de modèles structurels typiques ont été élaborés pour simuler les différentes formes des bâtiments. Ensuite, les propriétés des éléments (rigidité en flexion EI et rigidité axiale EA) et les charges initiales ont été définies pour les différents éléments des différents types de bâtiments. Puis les éléments ont été assemblés pour fournir des modèles structurels complets capables de représenter les bâtiments de Joeuf.

-- Utilisation de l'affaissement calculé comme déplacements imposés aux modèles pour calculer les forces internes, puis comparaison des forces internes à des critères de dommages, pour évaluer les niveaux de dommages de tous les bâtiments de Joeuf. 37% des bâtiments ont été trouvés en haut niveau de danger après l'affaissement causé par l'effondrement des deux couches de minerai. Une comparaison avec une méthode existante a montré que notre méthode pouvait fournir des résultats crédibles pour l'évaluation des dommages.

- Perspectives

-- En ce qui concerne la méthode des fonctions d'influence, il serait intéressant de prendre en compte les zones minières inclinées, qui sont couramment rencontrés dans certains pays.

-- La méthode d'évaluation des dommages aux bâtiments est théoriquement correcte, mais il est toujours intéressant de comparer les résultats obtenus par cette méthode à l'analyse des des dommages réellement observés après des affaissements qui se sont effectivement produit.

-- L'utilisation de modèles structurels 3D devrait également fournir des résultats plus pertinents.

-- Les interactions sol-structure pourraient être prises en compte dans un travail futur.

-- Dans nos modèles structurels, les connexions, c'est-à-dire les articulations, sont toutes considérées comme bien reliés, ce qui peut constituer une surestimation de la résistance des bâtiments dans l'étude de cas de Joeuf ville, où les connexions dans les anciens bâtiments ne peuvent pas vraiment toujours offrir les restrictions prévues.

-- L'influence des discontinuités dans les éléments brisés d'une structure pourrait être également discutée.

References

Abdallah M, Verdel T, Deck O. (2008). Vulnerability of masonry buildings to mining subsidence studied through experimental design. *Post-Mining 2008, Nancy, France*.

Akhaveissy H.A., Milani G. (2013). Pushover analysis of large scale unreinforced masonry structures by means of a fully 2D non-linear model. *Construction and Building Materials*, 41(0): 276 – 295.

Akira W, Qu Z. (2014). Materials and structural members for buildings in our age. *Building Structure*, 44(7): 1 – 8.

Al Heib M. (2002). Predicting the consequences of mines subsidence in Lorraine ferriferous region. Rapport INERIS-DRS-02-26146/RN02, Geoderis, INERIS, Nancy.

Al Heib M. (2008). State of the art of the prediction methods of short and long-term ground movements (subsidence and sinkhole) for the mines in France. *Coal Geology Research Progress, Nova Science Publishers,* pp. 53 – 76

Arcamone J. (1980). Méthodologie d'étude des affaissements miniers en exploitation totale et partielle. *Thesis of PhD, Institut National Polytechnique de Lorraine*.

ArcelorMittal. Sections and Merchant Bars - Sales Programme.

ATC. (1985). ATC-13: Earthquake damage evaluation for California. *Applied Technology Council (ATC), Redwood City, Calif*.

Attewell P.B., Yeates J. (1984). Tunnelling in soil. Ground movement and their effects on structures. *Surrey University Press*, edited by Attewell and Taylor .

Autodesk. Autodesk robot structural analysis metric getting started guide.

Bao S, Gong Y. (2006). Structural mechanics. *Wuhan University of Technology Press*.

Bentz C.E. (2000). Sectional analysis of reinforced concrete members. *Thesis of PhD, University of Toronto*.

Bhattacharya S, Singh M.M., Chen C. (1984). Proposed criteria for subsidence damage to buildings. *The 25th US Symposium on Rock Mechanics (USRMS),* pp. 747 – 755.

Boone S.J. (1996). Ground-movement related building damage. *Journal of Geotechnical Engineering*, 122(11): 886-896.

Boscardin M.D., Cording E.J. (1989). Building response to excavation-induced settlement. *Journal of Geotechnical Engineering*, 115(1): 1 – 21.

Bosiljkov V, Totoev Y.Z., Nichols J.M. (2005). Shear modulus and stiffness of brickwork masonry: an experimental perspective. *Structural Engineering and Mechanics*, 20(1): 21 – 44.

Brady B.H.G., Brown E.T. (2004). Rock Mechanics for underground mining. *Kluwer Academic Publishers*.

Burd H.J., Houlsby G.T., Augarde C.E., Liu G. (2000). Modelling tunnelling-induced settlement

of masonry buildings. *Proceedings of the ICE-Geotechnical Engineering*, 143(1): 17 – 29.

Burland J.B. (1995). Assessement of risk of damage to buildings due to tunnelling and excavation. *Earthquake geotechnical engineering*, Ishihara (ed), Balkema, pp. 1189 – 1201.

Burland J.B., Broms B.B., De Mello V.F.B. (1977). Behaviour of foundations and structures. *9th Int. conf. on soil mechanics and foundations engineering*, pp. 495 – 546.

Burland J.B., Wroth C.P. (1974). Settlement of buildings and associated damage. *Conf. settlement of structures*, pp. 611 – 654.

Burton P. (1979). Kinematics and Dynamics of Planar Machinery. *Prentice Hall*.

Burr A, Cheatham J. (1995). Mechanical Design and Analysis (2nd edition, section 5.2). *Prentice Hall*.

Cai Y, Vertel T, Deck O. (2014). On the topography influence on subsidence due to horizontal underground mining using the influence function method. *Computers and Geotechnics*, 61: 328 – 340.

Cui X, Miao X, Wang J, Shuo Y, Liu H, Song Y, *et al*. (2000). Improved prediction of differential subsidence caused by underground mining. *International Journal of Rock Mechanics and Mining Sciences*, 37(4): 615 – 627.

Cui, X, Wang J, Liu Y. (2001). Prediction of progressive surface subsidence above longwall coal mining using a time function. *International Journal of Rock Mechanics and Mining Sciences*, 38(7): 1057 – 1063.

Coulthard M.A., Dutton A.J. (1988). Numerical modelling of subsidence induced by underground coal mining. *The 29th US Symposium on Rock Mechanics (USRMS). American Rock Mechanics Association*, pp. 529 – 536.

Dai H, Lian X, Liu J, Liu Y, Zhou Y, Deng W. (2010). Model study of deformation induced by fully mechanized caving below a thick loess layer. *International Journal of Rock Mechanics and Mining Sciences*, 47(6): 1027 – 1033.

Dai H, Zhai J, Hu Y. (2000). Testing Study on Surface Displacement of Mountainous Region with Similar Material. *Chinese Journal of Rock Mechanics and Engineering*, 4: 501 – 504. (in Chinese)

DDE (Direction départementale de l'équipement de Moselle, Service, Aménagement, Habitat). (2005). Plans de prévention des risques miniers.

Deck O. (2002). Etude des conséquences des affaissements minierssur le bâti. *Thesis of PhD, Laego, Ecole des Mines Nancy.*

Deck O, Anirudh H. (2010). Numerical study of the soil–structure interaction within mining subsidence areas. *Computers and Geotechnics*, 37(6): 802 – 816.

Domede N, Sellier A, Stablon T. (2013). Structural analysis of a multi-span railway masonry bridge combining in situ observations, laboratory tests and damage modelling. *Engineering Structures*, 56: 837 – 849.

Donnelly L.J., De La Cruz H, Asmar I, Zapata O, Perez J.D. (2001). The monitoring and prediction of mining subsidence in the Amaga, Angelopolis, Venecia and Bolombolo Regions, Antioquia, Colombia. *Engineering Geology*, 59(1 – 2): 103 – 114.

Dzegniuk B, Hejmanowski R, Sroka A. (1997). Evaluation of the damage hazard to building objects on the mining areas considering the deformation course in time. *Proceedings of the 10th International Congress of the International Society for Mine Surveying, Fremantle, Australia*.

El-Sayed M, El-Heweity M, Abou-Elfath H, Mostafa R. (2011). A new beam-column model for seismic analysis of RC frames - Part I: Model derivation. *Alexandria Engineering Journal*, 50(4): 313 – 320.

Felix L.P. (1999). Compressive strength and modulus of elasticity of masonry prisms. *Thesis of master, Carleton University.*

Finno R.J., Frank T, Voss J, Rossow E, Blackburn J.T. (2005). Evaluating damage potential in buildings affected by excavations. *Journal of Geotechnical and Geoenvironmental Engineering,* 131(10): 1199-1210.

Fiorelli J, Dias A.A. (2003). Analysis of the strength and stiffness of timber beams reinforced with carbon fiber and glass fiber. *Materials Research*, 6(2): 193 – 202.

Fougeron J, Souley M, Homand F. (2005). Collapse/subsidence : role and influence of overburden in Lorraine iron mines case. *Post-Mining 2005, Nancy, France*.

Franzius J.N. (2004). Behaviour of buildings due to tunnel induced subsidence. *Thesis of PhD, University of London.*

Franzius J.N., Potts D.M., Burland J.B. (2006). The response of surface structures to tunnel construction. *Proceedings of the ICE-Geotechnical Engineering*, 159(1): 3 – 17.

Fuente J.V., Fernandez R, Albert V. (2010). Brick masonry elastic modulus determination using the numerical simulation and experiments of sonic wave propagation. *Simulation in NDT 2010*.

Geddes J.D. (1984). Structural design and ground movements. *Ground movement and their effects on structures, Surrey University Press*, edited by Attewell and Taylor.

Geoderis. (2000). Cartographie des zones influencées par l'exploitation minière dans le bassin ferrifère Briey - Longwy - Thionville. *Cédérom édité par la DRIRE de Lorraine*.

Geoderis. (2009). Source de Geoderis. Geoderis, Metz.

Goh H.K., Mair J.R. (2014). Response of framed buildings to excavation-induced movements. *Soils and Foundations*, 54(3): 250 – 268.

Golosinski T.S., Guo Y. (1996). Mining Science and Technology. *Taylor and Francis*.

Grünthal G. (1998). European Macroseismic Scale 1998 (EMS-98). *Cahiers du Centre Européen de Géodynamique et de Séismologie, Vol. 15, Luxembourg*.

Hamid T.R., Behzad F. (2014). Idealisation of soil–structure system to determine inelastic

seismic response of mid-rise building frames. *Soil Dynamics and Earthquake Engineering*, 66(0): 339 – 351.

HAZUS. (1999). Multi-hazard Loss Estimation Methodology Earthquake Model. Technical and User Manuals. *Federal Emergency Management Agency, Washington, DC*, chapter 2.

HAZUS. (2003). Multi-hazard Loss Estimation Methodology Earthquake Model. Technical and User Manuals. *Federal Emergency Management Agency, Washington, DC*.

He G, Yang L. (1991). Mining Subsidence. *Printing Press of China University of Mining and Technology*. (in Chinese)

He W. (2003). Mining Subsidence and Hazard in Mountainous Areas. *China Science and Technology Press*. (in Chinese)

Helmerich R, Niederleithinger E, Trela C, Bień J, Kamiński T, Bernardini G. (2012). Multi-tool inspection and numerical analysis of an old masonry arch bridge. *Structure and Infrastructure Engineering*, 8(1): 27 – 39.

Holla L. (1997). Ground movement due to longwall mining in high relief areas in New South Wales, Australia. *International Journal of Rock Mechanics and Mining Sciences*, 34(5): 775 – 787.

Jankowski R. (2009). Non-linear FEM analysis of earthquake-induced pounding between the main building and the stairway tower of the Olive View Hospital. *Engineering Structures*, 31(8): 1851 – 1864.

Ji-Xian C. (1985). The effects of mining on buildings and structural precautions adopted. 3e Int. Conf. *Large ground movements and structures (Cardiff)*, pp. 404 – 419.

Ji-Xian C. (1992). Study of deformation resistant structural systems for buildings in coal mining areas. *Proc. of the 4th int. conf. on ground movement and structures. Pentech press (London)*, pp. 356 – 369.

Kane T.R., Levinson D.A. (2005). Dynamics, Theory and Applications. *McGraw-Hill, New York*.

Klezhev P.E., Muller R.A., Shaglov S.E. (1980). Investigations of piled foundations for buildings in areas of mining subsidence. Edited by Geddes J. D. *Proc. of the 2nd international conference on ground movements and structures (Cardiff), Pentech press (London)*, pp. 264 – 274.

Knothe S. (1959). Observations of surface movements and their theoretical interpretation. *Colliery Engineering*, 36: 24 – 29.

Kratzsch H. (1983). Mining subsidence engineering. *Springer-Verlag*.

Kwiatek J. (1998). Protection des constructions sur les terrains miniers. (Translation from Polish: Ochrona objektow budowlanych na terenach gorniczyych.) *GIG 1998, Katowice*.

Lamond J.F., Pielert J.H. (2006). Significance of tests and properties of concrete and concrete-making materials. *ASTM International*, Vol. 169.

Leet K, Uang C.M., Gilbert A. (2011). Fundamentals of structural analysis (fourth edition).

McGraw-Hill, New York.

Lesage G. (1954). Etude des fondations. *Annales des mines de Belgique, Tome LIII, 4e livraison*, pp. 514 – 527.

Li G, Chen C, Jiang B, Shen Q. (2014). A Comparison between the Matrix Displacement Method and the Finite Element Method in Solving Frame Structure with SM Solver Software. *Applied Mechanics and Materials*, (7): 3042 – 3045.

Li W, Dai L, Hou X, Lei W. (2007). Fuzzy genetic programming method for analysis of ground movements due to underground mining. *International Journal of Rock Mechanics and Mining Sciences*, 44(6): 954 – 961.

Lian X, Jarosz A, Saavedra-Rosas J, Dai H. (2011). Extending dynamic models of mining subsidence. *Transactions of Nonferrous Metals Society of China*, 21: 536 – 542.

Liao C.P. (1993). Fuzzy influence function method for calculating mine subsidence in a horizontal seam. *Geotechnical and Geological Engineering*, 11(4): 235 – 247.

Liu G, Shi C, Liu Y. (2008). Analyses of the elastic modulus values of masonry. *Journal of Humn University (Natural Sciences)*, 35(4): 29 – 32.

Luo Y, Chen J. (2009). An influence function method based subsidence prediction program for longwall mining operations in inclined coal seams. *Mining Science and Technology (China)*, 19(5): 592 – 598.

Masoero E, Darò P, Chiaia M.B. (2013). Progressive collapse of 2D framed structures: An analytical model. *Engineering Structures*, 54(0): 94 – 102.

Melis M, Medina L, Rodríguez J.M. (2002). Prediction and analysis of subsidence induced by shield tunnelling in the Madrid Metro extension. *Canadian Geotechnical Journal*, 39(6): 1273 – 1287.

Milani G, Beyer K, Dazio A. (2009). Upper bound limit analysis of meso-mechanical spandrel models for the pushover analysis of 2D masonry frames. *Engineering Structures*, 31(11): 2696 – 2710.

Mohr S, Bairán J.M., Antonio M.R. (2010). A frame element model for the analysis of reinforced concrete structures under shear and bending. *Engineering Structures*, 32(12): 3936 – 3954.

Mosalam K, Glascoe L, Bernier J. (2009). Mechanical properties of unreinforced brick masonry, Section1. Contract DE-AC52-07NA27344 of the U.S. Department of Energy by Lawrence Livermore National Laboratory.

Nakamura N, Akita S, Suzuki T, Koba M, Nakamura S, Nakano T. (2010). Study of ultimate seismic response and fragility evaluation of nuclear power building using nonlinear three-dimensional finite element model. *Nuclear Engineering and Design*, 240(1): 166 – 180.

Nakamura N, Ino S, Kurimoto O, Miake M. (2007). An estimation method for basemat uplift behavior of nuclear power plant buildings. *Nuclear Engineering and Design*, 237(12-13): 1275

– 1287.

Nakamura N, Yabushita N, Suzuki T, Yamada J, Tsunashima N, Nakano T. (2008). Analyses of reactor building by 3D nonlinear FEM models considering basemat uplift for simultaneous horizontal and vertical ground motions. *Nuclear Engineering and Design*, 238(12): 3551 – 3560.

National Coal Board. (1975). Subsidence engineers' handbook. *National Coal Board, London, Great Britain*.

Nawy E. (2008). Concrete construction engineering handbook (second edition). *CRC Press, Taylor & Francis Group, LLC.*

Neuhaus E.H. (1965). A.B.C. de la construction des maisons d'habitation en zones d'affaissements miniers. *Editions Eyrolles*, translated by Soots.

Petit D. (2000). La maitrise des séquelles techniques à long terme des exploitations minières. *Les techniques de l'industrie minérale*, n°5 (mars 2000), 5 – 107.

Philip T.V., McCaffrey T.J. (1997). Ultrahigh strength steels. *Mechanical Engineering-New York and Basel-Marcel Dekker-,* pp. 149 – 162.

Papadrakakis M, Apostolopoulou C, Zacharopoulos A, Bitzarakis S. (1996). Three-Dimensional Simulation of Structural Pounding during Earthquakes. *Journal of Engineering Mechanics*, 122(5): 423 – 431.

Potts D.M., Addenbrooke T.I. (1997). A structure's influence on tunnelling-induced ground movements, *Proceedings of the ICE-Geotechnical Engineering*, 125(2): 109 – 125.

Ren W, Tan X, Zheng Z. (1999). Nonlinear analysis of plane frames using rigid body-spring discrete element method. *Computers & Structures*, 71(1): 105 – 119.

Reyes-Salazar A, Bojórquez E, Haldar A, López-Barraza A, Rivera-Salas J.L. (2014). Seismic Response of 3D Steel Buildings considering the Effect of PR Connections and Gravity Frames. *The Scientific World Journal*, vol. 2014, Article ID 346156.

Saeidi A. (2010). La vulnérabilité des ouvrages soumis aux aléas mouvements de terrains; Développement d'un simulateur de dommages. *Thesis of PhD, Laego, Ecole des Mines Nancy.*

Saeidi A, Deck O, Al Heib M, Verdel T. (2012). Comparaison de méthode d'évaluation de dommages de bâtis dans de zones minières, application â un cas du bassin ferrifére lorrain ---- Comparison of assessment methods of damage to building in mining areas, application to a case of the Lorraine iron basin. *Congrès international sur la gestion des rejets miniers et l'après-mine (GESRIM 2012)*.

Saeidi A, Deck O, Al Heib M, Verdel T, Rouleau A. (2013). Adjusting the Influence Function Method for Subsidence Prediction. *Key Engineering Materials*, 553: 59 – 66.

Saeidi A, Deck O, Al Heib M, Verdel T. (2015). Development of a damage simulator for the probabilistic assessment of building vulnerability in subsidence areas. *International Journal of Rock Mechanics & Mining Sciences*, 73: 42 – 53.

Saeidi A, Deck O, Verdel T. (2008). Development of a simulator of damage for evaluation of the vulnerability of buildings in subsidence zones – case study: Joeuf city. *Post-Mining 2008, Nancy, France*.

Saeidi A, Deck O, Verdel T. (2008). Développement d'un simulateur de dommages pour l'évaluation de la vulnérabilité des bâtiments en zone d'affaissement minier – application à la ville de Joeuf. *AUGC, Nancy, France*.

Saeidi A, Deck O, Verdel T. (2009). Development of building vulnerability functions in subsidence regions from empirical methods. *Engineering Structures*, 31(10): 2275 – 2286.

Saeidi A, Deck O, Verdel T. (2012). Development of building vulnerability functions in subsidence regions from analytical methods. *Géotechnique*, 62(2): 107 – 120.

Saeidi A, Deck O, Verdel T. (2013). Comparison of building damage assessment methods for risk analysis in mining subsidence regions. *Geotechnical and Geological Engineering*, 31(4): 1073 – 1088.

Selby A.R. (1999). Tunnelling in soils–ground movements, and damage to buildings in Workington, UK. *Geotechnical & Geological Engineering*, 17(3-4): 351 – 371.

Simonet F. (2001). Vulnerability du bâti, Nondkeil, Commune d'Ottange. Rapport 784 Nondkeil, Geoderis, Metz [4 volumes].

Skempton A.W., MacDonald D.H. (1956). Allowable settlement of buildings. *ICE Proceedings: Engineering Divisions*, 5(6): 727 – 768.

Son M, Cording E.J. (2005). Estimation of building damage due to excavation-induced ground movements. *Journal of Geotechnical and Geoenvironmental Engineering*, 131(2): 162 – 177.

Son M., Cording E.J. (2007). Evaluation of building stiffness for building response analysis to excavation-induced ground movements. *Journal of Geotechnical and Geoenvironmental Engineering*, 133(8): 995 – 1002.

Son M., Cording E.J. (2008). Numerical model tests of building response to excavation-induced ground movements. Canadian Geotechnical Journal, 45(11): 1611 – 1621.

Song X, Deng K, Yan Y, Dai H. (2007). Analysis of topography influence on ground displacement and deformation. *Mining Surveying*, 3(9): 70 – 72. (in Chinese)

Soots P. (1969). Le phénomène des affaissements miniers et la prévention de ses conséquences dommageables. *Cahiers du CSTB,* n° 96, cahier 836.

Speck R.C., Bruhn R.W. (1995). Non-uniform subsidence ground movement and resulting surface-structure damage. *Environmental and Engineering Geoscience*, 1(1): 61 – 74.

Spence R, Kelman I, Baxter P.J., *et al*. (2005). Residential building and occupant vulnerability to tephra fall. *Natural Hazards and Earth System Science*, 5(4): 477 – 494.

Stromberg L.L., Beghini A, William B.F., Glaucio P.H. (2012). Topology optimization for braced frames: Combining continuum and beam/column elements. *Engineering Structures*, 37(0):

106 – 124.

The European Union. (2002). EUROPEAN STANDARD EN 1991-1-1, Eurocode 1: Actions on structures - Part 1-1: General actions Densities, self-weight, imposed loads for buildings.

Timoshenko S. (1955). Strength of Materials, Part I, Elementary Theory and Problems (3rd Ed), *D. Van Nostrand Company*.

Wagner H, Schumann E.H.R. (1991). Surface effect of total coal seam extractions by underground mining methods. *Journal of the Southern African Institute of Mining and Metallurgy*, 91(7): 221 – 231.

Wang M, Yuan S. (2004). Computation of super-convergent nodal stresses of Timoshenko beam elements by EEP method. *Applied Mathematics and Mechanics*, 25(11): 1228 – 1240.

Whittaker B.N., Reddish D.J. (1989). Subsidence: Occurrence, Prediction and Control. *Editions Elsevier*.

Xu N, Kulatilake P.H.S.W., Hong T, Xiong W, Nan Y, Tian W. (2013). Surface subsidence prediction for the WUTONG mine using a 3-D finite difference method. *Computers and Geotechnics*, 48: 134 – 145.

Yu Z, Karmis M, Jarosz A. (1988). Haycocks C. Development of damage criteria for buildings affected by mining subsidence. *6th annual workshop generic mineral technology centre mine system design and ground control*, pp. 83 – 92.

Yuan S. (1993). The Finite Element Method of Lines. Beijing-New York: *Science Press*.

Yuan S, He X. (2006). A self-adaptive strategy for one-dimensional FEM based on EEP method. *Applied Mathematics and Mechanics*, 27(11): 1461 – 1474.

Yuan S, Xing Q, Wang X, Ye K. (2008). Self-adaptive strategy for one-dimensional finite element method based on EEP method with optimal super-convergence order. *Applied Mathematics and Mechanics*, 29(5): 591 – 602.

Zhang H, Liu L, Liu H. (2011). Mountain ground movement prediction caused by mining based on BP-neural network. *Journal of Coal Science and Engineering (China)*, 17(1): 12 – 15.

Zhao W, Liu L, Wang R. (2010). Experimental study on the elastic modulus of concrete solid bricking masonry. *Sichuan Building Science*, 36(4): 198 – 201.

Annex 1: The sample of subsidence data got by numerical simulations

Here, as in Table 39, is the first appearance of subsidence data got by numerical simulations. This sample data list is used to study the characteristics of subsidence changed by topography as mentioned in section 2.2.2. The subsidence curves (as in Figure 13) and maximum subsidence values (as in Table 4) can be derived from this table. The original distances between two surface points in numerical simulations are always 10 m; these data in Table 39 are reduced through removing several points.

Hereinafter, we won't offer such kind of table again. Instead, the processed data as in Figure 13 and Table 4 in section 2.2.2 will be provided directly.

Table 39. The subsidence data derived from the numerical simulations to study the characteristics of subsidence changed by topography (simplified, the distances between two points are all 10 m in numerical simulations)

Point position	Model					
	ag=0°, H=400m m_zone=400m		ag=0°, H=500m m_zone=400m		ag=15°, H=400m m_zone=400m	
X	HD (m)	VS (m)	HD (m)	VS (m)	HD (m)	VS (m)
-1200.00	0.00	-0.01	0.00	0.01	0.00	0.00
-1100.00	0.09	-0.01	0.12	0.01	0.02	0.00
-1000.00	0.19	-0.01	0.25	0.01	0.05	0.00
-900.00	0.31	0.00	0.41	0.01	0.09	0.00
-800.00	0.45	0.00	0.59	0.01	0.16	0.00
-700.00	0.64	0.00	0.82	-0.03	0.26	0.02
-650.00	0.76	-0.02	0.95	-0.07	0.33	0.03
-600.00	0.90	-0.05	1.10	-0.13	0.42	0.04
-550.00	1.07	-0.10	1.26	-0.22	0.56	0.04
-500.00	1.26	-0.20	1.43	-0.35	0.73	0.01
-480.00	1.34	-0.25	1.50	-0.42	0.82	-0.02
-460.00	1.42	-0.31	1.57	-0.50	0.91	-0.07
-440.00	1.50	-0.39	1.63	-0.58	1.01	-0.12
-420.00	1.59	-0.48	1.69	-0.68	1.11	-0.20
-400.00	1.67	-0.58	1.75	-0.78	1.22	-0.29
-380.00	1.75	-0.69	1.80	-0.90	1.32	-0.41
-360.00	1.83	-0.82	1.84	-1.02	1.43	-0.55
-340.00	1.90	-0.97	1.87	-1.16	1.52	-0.72
-320.00	1.95	-1.13	1.89	-1.31	1.60	-0.92

-300.00	2.00	-1.31	1.90	-1.46	1.67	-1.13
-280.00	2.02	-1.51	1.89	-1.62	1.71	-1.37
-260.00	2.03	-1.71	1.87	-1.79	1.72	-1.63
-240.00	2.01	-1.92	1.83	-1.96	1.70	-1.89
-220.00	1.97	-2.14	1.77	-2.13	1.64	-2.16
-200.00	1.90	-2.36	1.69	-2.30	1.55	-2.43
-180.00	1.81	-2.58	1.59	-2.47	1.43	-2.68
-160.00	1.69	-2.79	1.47	-2.62	1.28	-2.92
-140.00	1.54	-2.98	1.34	-2.77	1.09	-3.13
-120.00	1.37	-3.16	1.18	-2.90	0.88	-3.32
-100.00	1.18	-3.32	1.01	-3.02	0.65	-3.48
-80.00	0.97	-3.46	0.83	-3.12	0.41	-3.60
-60.00	0.74	-3.56	0.63	-3.20	0.15	-3.69
-40.00	0.50	-3.64	0.43	-3.26	-0.11	-3.75
-20.00	0.25	-3.69	0.21	-3.29	-0.37	-3.77
0.00	0.00	-3.70	0.00	-3.31	-0.63	-3.75
20.00	-0.25	-3.69	-0.21	-3.29	-0.88	-3.71
40.00	-0.50	-3.64	-0.42	-3.26	-1.12	-3.63
60.00	-0.74	-3.56	-0.63	-3.20	-1.34	-3.52
80.00	-0.97	-3.46	-0.82	-3.12	-1.55	-3.39
100.00	-1.18	-3.32	-1.01	-3.02	-1.74	-3.24
120.00	-1.37	-3.16	-1.18	-2.90	-1.90	-3.07
140.00	-1.54	-2.98	-1.33	-2.77	-2.04	-2.88
160.00	-1.69	-2.79	-1.47	-2.62	-2.16	-2.69
180.00	-1.81	-2.58	-1.59	-2.47	-2.25	-2.48
200.00	-1.90	-2.36	-1.69	-2.30	-2.31	-2.28
220.00	-1.97	-2.14	-1.77	-2.13	-2.35	-2.08
240.00	-2.01	-1.92	-1.83	-1.96	-2.37	-1.88
260.00	-2.03	-1.71	-1.87	-1.79	-2.37	-1.70
280.00	-2.02	-1.51	-1.89	-1.62	-2.35	-1.52
300.00	-2.00	-1.31	-1.90	-1.46	-2.32	-1.35
320.00	-1.95	-1.13	-1.89	-1.31	-2.27	-1.19
340.00	-1.90	-0.97	-1.87	-1.16	-2.21	-1.05
360.00	-1.83	-0.82	-1.84	-1.02	-2.15	-0.92
380.00	-1.75	-0.69	-1.80	-0.90	-2.08	-0.80
400.00	-1.67	-0.58	-1.75	-0.78	-2.00	-0.69
420.00	-1.59	-0.48	-1.69	-0.68	-1.92	-0.60
440.00	-1.50	-0.39	-1.63	-0.58	-1.84	-0.51
460.00	-1.42	-0.31	-1.56	-0.50	-1.76	-0.44

480.00	-1.34	-0.25	-1.50	-0.42	-1.68	-0.37
500.00	-1.26	-0.20	-1.43	-0.35	-1.60	-0.32
550.00	-1.07	-0.10	-1.26	-0.22	-1.41	-0.20
600.00	-0.90	-0.05	-1.10	-0.13	-1.23	-0.12
650.00	-0.76	-0.02	-0.95	-0.07	-1.06	-0.07
700.00	-0.64	0.00	-0.82	-0.03	-0.91	-0.03
800.00	-0.45	0.00	-0.59	0.01	-0.64	0.01
900.00	-0.31	0.00	-0.41	0.01	-0.43	0.01
1000.00	-0.19	-0.01	-0.25	0.01	-0.24	0.01
1100.00	-0.09	-0.01	-0.12	0.01	-0.09	-0.01
1200.00	0.00	-0.01	0.00	0.01	0.00	-0.03

Remark: VS means vertical subsidence; HD means horizontal displacement

Annex 2: Input and output data of the case studies of subsidence computation

(1) Case study 1 - an iron mine in France (in section 2.5.1)

From 2009 to 2011, our laboratory did some studies about an iron mine in Angevillers where a slow subsidence process has been recorded. The ground surface is slightly inclined to the west; its coordinates are listed in Table 40. Measured vertical subsidence is listed in Table 41. The coordinates of two likely collapsed mining zones are listed in Table 42. The topography, mining zones, and measured subsidence are shown in Figure 26.

Introducing the original symmetrical and our new asymmetrical influence function methods in 3D and taking the field conditions into account lead to the vertical subsidence results given in Table 43 and Table 44. The subsidence data are partly output in these two tables by reducing the mesh size of the surface to 50 to decrease the scales of the tables. The vertical subsidence iso-contours are given in Figure 26.

Table 40. The coordinates of the ground surface over an iron mine in Angevillers

Point ID	X	Y	Z	ID	X	Y	Z
1	920330	6925271	382.0	29	920730	6924971	362.5
2	920430	6925271	382.0	30	920830	6924971	369.0
3	920530	6925271	382.0	31	920930	6924971	369.0
4	920630	6925271	375.5	32	921030	6924971	375.5
5	920730	6925271	375.5	33	920330	6924871	349.5
6	920830	6925271	375.5	34	920430	6924871	343.0
7	920930	6925271	382.0	35	920530	6924871	349.5
8	921030	6925271	375.5	36	920630	6924871	356.0
9	920330	6925171	388.5	37	920730	6924871	362.5
10	920430	6925171	388.5	38	920830	6924871	369.0
11	920530	6925171	382.0	39	920930	6924871	369.0
12	920630	6925171	375.5	40	921030	6924871	375.5
13	920730	6925171	375.5	41	920330	6924771	323.5
14	920830	6925171	369.0	42	920430	6924771	336.5
15	920930	6925171	375.5	43	920530	6924771	343.0
16	921030	6925171	375.5	44	920630	6924771	356.0
17	920330	6925071	388.5	45	920730	6924771	362.5
18	920430	6925071	382.0	46	920830	6924771	369.0
19	920530	6925071	362.5	47	920930	6924771	369.0
20	920630	6925071	369.0	48	921030	6924771	375.5
21	920730	6925071	362.5	49	920330	6924671	330.0
22	920830	6925071	369.0	50	920430	6924671	336.5
23	920930	6925071	369.0	51	920530	6924671	349.5
24	921030	6925071	375.5	52	920630	6924671	356.0
25	920330	6924971	375.5	53	920730	6924671	362.5
26	920430	6924971	356.0	54	920830	6924671	375.5
27	920530	6924971	356.0	55	920930	6924671	375.5
28	920630	6924971	362.5	56	921030	6924671	375.5

Table 41. The measured vertical subsidence over an iron mine in Angevillers

Point ID	X	Y	Vertical subsidence (m)	Point ID	X	Y	Vertical subsidence (m)
R001	920918.9	6925222.3	0	R077bis	920761.0	6925362.8	0
R002	920946.4	6925251.2	0	R078bis	920731.1	6925404.4	0
R003	920979.2	6925295.7	0	R079ter	920714.0	6925449.0	0
R004	921004.4	6925323.0	0	R080bis	920695.0	6925495.7	0
R005	921029.4	6925354.4	0	R081bis	920681.7	6925538.9	0.01
R006	921079.1	6925393.3	0	R082bis	920667.3	6925585.3	0
R007	921115.5	6925390.0	0	R083bis	920644.2	6925629.7	0
R008	921138.0	6925443.9	0	R084bis	920620.9	6925674.1	0
R009	921154.4	6925481.4	0	R085bis	920591.6	6925729.4	0
R010	921169.5	6925521.2	0	R086bis	920551.7	6925801.6	0
R011	921181.2	6925563.9	0	R087bis	920522.4	6925848.5	0
R012	921222.3	6925586.3	0	R088bis	920495.7	6925896.6	0
R013	921227.0	6925534.5	0	R089bis	920468.8	6925944.6	0
R014	921235.4	6925484.1	0	R090bis	920442.1	6925997.5	0.05
R015	921305.8	6925494.0	0	R091bis	920406.4	6926062.9	0.04
R016	921317.9	6925424.1	0	R092bis	920382.4	6926121.7	0.02
R017bis	921307.7	6925370.6	0	R093	920823.2	6925195.6	0
R018	921289.9	6925337.1	0	R094	920765.4	6925202.1	0
R019	921327.2	6925333.7	0	R095	920703.0	6925206.6	0
R020	921276.7	6925292.1	0	R096bis	920649.6	6925210.9	0
R021	921237.1	6925250.5	0	R097	920672.4	6925152.2	0
R022bis	921199.0	6925205.5	0.01	R098	920709.2	6925117.6	0
R023	921163.9	6925164.8	0	R099	920749.9	6925093.6	0
R024	921127.9	6925113.5	0	R100	920730.3	6925068.6	0.01
R025	921097.2	6925058.7	0	R101	920700.7	6925037.9	0.01
R026	921049.0	6925025.1	0	R102	920669.1	6925010.0	0.01
R027	921005.7	6924993.6	0	R103	920627.6	6924999.8	0.01
R028	921013.7	6925057.0	0	R104	920658.7	6924961.0	0.02
R029bis	920975.0	6925090.2	0	R105	920682.6	6924933.2	0.04
R030	920944.7	6925116.5	0	R106	920706.9	6924892.5	0.1
R031	920906.1	6925154.3	0	R107	920708.6	6924842.0	0.31
R032bis	920883.0	6925186.0	0	R108	920779.4	6924807.6	0.24
R033	920956.0	6925147.0	0	R109bis	920810.3	6924826.3	0.12
R034	920980.6	6925185.8	0	R110	920866.9	6924863.9	0.06
R035	921005.7	6925216.4	0	R111	920944.1	6924912.2	0.02
R036bis	921033.6	6925248.7	0	R112	920899.9	6924962.0	0.01
R037bis	921060.0	6925283.8	0	R113	920859.8	6925010.6	0.01

R038bis	921079.3	6925316.4	0	R114	920900.4	6925061.2	0.02
R039	921101.1	6925355.8	0	R115bis	920816.0	6925056.6	0.01
R040	921158.3	6925395.3	0	R116	920815.1	6924998.3	0.01
R041	921205.5	6925406.6	0	R117	920763.3	6925019.3	0.02
R042	921256.4	6925411.2	0	R118	920735.4	6924992.1	0.01
R043bis	921206.3	6925357.9	-0.01	R119	920711.6	6924962.9	0.02
R044bis	921237.9	6925325.8	-0.01	R120bis	920677.0	6924827.1	0.47
R045	921284.6	6925544.4	0	R121c	920643.7	6924783.3	0.55
R046b	921363.3	6925585.9	0	R122b	920612.0	6924755.9	0.13
R047	921352.2	6925650.4	0	R123b	920580.1	6924728.4	0.1
R048	921387.4	6925690.2	-0.01	R124	920808.2	6924755.1	0.31
R049	921337.2	6925684.1	0	R125	920832.6	6924713.8	0.14
R050	921298.7	6925683.5	0	R126	920864.1	6924662.0	0.05
R051	921268.7	6925647.4	0	R127	920783.5	6925107.6	0.01
R052	921248.9	6925618.0	0	R128	920833.7	6925141.5	0
R053b	921182.7	6925607.5	0	R129	920612.0	6925205.5	0
R054	921188.0	6925631.2	-0.01	R130	920577.5	6925189.2	0
R055	921216.6	6925674.7	-0.01	R131	920621.4	6925161.5	0
R056	921242.0	6925712.6	-0.01	R132	920653.0	6925110.2	0
R057	921264.6	6925747.6	-0.01	R133bis	921080.8	6925000.6	0
R058	921289.2	6925787.0	-0.01	R134	921119.5	6924971.7	0
R059b	921173.3	6925637.3	-0.01	R135	921161.9	6924942.4	0
R060b	921164.1	6925688.6	0	R136bis	921201.2	6924914.5	0.02
R061bis	921161.5	6925722.8	0	R137bis	921242.2	6924884.7	0
R062bis	921159.6	6925764.6	0	R138b	921282.4	6924857.2	0.01
R063bis	921157.8	6925807.8	0	A001	921342.3	6925290.1	0
R064ter	921155.9	6925850.6	0	A003bis	921192.9	6925998.6	0
R065bis	921157.0	6925889.7	0.01	A005	920545.2	6925176.6	0
R066ter	921170.3	6925944.0	0.01	A007	920350.9	6926202.0	0.01
R067bis	920879.2	6925220.7	0	R139	920765.9	6924879.6	0.05
R068bis	920851.8	6925255.2	0	R140	920627.0	6924895.1	0.07
R069bis	920827.8	6925283.0	0	R141	920638.6	6924855.0	0.19
R070ter	920793.3	6925323.7	0	R142	920740.4	6924924.9	0.02
R071	920819.0	6925386.1	0	R143	920768.8	6924960.7	0
R072	920846.7	6925406.8	0	R144	920845.2	6924909.8	0.01
R073	920881.8	6925374.2	0.01	R145	920587.2	6924808.4	0.11
R074	920900.7	6925357.2	0.01	R146	920526.1	6924686.2	0.03
R075	920881.1	6925323.7	0.01	R147	920692.9	6924739.3	0.14
R076	920906.3	6925295.5	0	R148	920778.1	6924688.5	0.06

Table 42. The coordinates of the two likely collapsed mining zones in Angevillers

mzone1 (polygon)				mzone2 (polygon)			
Point ID	X	Y	Z	Point ID	X	Y	Z
1-1	218.33	211.66	205.00	2-1	375.76	262.75	205.00
1-2	291.80	306.34	205.00	2-2	436.79	242.91	205.00
1-3	339.16	272.75	205.00	2-3	423.74	152.74	205.00
1-4	266.04	176.91	205.00	2-4	350.89	170.09	205.00

Table 43. The calculated vertical subsidence data using the original symmetrical influence function method in Angevillers

Point ID	X	Y	Vertical subsidence (m)	Point ID	X	Y	Vertical subsidence (m)
1	920550	6924650	0.00	29	920750	6924650	0.01
2	920550	6924700	0.00	30	920750	6924700	0.06
3	920550	6924750	0.01	31	920750	6924750	0.20
4	920550	6924800	0.01	32	920750	6924800	0.28
5	920550	6924850	0.00	33	920750	6924850	0.18
6	920550	6924900	0.00	34	920750	6924900	0.04
7	920550	6924950	0.00	35	920750	6924950	0.00
8	920600	6924650	0.00	36	920800	6924650	0.02
9	920600	6924700	0.02	37	920800	6924700	0.10
10	920600	6924750	0.09	38	920800	6924750	0.28
11	920600	6924800	0.12	39	920800	6924800	0.27
12	920600	6924850	0.05	40	920800	6924850	0.09
13	920600	6924900	0.01	41	920800	6924900	0.01
14	920600	6924950	0.00	42	920800	6924950	0.00
15	920650	6924650	0.01	43	920850	6924650	0.01
16	920650	6924700	0.04	44	920850	6924700	0.04
17	920650	6924750	0.26	45	920850	6924750	0.12
18	920650	6924800	0.43	46	920850	6924800	0.12
19	920650	6924850	0.24	47	920850	6924850	0.04
20	920650	6924900	0.05	48	920850	6924900	0.00
21	920650	6924950	0.00	49	920850	6924950	0.00
22	920700	6924650	0.00	50	920900	6924650	0.00
23	920700	6924700	0.04	51	920900	6924700	0.00
24	920700	6924750	0.22	52	920900	6924750	0.01
25	920700	6924800	0.46	53	920900	6924800	0.01
26	920700	6924850	0.35	54	920900	6924850	0.00
27	920700	6924900	0.08	55	920900	6924900	0.00
28	920700	6924950	0.00	56	920900	6924950	0.00

Table 44. The calculated vertical subsidence data using the improved asymmetrical influence function method in Angevillers

Point ID	X	Y	Vertical subsidence (m)	Point ID	X	Y	Vertical Subsidence (m)
1	920550	6924650	0.00	29	920750	6924650	0.02
2	920550	6924700	0.00	30	920750	6924700	0.07
3	920550	6924750	0.02	31	920750	6924750	0.24
4	920550	6924800	0.02	32	920750	6924800	0.28
5	920550	6924850	0.00	33	920750	6924850	0.15
6	920550	6924900	0.00	34	920750	6924900	0.03
7	920550	6924950	0.00	35	920750	6924950	0.00
8	920600	6924650	0.00	36	920800	6924650	0.02
9	920600	6924700	0.02	37	920800	6924700	0.07
10	920600	6924750	0.13	38	920800	6924750	0.24
11	920600	6924800	0.20	39	920800	6924800	0.25
12	920600	6924850	0.07	40	920800	6924850	0.08
13	920600	6924900	0.00	41	920800	6924900	0.01
14	920600	6924950	0.00	42	920800	6924950	0.00
15	920650	6924650	0.00	43	920850	6924650	0.01
16	920650	6924700	0.04	44	920850	6924700	0.03
17	920650	6924750	0.28	45	920850	6924750	0.11
18	920650	6924800	0.48	46	920850	6924800	0.12
19	920650	6924850	0.29	47	920850	6924850	0.04
20	920650	6924900	0.03	48	920850	6924900	0.00
21	920650	6924950	0.00	49	920850	6924950	0.00
22	920700	6924650	0.00	50	920900	6924650	0.00
23	920700	6924700	0.03	51	920900	6924700	0.00
24	920700	6924750	0.20	52	920900	6924750	0.01
25	920700	6924800	0.41	53	920900	6924800	0.01
26	920700	6924850	0.32	54	920900	6924850	0.00
27	920700	6924900	0.06	55	920900	6924900	0.00
28	920700	6924950	0.00	56	920900	6924950	0.00

(2) Case study 2 - a coal mine in China (in section 2.5.2)

The subsidence of a transverse section of the #2307 working face, which is a fully mechanized caving coal mine working face in Jincheng city of China, is studied. Table 45 and Table 46 list the coordinates of the ground surface and the #2307 working face. The subsidence got by field surveying and subsidence calculated by the original as well as the new influence function methods can also be found in Table 47, Table 48 and Table 49. All these input and output data are shown in Figure 27.

Table 45. The coordinates of the ground surface over the #2307 working face in Jincheng

Point ID	X	Z	Point ID	X	Z
1	-482.50	928.76	15	86.51	907.26
2	-283.96	942.18	16	116.44	921.31
3	-262.82	931.74	17	171.81	929.69
4	-240.56	924.28	18	188.10	936.12
5	-210.74	914.34	19	215.79	938.27
6	-196.02	910.86	20	239.75	935.82
7	-175.26	903.41	21	255.34	942.25
8	-145.44	899.93	22	277.22	941.64
9	-126.86	893.21	23	293.04	944.09
10	-113.82	892.43	24	327.71	943.17
11	-85.08	880.73	25	343.76	939.19
12	-59.59	880.34	26	377.85	937.65
13	-4.47	902.97	27	402.75	939.19
14	55.39	904.92	28	419.73	943.48

Table 46. The coordinates of the #2307 working face in Jincheng

Point ID	X	Z	Point ID	X	Z
1	0.00	680.00	2	147.50	680.00

Table 47. The measured subsidence over the #2307 working face in Jincheng

Point ID	X	VS (m)	HD (m)	Point ID	X	VS (m)	HD (m)
1	-483.02	0.00	-0.04	17	153.04	-0.87	-0.76
2	-295.15	0.00	0.00	18	171.58	-0.65	-0.64
3	-230.03	-0.01	-0.02	19	186.72	-0.61	--
4	-195.46	0.00	0.00	20	204.64	-0.38	-0.57
5	-167.25	0.00	0.00	21	222.67	-0.27	-0.41
6	-92.11	0.01	0.02	22	240.21	--	-0.43
7	-57.04	-0.05	-0.06	23	257.95	-0.19	-0.40
8	-41.51	-0.15	-0.02	24	274.48	-0.15	-0.35
9	-23.98	-0.41	0.10	25	294.02	-0.10	-0.30
10	-10.81	-0.65	0.29	26	310.55	-0.10	-0.17
11	11.73	-1.24	0.55	27	327.59	-0.05	-0.22
12	29.26	-1.84	0.57	28	350.13	-0.01	-0.20
13	48.33	-2.63	0.01	29	376.18	0.00	-0.19
14	63.35	-2.41	-0.38	30	400.73	0.00	-0.22
15	82.40	-2.16	-0.85	31	419.76	0.00	-0.26
16	102.94	-1.56	-0.82				

Remark: VS means vertical subsidence; HD means horizontal displacement

Table 48. The calculated subsidence data using the original symmetrical influence function method in Jincheng

Point ID	X	VS (m)	HD (m)	Point ID	X	VS (m)	HD (m)
1	-220	0.00	0.00	31	80	-2.60	-0.09
2	-210	0.00	0.00	32	90	-2.52	-0.24
3	-200	0.00	0.00	33	100	-2.37	-0.35
4	-190	0.00	0.00	34	110	-2.20	-0.44
5	-180	0.00	0.00	35	120	-2.00	-0.51
6	-170	0.00	0.00	36	130	-1.80	-0.55
7	-160	0.00	0.00	37	140	-1.57	-0.56
8	-150	0.00	0.00	38	150	-1.35	-0.54
9	-140	0.00	0.00	39	160	-1.12	-0.50
10	-130	0.00	0.00	40	170	-0.91	-0.44
11	-120	0.00	0.00	41	180	-0.73	-0.39
12	-110	0.00	0.00	42	190	-0.57	-0.33
13	-100	0.00	0.00	43	200	-0.42	-0.26
14	-90	0.00	0.00	44	210	-0.30	-0.20
15	-80	-0.01	0.01	45	220	-0.19	-0.14
16	-70	-0.05	0.04	46	230	-0.11	-0.08
17	-60	-0.11	0.09	47	240	-0.06	-0.04
18	-50	-0.23	0.16	48	250	-0.03	-0.02
19	-40	-0.40	0.25	49	260	-0.01	-0.01
20	-30	-0.61	0.34	50	270	0.00	0.00
21	-20	-0.84	0.42	51	280	0.00	0.00
22	-10	-1.10	0.49	52	290	0.00	0.00
23	0	-1.36	0.54	53	300	0.00	0.00
24	10	-1.62	0.57	54	310	0.00	0.00
25	20	-1.88	0.57	55	320	0.00	0.00
26	30	-2.11	0.52	56	330	0.00	0.00
27	40	-2.31	0.45	57	340	0.00	0.00
28	50	-2.47	0.34	58	350	0.00	0.00
29	60	-2.57	0.20	59	360	0.00	0.00
30	70	-2.61	0.06	60	370	0.00	0.00

Remark: VS means vertical subsidence; HD means horizontal displacement

Table 49. The calculated subsidence data using the improved asymmetrical influence function method in Jincheng

Point ID	X	VS (m)	HD (m)	HD2 (m)	Point ID	X	VS (m)	HD (m)	HD2 (m)
1	-220	0.00	0.00	0.00	31	80	-2.04	-0.44	-0.54
2	-210	0.00	0.00	0.00	32	90	-1.75	-0.54	-0.66
3	-200	-0.01	0.00	0.00	33	100	-1.51	-0.60	-0.73
4	-190	-0.01	0.00	0.00	34	110	-1.32	-0.62	-0.76
5	-180	-0.01	0.00	0.00	35	120	-1.19	-0.66	-0.82
6	-170	-0.02	0.00	0.00	36	130	-1.07	-0.68	-0.84
7	-160	-0.02	0.00	0.00	37	140	-0.94	-0.67	-0.83
8	-150	-0.03	0.00	0.00	38	150	-0.82	-0.64	-0.79
9	-140	-0.04	0.00	0.00	39	160	-0.71	-0.60	-0.73
10	-130	-0.05	0.00	0.00	40	170	-0.61	-0.53	-0.65
11	-120	-0.06	0.00	0.00	41	180	-0.52	-0.46	-0.56
12	-110	-0.08	0.00	0.00	42	190	-0.36	-0.40	-0.50
13	-100	-0.06	0.00	0.00	43	200	-0.22	-0.33	-0.41
14	-90	-0.04	0.00	0.00	44	210	-0.11	-0.24	-0.30
15	-80	-0.03	0.00	0.01	45	220	-0.04	-0.16	-0.20
16	-70	0.00	0.07	0.07	46	230	-0.01	-0.10	-0.11
17	-60	-0.21	0.13	0.08	47	240	0.00	-0.06	-0.07
18	-50	-0.50	0.17	0.07	48	250	0.00	-0.04	-0.05
19	-40	-0.71	0.18	0.07	49	260	0.00	-0.03	-0.03
20	-30	-0.81	0.17	0.07	50	270	0.00	-0.01	-0.02
21	-20	-1.01	0.24	0.12	51	280	0.00	-0.01	-0.01
22	-10	-1.21	0.32	0.20	52	290	0.00	0.00	-0.01
23	0	-1.42	0.42	0.32	53	300	0.00	0.00	0.00
24	10	-1.62	0.53	0.46	54	310	0.00	0.00	0.00
25	20	-1.79	0.63	0.63	55	320	0.00	0.00	0.00
26	30	-2.10	0.51	0.50	56	330	0.00	0.00	0.00
27	40	-2.35	0.34	0.33	57	340	0.00	0.00	0.00
28	50	-2.53	0.14	0.12	58	350	0.00	0.00	0.00
29	60	-2.62	-0.07	-0.11	59	360	0.00	0.00	0.00
30	70	-2.37	-0.29	-0.36	60	370	0.00	0.00	0.00

Remark: VS means vertical subsidence; HD means horizontal displacement; HD2 means horizontal displacement when α_2 times 1.5

Annex 3: The building typology in mining subsidence area

The building typology in mining subsidence area, which is used in this thesis, is firstly put forward by our laboratory (Saeidi *et al*. 2008, 2009, and 2010). Relevant parameters of buildings for this typology are mainly chosen from the criteria used in the empirical methods (NCB 1975, Bhattacharya *et al*. 1984, Yu *et al*. 1988, Wagner *et al*. 1991, Dzegniuk *et al*. 1997, Kwiatek 1998) and on the accepted perception of the loading process of the buildings (Kratzsch 1983). The selection of parameters also refer to the typological studies in the city of Nonkeil located in the ferriferous basin regions in Lorraine (Simonet 2001), and the building typologies developed in other subjects, for example, volcanic engineering (Spence *et al*. 2005) or earthquake engineering (HAZUS 1999, ATC-13 1985, and EMS-98 1998). All these researches show that a typology must not be too complex to be operational.

Based on these studies, four main parameters, including structural material, length, foundation, and shape, are selected for the building typology. Each parameter may include several criteria. These chosen four parameters are explained as follows.

(1) Structural material

Four types of structural material are considered. The first two, the masonry structure and the reinforced concrete structure, are subdivided, because most of the buildings in the Lorraine region in France are of those types. Several categories are similar to those defined in EMS-98 (Grünthal 1998), such as rubble stone/fieldstone, unreinforced brick/concrete blocks, reinforced brick, and confined masonry.

a) Masonry structure

----- Poor masonry that consists of rubble stones, fieldstones, and adobe or earth bricks with poor quality mortar without protection against mining subsidence effects (MR)

----- Good masonry that consists of bricks or concrete blocks with good quality mortar and with a possible weak reinforcement (MB)

----- Reinforced and confined masonry that consists of bricks or concrete blocks with good quality mortar and with horizontal and vertical reinforcement (MC)

b) Reinforced concrete structure

----- Reinforced concrete frame structure (CF)

----- Reinforced concrete shear wall structure (CS)

c) Steel structure (ST)

d) Wooden structure (WO)

(2) Building length

According to the threshold values of length used in the empirical methods, and also according to the traditional length of buildings in the Lorraine region, five categories (L, M, H, V, and E) of building length are defined as in Table 50.

Table 50. Classification of building length

Description	Length value	Group name
Low	Less than 10 m	L
Medium	Between 11 and 20 m	M
High	Between 21 and 30 m	H
Very high	Between 31 and 40 m	V
Exceptional	More than 41 m	E

(3) Building foundation

Building foundations have been classified into nine categories (refer to Figure 99), depending on their depth into the ground and their resistance against lateral load.

----- Foundation under floor space with reinforced concrete floor (VB) or without concrete floor (VS), as in Figure 99(a)

----- Simple foundation with or without reinforced concrete slab (SB, SS), as in Figure 99(b)

----- Cellar without concrete slab and with or without reinforced concrete floor (CB, CC), as in Figure 99(c)

----- Cellar with concrete slab and with or without reinforced concrete floor (DB, DS), as in Figure 99(d)

----- Raft foundation (RA), as in Figure 99(e)

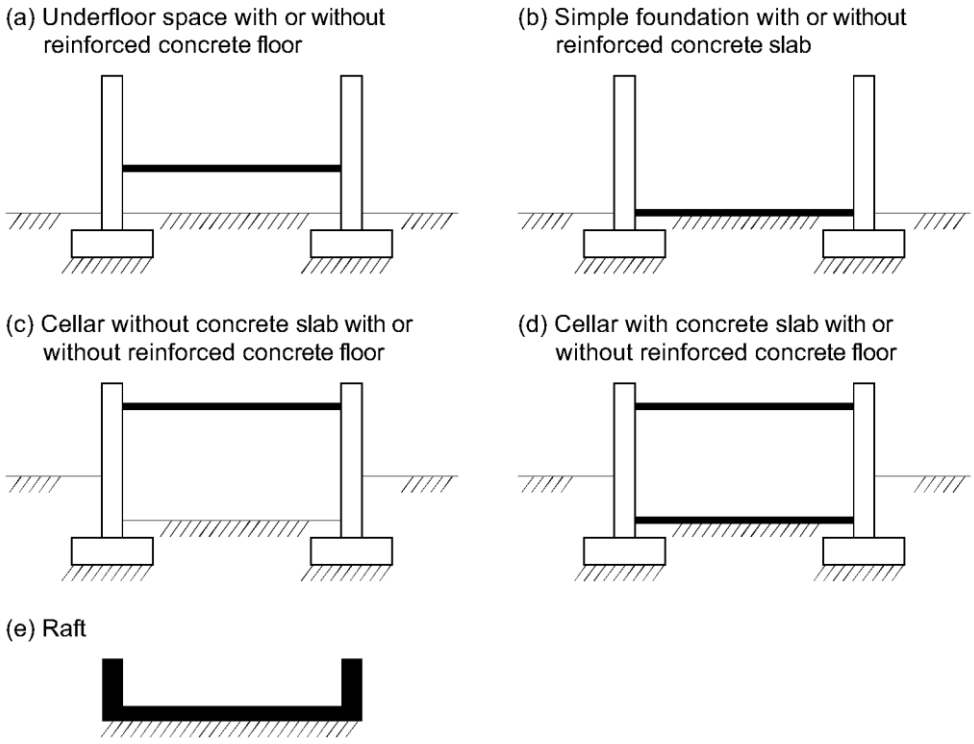

Figure 99. Types of foundations considered in the typology

(4) Building shape

For the shape of building, six categories have been defined according to the simplicity or compactness of the external shape, the regularity of the external shape, and the symmetry of the interior bearing walls.

----- Simple external shape with good symmetry or bad symmetry of the bearing walls (SR, SN)

----- Little dismembered external shape with good symmetry or bad symmetry of the bearing walls (LR, LN)

----- Strongly dismembered external shape with good symmetry or bad symmetry of the bearing walls (FR, FN)

All the aforementioned categories of the selected four relevant parameters of building for the building typology in mining subsidence area are summarized in Table 51. This developed typology can lead to 1890 theoretical building types (7 materials × 5 lengths × 9 foundations × 6 shapes).

Table 51. The summary of the categories of the selected four relevant parameters of building for the building typology in mining subsidence area

Material	Length	Foundation	Form
MR, MB, MC CF, CS ST WO	L M H V E	VB, VS SB, SS CB, CC DB, DS RA	SR, SN LR, LN FR, FN

In the ferriferous basin regions in Lorraine, most of the buildings are workers' housing estates with similar characteristics and are constructed of masonry (Simonet 2001). Around 70% of the buildings in these regions may be grouped into five types (as in Table 52). The name of each type is constructed by merging the name of each parameter.

Table 52. The most common building types in Lorraine region

Type name	Material	Length	Foundation	Form
MR M SS SR	MR	M	SS	SR
MR M DB SR	MR	M	DB	SR
MR H DB FN	MR	H	DB	LR
MC M DB LR	MC	M	DB	LR
CF M DB SN	CF	M	DB	SN

Annex 4: Some detailed information about the investigations in Joeuf

We did some investigations (Saeidi 2010) in the city of Joeuf to clarify the construction eras and the representations of the buildings. The main achievements are described in section 4.3.1, and the photographs of the buildings are shown in Figure 100.

Building No.50 (Parcelle 648) in zone 1

Building No.692 (Parcelle 372-373) in zone 1

Building No.330 (Parcelle 112) in zone 3

Building No.334 (Parcelle 89) in zone 3

Building No.525 (Parcelle 676) in zone 4

Building No.549 (Parcelle 660) in zone 4

Building No.1000 (Parcelle 249-250) in zone 5A

Building No.208 (Parcelle 177-178) in zone 6A

Building No.994 (Parcelle 174-175) in zone 5B

Building No.1036 in zone 6B

Building No.1004 (Parcelle 245-246) in zone 5E

Building No.963 (Parcelle 216-217) in zone 5E

Building No.1121 (Parcelle 1350-1351) in zone 7

Building No.1259 (Parcelle 1422-1425) in zone 7

Building No.1436 in zone 10

Building No.14 in zone 10

Building in zone 11

Building No.898 in zone 10

Building No.307 in zone 2A

Building No.264 in zone 2A

Building No.140 in zone 2B

Building No.131 in zone 2B

Building No.143 in zone 2C

Building No.145 in zone 2C

Building No.167 in zone 2D

Building No.218 in zone 2D

Building No.486 in zone 9

Building No.14 in zone 9

Figure 100. Photographs of the typical buildings in Joeuf

According to the building typology in mining subsidence area (Saeidi *et al*. 2008, 2009, and 2010, refer to Annex 3) and the investigated building characteristics (illustrated in Figure 69, Figure 70 and Table 27 in section 4.3.1), the types of the buildings in the visited zones (zones 1, 3, 4, 5, 6, 7, 10, and 11) are listed in Table 53. For the zones that have not been well visited (zones 2, 8, 9, 12, 13, 14, and 15), hypotheses are made based on the construction eras, the sizes, and the photographs of the buildings. Then, the building types in these zones are listed in Table 54.

Table 53. Types of the buildings in the visited zones (zones 1, 3, 4, 5, 6, 7, 10, and 11) in Joeuf (the positions of the zones can refer to Figure 69 and Figure 70 in section 4.3.1, the meanings of the building typology can refer to Annex 3)

Zone	Material	Length	Foundation	Shape	Type name
1, 5E, 7	MR	H	CB	LR	MR H CB LR
3, 4, 5A, 6A	MR	M	CB	SR	MR M CB SR
5B-6B, 10	MR	M	CB	LR	MR M CB LR
11	MC	M	VB	LR	MC M VB LR

Table 54. Types of the buildings in the unvisited zones (zones 2, 8, 9, 12, 13, 14, and 15) in Joeuf (the positions of the zones can refer to Figure 69 and Figure 70 in section 4.3.1, the meanings of the building typology can refer to Annex 3)

Zone	Material	Length	Foundation	Shape	Type name
2A, 2B	MC	H	DB	LR	MC H DB LR
2C, 9	MC	M	CC	LR	MC M CC LR
2D	CF	E	RA	SR	CF E RA SR
12	MC	H	DB	LR	MC H DB LR
8, 13, 14, 15	The buildings in these zones are quite heterogeneous, and most of the buildings are supposed to be unreinforced masonry.				

Furthermore, as illustrated in Figure 69, Figure 70, and Table 27, there are many connected houses in Joeuf. We will combine these connected houses together to reform new buildings with great lengths, that is, a set of connected houses is considered as one building unit.

This operation leads to some changes to the types of the buildings. In the case of the buildings in zones 3, 5A, and 6A, the individual buildings have a length of about 15 m (category M in our building typology), but the lengths of the combined buildings are about 30 m (category H). Also due to the combination, the shapes of the buildings change from simple to complex. Therefore, the original type MRMCBSR of the buildings in these zones converts to MRHCBLR. The combination work should also be done to the buildings in zones 1, 5E, 7, and 10, then the combined buildings can be considered as with high lengths (category H) and little dismembered external shapes (category LR). For zones 2A, 2B, and 11A, buildings are combined and are considered as with a length of about 30 m (category H).

Simulation of underground mining subsidence and its induced damages on buildings

The objective of this thesis is to improve the methods of subsidence computation and building damage evaluation, and to develop some tools based on these methods to study the mining subsidence and building damage cases in Lorraine.

By investigating the topography influence on subsidence under simplified mining conditions, and using numerical models with varying mining depths and ground surface angles, a new influence function method, which is based on a probability density function of a skew normal distribution, to simulate the element subsidence, was firstly developed and can be used to compute the mining subsidence caused by the excavation under non-flat surface.

Then, plane framed structural models were chosen to study the mechanical behavior of 3D buildings. For each building, two plane models located in the vertical sections passing through the principle inertia axes of the building's projective polygon were considered. Their geometry and mechanical characteristics were chosen according to the construction type and used materials of the building under consideration. Then, by using the matrix displacement method with some modifications, the internal forces and displacements for the entire structure could be computed. The achieved internal forces could then be compared to damage grade criteria to determine the extent of building damage.

Finally, by using the improved methods of subsidence computation and building damage evaluation, a real case application was performed in Joeuf city (France). The subsidence was computed and applied to the defined structural models as support displacements, and then the damage extents of the buildings in Joeuf were predicted.

Keywords: mining subsidence, topography influence, numerical simulation, asymmetrical influence function, building damage assessment, matrix displacement method, structural modeling

Simulation des affaissement miniers et de leurs conséquences sur le bâti

L'objectif de cette thèse est, d'une part, de proposer une amélioration des méthodes d'estimation des cuvettes d'affaissement et des méthodes d'évaluation des dommages susceptibles de se produire sous leurs effets et de l'autre, de développer des outils basés sur ces méthodes pour étudier les affaissements et les dommages sur des cas pratiques.

L'étude de l'influence de la topographie sur les cuvettes d'affaissement dans des conditions d'exploitation simplifiées grâce à des modèles numériques avec des profondeurs d'exploitation et des pentes du sol variables a permis de proposer une nouvelle fonction d'influence basée sur une densité de probabilité normale asymétrique lorsque la surface du sol est non-plane.

Une modélisation simplifiée des habitations en maçonnerie sous la forme de deux modèles de structures bidimensionnels croisés, alignés avec les axes d'inertie de la structure étudiée et dans lesquels la méthode des déplacements est mise en œuvre pour calculer les efforts internes et les déformations sous l'effet de déplacements imposées des fondations. Ces modèles simplifiés dont les caractéristiques géométriques et mécaniques sont définis pour chaque type de bâtiment étudié permettent d'estimer les efforts appliqués à chaque bâtiment d'une ville exposée à un affaissement de terrain et de fournir de nouveaux critères d'évaluation des dommages prenant en compte davantage d'informations que les méthodes habituelles.

Une estimation des dommages dans la ville de Joeuf sur la base des nouvelles méthodes proposées, tant pour le calcul de l'affaissement que pour l'estimation des dommages, a été réalisée.

Keywords: mining subsidence, topography influence, numerical simulation, asymmetrical influence function, building damage assessment, matrix displacement method, structural modeling